Doctoral theses at NTNU, 2019:317

Samuel Senanu

Cathode Wear in Aluminium Electrolysis Cells

Doctoral thesis

Samuel Senanu

ISBN 978-82-326-4230-4 (printed ver.)
ISBN 978-82-326-4231-1 (electronic ver.)
ISSN 1503-8181

NTNU
Norwegian University of
Science and Technology

NTNU
Norwegian University of Science and Technology
Thesis for the Degree of
Philosophiae Doctor
Faculty of Natural Sciences
Department of Materials Science and
Engineering

Doctoral theses at NTNU, 2019:317

NTNU
Norwegian University of
Science and Technology

Samuel Senanu

Cathode Wear in Aluminium Electrolysis Cells

Thesis for the Degree of Philosophiae Doctor

Trondheim, November 2019

Norwegian University of Science and Technology
Faculty of Natural Sciences
Department of Materials Science and Engineering

NTNU
Norwegian University of
Science and Technology

NTNU
Norwegian University of Science and Technology

Thesis for the Degree of Philosophiae Doctor

Faculty of Natural Sciences
Department of Materials Science and Engineering

ISBN 978-82-326-4230-4 (printed ver.)
ISBN 978-82-326-4231-1 (electronic ver.)
ISSN 1503-8181

Doctoral theses at NTNU, 2019:317

Printed by NTNU Grafisk senter

This thesis has been submitted to

Department of Materials Science and Engineering
Norwegian University of Science and Technology

in partial fulfilment of the requirements for
the academic degree

Philosophiae doctor

November 2019

Preface

The present thesis is based on work carried out at the Functional Materials and Materials Chemistry research group (FACET), Department of Materials Science and Engineering (IMA), Norwegian University of Science and Technology (NTNU), Trondheim, in the period January 2016 to April 2019. The work was done under the supervision of Professor Tor Grande (IMA) and co-supervised by Senior Research Scientist Dr Arne Petter Ratvik (SINTEF Industry) and Adjunct Assistant Professor and Research Scientist Dr Zhaohui Wang (IMA and SINTEF Industry).

The PhD project was financed by the Norwegian Research Council together with the industrial partners Hydro Aluminium AS, Alcoa, Elkem Carbon and Skamol AS through the CaRMa (Reactivity of Carbon and Refractory Materials used in Metals Production Technology) project.

All experimental work presented in this thesis has been conducted by the author, except the initial X-ray tomography experiments performed by Research Scientist Stein Rørvik, SINTEF industry. All the autopsies were carried out by the author, and these investigations took place at one smelter at Hydro Aluminium AS and two smelters at Alcoa Norway.

Parts of this dissertation have been published in the following publications:

S. Senanu, A.P. Ratvik and T. Grande, “Role of Pitting in the Formation of Potholes in Carbon Cathodes”, ICSOBA 41, p787-796, 2016

S. Senanu, C. Schøning, S. Rørvik, Z. Wang, A.P. Ratvik and T. Grande, “Cathode Wear Based on Autopsy of a Shutdown Aluminium Electrolysis Cell”, Light Metals (TMS), p561-570, 2017.

S. Senanu, A.P. Ratvik, T. Grande, “Pitting on Carbon Cathodes in Aluminium Electrolysis Cells”, ICSOBA 43, p643-654, 2018.

S. Senanu, Z. Wang, A.P. Ratvik, T. Grande, “Carbon Cathode Wear in Aluminium Electrolysis Cells”, JOM, 2019 (online).

A.P. Ratvik, S. Senanu, Z. Wang, and T. Grande, “Understanding Cathode Wear,” Australasia Aluminium Smelting Technology Conference, 2018.

Trondheim, November 4, 2019

Samuel Senanu.

Acknowledgements

I am deeply grateful for the opportunity to pursue a PhD degree at the Department of Materials Science and Engineering of the Norwegian University of Science and Technology. Sincere gratitude and appreciation go to my patient, intelligent and engaged supervisor, Professor Tor Grande. Firstly, for giving me the unique opportunity of working on this interesting, educative and challenging project and secondly, for being there for me throughout these three tough years. Professor, your patience, understanding and extensive knowledge in diverse fields of materials science made it possible for me to complete this herculean task. You always made sure I knew and understood what I was saying or writing and constantly challenged me to base all my discussions on facts and keep it simple. I would also like to thank my co-supervisor Dr Arne Petter Ratvik (SINTEF) for the many fruitful and interesting discussions on a variety of topics in your office, Arne Petter. Your in-depth knowledge in the fields of electrochemistry and carbon materials always proved useful in our discussions, and I learnt so much from you. Your office was always opened to me for discussions even without any prior appointments. I also thank you for accepting to have me in the CaRMa Project and proofreading all my articles as well as this PhD thesis together with Tor. To Dr Zhaohui Wang (SINTEF-NTNU), my second co-supervisor, I want to thank you, for introducing me to the FEM-COMSOL software program and for your invaluable input to my work.

Most of the work done in the course of this PhD was at Aluminium smelting plants, and for that reason, I want to thank the workers at the different smelters for allowing me to come and conduct autopsies at their plants. I want to thank the workers at my own Alcoa Mosjøen, this smelting plant and its workers would forever be a part of me. I especially want to thank G. Nyland, Dr K. Å. Rye, S. Stordahl, V. Villmones, E. Myrvold, Ø. Nilsskog, K. R. Elstad, A. Granå, N. Omdahl, F. T. Røli, T. Krutnes, A. Hoff, R. Leirvik, the team leaders and all workers at the cathode shop and Potrooms for the opportunity to work you. It was indeed great fun and joy working with you all, thank you all very much. I also want to thank E. Hagen, J. Hajasova, S. K. Sund and all the cathode workshop team for helping me with the autopsies at Hydro Sunndalsøra. I thank T. Nakkestad, J. I. Johannessen and K. Johansen for the autopsy at Alcoa Lista. Thank you to J.A Johansen (Elkem Carbon) and M. S. Jensen (Hydro) for providing me with carbon cathode samples and to Aksel Alstad (NTNU) for machining them for me. Fruitful discussions with chief research scientist A. Solheim (SINTEF), H. Gudbrandsen (SINTEF), V. Haslund and Dr W. Gebarowski made it possible for me to conduct the wetting experiments and for that, I thank you all very much. Thank you S. Rørvik (SINTEF) for introducing me to the world of CT scanning and 3D scanning.

Acknowledgements

Appreciations go to my immediate research group mates Gøril Jahrsengene (my office mate), Trond Brandvik and Raymond Luneng. You guys were always available when I needed someone. Your help contributed a great deal in providing a smooth transition from work life to school life after so many years away from school. It was always fun travelling to conferences and science meetings with you guys. Profound gratitude goes to all the researchers, engineers and leaders connected to the CaRMa project for always approving my publications and giving me good feedbacks. The dinners and discussions we had during our scientific meetings were amazing. To all the professors, researchers, colleagues and technical staff at K1 and K2, I say a big thank you for a good working environment. Special thanks go to Jostein M., Vidar B., Elin K., Hilde N, Eli B., Magnus and Kristin H. for all the help. To Katie, Solveig, Rani and Anuvansh, I say thank you for accepting to organize my PhD defence party.

Appreciations also go to my colleagues at SINTEF Industry EHTM group for providing a conducive working environment for me. I would especially thank my boss Egil Skybakmoen for showing interest in my project. I enjoyed our discussions on the complexity of cathode wear. I also want to thank Christian Schøning for being with me to conduct my first autopsy at Hydro Sunndalsøra and always asking me about my pittings and potholes. To Bjarte Øye, I thank you for the coffee, chocolates and laughter. Thank you to Ove Darel for helping me with my samples. To Camilla, Anne, Ana Maria, Karen, Hoai, Heiko, Jools and John Inge, I say thank you for providing a conducive working environment.

To Juliano, Torolf and Eva, I say a big thank you for taking care of my family in Mosjøen while I was away in Trondheim. You would forever be members of this family. To Ernest, Esther, Charles, Bright, Patricia, Theophilus, Joyce, John, Miriam, Samuel, papa Willie, mama Fifi, pastor Jean, Mama Espe, Obed, Naa, Frederik, Christiana, Seth, Abena, Gabriel, Gloria, Maa Paulina, Maa Hilda, Mr Ohene, Simeon, Ernestine, Ernest, Linda and many more, I say thank you for your friendship

Words cannot explain my profound gratitude to my family for all the sacrifices they had to make because of this project. Thank you very much to my mothers Philomena and Christiana for coming all the way from Ghana to help us even during the cold winters. Daddy Hector Senanu, thanks for everything. To my angels, Christina, Joseph and Sarah-Angela, it was your love, jokes, smiles and joy that fuelled this journey. To Sarah, my wife and best friend, I say it was your sacrifice, encouragement and love that made it possible. I love and appreciate you so much for being my backbone through it all. I dedicate this work to you and our wonderful kids.

Summary

The increasing global demand for aluminium has resulted in growing production of aluminium metal through increased production capacity and improvement of the electrolysis technology. This has caused a development towards larger cells and higher current densities, which have resulted in the use of more graphitized cathode blocks and larger anodes. These changes have also resulted in reduced cathode life, which has become one of the major challenges in the aluminium industry. Carbon cathode wear is the major cause of reduced cathode life. The main objective of this thesis was to investigate possible mechanisms behind carbon cathode wear, specifically the role of pitting on the carbon cathodes. The work consisted of two parts. Autopsies and characterizations of spent potlinings constituted the first part of the work. The second part focused on laboratory studies of wetting of carbon cathode materials since wetting has been pointed out as one important factor related to cathode wear.

Autopsies of six spent potlinings were conducted during the course of the study. The cells were operated at three different smelters with different cell technologies and with cathode blocks of different carbon types and properties. Macro wear patterns were documented by a combination of visual observations, photography and laser interferometry. Samples of the electrolyte at the cathode surface and cylindrical samples drilled out of the cathodes were collected and characterized by a combination of X-ray tomography, X-ray diffraction, optical and scanning electron microscopy as well as different computer software programs to characterize the micro wear.

Typical W and WW wear patterns were identified for the spent potlinings with prebaked anodes, while a relatively uniform wear was found for the Søderberg spent potlining. Closer inspections of all the cathode surfaces revealed a wear pattern characterized by pitting, resembling pitting corrosion of metals. X-ray tomography, as well as optical microscopy, revealed that the pitting observed did not correlate with the distribution of aggregates within the carbon matrix of the cathode blocks. The characteristic size of the pitting, measured by interferometry, did not correlate with the average aggregate size in the cathode blocks determined by X-ray tomography. No other evidence of aggregate or grain detachment was found in any of the spent potlinings. Furthermore, a uniform wear surface across the aggregates and the binder matrix indicates a non-preferential wear all over the carbon-electrolyte interface. It was therefore concluded that cathode wear in these potlinings was not dominated by grain pull-out or a detachment mechanism. Moreover, a difference in pitting size between the pitting spotted at the cathode block ends and the centre channel areas of the graphitic cathode blocks point to a wear process facilitated by high current density and faster transport rates. Also, an important finding was the partly overlapping and

clustered pitting observed in several of the potlinings. This observation suggests that new pittings evolve as the growth of older ones slow down.

In all the spent potlinings a layer of electrolyte, covering the whole cathode surface, was observed. Al_4C_3 was often found below the layer of electrolyte on the cathode surface. The presence of electrolyte and Al_4C_3 between the carbon cathode and the metal pad points to limited wettability of the carbon cathode by the molten Al metal pad. The electrolyte found on the cathode surface was shown to consist mainly of phases such as CaF_2, Na_3AlF_6 and Al_2O_3, while the bulk bath consisted mainly of phases like $NaCaAlF_6$, $Na_5Al_3F_{14}$ and Al_2O_3. These findings demonstrated that the electrolyte on the cathode surface was basic in composition relative to the composition of the bulk bath. The main phases found in the electrolyte within the pores of the cathode lining included NaF, implying a cryolite ratio higher than 3. This confirmed the basic nature of the electrolyte found on the cathode surface.

The following hypothesis for the pitting of the cathode surface was proposed based on the autopsies and wetting experiments. Cathode wear is closely linked to the formation of Al_4C_3, AlF_3 content in the electrolyte and the current density. Further, AlF_3 is consumed due to the formation of Al_4C_3 on the cathode surface. The consumption of AlF_3 results in a more basic bath which increases the liquidus temperature and results in partly or completely solidification of the molten bath close to the cathode surface. More basic bath also reduces the transport of Al_4C_3 away from the surface due to the lower solubility of Al_4C_3 in the basic bath. Frozen bath on the carbon cathode surface also slows down the formation of Al_4C_3 due to locally reduced current density and carbide dissolution. Supply of fresh molten bath with a higher AlF_3 content will restart the wear process through re-melting of the frozen bath or supply of a new reactive liquid phase, causing new carbide formation, dissolution and transport. Increased cathode surface temperature due to hot running cells can also re-melt the frozen bath and restart the wear process. The hypothesis was supported by finite element method simulations of the current density for a situation with partly solidified bath at the cathode surface. The simulations demonstrated that freezing of electrolyte drastically reduces the local current density at the cathode surface, which will locally hinder the formation of Al_4C_3.

The wettability of four different types of carbon cathode materials by molten electrolyte and aluminium was investigated by the immersion-emersion technique. The weight of a cylindrical sample was measured during an immersion-emersion cycle in the molten electrolyte or a combination of the electrolyte and molten aluminium. The electrolyte was contained in a graphite crucible also used as anode. A constant current was applied for 30 s at the final immersion position using the sample as the cathode. The wetting experiments carried out in molten electrolyte revealed that none of the carbon materials was wetted by the molten electrolyte. A change in wettability from non-wetting to wetting and the resulting electrolyte penetration into the carbon material occurred within seconds after cathodic

polarization. The wettability remained even when the current was switched off but declined over time. The amount of electrolyte that penetrated the carbon materials can be ranked as Anthracitic > Graphitic > Graphitized > Graphite. It was also shown that all the carbon materials were wetted by the electrolyte in equilibrium with molten Al, but the amount of electrolyte that penetrated into the carbon samples were clearly lower than under cathodic polarization. Moreover, cathodic polarization did not change the wetting induced by molten Al significantly. No wettability was achieved between the carbon materials and the molten Al even with cathodic polarization. Electrolyte and Al_4C_3 were confirmed present between the carbon cathode and Al metal on the cathodically polarized carbon samples.

Table of Content

List of Figures

List of Figures

List of Figures

List of Figures

List of Tables

List of Tables

List of Symbols

ACD	Anode-Cathode Distance (cm)
CB	Cathode Block
CR	Cryolite Ratio
CT	X-ray Computed Tomography
EDS	Energy Dispersive X-ray Spectroscopy
Em	Emersion
f_b	Buoyancy factor (g/cm)
FEM	Finite Element Methods
Imm	Immersion
MHD	Magneto-Hydro-Dynamic
m_m	Measured weight (g)
m_o	Weight of sample in gas (g)
m_σ	Weight corrected for buoyancy effect/Corrected weight (g)
P	Sample perimeter (cm)
Ra	Surface Roughness (µm)
SEM	Scanning Electron Microscopy
SPT	Sodium polytungstate
V	Volume of liquid displaced (cm^3)
XRD	X-Ray Diffraction
ρ	Density (g/cm^3)
γ_{sg}, γ^{sg}	Surface energy at solid-gas interface (J/m^2)
γ_{sl}, γ^{sl}	Surface energy at solid-liquid interface (J/m^2)
Θ_a/ Θ_r	Advancing contact angle /Receding contact angle (°)
σ_{lg}, σ^{lg}	Surface tension at liquid-gas interface (J/m^2)

1

Chapter 1. Background

1.1. Aluminium Electrolysis

The global aluminium production has increased steadily since the electrolysis process was established, and the total global production of aluminium reached 64.3 million tonnes in 2018 [1]. This is due to its numerous applications owed to its low density, corrosion resistance as well as its important metallic properties, such as electrical and thermal conductivity and mechanical properties.

Technically, the production of aluminium begins with the refinery of bauxite, the raw material, which contains 40-60 % Al_2O_3 in the form of different hydrous aluminium oxides, (gibbsite $Al(OH)_3$, boehmite AlO(OH) and diaspore AlO(OH)) to pure alumina using the Bayer process [2]. The Bayer process, developed in 1887 by Karl Joseph Bayer, involves the caustic digestion of crushed bauxite at high pressure and temperature, followed by clarification, precipitation, washing and calcination. Aluminium metal is produced from the alumina which has been extracted in the Bayer process [2].

Charles Martin Hall from the USA and Paul Louis Toussaint Héroult from France concurrently developed in 1886 the process by which aluminium could be produced from alumina in commercial quantities [2, 3]. The process, named the Hall-Héroult process, involves the electrolytic reduction of alumina (Al_2O_3) in a molten fluoride electrolyte consisting of mainly cryolite (Na_3AlF_6) contained in an electrochemical reduction cell [2-4]. The principle of the electrolysis cell is shown in Figure 1.1. Typical features of the Hall-Héroult reduction cell include the carbon anodes, which are consumed and conduct electrical current to the electrolyte and the cathode. Molten Al is the electrolytic cathode in the electrolysis cell. However, the carbon cathode lining is commonly denoted the cathode in the industry [5]. The overall reaction to produce aluminium by the Hall-Héroult process is described by equation (1.1).

$$\frac{1}{2}Al_2O_3(diss) + \frac{3}{4}C(s) \rightarrow Al(l) + \frac{3}{4}CO_2(g) \qquad (1.1)$$

Theoretically, it can be deduced from Equation (1.1) that 1.89 kg of alumina and 0.33 kg of carbon is required to produce 1 kg of aluminium metal on the cathode and 1.22 kg of CO_2 at the anode. The actual amounts of carbon consumed differ from the theoretical amount mainly due to air burn and reaction with CO_2 [2, 4, 5].

1.1. Aluminium Electrolysis

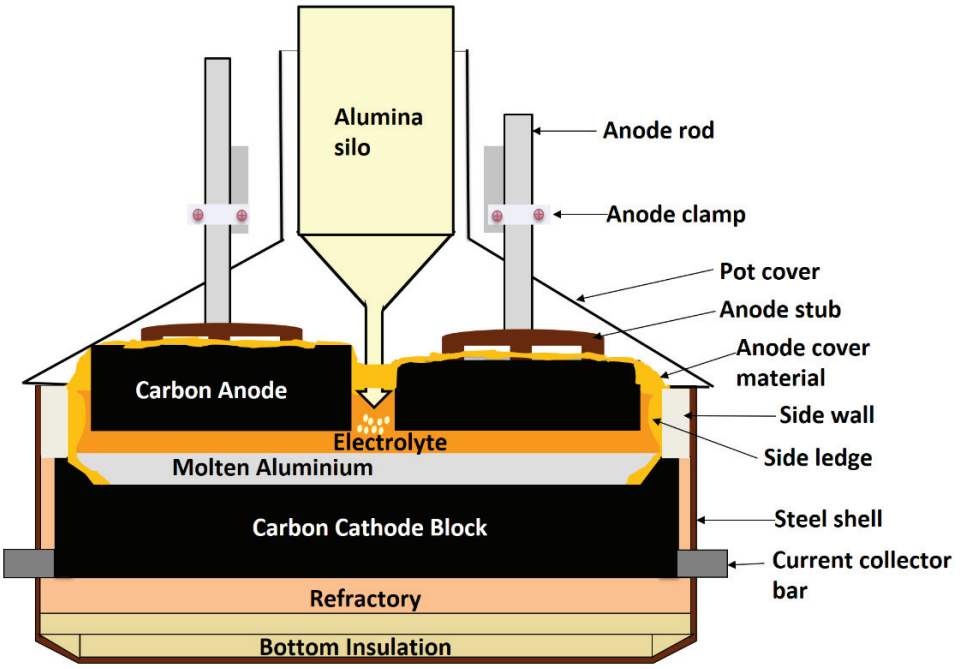

Figure 1.1. A cross-sectional sketch of an aluminium electrolysis cell (Prebaked Technology).

To protect the cell lining from the corrosive nature of the electrolyte and liquid aluminium, the thermal balance of the cell is carefully designed to allow sufficient heat loss through the sidewalls. The heat loss permits cryolite to freeze onto the sidewalls, and the frozen cryolite sideledge protects the sidewalls from the corrosive mixture of molten electrolyte and aluminium [2, 3]. The bottom carbon cathode surface, on the other hand, must remain bare for good electrical contact with the liquid aluminium. Thus, it cannot be protected by frozen cryolite as occurs for the sidewalls. This leaves the bottom carbon cathode lining as the main critical factor for the cathode life in a well-operated cell [2, 3]. This thesis focuses on the wear of the bottom carbon cathode lining.

The principles of the Hall-Héroult process have not changed since it was developed more than 120 years ago. However, the demand for high productivity has resulted in smelters moving to amperage regimes considered almost impossible some few decades ago. As amperage is increasing, smelters must simultaneously deal with higher energy costs, stricter environmental requirements and operational challenges. Attempts to solve these challenges have resulted in broad technological research and development in the areas of bath chemistry, materials science and design of cathode lining materials, etc. [3]. The overall aim includes high productivity, long pot life, reduced emissions (fluorides, CF_4, C_2F_6, CO_2, and CO), high-energy efficiency and optimal operating conditions.

1.2. Trends in Carbon Cathodes in the Aluminium Industry

Carbon cathode materials used in the aluminium industry can be classified into three main categories: anthracitic (or amorphic) cathode blocks, graphitic cathode blocks and graphitized cathode blocks [3]. The industry is experiencing a continuous shift towards more graphitized cathode blocks [3, 6]. The development of the amperage and energy consumption as well as the changes in the carbon materials used in cathodes are shown in Figure 1.2.

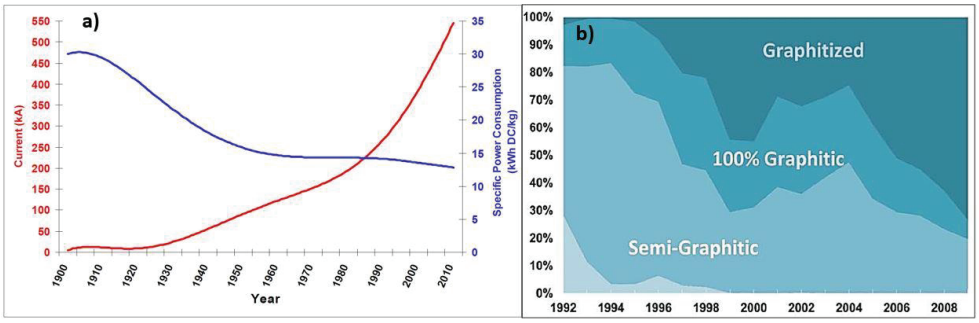

Figure 1.2. Trends in the aluminium industry. a) Amperage and specific power consumption with time [7] reprinted with permission from John Wiley and Sons. b) Development in carbon cathode blocks [6] reprinted with permission from ICSOBA.

The shift to more graphitized cathode blocks is directly linked to the industry's move to higher amperage and lower energy consumption regimes [3]. Some of the important advantages of the more graphitized carbon cathode blocks that make them more suitable for high amperage cells include lower sodium expansion and excellent electrical and thermal conductivity. However, it has been reported that the more graphitized carbon cathodes tend to wear faster. The trends in wear based on industrial experiences are graphitized > graphitic > anthracitic or amorphic cathode blocks [3]. The industry is currently trying to reduce the wear rate of the graphitized cathode blocks by providing more carbon or graphite per unit volume of the cathode block [3]. Higher carbon content per volume is provided through pitch impregnation after baking before graphitization. Thus these cathode blocks are called impregnated graphitized cathode blocks [3]. High-density graphitized cathode blocks are also another group of graphitized cathode blocks with more carbon per unit volume. A higher density of the carbon cathode can also be obtained by varying the aggregate coke fractions [8].

1.2. Trends in Carbon Cathodes in the Aluminium Industry

According to industrial experiences, graphitized blocks wear more, especially at locations of high current density [9, 10]. The locations with pronounced wear are at the ends of the cathode blocks, while there is significantly less wear at the centre channel or middle of the cathode blocks, known as the W or WW wear pattern [9-11]. The uneven wear pattern, especially the W wear pattern, is mostly attributed to the heterogeneity of current density along the carbon cathode blocks [12]. Numerical modelling has shown that the current distribution along a cathode block is influenced by its electrical conductivity [12]. The higher the electrical conductivity of a cathode block, the higher the probability of the current density peaking at its ends. Thus, the graphitized cathode blocks due to their relatively higher electrical conductivity would experience higher current densities at their ends than their low electrical conducting amorphic counterparts [12]. Current density peaks at ends of cathode blocks are regarded as harmful to the carbon cathode wear mechanism [3].

High local current densities may generate high local metal/bath velocities leading to rapid bath film exchange and consequently rapid aluminium carbide dissolution and transport at these locations [3, 13, 14]. These rapid bath film exchange rates may result in rapid erosion rates and eventually the formation of potholes at these locations [3]. Pothole formation is an extreme form of localized wear/erosion of the carbon cathode lining resulting in a narrow hole through the carbon cathode lining. Failure due to potholes is always preceded by direct contact between the molten metal and current collector bars resulting in tap out if proper actions are not taken [3, 15, 16].

In an extensive study to understand the carbon cathode wear in industrial Al electrolysis cells, Tabereaux et. al. [9] observed a wear pattern characterized by pitting on the cathode surface under the anodes near the cathode block ends where the wear was highest. Autopsy observations by Reny and Wilkening [10] showed that the wear surface of the graphitized cathode block was characterized by numerous small rounded holes 5 to 10 mm deep. These small rounded holes were explained as forming from abrasive wear by alumina particles. Further studies on the occurrence of pitting on the carbon cathode surface were done by Rafiei et. al. [17] and Patel et. al. [18]. They concluded from their laboratory experiments that pitting occurred as a result of particulate detachment owing to aluminium carbide formation within the binder matrix. Solheim [19] suggested that the pitting observed on the cathode surface could be formed and maintained by carbide dissolution owing to the periodic filling and removal of sludge on the cathode surface. The varying views on the mechanism(s) behind the occurrence of pitting on the carbon cathode surface suggest the phenomenon is not fully understood.

Wetting between the carbon cathode and the two melts, molten aluminium and cryolite, in the electrolysis cell plays an important role in the formation of aluminium carbide, which is a prerequisite for carbon cathode wear [20, 21]. The formation, dissolution and transport of aluminium carbide on the carbon cathode surface are suggested to be facilitated by the presence of a film of electrolyte [13, 21]. This is

because the dissolution of aluminium carbide in the electrolyte is about two orders of magnitude higher than in the metal [3, 13, 22]. The molten electrolyte is observed to penetrate the carbon cathode immediately after electrolysis commences [23, 24]. Electrolyte penetration into the carbon material is believed to be preceded by wetting between the carbon cathode and the electrolyte [3, 17, 20, 24]. Autopsies, as well as laboratory experiments, suggest there exist a layer of electrolyte between the carbon cathode and Al metal pad, however, there exist conflicting reports as to whether such a layer of electrolyte exists or not [3].

Reduced cathode life due to cathode wear is one of the major challenges the aluminium industry face as they increase productivity through high amperage levels and use of more graphitized carbon materials [3]. This is because the costs involved in replacing potlinings, production losses and the disposal of spent potlinings are high [3]. A modern high-amperage cathode may cost more than USD 150,000 in materials and workforce, while the disposal of spent potlining may cost about USD 1000 per tonne [3].

1.3. The Aim of the Work

This PhD project was one of four sub-projects within the CaRMa (Reactivity of Carbon and Refractory Materials used in Metals Production Technology) project. The overall objective of the CaRMa project was to understand the fundamental materials and process phenomena to facilitate improved performance of carbon, insulation and refractory materials in aluminium production. The present thesis work was devoted to carbon wear a degradation mechanism(s).

Autopsy of spent potlinings constituted the first part of the thesis. Initially, the focus was on the formation of potholes, but after the first autopsy the focus was changed to study the phenomena of pitting on the surface of the spent cathodes. Six autopsies were conducted at three different smelters in Norway, and the autopsies consisted of two major activities. First, visual observations and measurements of the surface profile were carried out to obtain information on topography, characteristics of the wear patterns as well as their variations. Second, microstructure and mineralogical composition of samples collected during the autopsies were investigated by combining scanning electron microscopy (SEM), energy dispersive spectroscopy (EDS), X-ray diffraction (XRD) and X-ray computed tomography (CT). The main focus in the investigations was dedicated to the phenomena of pitting, the bath chemistry at the cathode surface, possible aggregate detachment and the microstructural features at the bath-carbon interface. Based on the findings from the autopsies, a degradation mechanism of the bottom carbon cathode lining causing pitting on the surface was proposed. Finally, finite element method (FEM) modelling,

using the program COMSOL, was conducted to give support to the proposed carbon wear mechanism.

The second part of the thesis investigated the wetting of carbon cathodes by molten electrolyte and aluminium using an immersion-emersion technique. Three industrial-grade carbon cathode materials and a high-density graphite material were subjected to immersion-emersion cycles using pure electrolyte or electrolyte combined with molten Al. The carbon cathode samples were cathodically polarized after immersion into the liquid before emmersion. The work aimed to give new information concerning the conditions for wetting of the carbon materials by the electrolyte and how fast the weatability change during cathodic polarization. The wettability of carbon materials by molten electrolyte was finally discussed with respect to Na activity.

2

Chapter 2 Literature Review.

2.1. The Hall-Héroult Process

Aluminium production by the Hall-Héroult process takes place in an electrochemical reduction cell, commonly called pots [2, 4], which is shown in Figure 1.1. Two cell technologies based on the two types of anode designs can be found in the industry [2, 4]. The two anode designs employed are the prebaked anodes and the Søderberg anodes. The prebaked anodes are baked before insertion into the pots, while the Søderberg anodes are baked in-situ using heat from the reduction process [2, 4]. Due to cell size limitations, lower cell energy efficiency, and a more challenging recovery of emissions, no new Søderberg plants have been built for decades [25]. Today, most reduction cells employ the prebaked anode design, typically with 16 to 40 prebaked anodes depending on the pot size and amperage levels [2, 5]. Prior to inserting the prebaked anodes in the cell, the anodes are rodded with aluminium or copper rods using an iron yoke and stubs for electric current conduction and support. The rodded anodes are connected to the cell busbar system using anode clamps [2, 4]. Carbon anode consumption during the reduction process is a characteristic of the Hall-Héroult process. Thus, the prebaked anodes are usually replaced after 22 to 30 days when they are consumed to about a quarter of their original height. The spent anodes, called butts, are cleaned of all bath components, crushed and reused in the manufacturing of new anodes [5]. For the Søderberg anodes, briquettes of anode paste are continuously added on top of a rectangular steel casing where it passes slowly downwards to towards the hot bath where it is baked by the heat from the process [2, 4]. Both the Søderberg and prebaked anodes are made of petroleum coke and coal tar pitch, but with a lower pitch content in the prebaked anodes (13-16 wt%) as compared to the 25-28 wt% for the Søderberg anodes. When comparing the two anode cell designs, the Søderberg design is associated with lower current efficiency, higher cell voltage, higher energy consumption and higher emissions and Søderberg technology is no longer used in the construction of new smelters.

Equation 1.1 gives the overall reaction to produce aluminium by the Hall-Héroult process. However, the actual amounts used differ from this theoretical value, especially for the carbon anode due to secondary reaction with air or CO_2 from the electrochemical reaction. About 0.4 and 0.5-0.55 kg of carbon is consumed for the prebaked and Søderberg anode designs, respectively [2, 4].

The term cathode is often considered as the whole pot containing molten aluminium and electrolyte, but from an electrochemical point of view, the liquid aluminium metal is the real cathode in the cell [4]. Usually, a liquid metal height of about 10-20

cm is maintained in the electrolysis cell [5]. The bottom carbon lining in the cell is responsible for carrying electric current from the liquid aluminium. The bottom carbon lining thus plays the role of cathode together with the liquid aluminium, hence the name carbon cathode lining [4]. The carbon cathode lining is mainly made up of prebaked carbon blocks joined by a carbonaceous seam mix. The prebaked carbon blocks can be anthracitic, semi-graphitized or fully graphitized carbon [3]. The carbon cathode blocks are rodded with steel current collector bars by means of grooves at the bottom of the blocks and joined by cast iron or carbon ramming paste [3]. Layers of refractory bricks and aggregates are usually located directly underneath the bottom of the carbon cathode lining to protect the bottom insulation from bath components. The refractory materials used in the aluminium industry are grouped into alumino-silicate based refractories, anorthite based refractories and olivine-based refractories [2-4]. The bottom insulation, whose main function is to conserve heat within the cells is usually made up of diatomaceous earth bricks also called Moler bricks, calcium silicate boards and vermiculite insulation boards. The sidewall blocks located towards the steel shell sides are usually made up of higher thermal conducting materials such as Si_3N_4 bonded SiC or graphite in order to freeze out a sideledge [3]. Typical dimensions of the rectangular steel shell, in which the different lining materials, including carbon cathode blocks, refractories and insulation bricks, and sidewalls are assembled, vary from 9 to 18 m long, 3 to 5 m wide and 1 to 1.5 m deep [2, 5]. After installation of all lining materials, the operating cavity depth is about 0.4 to 0.5 m [2]. A cross-sectional sketch of a cell lining is shown in Figure 1.1. The average vertical distance between the top of the liquid aluminium cathode to the bottom of the carbon anode is termed ACD (anode-cathode distance) or interpolar distance. This interpolar distance is typically around 4 cm for most smelters [2].

The cells or pots in an aluminium smelting plant are connected in series. The connection is such that the cathode of one cell is electrically connected to the anodes of the next, forming what is called a potline [2, 4]. A modern smelting plant may consist of several potlines, each potline consisting of more than 300 cells in series [26]. The cells are placed either side-by-side or end-to-end (older plants). High amperage cells with amperages of up to 600 kA are normally placed side-by-side to reduce the unfavourable magnetic effects induced by the high electrical current as well as to reduce heat loss from the cells [2, 5]. End-to-end arrangements are usually employed for older potlines with lower amperage cells operating at amperages less than 200 kA [2, 5]. The end-to-end and side-by-side arrangements of the cells are shown by Figure 2.1. A very important advantage that comes with the series connection of cells is the ability to run each cell with an individual voltage [2, 4]. This allows individual adjustment to satisfy the specific requirements of each cell such as heat balance and operating conditions based on the age of the pot etc. [2, 4]. The series connection also allows for the use of high-voltage rectifiers in the aluminium industry. The maximum voltage of rectifiers employed in modern potlines can be over 1500 volts [5, 27].

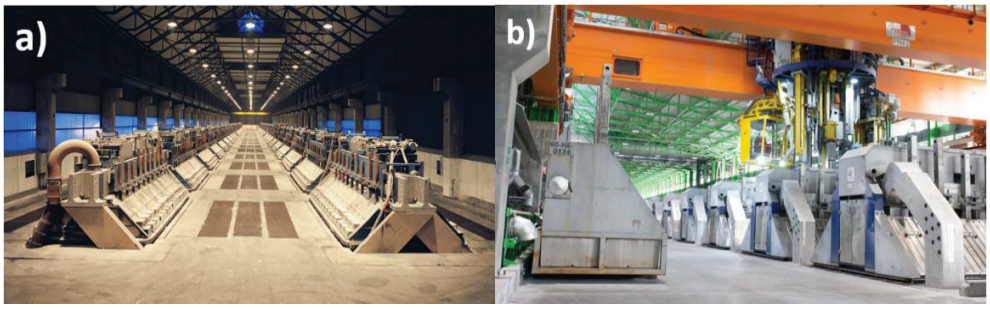

Figure 2.1. Hall-Héroult cell arrangements in the aluminium industry. a) End-to-End cell arrangement reprinted with permission from Alcoa Mosjøen. b) Side-by-Side cell arrangement printed from a Hydro smelter reprinted from Hydro AS. website [28].

The electrolyte consisting of mainly cryolite (Na_3AlF_6) is employed in the Hall-Héroult process mainly because of its ability to dissolve alumina as well as conduct electric current in its molten state [4]. In addition, the electrolyte contains 9-12 wt% aluminium fluoride (AlF_3) and 4-7 wt% calcium fluoride (CaF_2) [5]. Lithium fluoride (LiF) and magnesium fluoride (MgF_2) are in some smelters included in the electrolyte in addition to AlF_3 and CaF_2 [29]. The purpose of these additives to cryolite includes reducing the liquidus temperature (1010 °C to about 950 °C), adjusting the viscosity, interfacial tension, electrical conductivity, vapour pressure, density and other properties to ensure high productivity [2, 4]. The molten electrolyte is commonly called the bath in the industry. It is normal to find about 4 to 6 tonnes of electrolyte, equivalent to an electrolyte height of about 15-20 cm in most modern cells [2, 5]. To ensure that the electrolyte or bath is molten at all times for the electrolytic reduction process, a certain temperature above the liquidus temperature of the bath, called the superheat, is used [2]. An optimal superheat is essential for normal pot operations as it ensures good alumina dissolution and sideledge formation. With this in mind, most smelters keep their electrolyte temperature at 955-965 °C [2].

Aluminium production by the Hall-Héroult process involves adding alumina (Al_2O_3) in a powder form to the cryolitic electrolyte [2]. Alumina is supplied from an overhead bin or hopper built into the superstructure of the cell. About 1 to 2 kg alumina is added every 1 to 2 minutes through special automatic point feeders [2, 4]. Alumina concentration in the electrolyte is kept at 2-5 wt% for most smelters [30]. Alumina is targeted at this level to avoid operational problems such as anode effects and sludge. Anode effect is caused by alumina depletion in the electrolyte, while sludge may form due to high alumina doses, low superheat or additions at stagnant or low flow areas [2, 4, 30]. Alumina dissolves in the electrolyte forming aluminium oxyfluoride anions [2]. The oxide ions are discharged electrochemically at the anodes as intermediate products that further react with the carbon anodes to form gaseous carbon dioxide (CO_2), thereby consuming the carbon anodes in the process [2]. The aluminium-containing anions are also electrolytically reduced at the electrolyte-metal

interface to form the liquid metal [2]. Theoretically, about 1.89 kg of alumina and 0.33 kg of carbon is needed to produce 1 kg of aluminium metal on the cathode and 1.22 kg of carbon dioxide at the anode according to the overall reaction Equation 1.1. The metal produced is tapped from the cell by vacuum suction once a day using a ladle attached to an overhead crane or a truck [4]. The amount of metal produced at 100 % current efficiency is proportional to the amperage level, about 8.052 kg of Al / kA is produced every 24 hours [4].

Decomposition of alumina using carbon requires a voltage of about 1.18 volts [4]. However, the actual value reported in the industry is 1.5-1.7 volts due to anode overvoltage [4]. Typically, an operating voltage of 4-4.6 volts is required to overcome the electrical resistance of the electrodes (cathode and anode), electrolyte, busbars and their connections [4]. With the use of highly graphitized cathode blocks, changes in design and better stability strategies, smelters are now operating around the 3-4 volts range [2, 7]. The theoretical amount of energy required to produce a kg of aluminium is 6.34 kWh at 100 % current efficiency, however, reported data show that the best modern smelters are achieving between 12-13 kWh/kg Al [5, 7].

The interpolar distance or anode-cathode distance (ACD) ensures a separation between the cathodically produced liquid aluminium and the anodically produced carbon dioxide gas as well as allow current to pass through the electrolyte. These roles are very important for optimal operations because of the following reasons: Firstly, liquid aluminium will react exothermically in contact with carbon dioxide and form carbon monoxide and dissolved alumina in a back reaction if the ACD is too low, the reaction is given by Equation 2.1. This reaction reduces the current efficiency.

$$2Al(diss) + 3CO_2(g) \rightarrow Al_2O_3(diss) + 3\,CO(g) \qquad (2.1)$$

Secondly, the ACD allows for sufficient transport and feed of dissolved alumina to the reaction sites. Another important factor is the heat generation due to the ohmic resistance within the electrolyte required for keeping the electrolyte and metal molten [2, 3]. Finally, a sufficient interpolar distance will prevent short-circuiting between the metal pad movement due to electromagnetic forces, hence, avoiding noisy pots [2, 4].

2.2. Carbon Cathode Lining

Carbon has been used as the lining material of choice in cells since the discovery of the Hall-Héroult process due to its very beneficial properties when baked [3]. Properties such as stability towards molten electrolyte and Al, high electrical and thermal conductivity, mechanical strength, etc. are all important for containing the

molten electrolyte and Al in addition to conducting electric current over the whole cathode surface [3, 4]. Carbon has been characterized by the International Committee for Characterization and Terminology of Carbon [31] based on different factors. The following definitions pertain to the carbon cathodes used in the aluminium industry:

- Graphite is defined as an allotropic form of the element carbon that consists of layers of carbon atoms hexagonally arranged in a planar condensed ring. The layers are bonded together by Van der Walls forces and stacked parallel to each other. A key feature of graphite is that it has a high degree of crystallinity close to the ideal crystal structure [3].
- Graphitic carbon refers to all varieties of substances of the element carbon in the allotropic form of graphite, irrespective of structural defects.
- Graphitized carbon refers to graphitic carbon with a more or less perfect three-dimensional crystalline order obtained by heat treating a graphitizable carbon to temperature ranges of 2500-3000 K.
- Amorphous carbon refers to carbon material without long-range crystalline order. The deviation of C-C interatomic distance relative to graphite, including those in the basal plane, is greater than 5 %.

According to Sørlie and Øye [3], there are three main types of design and construction of the carbon lining in the aluminium industry as described below.

- Monolithic lining: In this design, the whole carbon lining is made by ramming a plastic carbon paste into place. Few smelters in the industry employ this design due to environmental considerations during ramming and baking.
- Prebaked carbon blocks: In this lining, prebaked blocks with carbonaceous paste (ramming paste) rammed into the seams and joints around them. This is the standard design for most smelters in the industry. The rammed seams and joints are considered the weak parts of this design.
- Glued semi-monolithic lining: This lining is made up of almost entirely prebaked carbon blocks glued together by carbon glue. The only sections not covered by the prebaked carbon blocks are the peripheral joints, these are sealed with carbonaceous paste (ramming paste). This design is considered beneficial for smelters where lining quality is the main reason for reduced cathode life. The high cost of precision milled blocks and labour has, however, limited the implementation in the industry.

Figure 2.2 below illustrates the different carbon cathode lining designs.

2.2. Carbon Cathode Lining

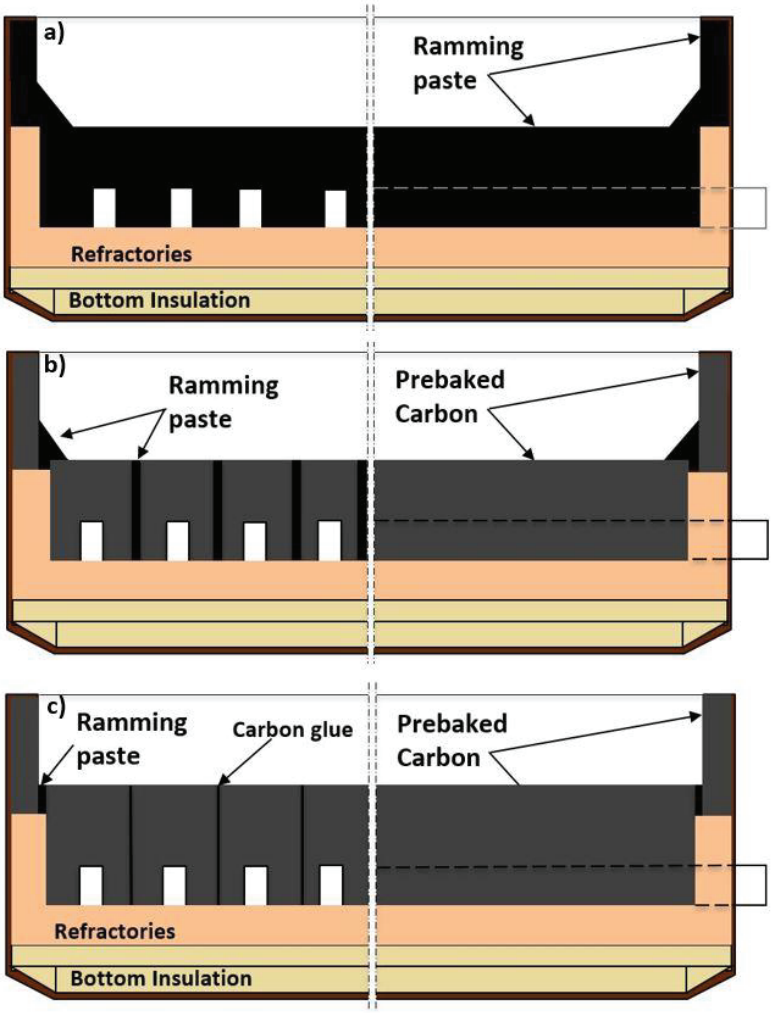

Figure 2.2. Carbon cathode lining designs in the aluminium industry. a) Monolithic carbon lining design made from only ramming paste. b) Standard design for the industry made from prebaked carbon with ramming paste in seams and joints c) Glued semi-monolithic lining design made almost entirely from prebaked carbon glued together. Figure was redrawn from Sørlie and Øye [3].

As described in Figure 2.2b the standard carbon cathode lining design currently employed in the aluminium industry consists of prebaked carbon cathode blocks and carbonaceous paste [3]. These prebaked carbon cathode blocks have been classified, based on the definitions by the International Committee for Characterization and Terminology, by Sørlie and Øye [3] as follows:

- Graphitized Cathode Blocks: These are cathode blocks where the whole block (filler and binder) consisting of graphitizable materials (petroleum coke and coal tar pitch) have been heat treated to temperatures of about 3000 °C in a graphitizing furnace. These cathode blocks are sometimes impregnated with pitch once or several times and baked to reduce open porosity before graphitization.
- Graphitic Cathode Blocks: These cathode blocks consist of graphitized petroleum coke and/or graphite electrode scraps as aggregate and coal tar pitch binder that has been heat treated to about 1200 °C. The binder is thus not graphitized.
- Amorphous Cathode Blocks: These are cathode blocks consisting of a gas or electro calcined anthracite and coal tar pitch binder that has been heat treated to 1200 °C. About 30-50 % graphite aggregates are sometimes used to replace some of the anthracite content of these blocks.

The carbon cathode blocks are produced by extrusion or vibro pressing of the raw materials (aggregate and binder) into rectangular shapes before being baked [32]. Figure 2.3 is a flowchart showing the stages in the production process as reported by Fourcault and Samanos [33].

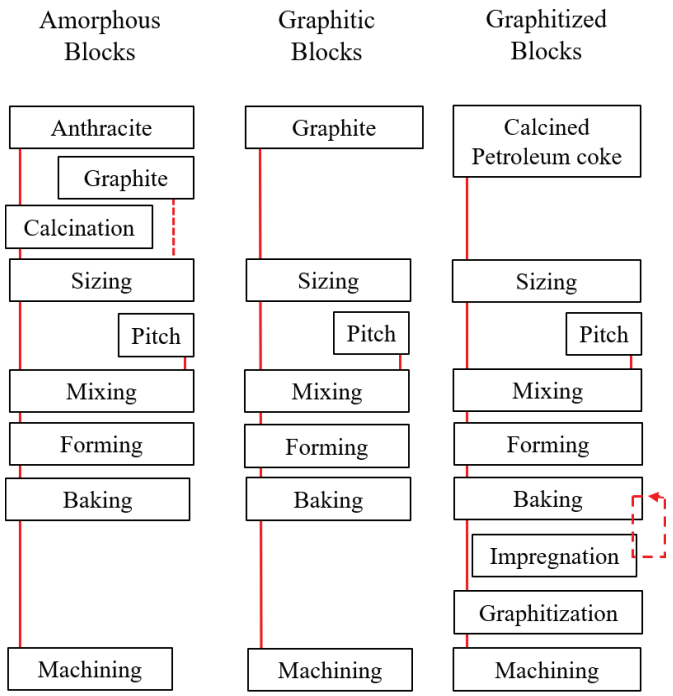

Figure 2.3. Typical flowchart for the production of the different types of cathode blocks. Redrawn from [3].

2.2. Carbon Cathode Lining

Thermal treatment of the green carbon cathode blocks results in preferred properties such as high electrical and thermal conductivity. Also, further heat treatment to higher temperatures (2500-3000 °C) leads to a higher degree of crystallinity due to graphitization. Figure 2.4 is a schematic diagram showing the structural changes of carbon material during thermal treatment. Properties of the fabricated carbon cathode block depend on important parameters such as level of calcination/graphitization, quality of aggregates and binder, forming method (extrusion, vibration and pressing), heating rate, final temperature, etc. [3]. Some of the important properties of the different cathode blocks used in the industry are given in Table 2.1.

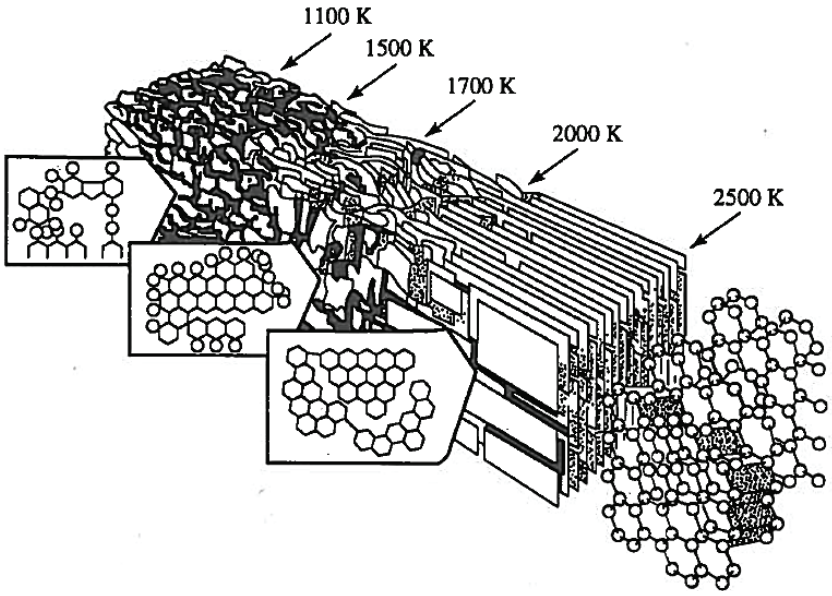

Figure 2.4. Structure of carbon material at different heat treatment temperatures. Reprinted from [34].

Table 2.1. Some important properties of the three carbon cathode types used in the aluminium industry. Reproduced from Sørlie and Øye [3]

Property	Amorphous			Graphitic	Graphitized
Filler Material:					
Anthracite, %	100	70-80	50	-	-
Graphite, %	-	20-30	50	100	-
Petroleum coke, %	-	-	-	-	100
Real density, gcm^{-3}	1.84-1.88	1.85-1.93	1.90-1.95	2.00-2.16	2.18-2.2
Bulk density, gcm^{-3}	1.52-1.58	1.53-1.60	1.57-1.61	1.60-1.66	1.57-1.68
Total porosity, %	15-19	15-19	17-21	20-24	24-28
Open porosity, %	13-16	15-16	16-17	18-20	20-24
Specific electrical resistance, μΩm	36-55	29-44	25-34	15-24	10-15
Thermal conductivity, $Wm^{-1}K^{-1}$	6-14	8-15	12-27	20-45	100-140
Linear thermal expans. coefficient, $\mu mm^{-1}K^{-1}$	2.2-2.6	2.2-2.6	2.2-2.6	1.9-2.6	1.8-3.6
Crushing strength, MPa	18-33	18-32	19-33	19-34	18-27
Bending strength, MPa	6-8	6-10	7-10	8-10	6-12
Ash content, %	4-6	3-6	2-4	0.5-1.3	0.1-0.6
Sodium expansion, %	0.5-1.3	0.3-1.0	0.2-0.7	0.1-0.4	<0.1-0.8
Therm. shock resistance	1	1.5	2.5	3.5	25
Abrasion index (relative to 100 % amorphous)	1	2	4	4	200

The ramming paste is important for the carbon cathode lining as it seals all gaps between the carbon cathode blocks as well as the cathode periphery. It is composed of a filler, usually amorphic carbon, and a synthetic organic binder/resin that has replaced the coal tar pitch used in the past. The ramming paste is baked during pre-heating of the new cathode lining where it plays an important role in shrinking due to carbonization to allow for thermal expansion of the cathode blocks. The porous and amorphic nature of the baked ramming paste means it has a relatively low electrical and thermal conductivity as compared to the carbon cathode blocks [3].

2.3. Wear of the Carbon Cathode Lining

Autopsy of spent cathode linings is a very important investigation technique to determine reasons for pot failures as well as determine the integrity of linings for new cell designs or potential for current creep. It can also be used to look into cell performance opportunities, study chemistry and physics of linings, study cathode wear mechanisms, etc. [3, 35-39]. The temporarily or permanently shut down pot planned for autopsy is normally allowed to cool in a dry and enclosed space to minimize contact with moisture [3]. Careful removal of bath and metal followed by vacuum cleaning to reveal details on the carbon cathode surface is done for the analysis of wear patterns etc. Digging out sections of the spent potlining to reveal the cross-section of the cathode lining is also done to diagnose lining integrity as well as study chemistry and physics of the cathode lining. Images from an autopsy of a spent pot lining are shown in Figure 2.5.

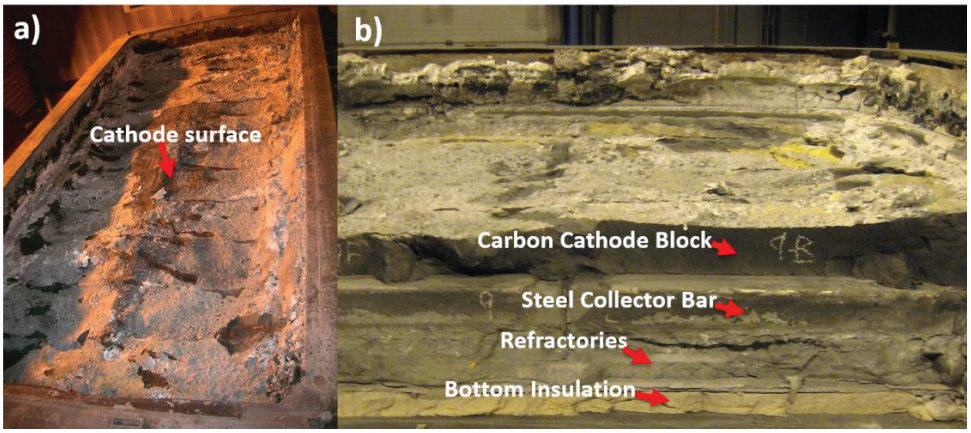

Figure 2.5. Spent potlining for autopsy studies. a) Cleaned cathode surface for wear analysis. b) Excavated spent potlining for examining lining integrity, chemistry and physics analysis.

An autopsy can vary between a full comprehensive examination of the whole spent potlining to limited sampling. Comprehensive examinations are mostly conducted on permanently shut down pots and comprises cathode surface analysis, such as wear patterns, as well as analyzing the conditions of the lining and sampling at locations of interest for further examinations. The limited or non-comprehensive examination, mainly conducted on temporarily shut down cells, involves surface analysis as well as sampling at locations of interest [3]. Activities such as gathering operational pot data, visual inspection, photography, wear measurements either manually or by 3D scanning, documentation, sampling etc. are undertaken during the autopsy process [3]. The autopsies presented in the present PhD thesis focused mainly on the cathode surface.

2.3.1. Sodium in the Carbon Cathode Lining.

Sodium is proposed to form from the electrochemical and chemical reactions occurring on the carbon cathode surface. Equations 2.2, 2.3 and 2.4 show the reactions responsible for generating Na in the carbon cathode lining [2, 40].

$$Na^{+}(diss) + e^{-} = Na\,(inC) \quad (2.2)$$

$$3NaF(diss) + Al(l) \rightleftharpoons 3Na(inAl) + AlF_3(diss) \quad (2.3)$$

$$Na(inAl) = Na\,(inC) \quad (2.4)$$

Sodium penetration into the carbon cathode lining was proposed by Dell [41] to occur by sodium vapour transport through pore networks as the metal is above its boiling point at electrolysis conditions. Dewing [42] on the other hand proposed sodium to penetrate the carbon structure by a solid diffusion process through the carbon lattice and along grain boundaries. Diffusion of Na through the carbon lattice was also confirmed by Krohn et. al. [40]. Intercalation of Na into carbon is said to be driven by the charge transfer between the Na metal and the π-electron system of the carbon material. Amorphous carbon materials will favour charge transfer with electron donors because of their low Fermi levels while carbon materials with high Fermi levels such as graphite favour charge transfer with electron acceptors. Thus, amorphous carbon materials will readily react with Na [40].

Laboratory investigations of the penetration of Na and bath into the carbon cathode lining, showed that Na is the first component to penetrate the carbon cathode material during cathodic polarization. Na penetration into the carbon cathode enables electrolyte penetration due to improved wetting [23, 40]. Mittag et. al. [43] observed a higher Na uptake for the anthracitic materials than the graphitic materials during an investigation of Na uptake in a 100 kA cell. They, however, observed a higher than expected consumption of Na in the form of NaF by the carbon cathodes investigated. The observations were attributed to migration of Na further down the carbon cathode. The presence of Na further down the carbon cathode lining was later confirmed by Tschöpe et al. [44] who observed Na within the reaction fronts of the refractory lining.

Sodium expansion is a very important issue in the aluminium industry due to the devastating effects of extensive swelling and cracking on the cathode lining [40]. The swelling and cracking effects arise from the intercalation compounds such as $C_{64}Na$ and $C_{12}Na$, which are larger than the spacing between the carbon layers [3, 40]. As mentioned earlier, the graphitic carbon materials do not favour charge transfer with

electron donors like Na. Thus, Na expansion is observed to be lower for the graphitic carbon materials relative to the amorphic carbons [3, 45]. All the factors that influence the Na activity like the cryolite ratio (CR) and current density, influence the Na expansion [46]. Finally, Na expansion is observed to be a reversible process due to the fact that Na reverts when the factor(s) responsible for its insertion or penetration into the carbon material is/are removed [45-49].

2.3.2. Reported Autopsy Observations

Several authors [3, 9-11, 15, 35-37, 39, 50-53] have reported autopsies of spent potlinings, as well as online measurements, to study the degradation of the carbon cathode lining. Dell [15, 51, 52] observed the occurrence of potholes on the spent carbon bottom linings. They described the potholes as aluminium-filled depressions shaped like inverted cones that could occur throughout monolithic bottom linings but occur mostly at the tamped seam ends of block-lined cells.

Analysis of spent potlinings with graphitized cathode blocks by Lombard et al. [39] revealed that the highest cathode wear systematically occurred at the carbon cathode block ends under the anodes while the locations around the centre channel showed the least wear. This wear pattern is referred to as the W wear pattern. The cathode blocks were also observed to be more eroded than the neighbouring ramming joints. The high abrasion resistance of its anthracitic components was given as the reason for the low wear.

Tabereaux et al. [9] conducted on-line measurements of the wear profile, over a period of three consecutive years, of prebaked cells (AP-18 technology) operating at 180 kA with different grades of carbon cathode blocks. Their measurements showed that the carbon cathode wear was linear only during the first 1600-1800 days of operation. Their data showed that the wear rates flatten out after these first 1600-1800 days. They also observed that locations under the anode positions near the ends of the cathode blocks had the highest wear. The wear pattern at the locations with maximum wear was observed to be rough with pitted appearance. The cathode blocks were generally observed to be more eroded than the ramming joints between them. Tap hole measurements showed variable wear rates being dependent on cell technology and plants. The results also demonstrated that for the first four years, the graphitized cathode blocks possessed average wear of 2 to 3 cm/year while the average wear of the graphitic blocks was 1.2 to 1.8 cm/year and 0.9 to 2.2 cm/year for the amorphic blocks (with 15-30 % graphite aggregates).

Reny and Wilkening [10] conducted wear measurements on cells lined with graphitized cathode blocks in operation and after shut down. Their measurements showed that the W wear pattern was already visible after 500 days of cell operation.

They also observed that the cathode blocks were more worn out than the ramming joints. Measurement close to the tap holes showed that mechanical wear at these locations did not take place at critical levels. They also observed numerous small rounded holes about 5 to 10 mm deep on the cathode surface at the locations with the highest wear. They explained these small rounded holes as forming because of abrasion actions from alumina particles residing within the deep wear zones of the W wear pattern. Similar to the observation by Tabereaux et al. [9], they also observed the wear to be linear during the first 1200 days (3.5 years) after which it levelled off over the lifetime of the cells.

Wear profile measurement using laser scanning profilometry on the cathode surface of spent potlinings lined with graphitized cathode blocks and alumina point feeders arranged along the centre channel revealed a wear pattern referred to as the WW wear pattern [11, 50]. An inner W wear pattern close to the centre channel was observed in addition to the normal W wear pattern discussed above. The inner W wear pattern is normally identified as locations with relatively high wear on both sides of the centre channel. Even though the WW wear pattern is documented, the actual mechanism behind the inner W wear pattern has, however, not been extensively discussed in the literature. Solheim [19] attributed the inner W wear, to a mechanism involving non-stationary diffusion of aluminium carbide into a layer of sludge which is periodically removed and renewed during the underfeeding-overfeeding cycles of the alumina feeding. The periodic removal and renewal of the sludge layer found on the cathode surface on both sides of the centre channel causes the high wear observed relative to the centre channel.

Sludge on the cathode surface, low current density and slow transport rates are amongst the possible reasons given for the low wear at the centre channel [3, 50]. Sludge is formed on the cathode surface when alumina does not dissolve into the electrolyte [54, 55]. The role of sludge in the carbon cathode wear process is suggested to be connected to its abrasive effect and high electrical resistance [3, 54]. The abrasive action of alumina is, however, not considered to contribute significantly to cathode wear since sludge does not move much on the cathode surface due to poor wetting between the metal pad and the sludge [3, 54]. The high electrical resistance of sludge is, however, considered a very important factor due to the uneven current density distribution it induces on the cathode surface [54]. The high electrical resistance will cause less current to flow where the sludge is located forcing high current densities at locations without sludge. These locations with higher than average current densities could then experience high wear due to the electrochemical nature of wear [56, 57]. During a sludge profile measurement exercise, Geay et. al. [54] observed the sludge profile to be similar to the wear profile and hence concluded that the sludge protects the carbon surface on which it settles.

Observations of wear have demonstrated that localized wear increases with increased block graphitization [3, 9]. The wear rate for the different grades of carbon cathode

blocks from the industrial measurements is graphitized > graphitic > anthracitic carbon [3, 9].

Lossius and Øye [53] analysed carbon cathode samples with different degrees of graphitization from 16 industrial cells with pot age ranging from 10 to 2534 days with powder X-ray diffraction (XRD) to study the distribution of electrolyte components within the carbon cathode. They observed that the electrolyte penetrated the amorphic carbon cathode samples faster than the graphitic carbon cathode samples. The high rate of electrolyte penetration for the more amorphic carbon cathodes as compared to the graphitic carbon cathodes, observed at the initial stages of electrolysis, was attributed to the easy filling of the larger pores of the amorphic samples by the electrolyte. This is because melt filling of the graphitic cathode samples would take time due to their relatively smaller pores. The chemical composition of the electrolyte in the cathode samples was observed to be very basic with cryolite ratio (CR) greater than 3. The basic nature of the electrolyte melt within the carbon cathode was also confirmed by the absence of calcium cryolite phases like $NaCaAlF_6$ and $Na_2Ca_3Al_2F_{14}$. The main phases observed within the intruding electrolyte were Na_3AlF_6, NaF, CaF_2 and $Na_2O{\cdot}Al_2O_3$. Al_4C_3 was observed in the carbon cathode lining.

2.3.3. Carbon Cathode Wear Tests

Several laboratory tests have been developed to study cathode wear [13, 14, 17, 18, 21, 44, 56-81]. Most of these tests are conducted at conditions similar to industrial cells as outlined by Sørlie and Øye [3]. The tests to study the mechanisms of carbon cathode wear can be grouped into three categories namely physical or mechanical, chemical and electrochemical wear tests [3, 58]. The following paragraphs give an overview of laboratory tests used to investigate the three different carbon cathode wear mechanisms.

Physical or mechanical wear tests are conducted to investigate the resistance of carbon cathode materials towards physical abrasion, and these tests are therefore sometimes referred to as physical abrasion tests. Liao and Øye [58, 68] developed methods for determining the abrasion resistance of carbon cathode materials. The methods comprised rotating carbon samples either in a slurry made up of sodium polytungstate (SPT) aqueous solution and alumina at room temperature or cryolitic melts with alumina at industrial operation temperatures (960 °C). The set up for the abrasion wear tests conducted by Liao and Øye is shown in Figure 2.6.

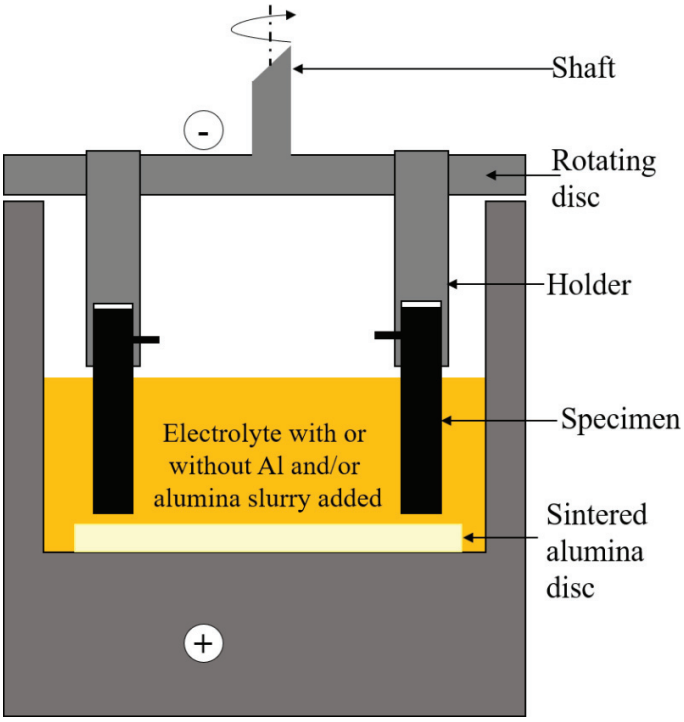

Figure 2.6. Set-up for carbon cathode wear tests with and without Al electrolysis used by Liao and Øye. Redrawn from [3].

Toda and Wakasa [59] developed a method quite similar to the one by Liao and Øye [58, 68] in which they tested the abrasion resistance of different carbon cathode samples in a slurry of water and alumina (75 wt% alumina and 25 wt% water).

Chemical wear tests are conducted to determine the degradation or wear resistance of the carbon cathode samples towards the corrosive mixture of molten aluminium and cryolite. The formation and removal of aluminium carbide is generally accepted to be the mechanism behind chemical wear [58]. Thus, most of the tests conducted to investigate the chemical wear mechanism involve carbide formation.

Doward [21] performed tests to investigate aluminium carbide formation by keeping Al and cryolite in a reactor-grade graphite crucible and heating up to 1000 °C for 30 minutes in an air atmosphere. Grjotheim et al. [82] performed aluminium carbide formation tests in an inert argon atmosphere using a carbon crucible with a mixture of molten Al and cryolite. They also investigated the effect of electrolyte components on the carbide formation process by varying the amounts of alumina and cryolite ratios (CR). Hollingshead and Brown [83] developed a test to determine the rate of solution of carbon in a mixture of molten aluminium and electrolyte at different melt temperatures and rotation speeds (peripheral velocities of the samples). Their experimental set-up used is displayed in Figure 2.7. The carbon sample was suspended in the molten aluminium and cryolite using a copper rod that is connected

to an electric motor from which it could be rotated. The crucible containing the melt was opened to air to allow for oxidation of the dissolved aluminium carbide.

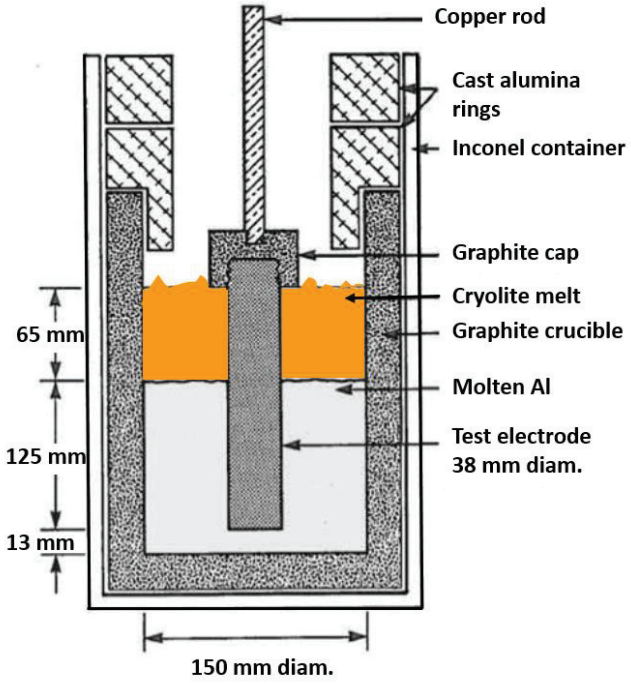

Figure 2.7. Hollingshead and Brown's experimental set-up for the rate of solution of carbon in molten aluminium and cryolite test. Redrawn from [83].

To investigate the solubility of aluminium carbide in the cryolite melt, Ødegård et al. [22] kept a tight lid graphite crucible containing a mixture of molten Al and cryolite closed for 5 hours at a temperature of 1020-1335 °C. Samples of the melt obtained after the 5 hours testing were ground and treated with a 10 % hydrogen chloride solution to form methane and hydrogen gases, which were then analysed by gas chromatography.

Skjølsvik et al. [84] investigated chemical wear with carbon rods rotating in a cryolite melt and molten Al in an inert atmosphere. They also kept the melt temperature at ca. 990 ± 3 °C for all the tests, the experimental set-up is shown in Figure 2.8a. Xue and Øye [85] investigated chemical wear of graphite and carbon/TiB_2 cathode materials using a set-up similar to the one developed by Skjølsvik et al. [84]. Xue and Øye used alumina tubes to shield the carbon sample from the cryolitic melt. The experimental set-up is shown in Figure 2.8b.

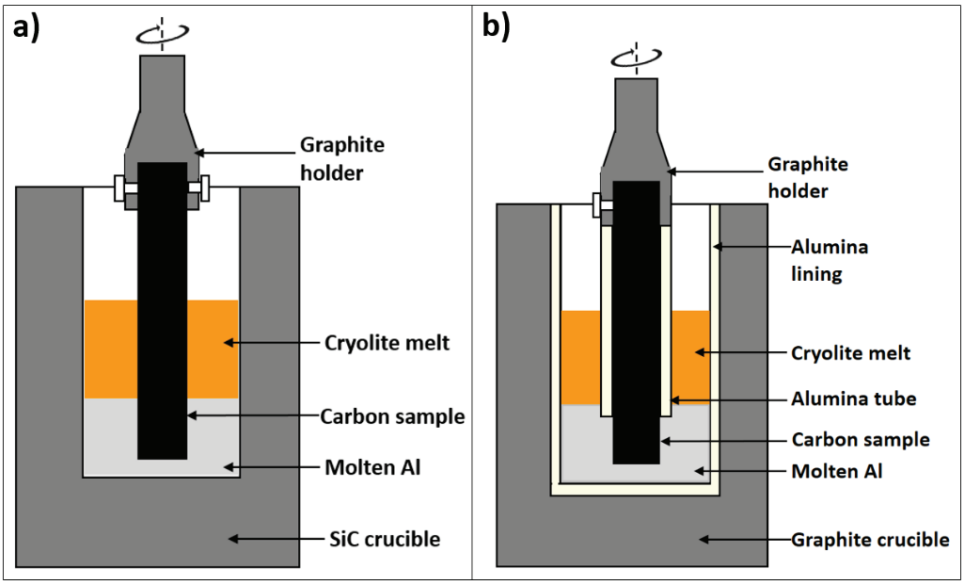

Figure 2.8. Experimental set-up for chemical cathode wear tests. a) Set-up developed by Skjølsvik et al. [84]. b) Set-up developed by Xue and Øye [85].

By introducing aluminium to the cryolitic melt in the set-up shown in Figure 2.6, Liao and Øye [58] investigated chemical wear of the carbon cathode material. They also investigated the effect of alumina on chemical wear of the carbon cathode.

Novak et al. [86] tested the formation of aluminium carbide in the absence of cryolite in a diffusion couple of aluminium and carbon in an alumina crucible and heating up to temperatures of about 1200 °C under an inert atmosphere.

Electrochemical wear tests also involve the formation, dissolution and transport of aluminium carbide as in the case of the chemical wear tests [11, 14, 18, 56, 58, 84, 85, 87]. For the electrochemical wear tests, also the effect of electric current (current density) on the carbon cathode wear process was investigated [56, 87]. Gudbrandsen et al. [61] investigated carbon cathode dissolution in alumina saturated cryolite melt with a cryolite ratio (CR) of 1.8 at 940 °C under inert atmosphere. Constant electric current was applied for each experiment by means of a galvanostat and a steel stirrer was used to establish uniform hydrodynamic conditions. Liao and Øye [57, 58] investigated electrochemical wear using the cell shown in Figure 2.6 by polarizing the cathode sample in the cryolitic melt-aluminium mixture. Wilkening and Reny [56] using a set-up similar to the one by Liao and Øye [57, 58], except the carbon cathode sample was axially vibrated instead of rotated, also investigated the effect of electric current on the wear of the carbon cathode. They also investigated the effect of excess AlF_3.

2.3. Wear of the Carbon Cathode Lining

Rafiei et al. [17] designed the inverted cell configuration set-up to investigate electrochemical wear of carbon cathode materials. They investigated the extent of carbide formation within the carbon matrix of different carbon cathode samples. Their set-up consisted of an electrolysis cell with a carbon cathode hanging by a steel rod in the electrolyte and a liquid aluminium anode at the bottom of the cell, allowing produced aluminium at the cathode to be returned to the anode where aluminium is oxidised. The bath was saturated with alumina and kept at a temperature of 975 °C during electrolysis while the whole system was purged with N_2 gas [17]. Various researchers including Patel et al. [18, 88], Vasshaug et al. [60, 89], Sato et al. [90], Tschöpe et al. [14, 65, 67] and Wang et al. [64] used either the original version or modified versions of the inverted cell configuration to investigate the electrochemical wear of carbon cathodes. The modified versions include connecting the carbon sample to a rotating steel rod to allow for carbon sample rotation [14, 60, 64, 65, 89], covering the top and bottom parts of the carbon sample with an insulator to ensure a defined cathode area [14, 60, 65, 89] and, in some tests creating slots on the carbon surface [14]. Figure 2.9 is a modified version of the inverted cell configuration set-up.

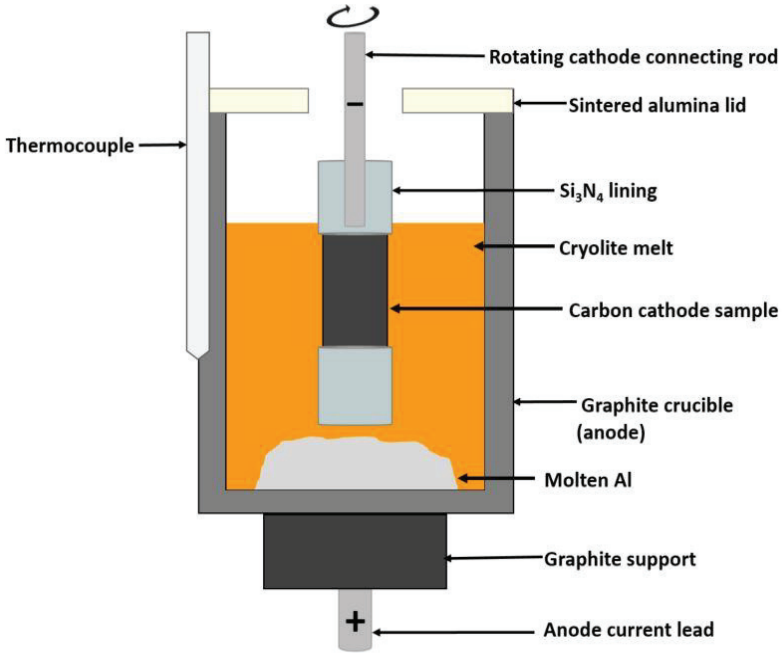

Figure 2.9. Experimental set-up based on the inverted cell configuration. Redrawn and modified from [64] with permission from Springer. Copyright © 2016.

2.3.4. Carbon Cathode Wear Mechanisms

A summary of the three carbon cathode wear mechanisms based on autopsies, measurements in industrial cells as well as laboratory tests as described in the previous paragraphs is given in the following.

Physical or mechanical wear can result from pot operation activities such as cavity cleaning during anode change and metal tapping [3]. Alumina particles moving along the carbon cathode surface is also suggested to contribute to physical wear due to its abrasive nature [58]. Liao and Øye [58] observed from their tests that the carbon cathode materials tend to wear more in aqueous alumina slurry mixtures than cryolitic melts-alumina slurry mixtures. This was explained by the differences in the abrasive nature of the alumina in the aqueous alumina slurry and cryolitic melt-alumina slurry as the cryolitic melt dissolves the abrasive edges on the alumina particles [58]. The high surface tension of the cryolitic melts and their poor wettability towards carbon were also given as possible reasons for the relatively low wear in cryolitic melts. Factors such as rotation speed, viscosity and density of slurry were observed to have an impact on the abrasion for all the carbon samples [58]. Physical or mechanical wear tests by Liao and Øye [58], as well as Toda and Wakasa [59], revealed that physical wear was greatly influenced by the degree of graphitization. Toda and Wakasa [59] observed the abrasion resistance of anthracitic cathode materials to be more than three times higher than that of the graphitic cathode blocks. Their test methods resulted in the following ranking of carbon cathode materials concerning abrasion resistance:

Graphite ≈ Semi-graphitized < Semi-graphitic < Anthracitic

The small rounded holes on the carbon cathodes that was observed by Reny and Wilkening [10] in their autopsies were assumed not to be purely chemical in nature due to their smooth surface. According to Reny and Wilkening [10], the small rounded holes did not originate from detached particles from the matrix as they were rounded through all matrix grains. The small round holes were rather assumed to originate from alumina particles (that spent time within the deep cavities of the location with the highest wear) abrading the carbon while being transported by small eddies in the metal [10].

According to Wilkening and Reny [56], erosion measurements done in reduction cells with graphite cathode blocks of very good mechanical abrasion resistance index showed very poor erosion resistance. Wear tests to rank carbon cathode materials of different graphitization by Tschöpe et al. [67] showed no significant differences in the wear rates despite the differences in abrasion resistance. Finally, the rate and pattern of carbon cathode wear observed in the aluminium industry point to chemical or electrochemical wear process mechanism as most likely [3, 9].

2.3. Wear of the Carbon Cathode Lining

Chemical wear mechanism involves the formation, dissolution and transport of aluminium carbide, Al_4C_3. The aluminium carbide involved in the wear process is formed through a chemical reaction process [3]. The reactions leading to the chemical formation of aluminium carbide are displayed by Equations 2.5 and 2.6.

$$4\,Al\,(l) + 3\,C(s) = Al_4C_3\,(s) \qquad (2.5)$$

$$4Na_3AlF_6(diss) + 12Na(in\ C) + 3C = Al_4C_3\,(s) + 24NaF(diss) \qquad (2.6)$$

Sodium generated from the electrochemical and chemical reactions shown by Equations 2.2, 2.3 and 2.4 can react with the carbon cathode and electrolyte components to form aluminium carbide as displayed by Equations 2.6 [3, 53].

The reaction shown in Equation 2.5 is thermodynamically favourable at all temperatures of concern (Gibbs energy of -147 kJ at 970 °C) [3]. However, the poor wettability of molten aluminium towards carbon [2, 3, 21] means a very limited amount of carbide formation from the direct contact between aluminium and carbon at temperatures below 1000 °C [3, 21, 58, 86]. Laboratory tests by Doward [21], Grjotheim et al. [82] and Novak et al. [86] showed the presence of an oxide film around aluminium metal preventing wetting of the carbon cathode. Doward [21] observed that the carbide formation reaction is strongly enhanced when a cryolitic melt is introduced to a system consisting of carbon and molten aluminium. Cryolite is proposed to act as a solvent for the oxide film around the molten Al [21]. It was further observed that most of the carbide formation occurred at the graphite/cryolite interface suggesting a mechanism involving aluminium diffusion through an intermediate layer of cryolite.

Liao and Øye [58] also observed that by introducing aluminium to a cryolitic melt, cathode wear by carbide formation was activated. Thus, chemical wear of the carbon cathode is active when both Al and cryolite are present [58]. Grjotheim et al. [82] observed from their laboratory tests that the carbide formation process decreases with increasing alumina concentration (within the range of 0-4 wt%) and cryolite ratio (within the range of 2.4 to 3.8). They also observed that carbon materials with larger pores yielded larger volumes of aluminium carbide. The carbide formation reaction was also observed to proceed until saturation of the melt and to a certain carbide layer thickness upon which the formed layer acts as a diffusion barrier thereby retarding or stopping the formation process [82]. Hollingshead and Brown [83], also observed coatings of aluminium carbide of about 0.03 to 0.04 mm on all their carbon cathode samples exposed to molten Al and cryolite for 24 hours. Apart from aluminium carbide, aluminium oxy-carbide (Al_2OC) formation was also observed on carbon surfaces in cryolite melts containing alumina [21, 91]. Xue and Øye [85] proposed

the following kinetic stages for the carbide formation process based on their laboratory results:

- An onset stage where Al diffuses through an oxide layer to meet carbon and form aluminium carbide.
- A growth stage where the formed carbide at the interface continues to grow and extend into the aluminium, with growth maintained by carbon diffusing through the formed carbide to meet Al.
- A final stage where the carbide layer grows in volume, leading to volume expansion and breaking of interfacial bonds.

The presence of a carbide layer that acts as a diffusing barrier retarding further carbide formation, as discussed above, means the rate determining step in the cathode wear process is the carbide dissolution process [3].

Studying the wear of carbon in a mixture of molten Al and cryolite melt, Liao and Øye [58] observed relatively higher wear for the part of the carbon in contact with cryolitic melt than the part of the carbon in contact with the molten Al. This was attributed to the difference between aluminium carbide solubility in molten cryolite and molten Al. Aluminium carbide solubility in the metal at electrolysis conditions is assumed to be less than 0.01 wt% [21] and several orders of magnitude lower than in the bath.

Carbide solubility in cryolitic melts investigations by Ødegård et al. [22] showed a maximum carbide solubility of 2.15 wt% at 1020 °C and cryolite ratio (CR) of 1.8. A reaction based on this maximum carbide solubility was consequently proposed as shown by Equation 2.7.

$$Al_4C_3(s) + 5AlF_3(diss) + 9NaF(diss) = 3Na_3Al_3CF_8\,(diss) \qquad (2.7)$$

They also observed that carbide solubility in the bath increases with increasing temperature. The cryolite ratio (CR) was observed to be the most important parameter to influence carbide solubility [22]. Molten electrolyte and Al velocity were observed to influence carbon cathode wear by enhancing the transport mechanisms occurring at the interface [85]. Tschöpe et al. [14] observed that by increasing the speed of rotation of a cathode sample immersed in the bath, the wear rate increased. This was attributed to mass transport of carbide to the electrolyte.

As the dissolution of carbide in the metal is low compared to the solubility in the cryolite melt, it is proposed that the presence of a bath film at the carbon-metal pad interface is very important in the erosion of carbon cathodes [3, 13]. The continuous presence of cryolite at the carbon-metal interface is enhanced by the convective patterns set up by the magnetic field within the metal pad [13]. Once the carbide is dissolved and transported to the electrolyte above the aluminium metal pad, it is oxidized by the anode gases as shown by Equation 2.8 [3, 83].

$$Al_4C_3(diss) + 6\,CO_2(g) = 2Al_2O_3(diss) + 6CO(g) + 3C \quad (2.8)$$

Hollingshead and Brown [83] found no significant differences in the rate of solution of the different types of carbon cathode materials (amorphic and graphitic) they tested. They, therefore, concluded from their test results that chemical wear of all carbon cathode materials (amorphic and graphitic) should be the same given the same metal velocity and abrasion resistance.

The electrochemical wear mechanism also involves the formation, dissolution and transport of aluminium carbide from the cathode surface. However, unlike the chemical wear mechanism, the carbide formation process is influenced by electrical current density. Keller et. al. [92] proposed that bath penetrating into the carbon cathode and sludge on the cathode surface will cause electrochemical reactions to occur due to the more negative potentials that exist on the cathode block due to ohmic voltage drop. Electrochemical reactions such as the one given in Equation 2.9 would occur due to the presence of electrolyte on the carbon cathode surface [17]. The two half-reactions represented by Equation 2.9 illustrates the electrochemical carbide formation reaction.

$$Anodic: \quad 4Al(l) + 12F^- = 4AlF_3(diss) + 12e^- \quad (2.9a)$$

$$Cathodic: \quad 3C(s) + 4AlF_3(diss) + 12e^- = Al_4C_3(s) + 12F^- \quad (2.9b)$$

Tests by Gudbrandsen et al. [61] showed that the carbon cathode could be consumed cathodically in cryolite melts according to Equation 2.10b, the anodic half reaction has been included as Equation 2.10a. The Al_4C_3 formed is dissolved in the electrolyte as is shown in Equation 2.6.

$$4Al(l) + 12NaF(diss) = 4AlF_3(diss) + 12Na^+ + 12e^- \quad (2.10a)$$

$$3C(s) + 9AlF_3(diss) + 12Na^+ + 12e^- = 3Na_3Al_3CF_8(diss) + 3NaF(diss) \quad (2.10b)$$

The rate of carbon consumption was observed to increase with increasing current density until a steady state was reached where the carbon consumption remained constant irrespective of the current density.

The non-linearity of carbon cathode wear observed by Reny and Wilkening [10] and Tabereaux et. al. [9] was explained to result from a reduction in current density due to the freezing of sludge or bath components. According to Reny and Wilkening [10], the closeness of the high thermal conducting collector bars after more than 2/3 of the carbon cathode has been worn out would cause cooling of the carbon cathode. This cooling effect would lead to freezing of sludge or bath components at the location

thereby diverting the current path to other locations due to the high electrical resistance of the frozen sludge or bath.

Furthermore, Wilkening and Reny [56] observed no wear when the current was switched off during a carbon cathode wear test. The carbon cathode wear was observed to increase with increasing current density and AlF_3 content.

Rafiei et al. [17] proposed a wear mechanism based on results from carbon cathode wear tests they conducted. The mechanism involves aluminium carbide formation within the pores and cracks of the carbon cathode as a result of sodium penetration of the carbon cathode through intercalation at the start of electrolysis. They observed aluminium carbide within the pores of the carbon cathode and also identified the carbide formation to increase with increasing current density. Moreover, Rafiei et al. [17], suggested that carbide formation will be more favourable for anthracitic cathodes than the graphitic cathodes due to the high thermodynamic activity of disordered carbon. Considering the presence of a film of electrolyte between the carbon cathode and Al metal pad, Rafiei et al. [17] proposed a mechanistic interpretation of aluminium carbide formation through the anodic dissolution of Al at the metal/electrolyte interface and cathodic reduction at the carbon/electrolyte interface. From the half reactions (2.7a and 2.7b), it is deduced that increasing the current will increase the driving force for the anodic dissolution of Al^{3+} and will increase the driving force for the transport of Al^{3+} ions to and into the cathode material, thus increasing the chance of aluminium carbide formation [17].

Patel et al. [18], employing the inverted cell configuration, tested the wear of graphitized and graphitic carbon cathode materials with varying open porosities and pore size distribution. Their tests showed that test parameters such as bath chemistry, granulometry, porosity, cut direction and current density were key variables in the cathode wear process. They observed that increased AlF_3 content, porosity and current density resulted in increased cathode wear considerably more than any other variable. According to them, high porosity will lead to increased bath penetration into the carbon cathode resulting in a higher degree of degradation reactions occurring within the sample. Increasing current density will result in the increased electrochemical formation of aluminium carbide as the reaction depends highly on the current density due to its electrochemical nature. Increasing the excess AlF_3 content will lead to increased carbide solubility in the melt resulting in the higher dissolution of the carbon cathode material. Close observation of the carbon cathode samples after the wear tests showed varying degree of roughness at the wear surface. They observed that the degree of roughness correlated with the level of porosity within the samples, the high porosity samples had the highest degree of roughness. They explained the roughness on the surface to be caused by particle detachment resulting from the weakening of the carbon structure due to internal carbide formation within the porosity of the samples. High porosity samples would have higher particle detachment due to a high degree of internal carbide formation and hence a higher

degree of roughness at the wear surface. Proof of aluminium carbide formation within the pores of the carbon cathode samples was obtained from electron microscopy.

Tschöpe et al. [14] used cylindrical carbon cathode samples that had slots on them to investigate the effect of current density variations on carbon cathode wear. From the tests, the least wear was observed at the locations simulated to have the lowest current densities while the highest wear was observed at the locations simulated to have the highest current densities. They also observed that the rotation of the samples contributed to the carbon cathode wear process. Another wear test conducted by the same author [67] using the same experimental set-up to investigate electrochemical wear of three different carbon cathode materials (high-density graphitized, graphitized and anthracitic cathode materials) revealed a non-significant difference in electrochemical wear for the three cathode materials.

Wang et al. [64] performed wear tests using the same set-up as Tschöpe et al. [14, 65, 67], and they also observed the electrochemical wear to increase with increasing current density until the limiting current density was reached, as described by Gudbrandsen et al. [61]. However, they observed a further increase in carbon consumption upon increasing the current density above 1 A/cm^2. The authors explained this behaviour by the increase in sodium activity as the current density is increased. This was explained as increased sodium activity at the high current densities leading to an increase in aluminium carbide formation, which would be observed as high carbon consumption.

2.3.5. Potholes

Potholes are observed on the carbon cathode surface during autopsy investigations in the aluminium industry [3, 16, 51]. Pothole formation is a cathode wear mechanism characterised by localized erosion of the carbon lining [3]. The cavity created may sometimes have the approximate appearance of an inverted cone but can also have shapes that are more irregular. At failure, the pothole will always extend from the surface down to a collector bar leading to tapout through the bar if no drastic action is immediately taken [3, 51]. Autopsy studies have shown that 80-90 % of pot failures can be traced back to pothole formation [16].

Siew et al. [16], described potholes as eroded holes in the carbon cathode that are roughly hemispherical in the base and can range in size from golf balls to basketballs. They also proposed that potholes generally have steep sides that form angles of 70-90° with the cathode surface and have an aspect ratio of equal or slightly greater than one as shown in Figure 2.10.

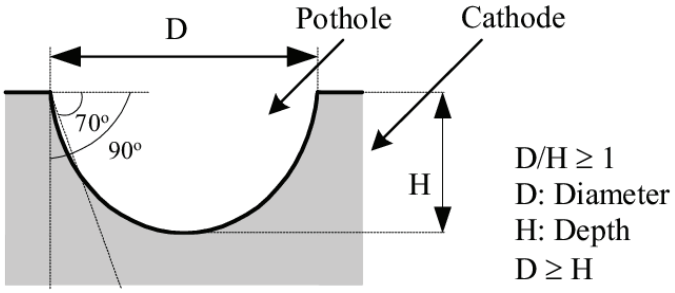

Figure 2.10. Schematic diagram of a pothole. Reprinted with permission from TMS [16]. Copyright © 2005 by the Minerals, Metals & Materials Society. Used with permission.

Dell [51] proposed a mechanism for pothole formation that involves a preferential current path through metal-filled cracks down to the collector bars. The local high current density at this location combined with magnetic flux produces a whirlpool effect. The rapid movement of the metal pad due to this whirlpool effect combined with the abrasive action of suspended solids results in pothole formation. The whirlpool effect or metal swirling theory was also used by Waddington [93]. Waddington reported that if a metal vein located on the carbon cathode carry current, then circulation or swirling of the metal pad induced by magnetic fields could occur. The circulating metal at the location with metal vein will cause continues removal of any carbide that forms, thereby allowing the metal vein to be gradually enlarged [93].

According to Rafiei et al. [87] and Patel et al. [18] high current densities on the carbon cathode would lead to a faster rate of aluminium carbide generation within the binder matrix of the carbon cathode leading to weakening and finally particulate detachment. Formation of aluminium carbide within the relatively amorphic binder is due to the high thermodynamic activity for disordered carbon. High carbide formation within the binder matrix would result in weakening of the carbon structure due to frost heave growth of the carbide layer. The voids created from particulate detachment would be filled by aluminium metal further enhancing carbide formation and transport due to the metal's high conductivity and reduced distance to the collector bars. The accelerated erosion at this location would then lead to pothole formation. Figure 2.11 is a sketch illustrating the particulate detachment mechanism.

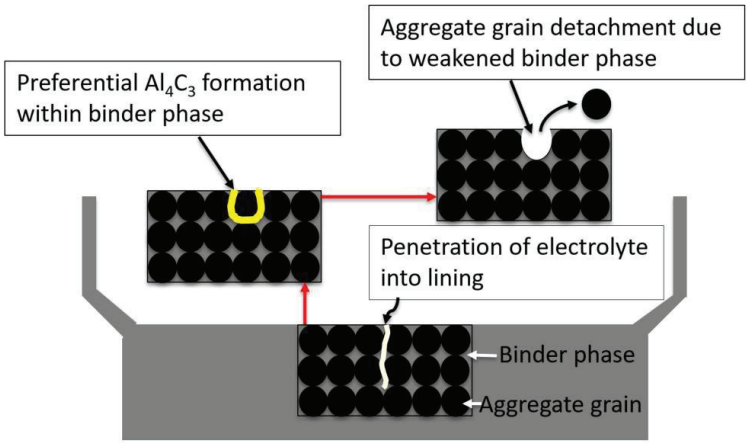

Figure 2.11. An illustration of the particulate detachment mechanism. Reprinted with permission from TMS [16]. Copyright © 2005 by the Minerals, Metals & Materials Society. Used with permission.

Weaknesses in the pot lining such as cracks or gaps formed from the effect of ramming paste shrinkage, low-density areas or foreign bodies present in the cathode lining can also initiate pothole formation [3]. Molten aluminium metal can penetrate the cathode at these weak spots resulting in a local increase in current density. These localized increases in current density create local magnetohydrodynamic (MHD) disturbances in the metal pad. Increased MHD disturbances would lead to a rapid exchange of the bath film under the metal pad causing an increased dissolution and transport rates of aluminium carbide resulting in high erosion rates and consequently pothole formation [3]. The erosion rate can greatly accelerate as the bottom of the metal-filled pothole gets closer to the collector bars. Siew et al. [16] have given a summary of possible pothole initiation mechanisms.

2.5. Wetting of Carbon Cathodes

2.5.1. Phenomenology and Measurements of Wetting

Wettability of a liquid refers to its ability to spread out or adhere to a solid surface [94]. This ability to spread out or adhere onto a solid surface is determined by the force balance between the internal and external forces acting on the liquid [95]. Internal forces such as cohesive forces between the molecules of the liquid causes the liquid to contract into a spherical droplet or bubble to attain the lowest possible surface free energy [95]. External forces such as gravitational and adhesive forces acting on the liquid droplet, on the other hand, lead to deformation of the droplet and cause it to spread out and wet the solid surface [95]. The surface tension of a liquid,

σ, measured in J/m^2 is the ability of the liquid to contract its surface area (due to intermolecular forces) to form a spherical droplet thereby avoiding spreading on the solid surface. The energy required to create a unit solid surface area is called the surface energy, γ, and is measured in J/m^2. The term "surface tension" is used for liquid-gas interfaces, while "surface energy" is used for solid-gas and solid-solid-liquid interfaces [96]. For a liquid droplet to spread on a solid surface, the total change of the surface energy per unit surface area (J/m^2), which is a measure of the free energy of the system, should be as low as possible [97]. The total change of surface energy is given by Equation 2.15.

$$dF = \sigma_{lg} + \gamma_{sl} - \gamma_{sg} \quad (2.15)$$

Where σ_{lg} is the surface tension at the liquid-gas interface (surface tension of the liquid), γ_{sl} is the surface energy at the solid-liquid interface and γ_{sg} is the surface energy at the solid-gas interface (surface energy of the solid). From Equation 2.15 it can be seen that the lowest possible free energy of the system is attained when the last term γ_{sg} (surface energy of the solid) is greater than the sum of the first two terms ($\sigma_{lg} + \gamma_{sl}$). Thus, wetting is favourable for solids with higher surface energies [97]. Figure 2.11 is a sketch illustrating the interfaces that occur when a liquid phase is brought into equilibrium with a solid surface in a gaseous environment. The angle made at the point of contact between the three phases (solid, liquid and gas) is referred to as the contact angle, θ, as shown in the Figure 2.12, and is used to characterize the degree of wettability of a solid surface by a liquid droplet.

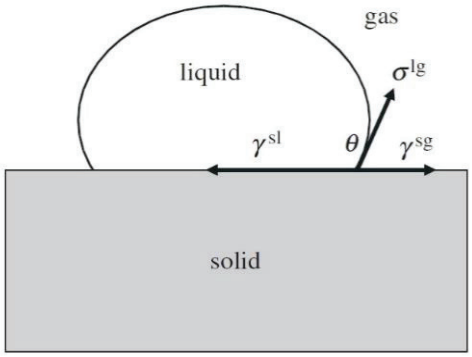

Figure 2.12. A sketch showing the interfaces and contact angle,θ, of a liquid phase in contact with a solid surface in a gaseous environment. σ^{lg} is the liquid-gas surface tension, γ^{sl} is the solid-liquid surface energy and γ^{sg} is the solid-gas surface energy [96].

The terms shown in Figure 2.11 can be rearranged to give the surface energy balance at equilibrium conditions using the Young-Dupré equation as follows:

$$\gamma^{sg} = \gamma^{sl} + \sigma^{lg} cos\theta \quad (2.16)$$

2.5. Wetting of Carbon Cathodes

An equation to determine the wettability can be obtained from Equation 2.16 as follows:

$$Cos\theta = \frac{\gamma^{sg} - \gamma^{sl}}{\sigma^{lg}} \tag{2.17}$$

Cosθ is referred to as the wetting coefficient and it gives a measure of the wettability of a solid surface by a liquid droplet [96]. A solid surface is not wetted (de-wetting) if $\cos\theta \leq -1$. This occurs when $\gamma^{sl} > \gamma^{sg}$ meaning the interface between the solid and gas is energetically favoured over the interface between the solid and liquid (thus a gas film is in contact with the solid surface instead of the liquid) [96]. A solid is partly wetted (neutral wetting) for $-1 < \cos\theta < 1$. This occurs when γ^{sl} and γ^{sg} approach each other in a situation where the interface for each of the phases are somewhat favoured (a situation where both liquid and gas are in contact with solid surface). Perfect wetting of the solid is achieved for $\cos\theta > 1$, that is when $\gamma^{sg} > \gamma^{sl}$, meaning the solid-liquid interface is more favourable over the solid-gas interface (thus the liquid film is in contact with the solid surface). The wetting is enhanced as the difference ($\gamma^{sg} - \gamma^{sl}$) approaches and becomes larger than σ^{lg}. Thus, a solid with high surface energy would favour wetting by a liquid more than one with low surface energy [96].

The contact angle θ, given by Equation 2.17, is normally obtained for a specific liquid droplet position on a solid surface in a solid-liquid-gas thermodynamic system [95]. The contact angle obtained this way is called the static contact angle as it represents the contact angle made at a particular position. However, the phenomenon of wetting on non-homogeneous and rough solid surfaces results in different metastable states for a liquid droplet in contact with the solid surface [95]. The liquid droplet would advance to occupy new surfaces giving rise to different static contact angles during wetting [94, 95]. The varying contact angles as the three-phase contact line changes due to the liquid droplet moving along the solid surface gives rise to a dynamic contact angle [95]. The contact angle achieved by the advancing liquid droplet is referred to as the advancing contact angle, θa, whereas the contact angle made by the receding liquid droplet is called the receding contact angle, θr. As the liquid droplet advances along the solid surface, its contact angle increases until a maximum is reached. For the receding liquid droplet however, the contact angle decreases until a minimum is reached. Thus, the advancing contact angles approach a maximum value while the receding contact angles approach a minimum value within the range of angles made with the solid surface. Conducting the wetting measurements at very low speeds, the dynamic contact angles can be measured to be close to a properly measured static contact angle [95]. The difference between the advancing and receding contact angles is termed the contact angle hysteresis or wetting hysteresis. Figure 2.13 is a sketch illustrating the two contact angles for a liquid droplet.

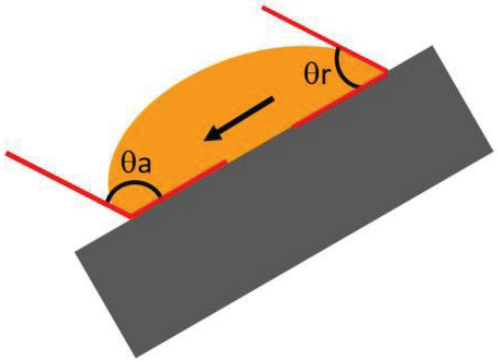

Figure 2.13. Schematic of the advancing (θa) and receding (θr) contact angles. Black arrow shows direction of movement of the liquid droplet.

Several techniques exist for the measurement of factors such as the contact angle, surface energy, surface tension, etc. that determines the wettability [95, 97]. A summary of two of the most employed techniques is given in the following.

The Sessile Drop Method involves studying the shape of a liquid droplet on a substrate [97, 98]. Since the shape of the liquid droplet on the substrate is determined by the actions of gravity and surface tension [97], it is possible to determine the surface tension of the liquid once the dimensions of the droplet formed is known [97]. The contact angle, as well as the dimensions of the liquid droplet needed to determine the surface tension, are obtained by photographing the droplet. Computer software is then used to determine the contact angles and dimensions of the droplet [97, 98]. The devices employed for the sessile drop technique usually consist of different types of vacuum furnaces for heating the samples (to form the liquid droplet) [98]. Dynamic contact angles can also be achieved with some of the setups by filling and draining the liquid droplet during the measurements [98, 99].

The Immersion-Emersion Method is a variant of the Wilhelmy balance method and involves measuring the changes in the forces acting on a solid sample as it is moved in (immersion) and out (emersion) of a liquid [95, 100]. Thus, for this technique measuring contact angles is reduced to measuring weight and length of a solid sample that can be done with high accuracy [94, 95]. Several researchers have employed this technique to measure wetting [94, 99-101]. The changes in force detected by the sensitive load cell connected to the solid sample in contact with the liquid is a result of gravity and buoyancy resulting from displaced liquid and the wetting force. The total detected force change, F, is given by Equation 2.18,

$$F = \sigma_{lg} P cos\theta + mg - V\Delta\rho g \qquad (2.18)$$

where σ_{lg} is the liquid surface tension, J/m^2, P is the perimeter of the solid sample, cm, θ is the contact angle (°), m is the mass of sample, g, V is the volume of displaced

liquid,cm^3, $\Delta\rho$ is the difference in density between the two fluids, g/cm^3, and g is the acceleration due to gravity, m/s^2 [95]. The first term of Equation 2.16 is the contribution from the wetting force while the last term comes from the buoyancy due to liquid displaced. Figures 2.14a is a sketch illustrating the different situation during an immersion and emersion cycle. Figure 2.14b is a graph representing the changes in the force acting on the solid sample as it moves in and out of the liquid.

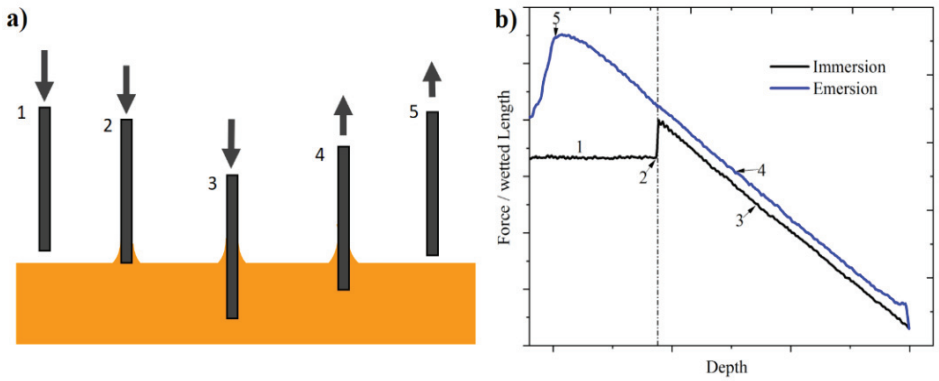

Figure 2.14. Immersion-emersion technique. a) Illustration of the immersion-emersion cycle. (1) The sample approaches the surface of the liquid (no change in force registered). (2) The sample contacts liquid surface causing the liquid to rise resulting in a positive force change as shown in the graph. (3) The sample is immersed further causing an increase in the buoyancy (last term of Equation 2.16) leading to a decrease in the force detected by the balance. (4) The sample is pulled out of liquid resulting in a continuous increase in force registered until point 5 where the liquid leaves the sample, resulting in a decrease in the force registered. b) Changes in forces acting on the solid sample during immersion and emersion. Redrawn and modified with permission from Springer. Copyright © 2013 [95].

2.5.1. Previous Wetting Investigation of Carbon Materials

Wetting is a very important phenomenon in several industrial applications due to the numerous interfacial processes occurring [95, 98]. The aluminium industry has several processes occurring at different interfaces during aluminium production [94, 100]. Wetting between the cryolite melt and the carbon anode is considered very important for the behaviour of the gas bubbles found on the anode surface during normal operations as well as during anode effects. The onset of the anode effect is observed to be preceded by de-wetting of the carbon anode by the molten electrolyte due to changes in electrolyte composition, mainly alumina depletion [102]. Laboratory investigations on the wettability of carbon by cryolite melts have been discussed in the aluminium electrolysis book by Thonstad et al. [2].

Doward [21] performed a series of contact angle experiments to determine the wettability of graphite by cryolite melt and Al. It was observed that for molten Al and graphite, the contact angle approached 180 ° indicating perfect non-wetting. A non-wetting situation was also observed between the cryolitic melt and graphite as the contact angle was about 115 °. However, upon the introduction of metallic Al to the cryolitic melt, perfect wetting was observed between the cryolitic melt and the graphite and a thin intermediate layer of the cryolite melt was observed between the graphite and Al metal. Dissolved Al metal was referred to as the primary wetting agent for cryolite on graphite. The non-wetting situation between graphite and Al metal was attributed to the stable oxide layer around the metal. Cryolite is proposed to dissolve this oxide layer. Based on the observation of a thin intermediate layer of cryolite between the graphite and Al metal, an Al_4C_3 formation process involving the transport of Al through the cryolite layer was proposed.

Laboratory tests by Qiu et al. [103] to study the wettability of carbon electrodes by a cryolite-alumina melt during aluminium electrolysis showed that cathodic polarization of the electrodes resulted in very good wetting between the cryolite-alumina melt and the carbon cathode. The reason given for the improved wetting between the carbon and the melt upon cathodic polarization was a phenomenon called "cathodic attraction

Radiographic observation of a Hall-Héroult electrolysis cell by Utigard and Toguri [104] showed that the contact angle formed by a drop of molten Al on the bottom of a graphite crucible varied between 150 ° and 170 °. No change in the contact angle was observed when a cell current was applied, and the bath composition was changed. The molten electrolyte was, however, observed to wet the graphite crucible during the measurements.

Tests by Kvande et al. [24] using a micro-electrolysis cell demonstrated that increasing cathodic current density increased the wetting between the electrolyte and the carbon cathode as well as bath penetration into the carbon cathode. The wettability was observed to remain constant around 110 ° to 115 ° irrespective of the contact time and electrolyte composition when no current was applied. Upon cathodic polarization of the carbon cathode samples, the wettability changed from non-wetting to wetting. The change in wettability was attributed to electro-capillary forces at the electrolyte-cathode interface. It was pointed out that the electro-capillary forces would cause changes in the structure of the bath layer at the interface, resulting in a reduction in the surface tension and thereby enhancing the wetting and consequently bath penetration into the carbon cathode.

Solheim et al. [100], Martinez et al. [94], Sommerseth et al. [105], Eidsvaag et al. [106], Haslund et al. [99], Åsheim et al. [101] have all employed the immersion-emersion technique to investigate the wettability of carbon electrodes by molten electrolyte and Al. A common observation made during wetting tests involving

carbon anodes and the molten electrolyte was improved wettability with increasing alumina concentration of the cryolite melt [100]. Polarization of the carbon anode was also observed to improve the wettability, however, at higher current densities it was observed that the wettability decreased. This was attributed to the formation of anode gases at these higher current densities [106]. The wetting tests by Haslund et al. [99] to investigate the wettability of different sets of carbon-TiB_2 composites towards molten Al did not yield any conclusive results.

3

Chapter 3. Experimental

3.1. Autopsy of Spent Potlinings

To investigate the mechanism(s) behind the carbon cathode wear in aluminium electrolysis cells, six autopsies were conducted at three different smelters during the course of this PhD work. Information concerning the pots autopsied such as cell technology, amperage, age and properties of the carbon cathode blocks is given in Table 3.1 [107-109]. The autopsies conducted were mostly focused on the top surface of the carbon bottom lining. Prior to the autopsies, the shutdown cells were allowed to cool for three days in a dry area under ambient air before residual bath and metal were carefully removed from the carbon bottom lining. All remaining debris on the carbon cathode surface was then removed by vacuum cleaning, revealing all important details such as cracks, potholes, pitting, metal plugs, adhered sludge, etc. A picture depicting the general top surface of the bottom blocks after cleaning is shown in Figure 3.1. The carbon cathode blocks of each spent potlining were labelled using a yellow marker for easy documentation.

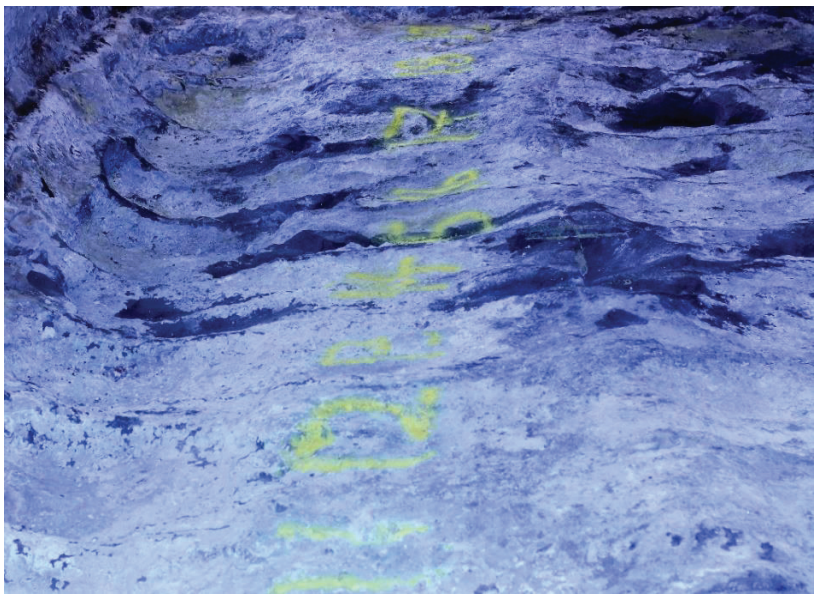

Figure 3.1. A typical top surface of an autopsied spent potlining.

3.1. Autopsy of Spent Potlinings

Table 3.1. Summary of the six spent potlinings including, technology, pot age, carbon material and properties [107-109].

Pot	Technology	Amperage (kA)	Cathode Current Density (A/cm^2)	Pot Age (days)	Cathode Block Trade name	Carbon Type	Apparent density (g/cm^3)	Open porosity (%)	Specific electrical resistivity ($\mu\Omega m$)
1	Prebaked-Side by Side	313	0.8	2461	TG2	Graphitized and Impregnated	1.73±0.03	14±2	11±2.5
2	Prebaked-End to End	175	0.8	3154	HC10	Graphitic (100 % Graphite)	1.58	19±1.3	20±1
3	Prebaked-Side by Side	313	0.8	1731	D	Graphitized - High Density Isotropic	1.78	14±1	10.5±1.5
4	Prebaked-End to End	175	0.8	2849	5BGNR	Graphitic (100 % Graphite)	1.65±0.03	19±1.5	16±2
5	Prebaked-End to End	175	0.8	1028	PB10	Graphitic (100 % Graphite)	1.61	20	20
6	Søderberg-End to End	128	0.6	2732	HC3	Semi-Graphitic (30 % Graphite)	1.53		30

3.1.1 Macroscopic Characterization of Wear

Optical photography and laser interferometry were employed to document topological features as well as other important features on the top surface of the different carbon bottom linings. Details such as pitting, potholes, sludge, cracks, metal plugs, etc. were captured using a camera, while the wear patterns/profiles, as well as the potholes, were manually measured. Figure 3.2a shows a section of a spent potlining with the instruments for manual measurement. The manual measurements involved using a laser for referencing, an aluminium bar to accurately locate the cathode block and a ruler to measure the wear. Each of the individual cathode blocks was measured from one end to the other end at regular intervals of 40 cm apart. Potholes identified on the spent potlining were also manually measured, an example of a pothole being measured is shown in Figure 3.2b.

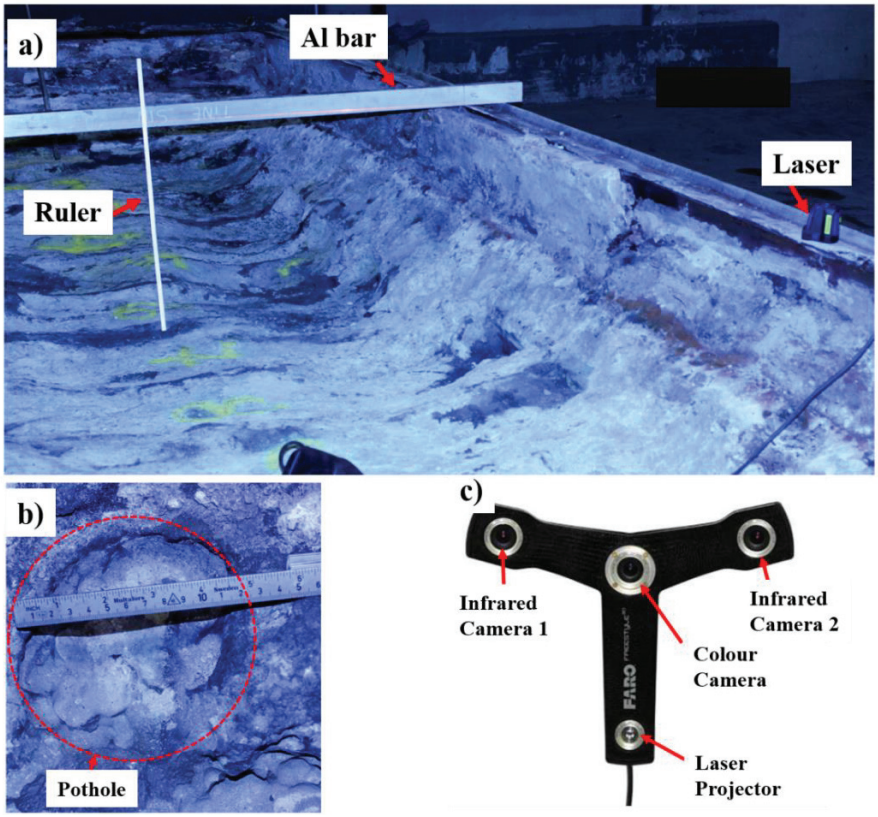

Figure 3.2. Cathode wear measurement techniques. a) An image of a spent potlining, showing the instruments for the manual measurements. b) Measurement of a pothole. c) The FARO freestyle handheld 3D laser scanner.

3D laser scanning with a FARO freestyle handheld 3D laser scanner as shown in Figure 3.2c was employed in documenting the wear profile of pot 3. The 3D laser scanner equipped with a laser projector, a colour camera and two infrared cameras accurately documents all structures on the carbon bottom lining in 3D and creates high-definition point clouds. The high-definition point clouds data were analysed using the MeshLab software program to obtain 3D images of the surface profile including the wear profile and other important features such as pitting on the cathode surface.

Characterization of pitting on the cathode surface of pot 3 was done by counting and measuring the characteristic diameters of the individual pitting captured on the 3D images employing a length measurement tool in the MeshLab software program. Pitting on the cathode surface of pots 2 and 4 were characterized by using the public domain software ImageJ to analyse optical photographs captured from areas with distinct pitting.

3.1.2. Sampling

In order to investigate the mechanism(s) behind carbon cathode erosion, cylindrical carbon cathode samples from different locations with high and low wear were obtained by drilling out vertical cylinders out of the lining using an electrical drilling machine. Figure 3.3a illustrates the orientation of the carbon cathode blocks. Different electrical drilling machines with different capacities were employed for the sampling. The larger drilling machines could drill samples up to a depth of 32 cm with a diameter of 10 cm, labelled 2 in Figure 3.3a, while the smaller ones could drill up to depths of 10 cm and diameters of 6 cm, labelled 1 in Figure 3.3a. The large autopsy samples with depths of about 32 cm (see Figure 3.3b) were used to investigate the distribution of phases within the carbon bottom lining all the way down to the refractory lining. The small samples seen in Figure 3.3c, with depths and diameters up to 10 and 6 cm respectively were used for CT scanning and microscopy analyses. All the carbon autopsy samples were vacuum packed on site to avoid hydration.

To understand the chemistry of the bath film on the cathode surface, samples of the solidified bath on the cathode surface were collected by hand and stored in plastic bags.

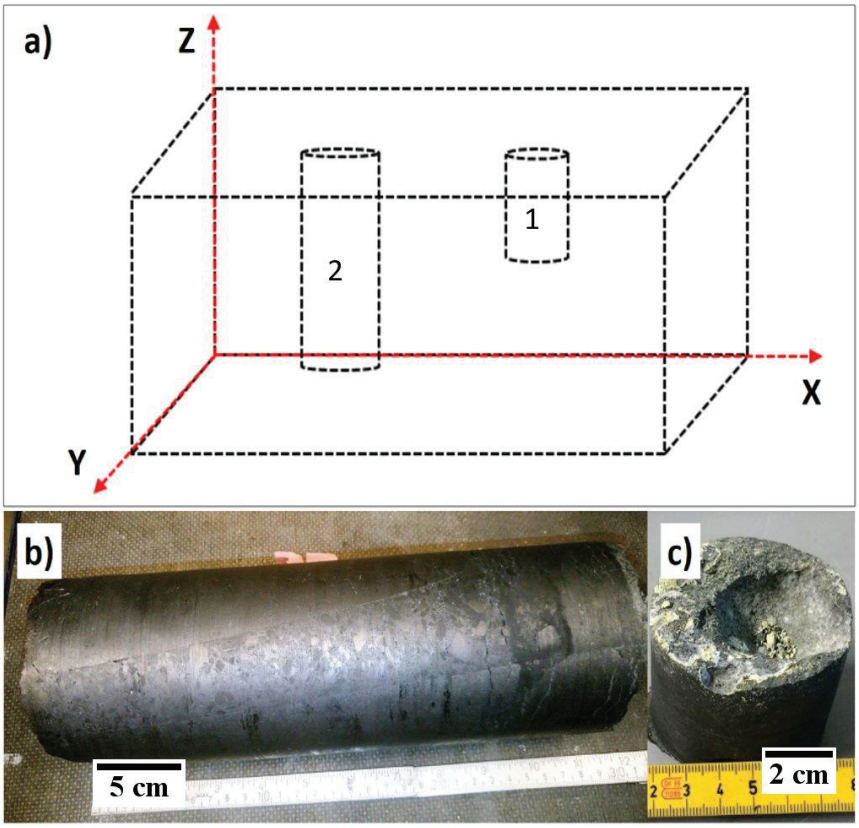

Figure 3.3. Sampling during autopsies. a) A sketch showing the locations and orientations of the cylindrical carbon cathode samples. Sample 1 was only used for profile analysis while sample 2 was used for the analyses explained in this thesis. b) An autopsy sample drilled from a depth of 32 cm used for phase distribution analysis. c) An autopsy sample drilled from depths of up to 10 cm used for CT scanning and microscopy analyses.

3.1.3. Characterization of Autopsy Samples

Scanning electron microscopy (SEM), optical microscopy, X-ray computed tomography (CT scanning), 3D scanning, as well as manual measurements were employed to characterize the wear profiles of the carbon cathode samples collected during the autopsies.

Powder X-ray diffraction (XRD) was employed to determine qualitatively the phase distribution within the carbon cathode samples as well as the chemistry of the frozen bath collected from the cathode surface. For the phase distribution analysis, the autopsy sample, about 32 cm in height was sliced into 8 discs of about 4 cm thick.

3.1. Autopsy of Spent Potlinings

The sliced carbon samples, as well as the frozen bath components collected from the cathode surface, were milled to powder with a ball mill for about 2 minutes and sieved with a sieve mesh size of about 65 µm. The powdered samples were then mounted onto a plastic holder for the XRD. A Bruker D8 Advance Davinci 1 X-ray diffractometer equipped with a LynxEye detector was used to obtain diffractograms across a 2-theta range of 6° to 75° for all the qualitative phase analyses conducted. The different phase compositions represented by the different diffractograms were determined by means of the DIFFRC.EVA V4.2.1A evaluation software program using the International Centre for Diffraction Data (ICDD) Powder Diffraction File™ (PDF®) database, PDF-4+, 2019. Table 3.2 displays the Powder Diffraction File (PDF) references used for the XRD analysis.

Table 3.2. Powder Diffraction File (PDF) references used for the XRD analysis.

Phase	Formula	PDF reference
Aluminium carbide	Al_4C_3	PDF 00-035-0799 (ICDD, 2019)
Aluminium oxide	Al_2O_3	PDF 00-046-1212 (ICDD, 2019)
Beta alumina	$Na_2Al_{11}O_{22}$	PDF 04-010-5172 (ICDD, 2019)
Calcium fluoride	CaF2	PDF 00-035-0816 (ICDD, 2019)
Cryolite	Na_3AlF_6	PDF 00-025-0772 (ICDD ,2019)
Chiolite	$Na_5Al_3F_{14}$	PDF 00-030-1144 (ICDD, 2019)
Graphite	C	PDF 00-056-0159 (ICDD, 2019)
Nepheline	$NaAlSiO_4$	PDF 04-010-3961 (ICDD, 2019)
Sodium calcium aluminium fluoride	$NaCaAlF_6$	PDF 04-009-4851 (ICDD, 2019)
Sodium fluoride	NaF	PDF 00-036-1455 (ICDD, 2019)

Prior to the microstructural analysis, the carbon cathode samples were cut into smaller pieces, embedded into epoxy and electrically conducting resin which contains carbon fillers (polyfast) and cured overnight before mechanically polishing to obtain a smooth surface.

Optical microscopy was performed using a REICHERT MeF3A optical microscope whilst scanning electron microscopy (SEM) was conducted using a Hitachi S-3400N Scanning Electron Microscope. Energy Dispersive X-ray Spectroscopy (EDS) mapping was performed using an Oxford Instrument Aztec system to analyse the different elements within the phases present at the interface, as well as within the pores of the carbon cathode samples.

X-ray computed tomography (CT) was employed to study and characterize the microstructure of the carbon cathode samples. The CT data was acquired by a Nikon XTH225ST instrument (cone beam volume CT). A tungsten reflection target was used, with an acceleration voltage of 140 kV and a current of 135 µA. The imaging was done with an integration time of 1 second, amplification of 18 dB, with 3142 projections per 360º. The distance from the source to sample was 226.7 mm, distance

from the source to the detector was 1124.8 mm, detector size 400x400 mm, resulting in a voxel size of 40.2 µm. The images were exported as 16-bit TIFF and processed using the public domain software ImageJ. The autopsy samples were used without further preparation but were placed into a plastic container to provide stability during scanning.

The linear intercept method was employed to analyse the CT scanning images to determine the average coke aggregate size distribution within the carbon matrix of the graphitized cathode blocks investigated during the autopsy of pot 3. The linear intercept technique employed involved drawing straight random lines through a CT image showing the aggregates and counting the number of aggregates being intercepted by the lines. The average aggregate size is then determined by dividing the number of aggregates intercepted by the actual length of the line. A CT image showing aggregates being intercepted is given in Figure 3.4.

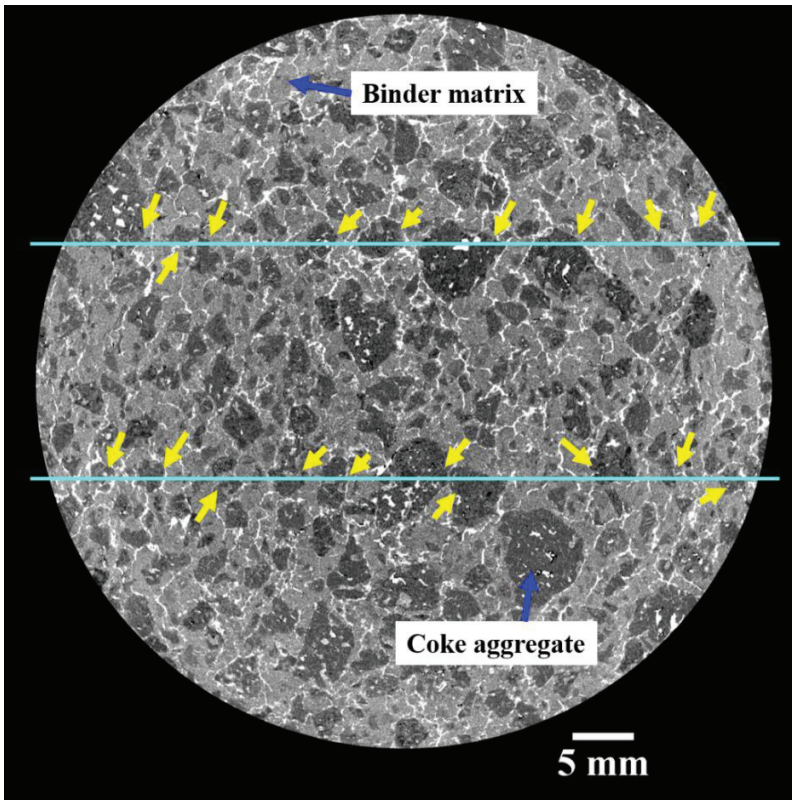

Figure 3.4. A CT image showing aggregates being intercepted, yellow arrows indicate the coke aggregates being intercepted during the linear intercept method.

An overview of the different techniques employed during the autopsies is given in table 3.3.

Table 3.3. Overview of activities and characterization techniques employed.

Pot	SEM /EDS	Optical Microscopy	CT Scanning	Powder XRD	Pitting/Pothole Analysis	3D scanning	Linear Intercept
1	X	X	X	X	X	-	-
2	-	X	-	X	X	-	-
3	X	X	X	-	X	X	X
4	-	-	-	X	X	-	-
5	-	-	-	-	X	-	-
6	X	X	-	-	X	-	-

3.2. Wetting Measurements

To understand the autopsy observation of a thin layer of frozen electrolyte on the top surface of the carbon block, laboratory wetting measurements were conducted. The measurement technique, also called the immersion-emersion technique, involves dipping the carbon cathode material gradually into the molten electrolyte and/or Al while measuring the weight changes, and repeating as the carbon is withdrawn from the melt. The technique is described in the literature review.

3.2.1. Apparatus

The apparatus employed for the wetting measurements, shown in Figure 3.5, is based on the immersion-emersion technique and was originally designed and built by Martinez et al. [94]. The apparatus consists of a Schunk-Tokai graphite crucible, with an inner height and diameter of 110 mm and 76.5 mm, respectively, containing the liquid(s) to be tested. The carbon sample was suspended from a load cell and a linear actuator driven by a stepping motor for moving the graphite crucible up and down. As the apparatus has mostly been used to study wetting of carbon anodes, modifications such as switching the polarity and inserting a high-alumina crucible into the graphite crucible to separate molten Al from the anodic graphite crucible were done.

The outer part of the apparatus consists of a water-cooled, gas-tight, vertical tube furnace with a replaceable mullite inner tube (100 mm diameter and 700 mm length) sealed on both sides by water-cooled steel lids with O-rings. The whole furnace was mounted on a freestanding aluminium structure. To allow for the vertical movement of the graphite crucible containing the liquid(s), the graphite support for the crucible

was connected to an actuator (IAI ROBO Cylinder RCP2 series with ±0.02 mm accuracy) using a 12 mm diameter stainless steel rod.

The weight of the sample was monitored using a high sensitivity FUTEK LSB200 (FSH02665) load cell with a load capacity of 22 N and temperature compensation up to 72 °C. The carbon cathode samples were mounted on a steel rod hanging from the load cell that was located outside the furnace to avoid heat radiation. Electrical connection to the sample was through a highly stranded copper wire connected to the steel rod on which the carbon sample hangs. Due to the sensitive nature of the load cells, additional weights were added on top of the sample for stability during the measurements.

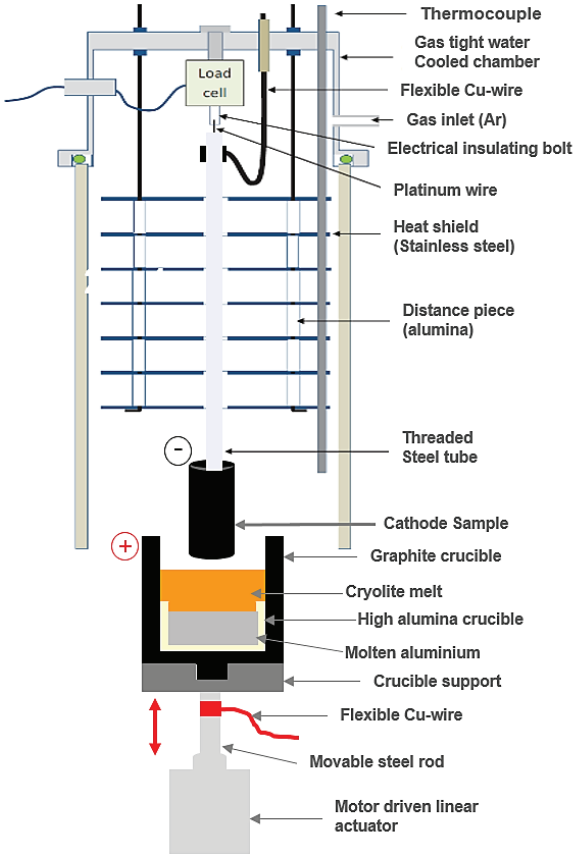

Figure 3.5: A sketch of the internal parts of the wetting apparatus with the load cell attached to the carbon sample, the crucible containing molten electrolyte and/or Al, and the actuator for vertical movement of the crucible.

The temperature of the sample was monitored via a thermocouple at the top section of the furnace while the temperature of the crucible and the liquid(s) it contained was monitored by a thermocouple within the stainless-steel rod attached to the actuator.

3.2. Wetting Measurements

The combination of heat shields and water-cooling helped keep the temperature at the top section of the furnace below 42 °C, thereby avoiding overheating of the load cells. Polarization of the carbon cathode sample during the wetting test was achieved by means of a power supply (HP 6032A, 50A/60 V). To avoid high voltages, polarization of the samples was only done when they were immersed in the molten electrolyte or Al. All pieces of equipment connected to the wetting apparatus were controlled and logged in Lab View. Load cell data was logged via a FUTEK IPM650 micro-controller with a 24-bit A/D converter while current and voltage data were logged with a NIcDAQ 9174 data acquisition unit with an NI9205 module. Temperature data was recorded by the NI9211 module. Sampling frequency was usually kept at 5 Hz [94].

3.2.2. Materials and Materials Characterization

Three industrial grade carbon cathode materials and a fine grain, high-density graphite material were tested by the immersion-emersion technique:

- Anthracitic carbon (grade G0320) corresponding to 70 % electro-calcined anthracite and 30 % graphite and binder heated to 1200 °C
- Semi-graphitized or graphitic carbon (grade PB10) corresponding to 100 % graphite and binder heated to 1200 °C
- Graphitized carbon (grade EG) prepared from calcined petroleum coke and binder heated to over 2500 °C
- Fine grain high-density graphite (grade G348) with uniform structure prepared from fine graphite grains by cold isostatic pressing (CIP).

The test specimens were 15 mm in diameter and 80 mm long.

An Alicona Infinite Focus 3D optical profilometer was used to characterize the surface roughness of the

pristine carbon materials while the permeability was measured using a Carbon R&D RDC - 145 air permeability apparatus. The densities of the different carbon cathode samples were determined by measuring the volume and mass. The samples were screwed onto a 250 mm long stainless-steel rod (6 mm diameter) suspended onto a platinum wire to ensure that the lower surface of the sample was horizontal.

The electrolyte employed for the experiments was chosen to reflect industrial electrolyte compositions and had a cryolite ratio (CR) of 2.2 and comprised of 80.75 wt% synthetic cryolite (≥ 97 %, Fluorsid), 4.5 wt% CaF_2 (97 %, Merck), 11.75 wt% AlF_3 (≥ 90.5 %, Noralf, Fluorsid) and 3 wt% γ-alumina (≥ 99.5 %, Merck). Aluminium metal was added as shots.

3.2.3. Experimental Procedure

The assembly was heated to 970 ± 2 °C at a heating rate of about 322 °C/h. The wetting measurements were performed by immersion of the carbon sample from an initial position about 10 mm from the surface of the melt into the crucible at a rate of 0.2 mm/s to a specific lower position, normally 10 mm from bottom of crucible or top of the metal pad. It was then kept at this position for a short time, usually 30 or 60 s, before being moved back to the initial position at the same rate of 0.2 mm/s. An immersion cycle in this study refers to the movement from the initial position to the final lower position, while, an emersion cycle refers to movement from the lower position back to the initial position. Figure 3.6 illustrates the positions taken by the carbon sample during the immersion and emersion cycles with only molten electrolyte present. Polarization of the samples in the cathodic direction was done for 30 seconds (on molten electrolyte) and 60 seconds (molten electrolyte and Al) applying a current density of 1 A/cm^2 at the lower position of immersion.

For tests conducted in molten electrolyte, the height of melt was about 50 mm as illustrated in Figure 3.6. For tests including both molten electrolyte and aluminium metal, about 25 mm of molten metal and 35 mm of molten electrolyte were used. To investigate the wettability of aluminium metal towards the carbon cathode, about 35 mm of molten Al and 10 mm of molten electrolyte were used. The addition of 10 mm of molten electrolyte was due to difficulties with the experiments using only the molten metal.

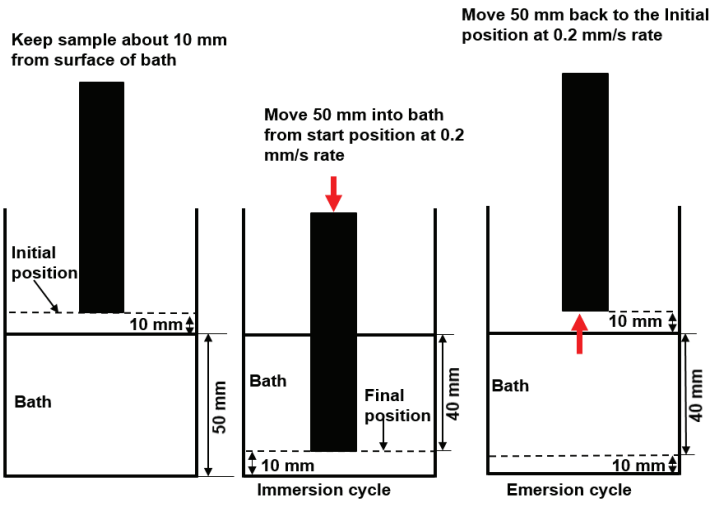

Figure 3.6. Positions of the carbon sample relative to molten electrolyte during the immersion and emersion cycles in molten electrolyte.

3.3. Finite Element Simulation of Carbon Cathode Wear

After the wetting experiments, cross-sections of the tested carbon samples were embedded in epoxy overnight and mechanically polished. The mechanically polished samples were then analysed by optical and scanning electron microscopy as well as EDS analysis using the instruments described in section 3.1.3.

3.3. Finite Element Simulation of Carbon Cathode Wear

Finite element simulations using COMSOL Multiphysics 5.3® software were done to support the hypothesis presented for cathode wear.

The FEM model employed in this work consisted of a thin bath film (µm thickness) with different configurations of solid and liquid bath on a carbon cathode surface. By applying a potential across the thin bath film in a vertical direction, the current density along the carbon cathode at the locations with either molten or frozen electrolyte was modelled. Assuming the electrolyte was purely cryolite, the electrical conductivities of the molten and frozen electrolyte were set to 214 and 2.14 S/m, respectively, while that of the carbon cathode was set to 10^5 S/m [2, 3, 110, 111]. The thickness of the electrolyte film (molten and frozen) was kept at about 50 µm while the potential applied across this film was chosen to be 3 mV. Assumptions made included the electrolyte as purely cryolite with no droplets of Al, migration of ions as the main charge transfer mechanism as well as current flow only in the vertical direction. The governing equation for this model is $V = IR$, where V is the voltage drop across the electrolyte film in volts, I is the current in amperage and R is the electrical resistance within the electrolyte film in ohm. Figure 3.7 illustrates the geometry of the model used in the simulation.

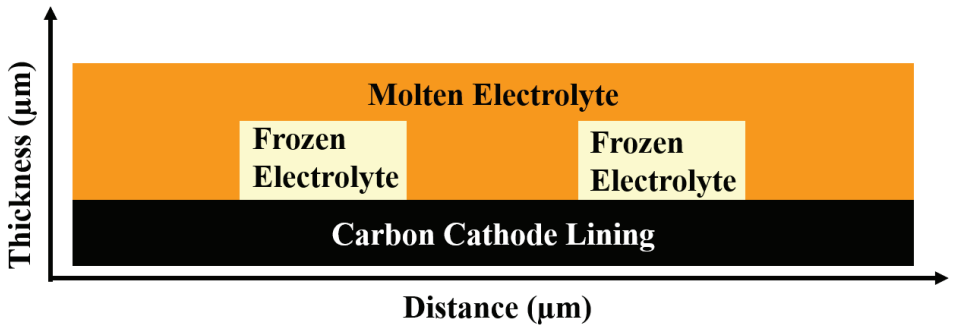

Figure 3.7. Geometry of the electrolyte film on the carbon cathode surface used in the COMSOL simulation.

4

Chapter 4. Autopsy of Spent potlinings

4.1. Autopsy of Pot 1

4.1.1. Macroscopic Observations

Visual observations from the first autopsy conducted on a spent prebaked technology pot arranged side-by-side showed a thin layer of frozen electrolyte or bath covering the whole surface of the carbon cathode. This is shown in Figure 4.1a, where the white part is frozen electrolyte. Two drilled cylindrical samples, displayed in Figures 4.1b and 4.1c, demonstrate the presence of a solidified electrolyte layer. The typical thickness of the layer of frozen electrolyte was found to be 640±300 µm. Additional data from the measurements of the thickness of frozen electrolyte on the cathode surface of pot 1 is provided in Appendix 10A.

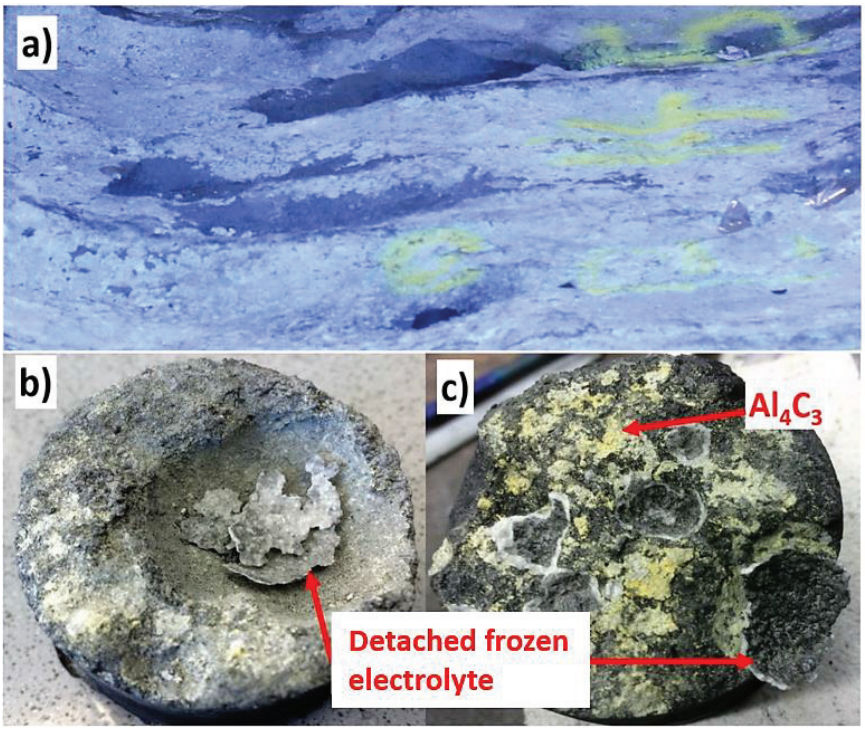

Figure 4.1. Cathode surface of pot 1. a) White frozen electrolyte covering the whole carbon cathode surface. b) A detached frozen electrolyte within a pothole on a carbon cathode sample. c) Aluminium carbide layer observed below a detached frozen electrolyte.

4.1. Autopsy of Pot 1

Aluminium carbide was typically observed as a thin yellowish layer in direct contact with the carbon cathode, and below the thin layer of frozen electrolyte on most of the carbon cathode surfaces. The presence of carbide below the thin layer of frozen bath is shown in Figure 4.1c. Aluminium carbide was also found to be present within the ramming joints between the carbon cathode blocks.

An overview of the observed wear pattern and features on the cathode surface is shown in Figure 4.2. The position where cylindrical samples were drilled out of the cathode is also marked in the figure. The wear profiles measured at different positions across the cathode are shown in Figure 4.3. A generally non-even wear was observed all over the cathode blocks, and the ramming joints were observed to be less worn compared to the carbon blocks. The typical wear pattern was characterized by highest wear at both side ends of the spent potlining and less worn at the centre channel. Another location of relatively higher wear than at the centre channel, however, was discovered on both sides of the centre channel. This wear pattern corresponds to the WW wear pattern reported by Skybakmoen et al. [11]. Cathode block 19, which was located at the suction end of the spent potlining, was observed to have high amounts of sludge on the cathode surface and exhibited the least wear while cathode block 1, located at the tapping section, showed the highest wear of all the cathode blocks at the centre channel area.

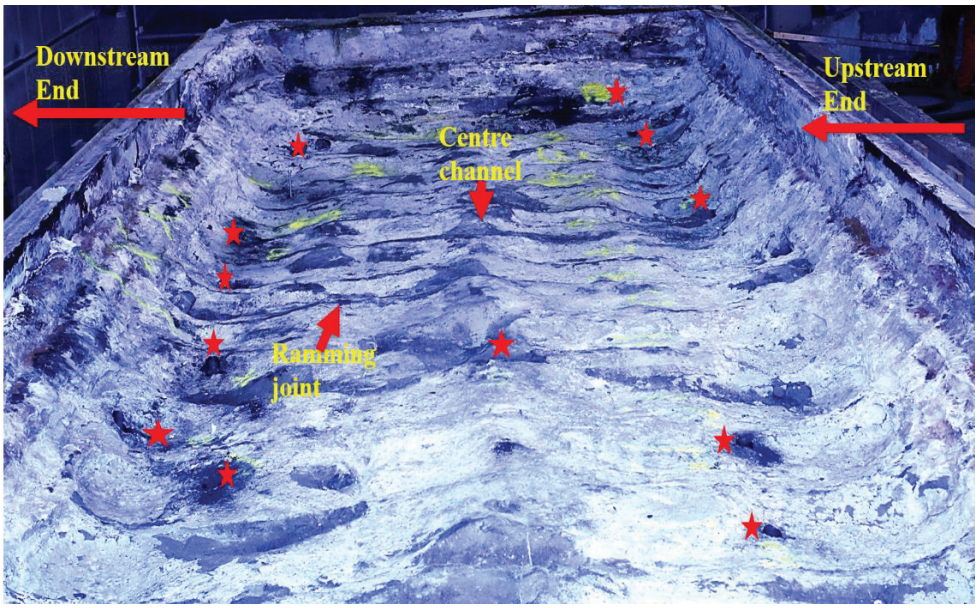

Figure 4.2. The cathode surface of pot 1 with the "WW" wear pattern. Red stars show positions where autopsy samples were drilled.

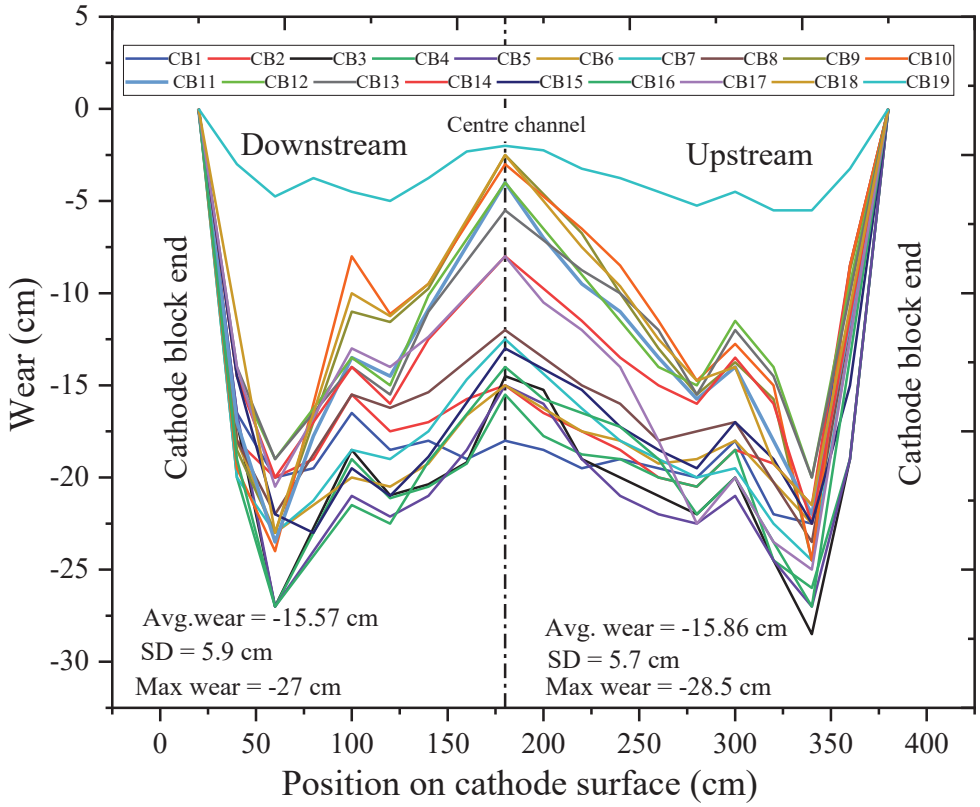

Figure 4.3. Wear pattern measured across pot 1 at different positions, CB1 corresponds to cathode block 1 and CB2 cathode block 2 and so on. The data used for the figure is given in Appendix 10A.

Potholes as presented in the present autopsies refer to all locations on the cathode surface characterized by high wear with a roughly hemispherical base and steep sides as discussed by Siew et al. [16]. Different sizes and shapes of potholes were observed at different locations on the cathode surface. However, most of the potholes were seen close to the cathode block ends of the spent potlining. Representative examples of the potholes observed are shown in Figure 4.4. The large-sized potholes, such as those seen close to the side ends of the spent potlining, could measure up to 55 cm in diameter and about 7-10 cm in depth while the medium-sized ones measured around 5-15 cm in diameter with depths reaching up to 6 cm. The small-sized potholes, which were sometimes noticed to cluster together forming medium or large-sized potholes, measured around 2-5 cm in diameter as shown in Figure 4.4 with depths of about 1-2 cm. Table 4.1 gives a summary of typical dimensions of the potholes observed in the autopsy of pot 1. The potholes size measurements data is given in Appendix 10A.

4.1. Autopsy of Pot 1

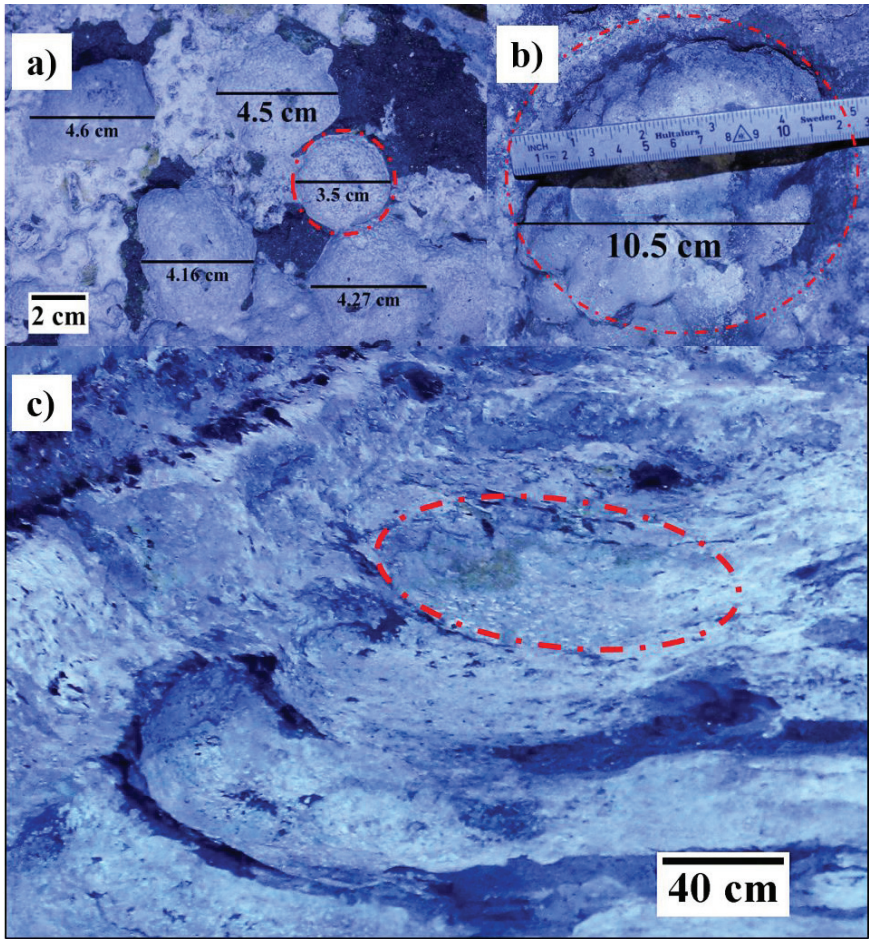

Figure 4.4. Potholes on pot 1. a) Small-sized potholes found on the cathode blocks from pot 1. b) Medium-sized potholes on carbon cathode surface from pot 1. c) Large-sized potholes found at ends of cathode blocks from pot 1. Red dashed circles illustrate some of the potholes. Typical diameters are given in the pictures.

Table 4.1. Summary potholes found on the spent potlining of pot 1 with 19 cathode blocks.

Diameter range of Pothole, cm	Average diameter of Potholes, cm	Average depth of Potholes, cm	Maximum diameter of Pothole, cm	Number of Potholes per Cathode block	Number of Cathode blocks with Pothole
2-5	4.0±0.3	1.6±0.2	4.6	0.8	15
5-15	9.4±1.0	4.5±0.7	10.5	0.16	3
15-55	46.4±5.3	8.8±1.7	52.7	0.68	13

A variation in the degree of carbon wear was observed at the cathode block ends of the spent potlinings. In some areas, carbon was nearly worn down to the collector bars with just a few millimetres of carbon remaining. These findings show that the wear rate can vary significantly at different locations of the cathode surface.

Closer examination of the carbon cathode surface at the locations with the highest wear revealed a wear pattern characterized by pitting. The occurrence of pitting at the location with the highest wear is displayed in Figure 4.5. Pitting was also seen on the ramming joints between the carbon cathode blocks.

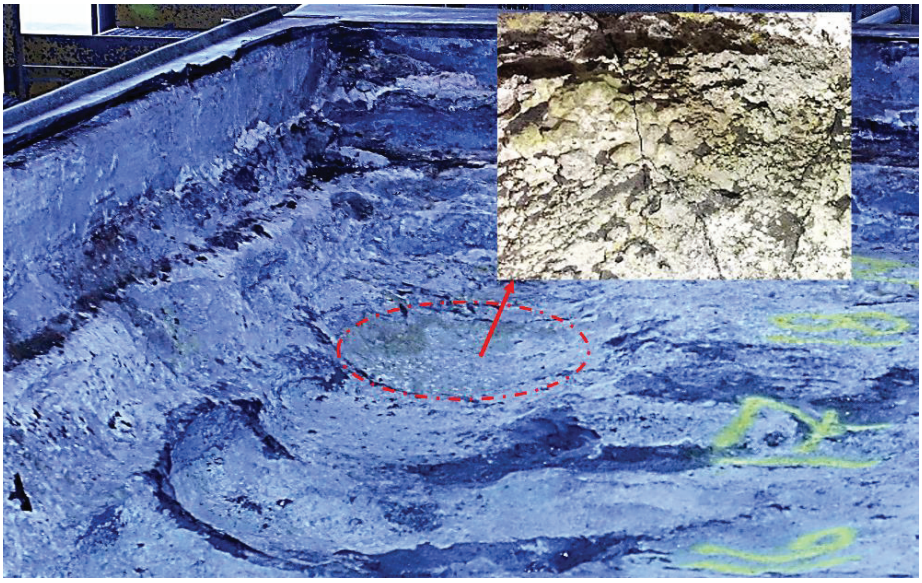

Figure 4.5. Pitting within the potholes at cathode blocks ends. Insert shows the pitting on the cathode surface within the pothole.

4.1.2. Microscopic Observations

4 cylindrical samples drilled from 4 different cathode blocks were investigated by X-ray computed tomography (CT). A typical sample is shown in Figure 4.6a, and a representative CT micrograph is displayed in Figure 4.6b. Light regions in the CT images correspond to solidified electrolyte components, while the dark and light grey regions represent the aggregates and binder matrix of the carbon material respectively. The completely black regions in the image correspond to areas with no material. The CT image depicted in Figure 4.6b revealed the larger degree of porosity in the ramming joint, resulting in more bath infiltration relative to the cathode blocks. The images demonstrate that all the carbon materials were completely infiltrated by molten bath during the operation of the pots.

4.1. Autopsy of Pot 1

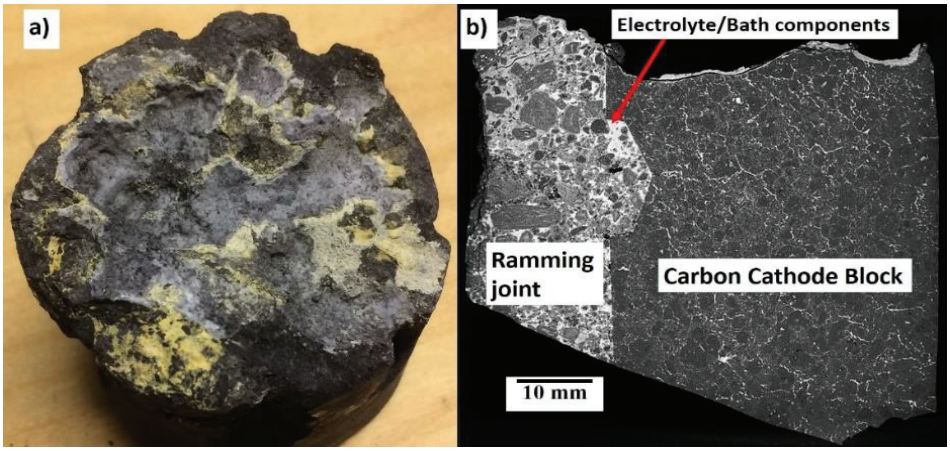

Figure 4.6. a) A typical carbon sample from pot 1 used for CT scanning. b) A CT image showing the varying degree of electrolyte penetration between the cathode block and the ramming joint.

The CT images did also provide detailed information about the microstructure of the samples and the topography of the cathode surface. As mentioned earlier, the aggregates are clearly visible in the images as dark grey, while the binder matrix with significant porosity appears light grey. The CT images also revealed that the surface of the spent cathode lining is relatively smooth at the scale of the image and that the wear is uniform across both the binder matrix and aggregates as shown by Figure 4.6b. Other examples of CT scanning images, showing the surface wear profile along the carbon-electrolyte interface, are displayed in Figures 4.7, 4.8, 4.9 and 4.10.

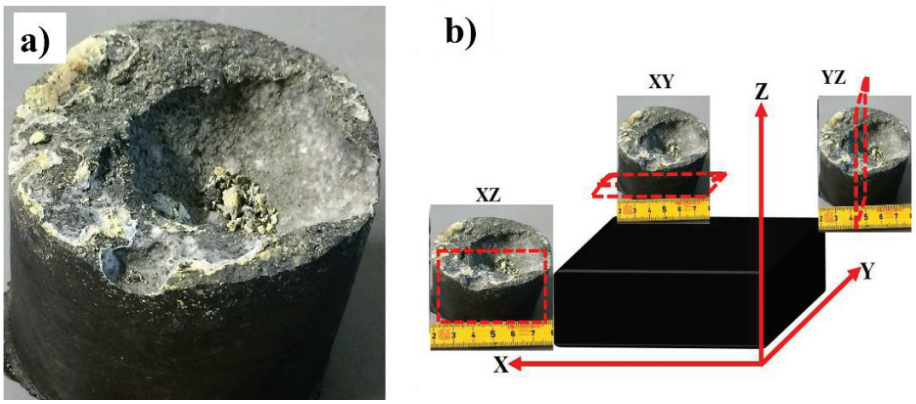

Figure 4.7. a) Carbon autopsy sample from cathode block 12 of pot 1. b) Illustration of the XY, XZ and YZ orientation of the CT images.

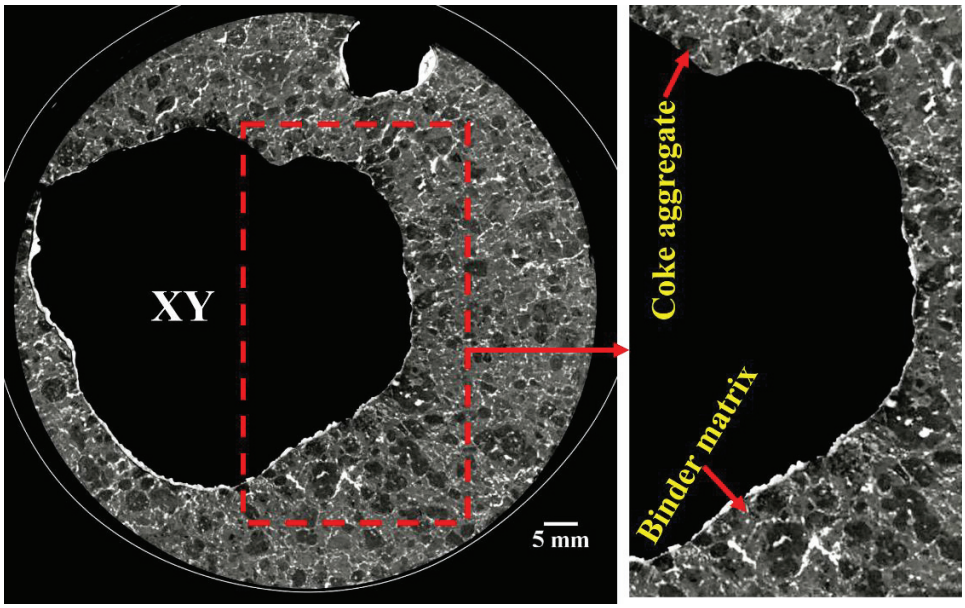

Figure 4.8. CT image showing the wear profile along the XY orientations for the pothole sample showed in Figure 4.7

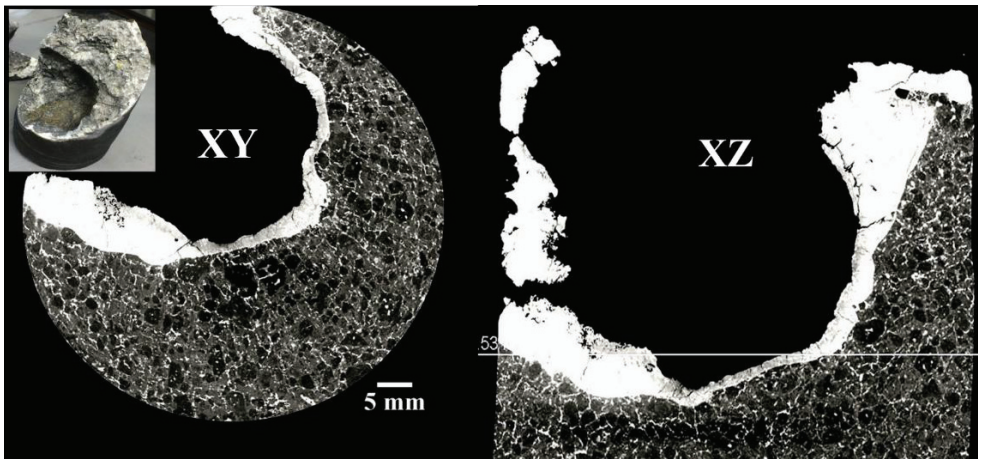

Figure 4.9. CT images in the XY and XZ orientations for a pothole sample drilled from cathode block 11 of pot 1. Insert in the XY orientation image is the sample used for the CT scanning.

4.1. Autopsy of Pot 1

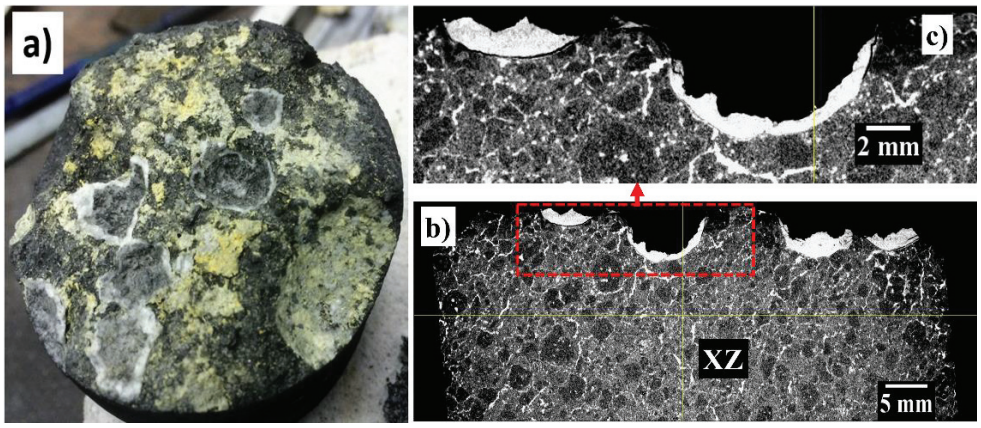

Figure 4.10. a) Carbon autopsy sample from cathode block 10 of pot 1. b) CT images showing the wear profile in the XZ orientation. c) The highlighted section of the image shown in Figure 4.9b displaying the relatively uniform front at the wear surface.

Furthermore, the CT images showed that the wear was relatively uniform across the cathode surface suggesting a non-preferential wear for the binder matrix and coke aggregates. No evidence of coke aggregate pull-out could be detected from the CT images.

Optical microscopy and SEM/EDS gave additional information on the microstructure as well as phases present at the cathode surface. Optical micrograph of the microstructure of the carbon cathode material is shown in Figure 4.11a. The aggregate, as well as the binder matrix, marked in the images, are possible to identify using polarized light. It was also possible to identify the natural boundaries of the coke aggregates to follow the changes as the carbon materials wear. The optical micrograph of the cathode wear surface is displayed in Figure 4.11b. The relatively even wear surface of the coke aggregates is evident at this magnification. Furthermore, Figure 4.11b revealed remains of worn-out coke aggregates within the carbon matrix at the carbon-electrolyte interface. No evidence of coke aggregates pull-out was seen from the optical micrographs. At higher magnifications as depicted in the SEM image in Figure 4.12, the wear surface of the aggregates towards the electrolyte appears to be uneven in contrast to the even wear surface at relatively low magnification.

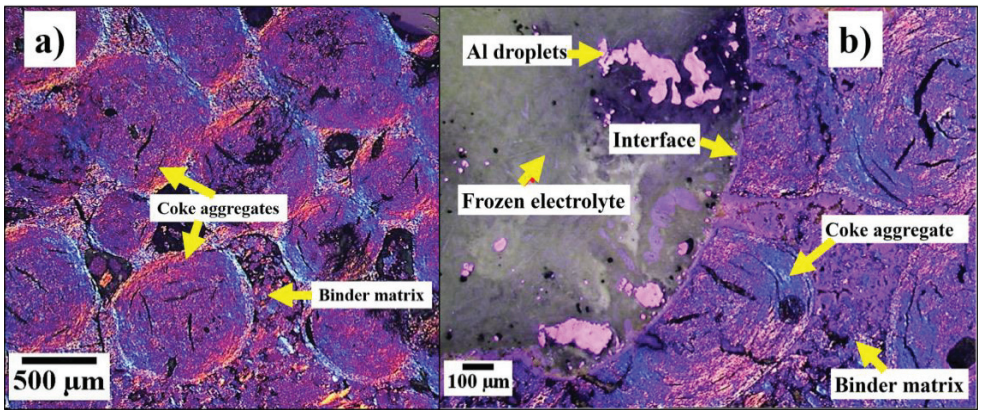

Figure 4.11. a) Microstructure showing the components within the carbon cathode material of pot 1. b) Typical wear surface along the carbon-electrolyte interface of the carbon samples investigated. Additional data is provided in Appendix 10D.

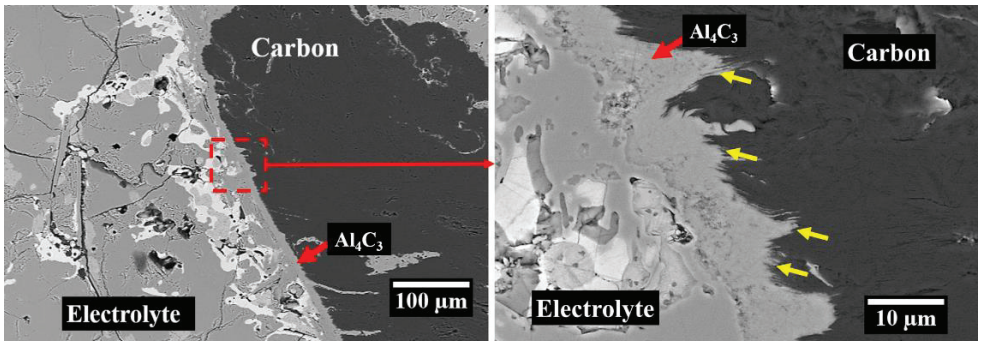

Figure 4.12. Wear surface at the carbon-electrolyte interface at high magnification. Carbon sample collected from pot 1. The yellow arrows on the highlighted section of the image show the uneven reaction front observed at high magnification. Additional data on the wear surface at high magnification is given in Appendix 10D.

Optical microscopy and SEM/EDS were used to determine the phases present at the carbon surface as well as within the pores of the carbon cathodes. A typical example of the presence of aluminium carbide, aluminium and solidified electrolyte at the carbon-electrolyte interface are shown in Figures 4.13. Corresponding observations of the presence of aluminium carbide and solidified fluorides within the pores of the carbon are shown in Figure 4.14, including an optical micrograph and EDS element maps in the same region. Aluminium carbide was represented as areas rich in Al and O. Oxygen is present due to hydration and/or oxidation of the carbide layer. The limited wettability of the carbon cathode material by the Al metal pad can also be seen from the figure. The material observed to be in direct contact with the carbon cathode was aluminium carbide. Aluminium carbide is represented as a phase rich in

the elements Al and O in both Figures 4.13 and 4.14. Additional data to confirm the presence of aluminium carbide is provided in Appendix 10D.

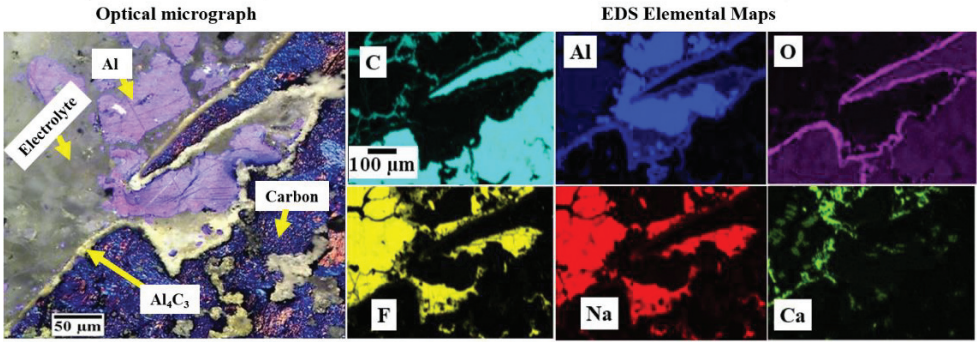

Figure 4.13. Phases at the carbon-electrolyte interface of pot 1.

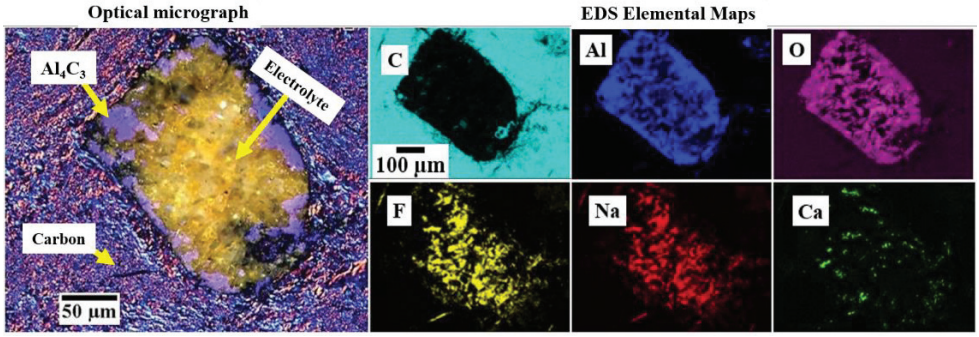

Figure 4.14. Presence of aluminium carbide within the pores of the carbon cathode material of pot 1.

4.1.3. Phase Composition of Solidified Bath

Powder XRD diffractograms of the solidified bath samples collected from different locations of the pot are shown in Figure 4.15. Na_3AlF_6, Al_2O_3, $Na_5Al_3F_{14}$ and $Na_2Ca_3Al_2F_{14}$ were identified as the main phases in the bulk solidified bath in line with the composition of a typical industrial electrolyte. Bath samples collected from within potholes and close to the cathode surface were significantly different from the main bath, consisting mainly of CaF_2, Na_3AlF_6 and Al_2O_3. The absence or significantly reduced amounts of the two phases $Na_5Al_3F_{14}$ and $Na_2Ca_3Al_2F_{14}$ in the samples from these two locations demonstrated that the solidified bath at the interface was basic compared to a typical industrial electrolyte.

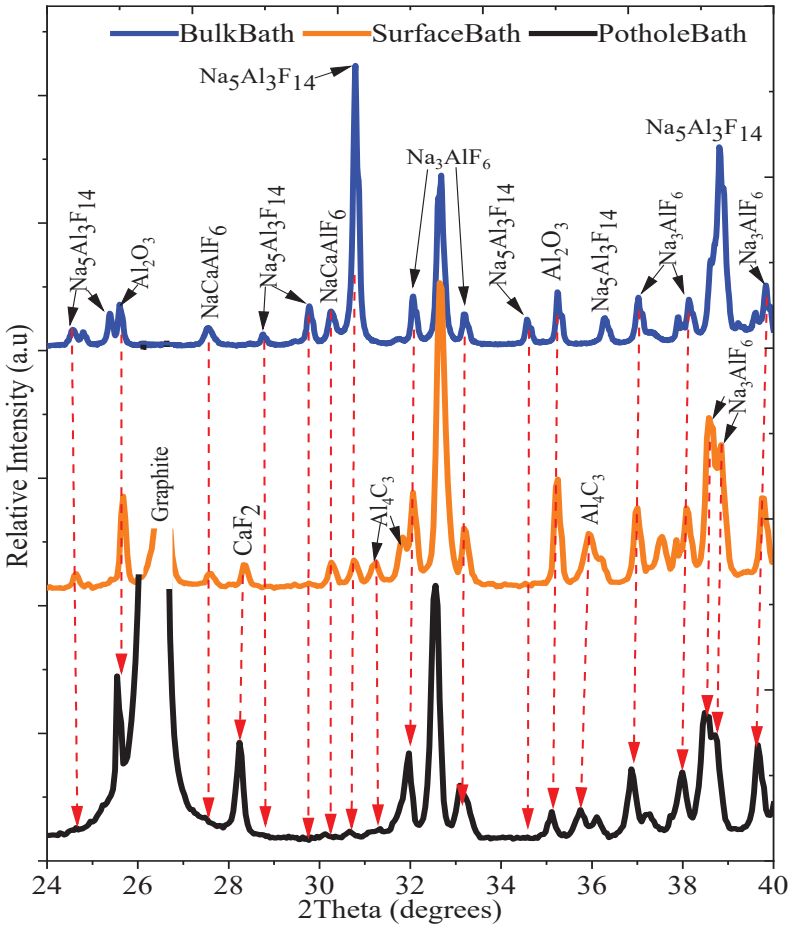

Figure 4.15. Powder XRD patterns of the solid bath samples collected from the bulk bath (blue line), cathode surface (orange line) and pothole (black line) from pot 1. Red dashed arrows correspond to the position of Bragg reflections used to identify the main phases in the samples.

4.2. Autopsy of Pot 2

4.2.1. Macroscopic Observation

Pot 2, a prebaked technology pot arranged end-to end, displayed the uneven W wear pattern characterized by highest wear at both side ends of the spent potlining and least wear at the centre channel. The characteristic wear pattern is visible in the image shown in Figure 4.16. A quantitative representation of the wear profile across the

cathode are shown in Figure 4.17. The cathode surface was covered with electrolyte and aluminium carbide as observed in previous autopsies.

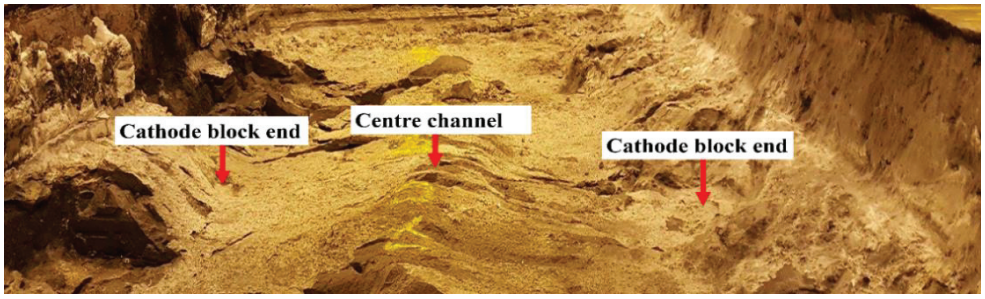

Figure 4.16. Cathode surface of pot 2 showing the W wear pattern.

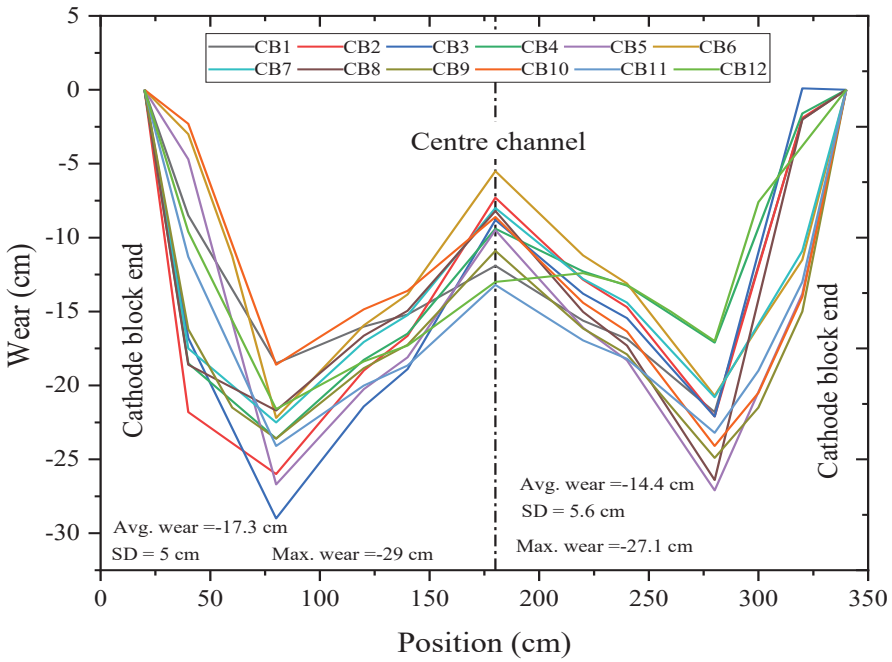

Figure 4.17. Wear pattern measured across pot 2 at different positions, CB1 corresponds to cathode block 1 and CB2 cathode block 2 and so on. The data for plotting the figure is given in Appendix A.

Potholes were observed on the cathode surface close to the ends of the cathode blocks. These were of different sizes with the largest diameters being over 50 cm and the smallest being around 3 cm. Some of the different pothole sizes observed can be seen in Figure 4.18. Table 4.2 gives a summary of the potholes observed.

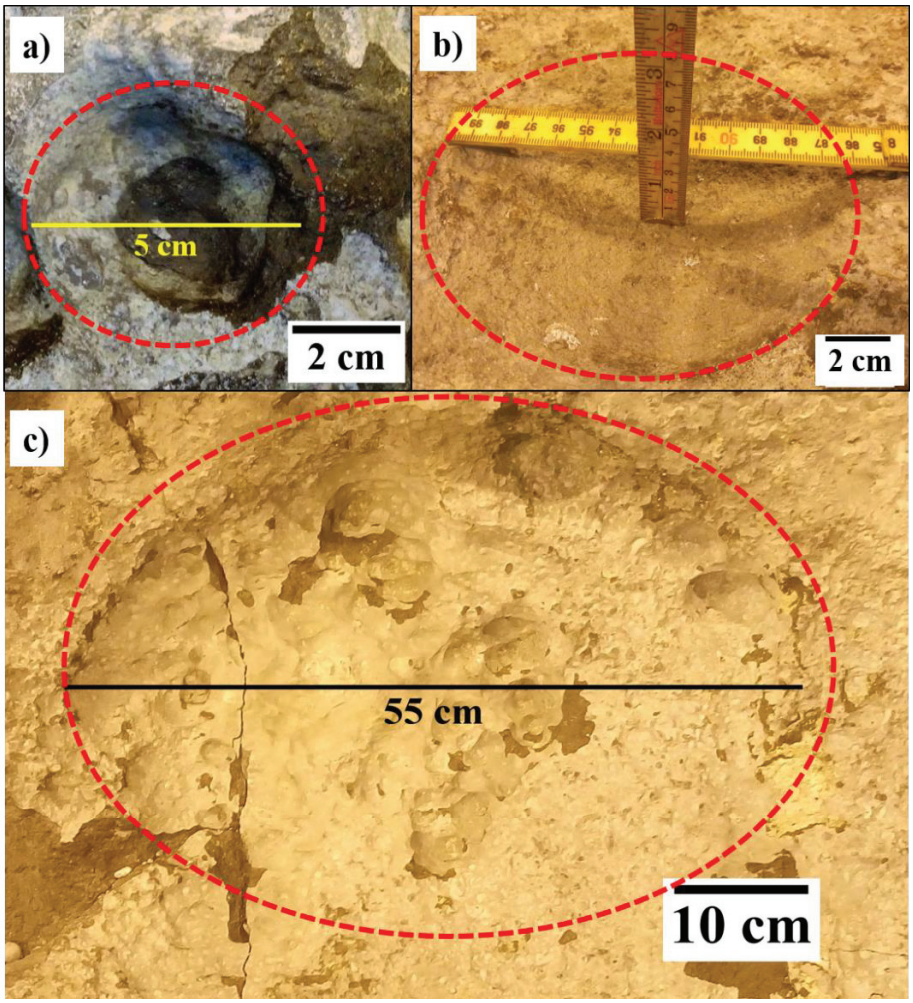

Figure 4.18. Potholes on pot 2. a) Small-sized potholes found on the cathode blocks from pot 2. b) Medium-sized potholes on carbon cathode surface from pot 1. c) Large-sized potholes found at ends of cathode blocks from pot 1. Red dashed circles illustrate boundaries of the potholes. Additional information is given in Appendix 10A.

4.2. Autopsy of Pot 2

Table 4.2. Summary of potholes found on the spent potlining of pot 2 with 12 cathode blocks.

Diameter range of Pothole, cm	Average diameter of Potholes, cm	Average depth of Potholes, cm	Maximum diameter of Pothole, cm	Number of Potholes per Cathode block	Number of Cathode blocks with Pothole
2-5	3.3±0.8	1.4±0.6	5	1	12
5-15	9.1±3.4	4.1±2.8	14	0.7	8
16-55	36.7±12.7	14.9±3.3	55	0.5	6

Close observation of the cathode surface of this pot showed pitting all over the cathode surface. Overlapping pittings were also detected on the same area of the cathode surface as shown in Figure 4.19. These overlapping pittings were also observed close to the locations with potholes and in some cases within the potholes.

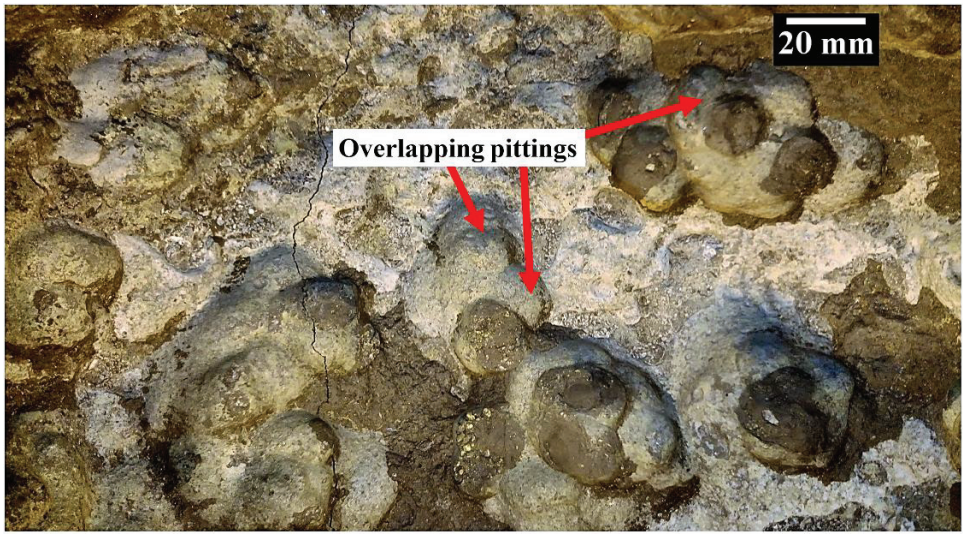

Figure 4.19. Overlapping pitting on the same area of the carbon cathode surface of pot 2.

It was seen in some cases that the pitting at the ends of the cathode blocks where the wear was highest were relatively larger in size, and thus had larger characteristic diameters, than those close to the centre channel. This is demonstrated in Figure 4.20. Characterization of the pitting size distribution at the centre channel and cathode block ends using the ImageJ software program to analyse optical photographs taken at the two locations was done to verify the observation. An image illustrating the pitting size distribution and a corresponding histogram obtained from the pitting size characterization are shown in Figures 4.21 and 4.22. Additional information is presented in Appendix 10B

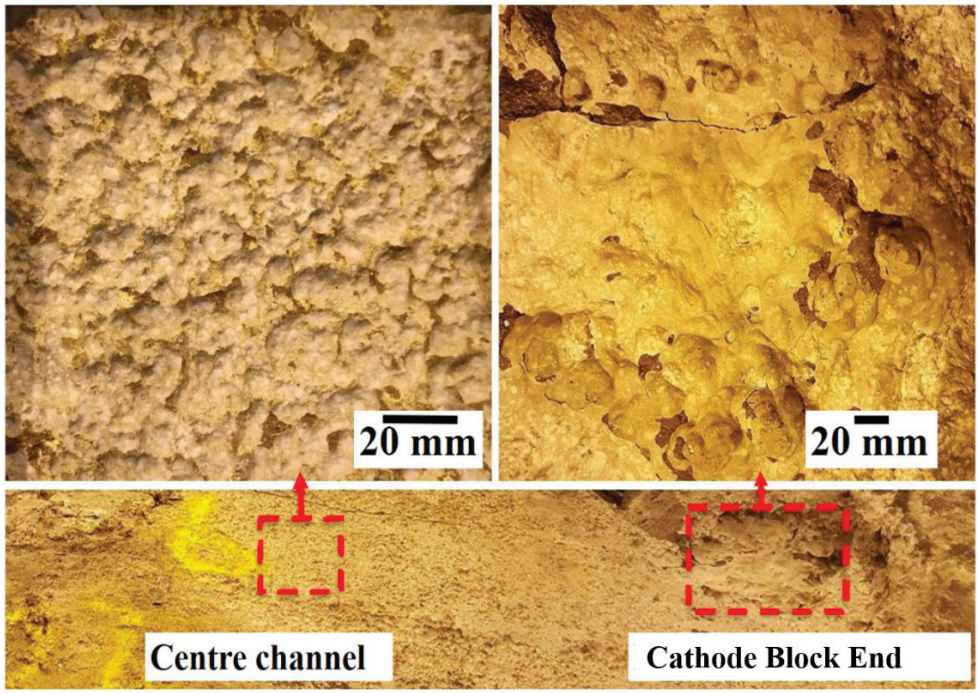

Figure 4.20. Differences in pitting size between those at the centre channel area and the end of cathode blocks for cathode block 9 of pot 2.

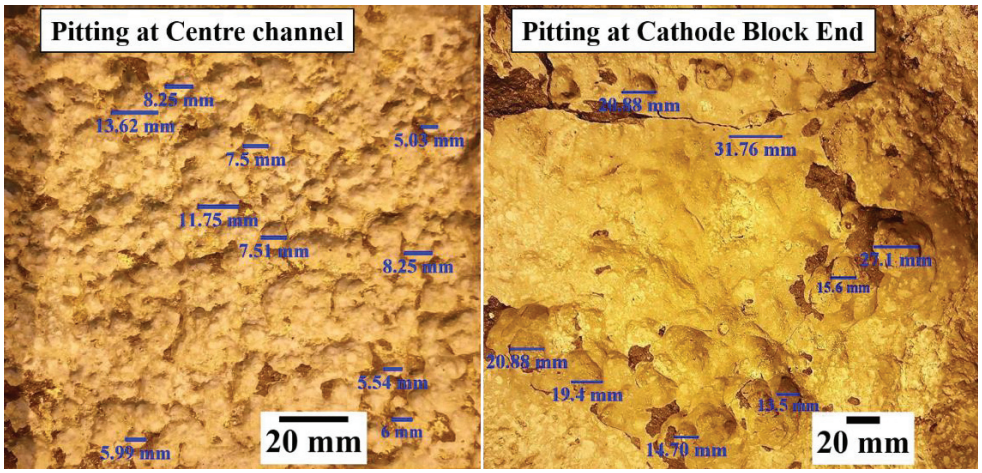

Figure 4.21. Pitting size distribution on the cathode surface at the centre channel and the cathode block ends for cathode block 9 of pot 2. Additional data is provided in Appendix 10B.

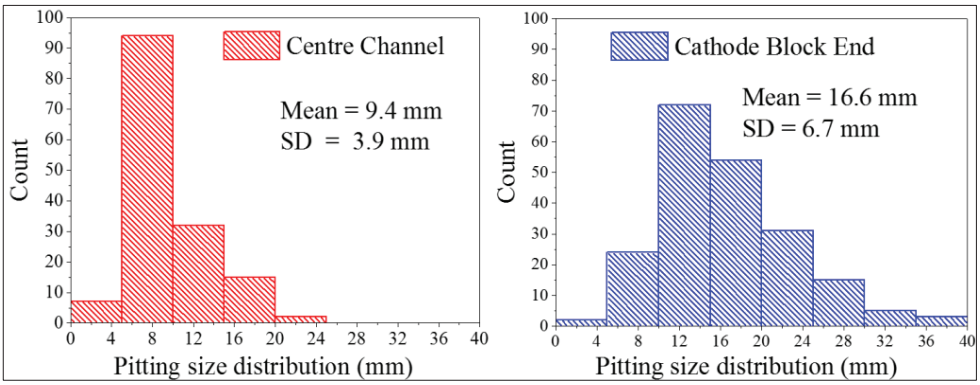

Figure 4.22. Pitting size distribution at centre channel and cathode blocks end for pot 2. Additional data is given in Appendix 10B.

4.3.2. Microscopic Observations

Optical microscopy was employed to investigate the microstructure of the autopsy samples as well as the interface between carbon and bath. Micrographs showing the microstructure within the carbon material and features at the interface between carbon and bath are depicted in Figures 4.23 and 4.24, respectively.

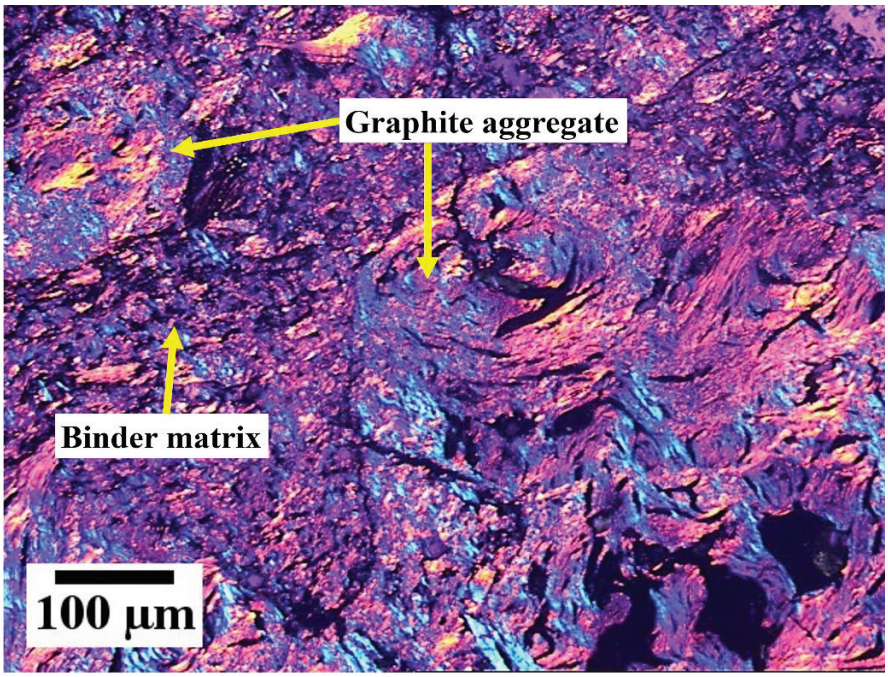

Figure 4.23. Microstructure of the graphitic cathode block showing the graphite aggregates and binder matrix within the carbon matrix of pot 2.

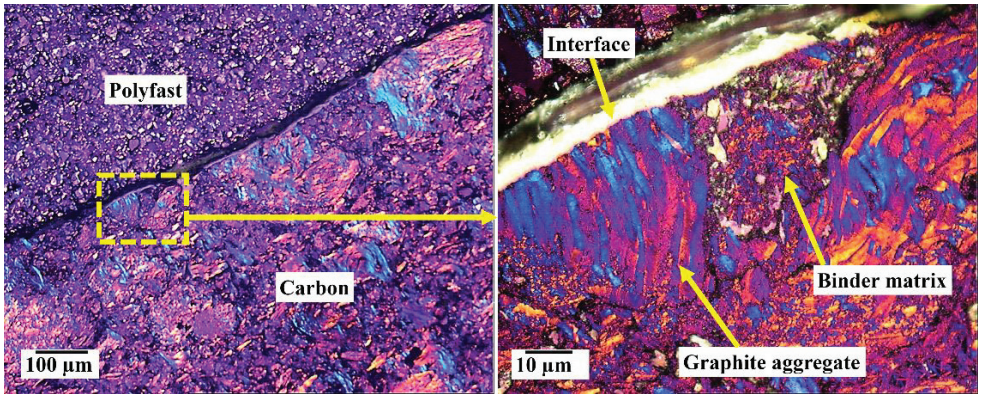

Figure 4.24. Wear surface at the carbon-electrolyte interface of pot 2. A relatively uniform wear of the aggregate and binder matrix can be seen in the highlighted section of the micrograph.

Another observation was the formation of aluminium carbide within the pores of the spent potlining, and this is captured in Figure 4.25. Aluminium carbide is in direct contact with the carbon material and dispersed in the electrolyte.

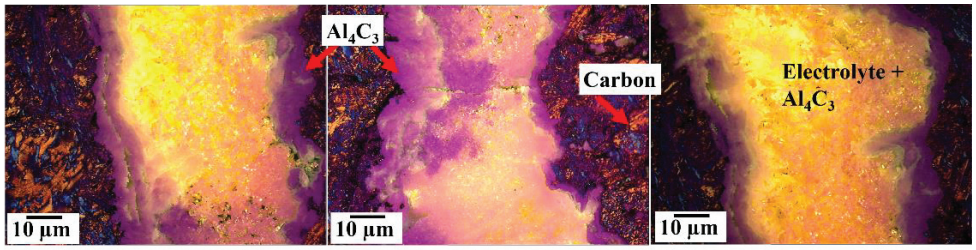

Figure 4.25. Aluminium carbide within the pores of the carbon cathode material of pot 2. Aluminium carbide can be observed as the purple coloured material in close contact with the carbon and in the electrolyte.

4.3.3. Phase Composition of Solidified Bath

Solidified bath samples collected from different locations of the spent potlining and analysed using powder XRD revealed that the bulk bath consists mainly of Na_3AlF_6, Al_2O_3, $Na_5Al_3F_{14}$ and $Na_2Ca_3Al_2F_{14}$. The bath in direct contact with the cathode surface contained phases such as CaF_2, Na_3AlF_6 and Al_2O_3. This confirms the relatively basic nature of the bath in close contact with the cathode surface as the phases $Na_5Al_3F_{14}$ and $Na_2Ca_3Al_2F_{14}$ require acidic bath to form. The powder XRD diffractograms of the phases are given in Figure 4.26.

4.2. Autopsy of Pot 2

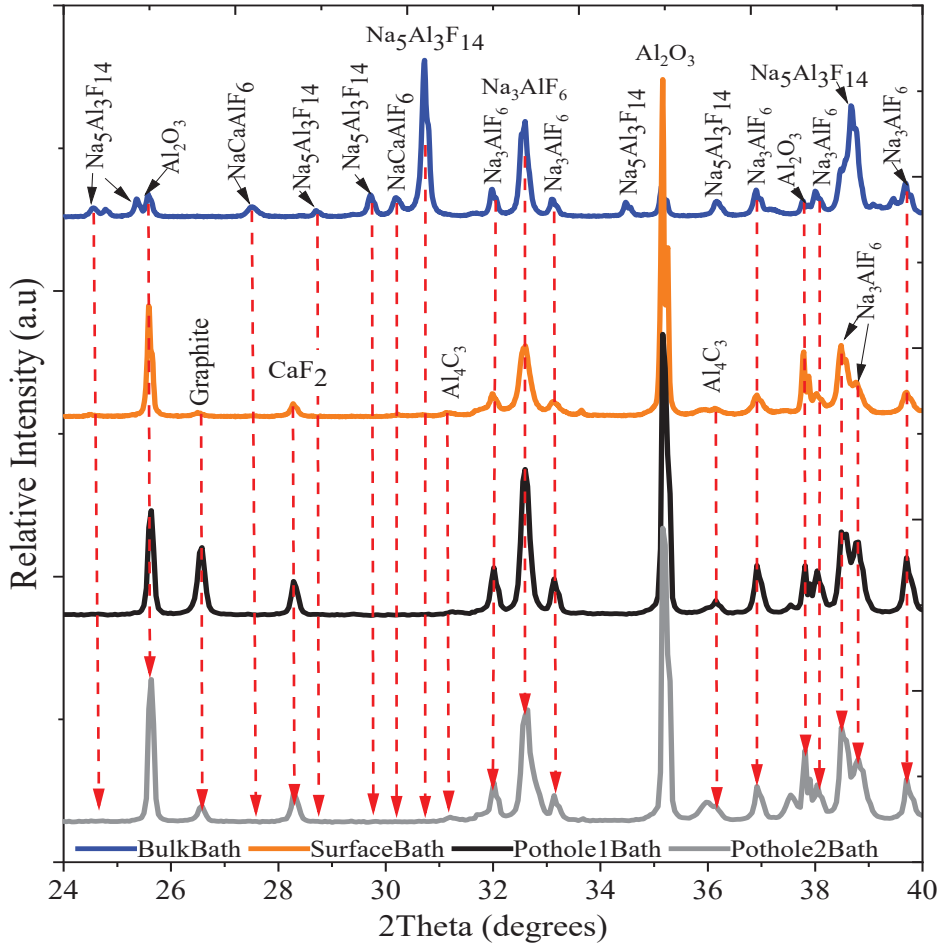

Figure 4.26. Powder XRD patterns of the solid bath samples collected from pot 2. Bath samples from the bulk bath (blue line), the cathode surface (orange line) and potholes (black and grey lines). Red dashed arrows correspond to the position of Bragg reflections used to identify the main phases in the samples.

4.3.4. Phase Distribution Within the Carbon Bottom Lining

Powder X-ray diffraction patterns of samples obtained from different depth from the cathode surface are displayed in Figure 4.27. The powder XRD patterns demonstrate a gradual increase in NaF content and a corresponding decrease in cryolite (Na_3AlF_6) content from the carbon cathode surface down to the refractory lining. Al_4C_3 was found to be present in the powder XRD pattern of the uppermost layer. Phases representing the different forms of alumina such as β-Al_2O_3 were also identified at different locations within the carbon cathode. Other phases like $NaAlSiO_4$ were also

identified. CaF_2 was noticed to be relatively stable almost throughout the whole carbon cathode except the last layer which was suspected to be a refractory layer. The presence of NaF and CaF_2 throughout the carbon cathode demonstrates the basic nature of the solidified bath within the porosity of the carbon cathode. The basic nature of solidified bath within the porosity of the carbon bottom lining confirms the relatively basic nature of the solidified bath in direct contact with the cathode surface as compared to the bulk bath.

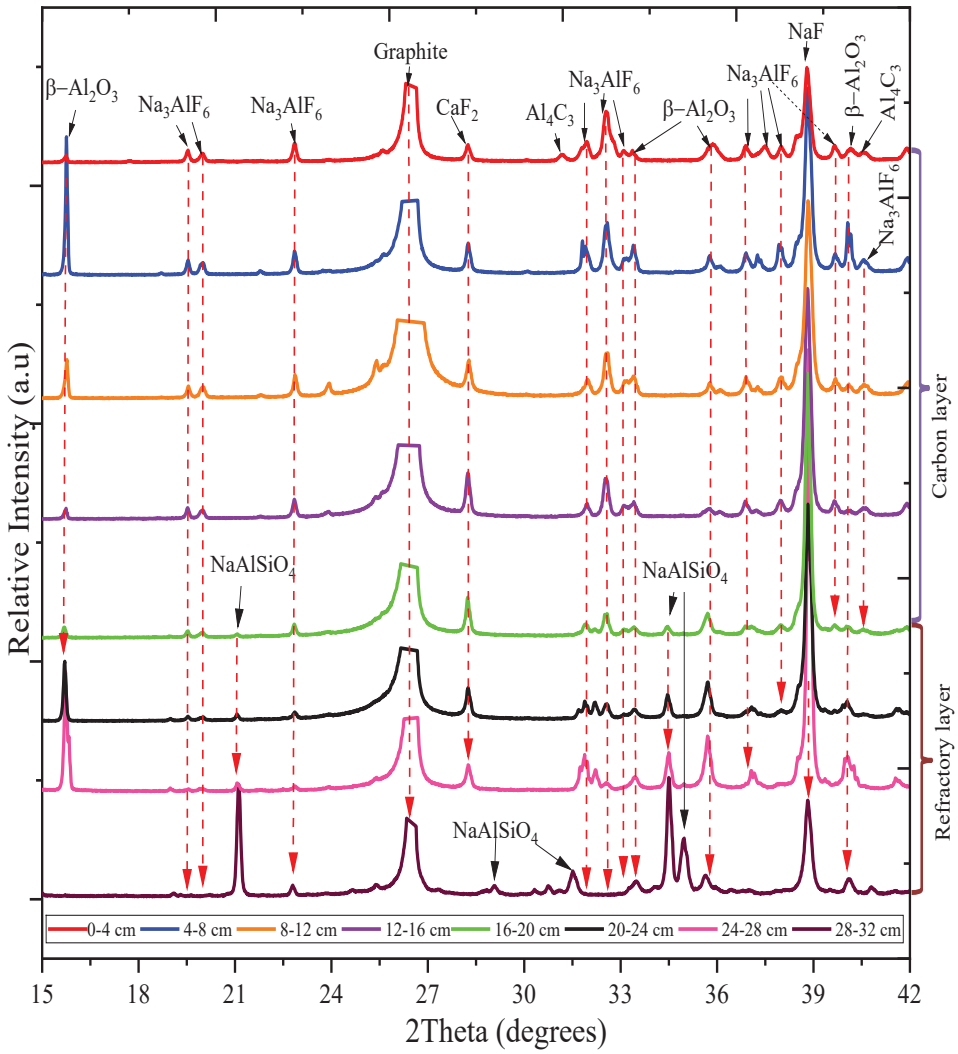

Figure 4.27. Powder XRD patterns of phases within carbon samples located at different distance from the cathode surface. The legend shows the distance from the cathode surface. Red dashed arrows correspond to the Bragg reflections used to identify phases.

4.3. Autopsy of Pot 3

4.3.1. Macroscopic Observation

The WW wear pattern in addition to a layer of frozen bath and aluminium carbide covering the surface of the carbon cathode lining was also characteristic for this pot which was also a prebaked technology pot arranged side-by-side. The ramming joint was observed to be less worn-out as compared to the neighbouring cathode blocks. A photograph of the cathode is shown in Figure 4.28, while a 3D image of the topography of the cathode is displayed in Figure 4.29.

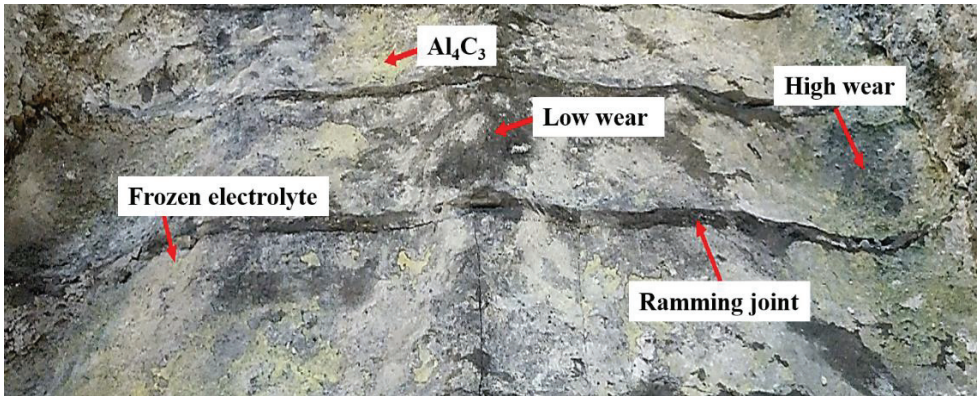

Figure 4.28. Cathode surface of pot 3 showing the frozen electrolyte, Al_4C_3 and the relatively less worn out ramming joints as well as the high and low worn out areas.

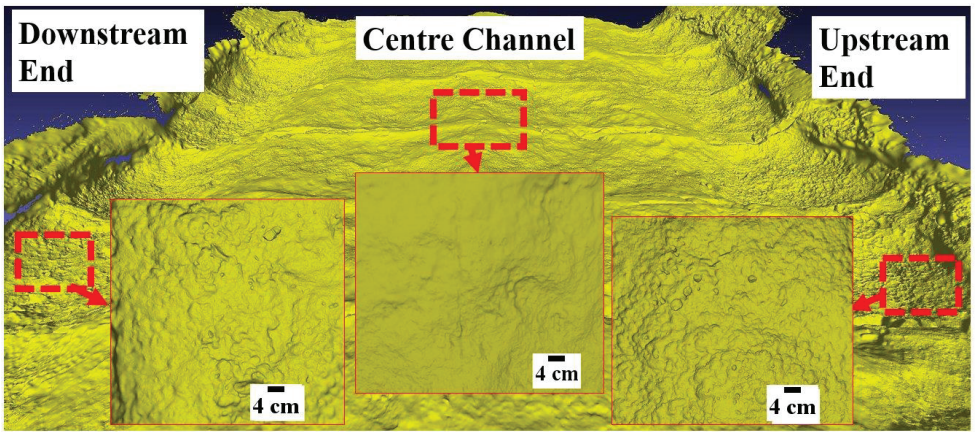

Figure 4.29. A 3D image of the wear profile of pot 3. Red dotted rectangles show pitting at the upstream and downstream ends as well as the centre channel.

The highlighted sections of the 3D image shown in Figure 4.29, display the occurrence of pitting on the cathode surface. Pitting was seen to be more pronounced at the upstream and downstream ends of the cathode lining where the wear tends to be the highest. The centre channel area that displays low wear showed relatively less pronounced pitting. Close observation of the pot tapout location also revealed pitting. The ramming joints between the cathode blocks were also observed to have pitting on the surface albeit a lesser degree of occurrence as shown in Figure 4.33. It is also important to mention that within the pitting were small sized circular wear patterns. Some of the pitting occurrence on pot 3 are displayed in Figures 4.30, 4.31, 4.32, 4.33 and 4.34.

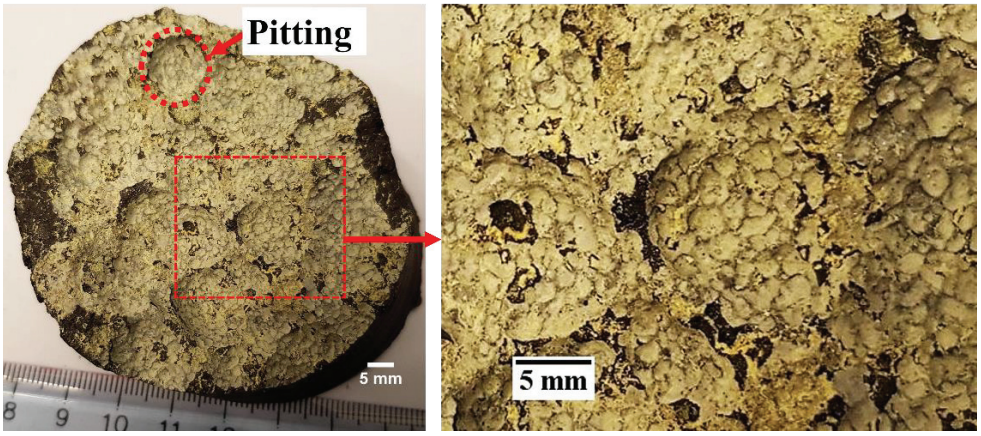

Figure 4.30. Location with pitting showing small-sized circular erosion patterns.

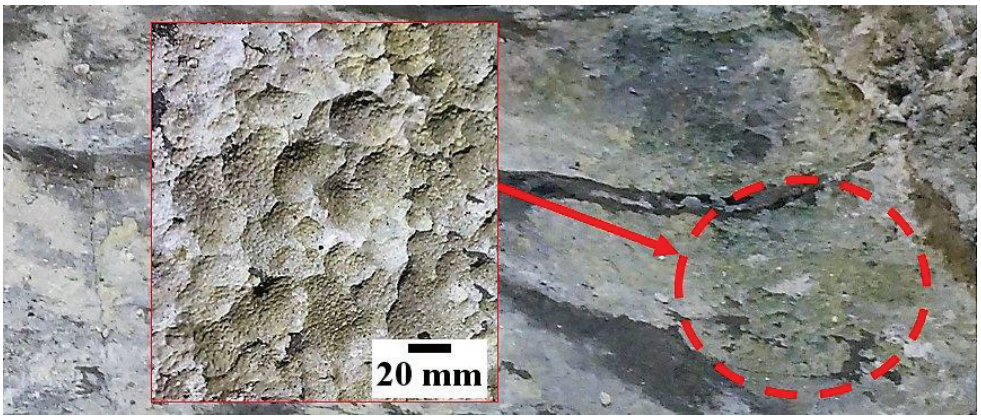

Figure 4.31. Pitting at locations with highest wear such as the cathode block ends. Additional information is given in Appendix 10

4.3. Autopsy of Pot 3

Figure 4.32. Pitting on the cathode surface surrounding the pothole that led to tapout of pot 3. Red dashed circle highlights the tapout hole.

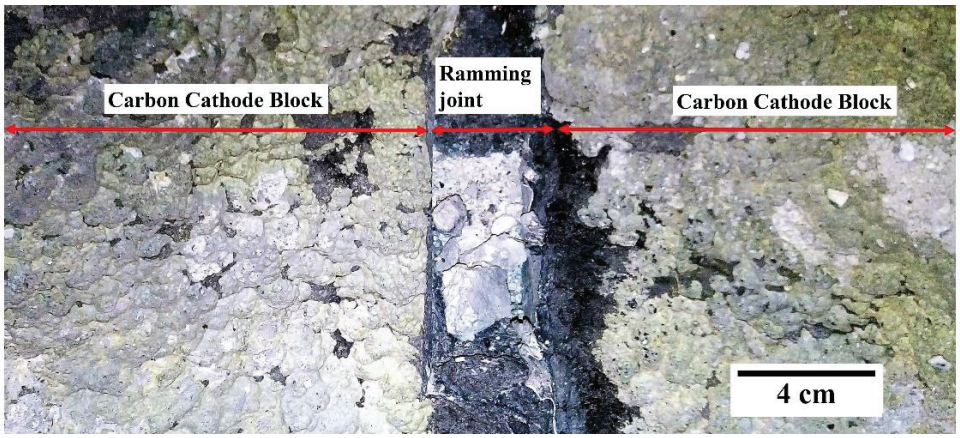

Figure 4.33. Pitting on ramming joint between cathode blocks.

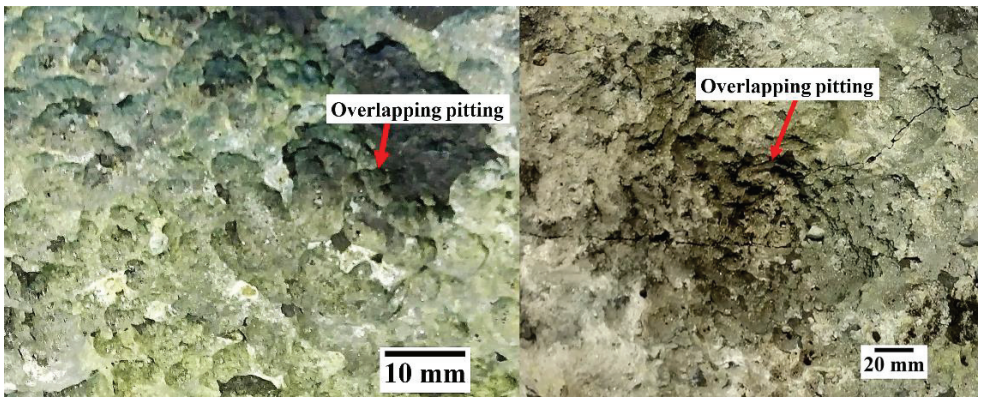

Figure 4.34. Overlapping pitting at the same cathode surface location of pot 3.

The 3D images were also used to characterize the pitting size distribution at the cathode block ends where they were more pronounced. An example of a 3D image used to determine the size of the pitting is given in Figure 4.35. Histograms displaying the size distributions on some of the cathode blocks on pot 3 are displayed in Figure 4.36. The average sizes and standard deviations are given in the diagrams. The average pitting size was in the range of 7-9 mm. The high standard deviations reflect the varying sizes of the pitting observed on the cathode surface.

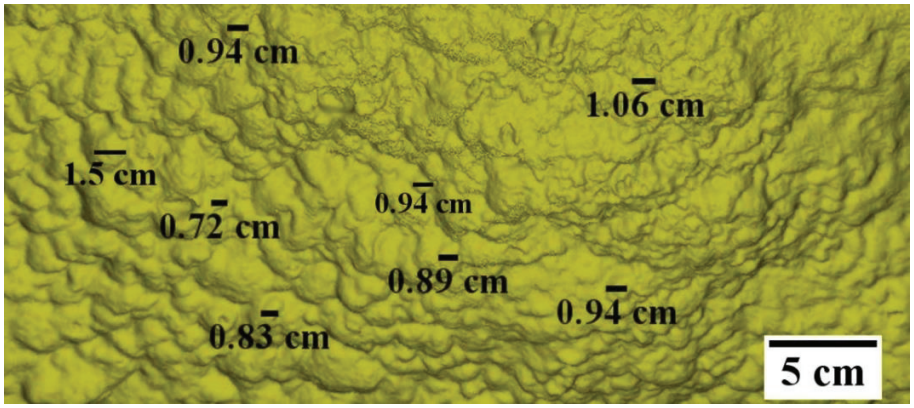

Figure 4.35. An example of a 3D image used to determine the average pitting size on pot 3.

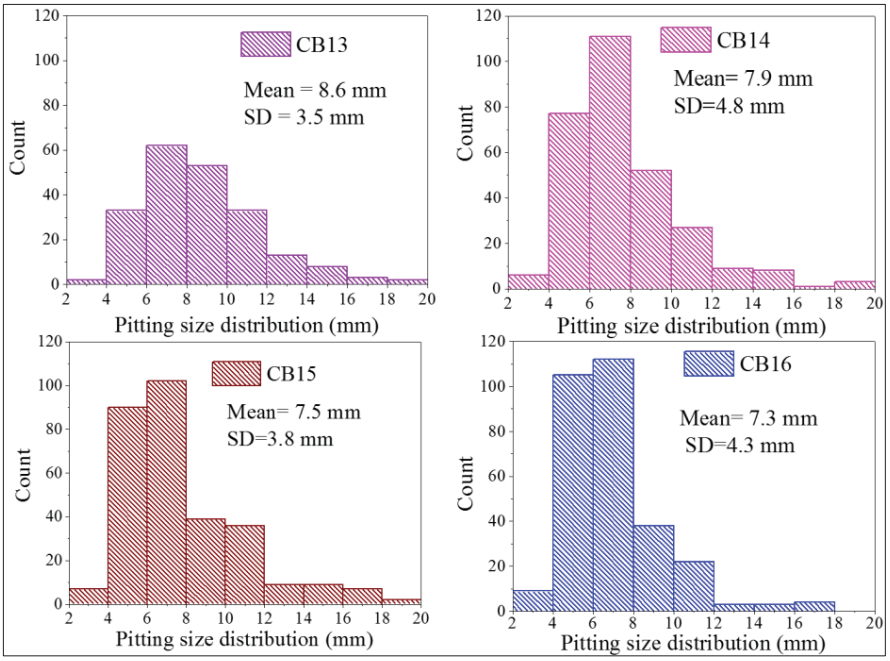

Figure 4.36. Size distribution of pitting on the cathode surface of pot 3. CB13: Cathode Block 13, CB14: Cathode Block 14, CB15: Cathode Block 15, CB16: Cathode Block 15.

4.5.2. Microscopic Observations

The X-ray computed tomography was also employed to investigate 5 autopsy samples collected from 5 different cathode blocks of pot 3. The CT images obtained provided detailed information about the microstructure of the samples and the topography of the cathode surface. The microstructures of four different cathode samples are shown in Figure 4.37. The larger coke aggregates are clearly visible in the images as dark grey, while the binder with significant porosity appears light grey. As pointed out earlier, the bath components appear as white. The images demonstrate that all the materials were completely infiltrated by molten bath during the operation of the pot.

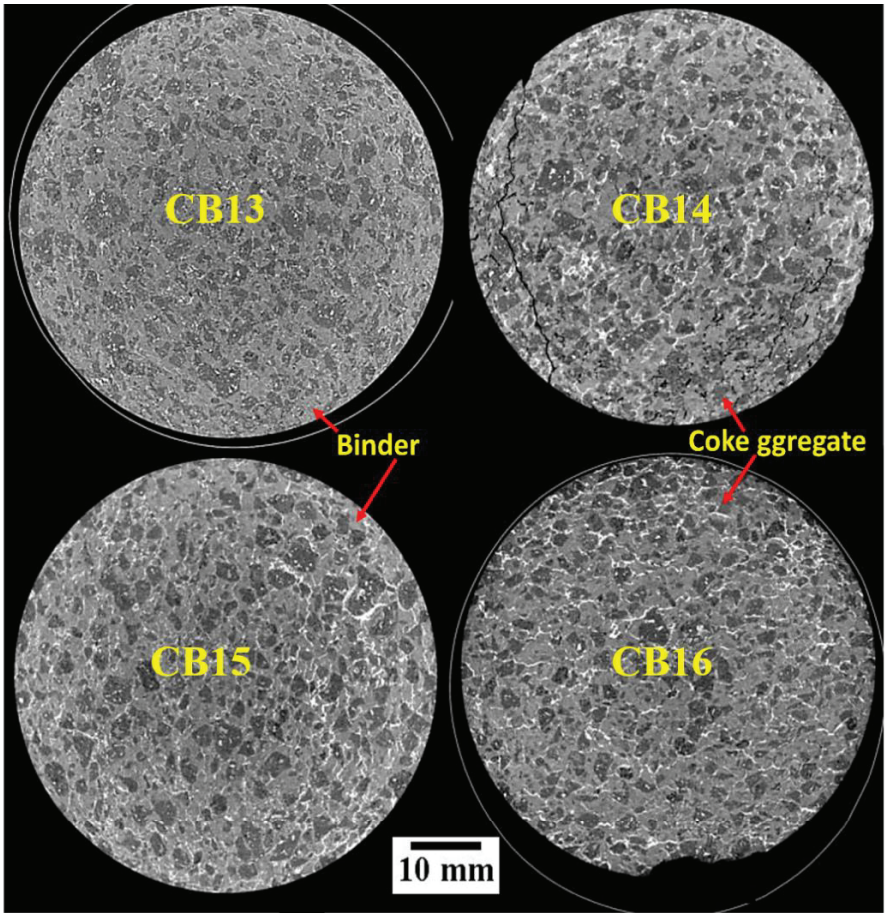

Figure 4.37. CT scanning images of cathode samples from cathode blocks 13, 14, 15 and 16 revealing the microstructures of the cathode material from pot 3.

The average sizes of the large aggregates within the carbon materials were determined using the linear intercept method mentioned in chapter 3. The CT images used were obtained from three carbon samples collected from three different cathode blocks

(cathode block 13, 14 and 15). Histograms representing the coke aggregate size distribution are displayed in Figure 4.38. The average coke aggregate size and standard deviation are given in the figure. The average coke aggregate size measured employing the linear intercept method was about 2 mm.

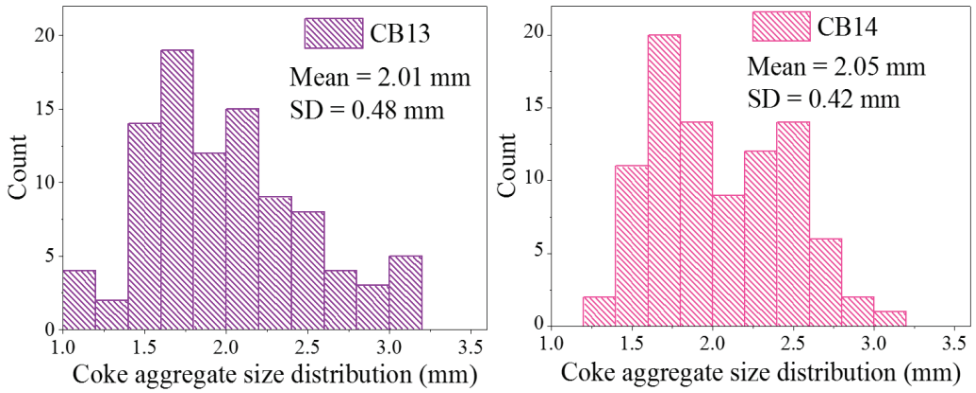

Figure 4.38. Coke aggregate size distribution within the cathode blocks of pot 3. CB13: Cathode Block 13 and CB14: Cathode Block 14. Additional data is given in Appendix 10C.

Examples of CT images, showing the surface wear profile along the carbon-electrolyte interface, are shown in Figures 4.40 and 4.41. Additional information is given in in Appendix 10D. A representative picture for all the other autopsy samples investigated is given in Figure 4.41. Figure 4.41 displays the wear profile at the carbon-electrolyte interface in the XZ orientation for the 5 autopsy samples investigated.

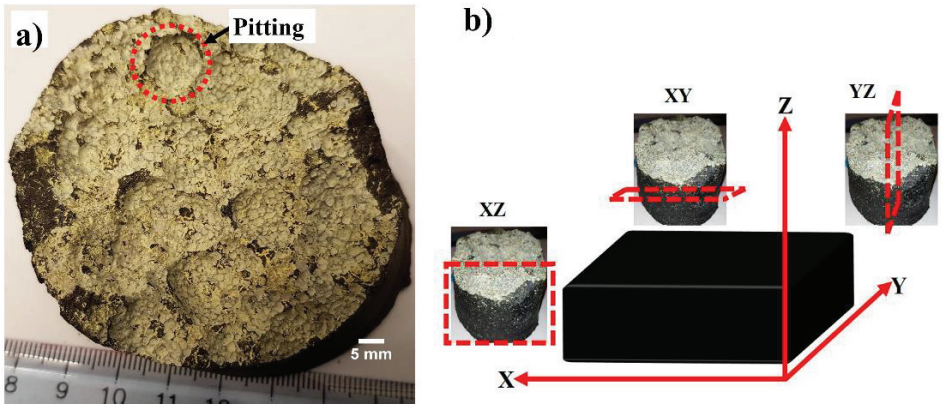

Figure 4.39. a) Carbon sample from cathode block 16 of pot 3. b) XY, XZ and YZ Orientations for CT images.

4.3. Autopsy of Pot 3

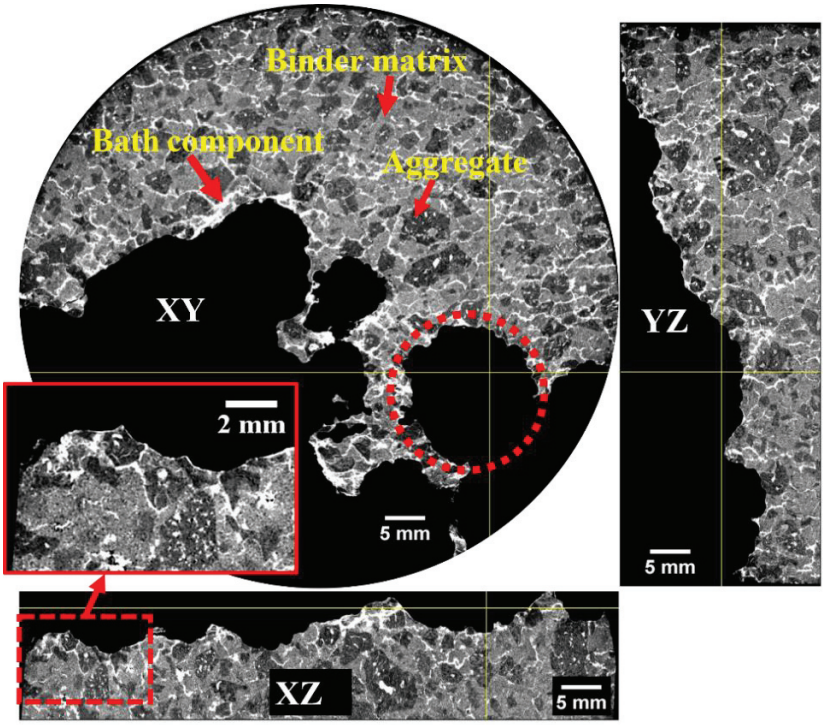

Figure 4.40. CT images showing the wear surface at locations with pitting on pot 3. Red dotted circle shows location with pitting.

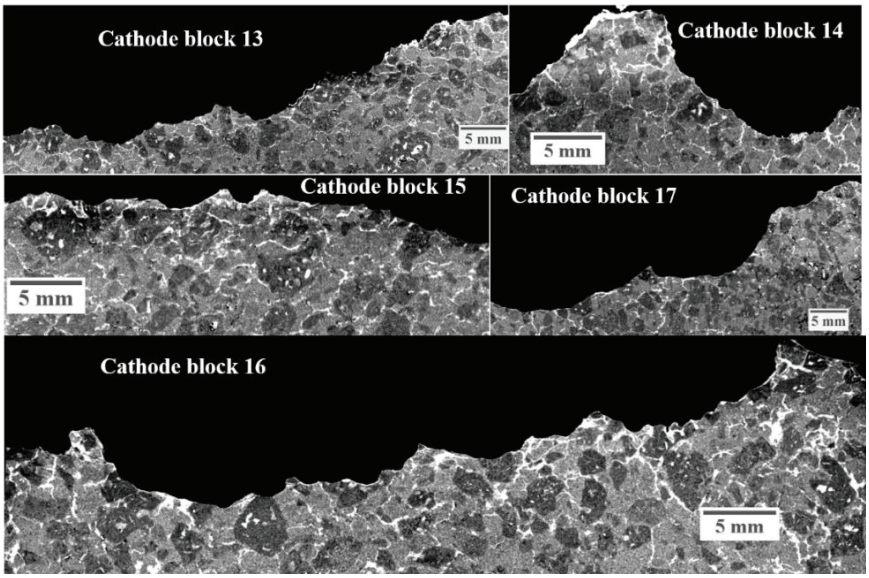

Figure 4.41. Wear surface at the XZ orientation of cathode samples from 5 different cathode blocks of pot 3 showing remains of partly worn out coke aggregates within the carbon matrix.

The CT images revealed a relatively uniform wear across both the binder matrix and coke aggregates. Remains of partly worn-out coke aggregates could be seen within the carbon matrix. As with the previous autopsies, there was no evidence of coke aggregate pull-out of the carbon matrix.

Optical micrographs showing the natural boundaries of the aggregates within the microstructure as well as the worn-out surface at the carbon-electrolyte interface of the carbon cathode material are shown in Figures 4.42 and 4.43.

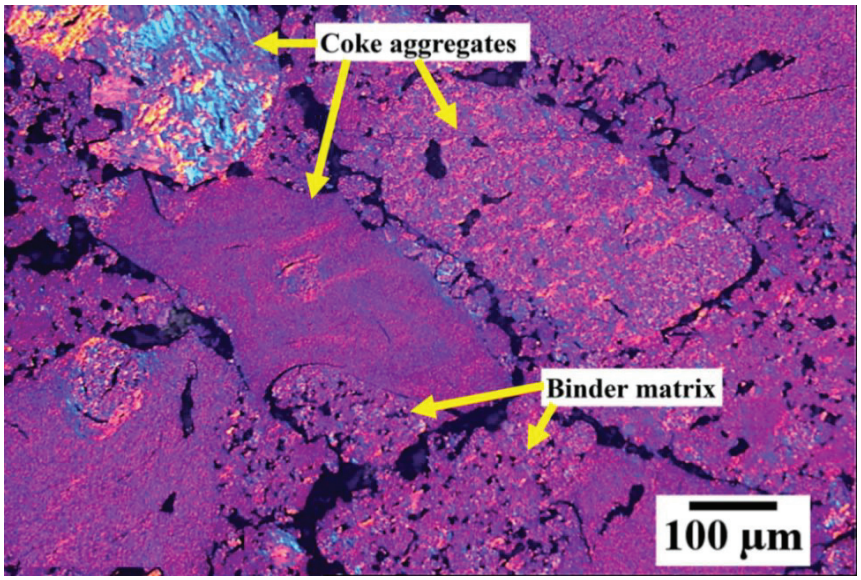

Figure 4.42. Microstructure showing components within carbon cathode material from pot 3.

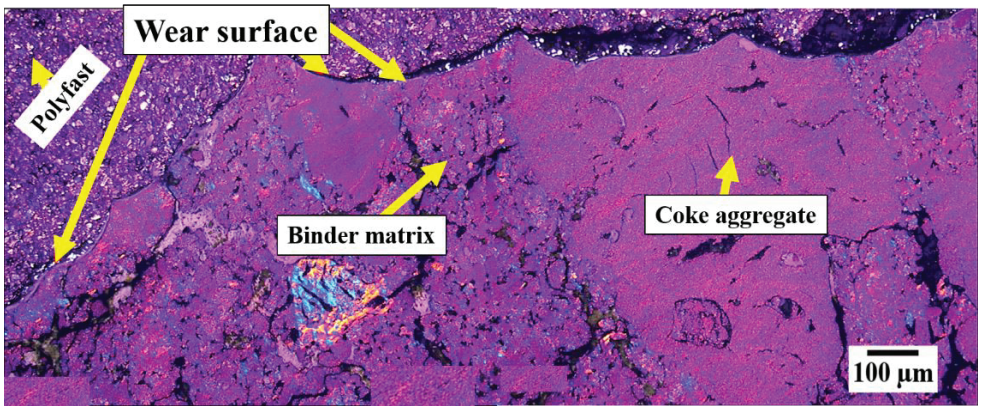

Figure 4.43. Wear surface along the carbon-bath interface of pot 3. Remains of partly worn out coke aggregates can be seen within the carbon matrix.

The optical micrographs confirmed the uniform wear surface across the cathode surface with no preferential wear between the coke aggregates and binder matrix. Remains of partly worn-out coke aggregates were also observed within the carbon matrix. A relatively circular wear surface cutting across both binder matrix and coke aggregates was also observed. The micrographs also showed no indication of coke aggregate pull-out.

4.4. Autopsy of Pot 4

4.4.1. Macroscopic Observation

Pot 4, a prebaked technology pot arranged end-to-end, was autopsied to augment the data gathered from the previous autopsies, specifically pot 2 due to the similar cell technology, arrangement and cathode block properties. The analysis was thus not as thorough as the first three discussed above. The pot displayed the usual uneven W wear pattern described in the previous pages. An optical mage of the cathode is shown in Figure 4.44 and the measured wear profile across the cathode is plotted in Figure 4.45. Close examination showed pitting all over the cathode surface. It was further observed that the pitting at the centre channel had a relatively smaller diameter than those at the ends of the cathode blocks, specifically at the areas with the highest wear. These observations are depicted in Figures 4.46 and 4.47. A histogram displaying the pitting size distribution between these two locations is given in Figure 4.49.

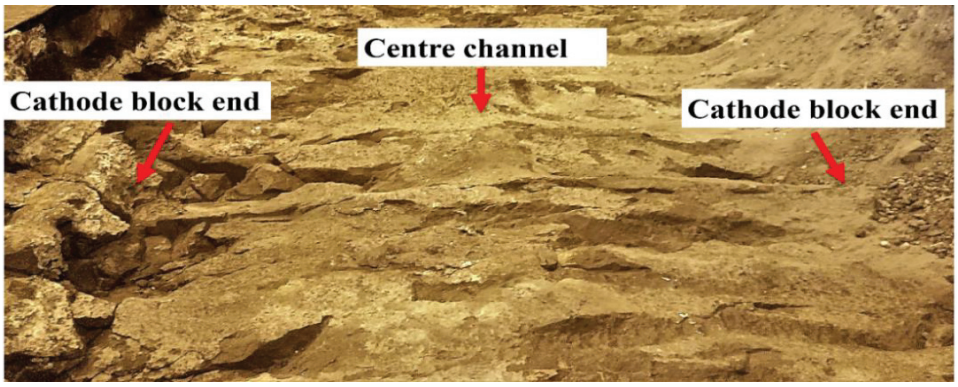

Figure 4.44. Cathode surface of the spent potlining from pot 4.

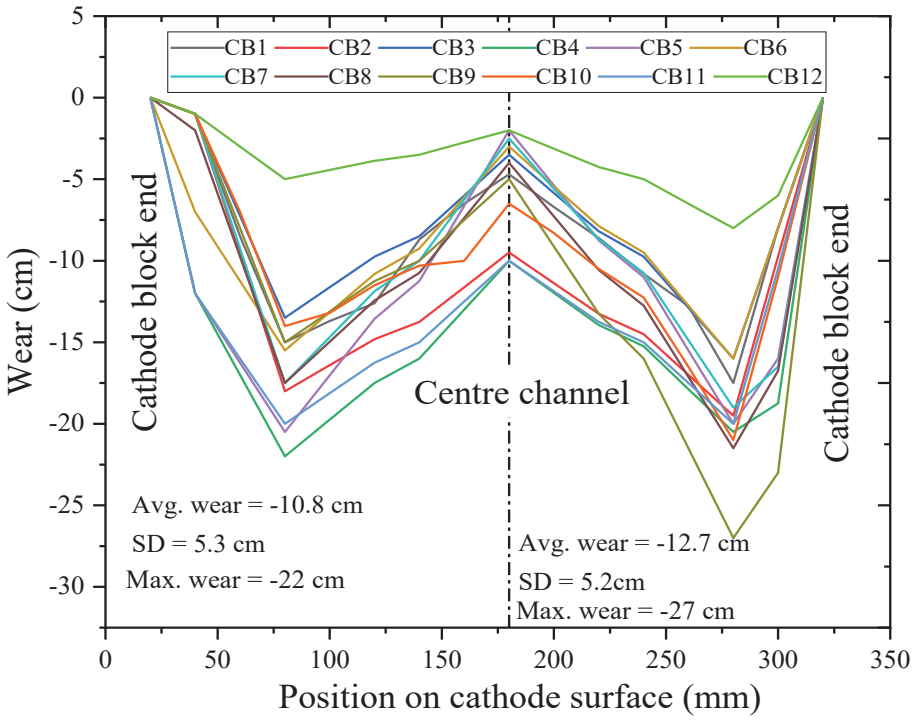

Figure 4.45. Wear pattern measured across pot 4 at different positions, CB1 corresponds to cathode block 1 and CB2 cathode block 2 and so on. Data for the plot is in Appendix 10A.

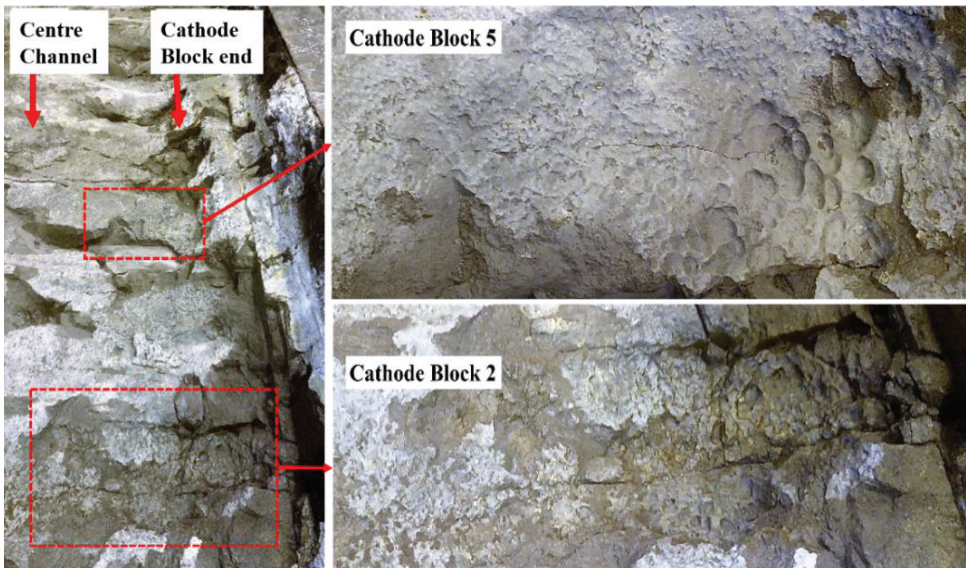

Figure 4.46. Section of two cathode blocks of pot 4 showing pitting at the centre channel and cathode block end.

4.4. Autopsy of Pot 4

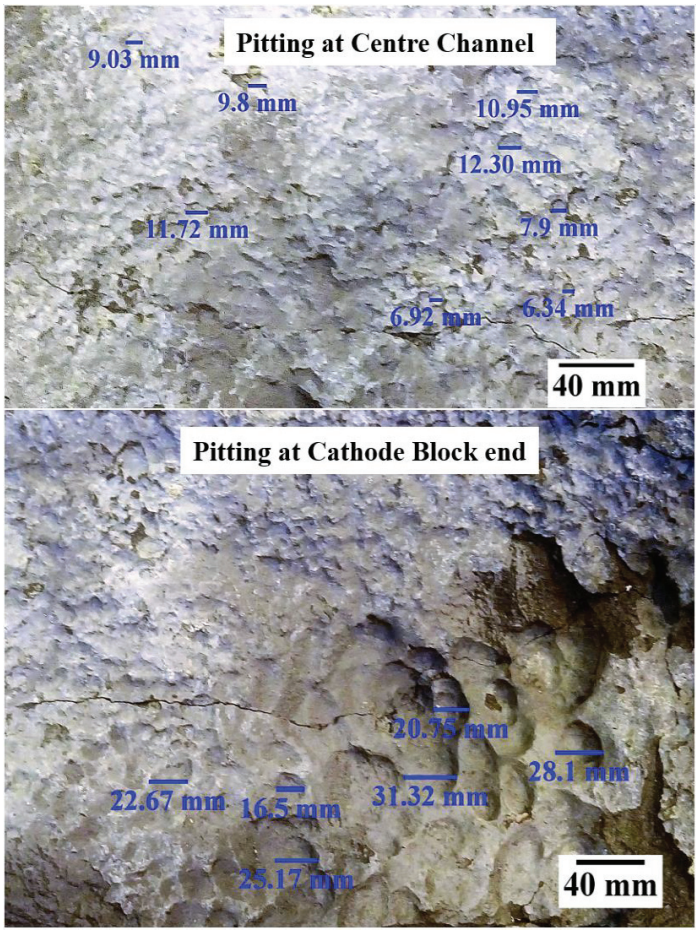

Figure 4.47. Pitting size distribution at centre channel and cathode block end for cathode block 5 of pot 4.

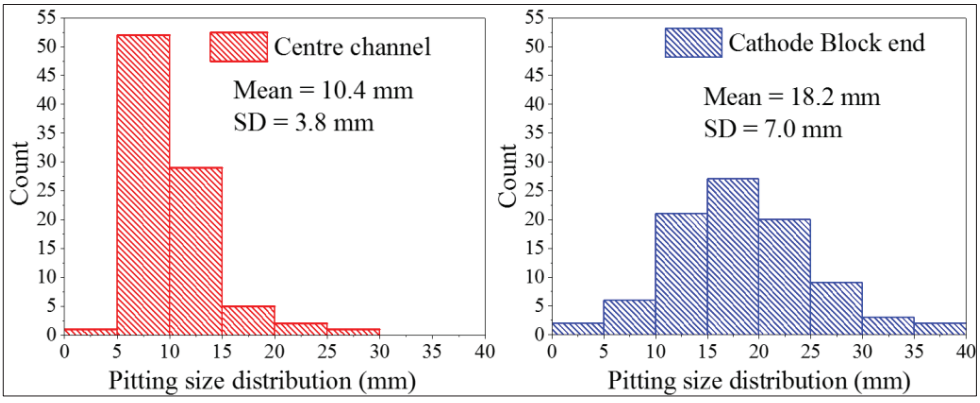

Figure 4.48. Pitting size distribution at the centre channel and cathode block ends of pot 4. Data for plotting the histograms can be found in Appendix 10B.

4.4.4. Phase Distribution Within the Carbon Bottom Lining

Powder X-ray diffraction patterns of samples obtained from different depth from the cathode surface are displayed in Figure 4.49. The phases identified by the powder XRD patterns were similar to that of pot 2 and confirmed the basic nature of the frozen electrolyte within the porosity of the carbon cathode lining. The relative basic nature of the bath in direct contact with the cathode surface as compared to the bulk bath can thus be inferred from the results.

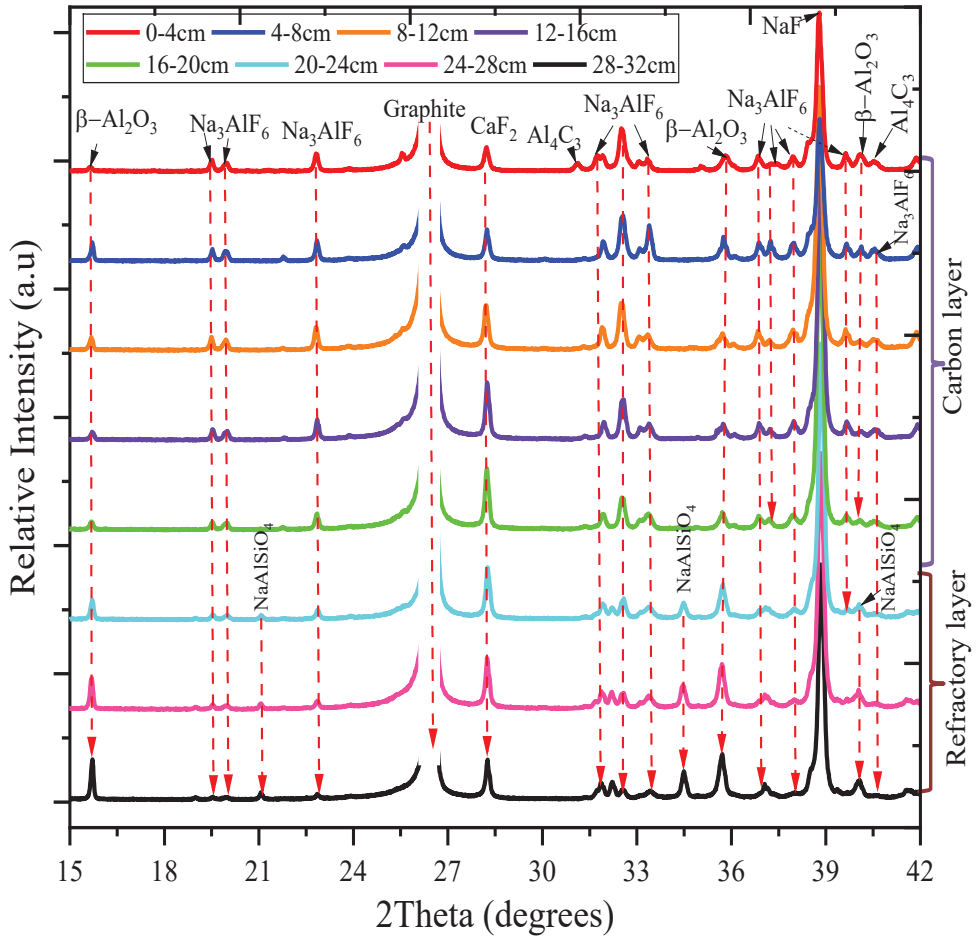

Figure 4.49. Powder XRD patterns of phases within carbon samples located at different distances from the cathode surface. The legend shows the distance from the cathode surface. Red dashed arrows correspond to the Bragg reflections used to identify phases.

4.5. Autopsy of Pot 5

4.5.1. Macroscopic Observations

Pot 5, a prebaked technology pot arranged end-to-end had a tapout after 1028 days and was autopsied to obtain more data on pitting on the cathode surface. The analysis was thus focused on the macroscopic observation. Pitting was identified on the cathode surface despite the young age of 1028 days. The general wear pattern was uniform except for the pothole locations and cathode block ends.

Frozen electrolyte, sludge and aluminium carbide was seen covering the cathode surface. An image of the cathode surface is shown in Figure 4.50, while the wear pattern is plotted in Figure 4.51. Three potholes were observed on the spent potlining. All the potholes including the one that led to tapout were observed close to the cathode block ends. One of the potholes was observed to be filled with aluminium. Pitting was observed within the pothole after the lump of Al had been removed. The locations of two of the potholes are shown in Figure 4.52 while the pothole containing Al is displayed in Figure 4.53.

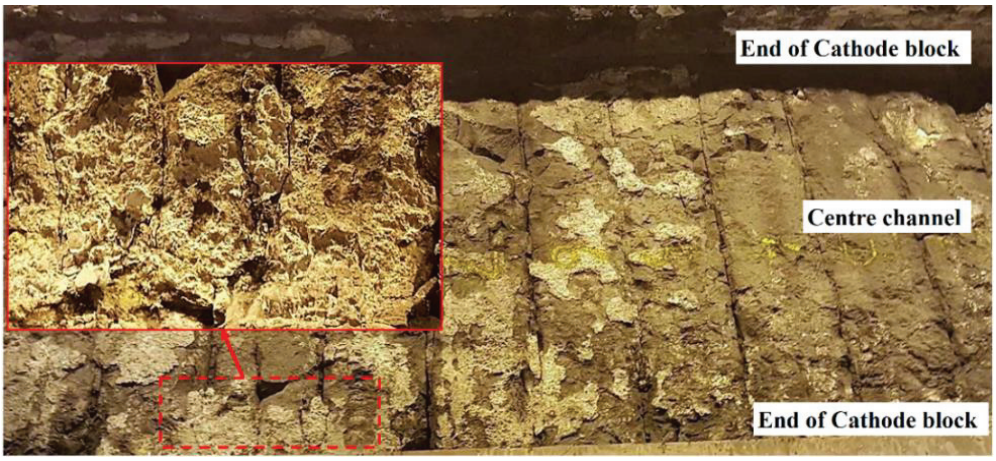

Figure 4.50. Cathode surface of pot 5 showing a relatively uniform wear. Highlighted spot illustrates the occurrence of pitting.

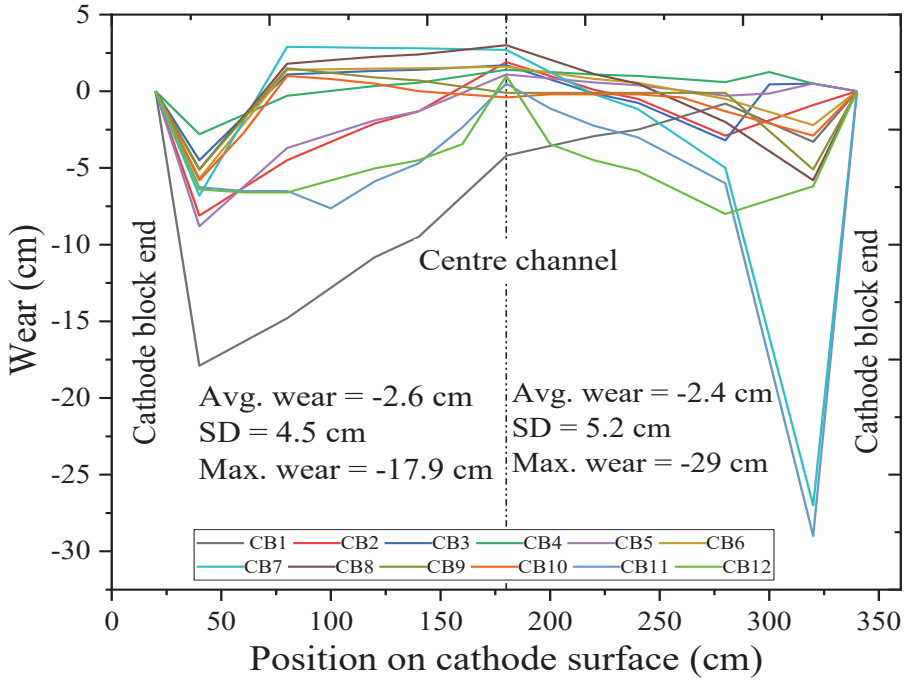

Figure 4.51. Wear pattern measured across pot 5 at different positions, CB1 corresponds to cathode block 1 and CB2 cathode block 2 and so on. Data for plots are given in Appendix 10A.

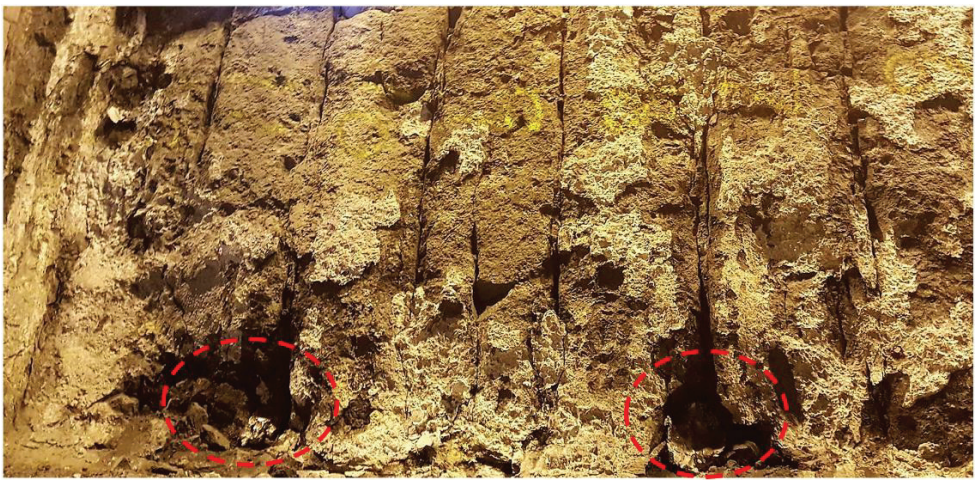

Figure 4.52. Cathode surface of pot 5 showing a layer of electrolyte and the pitting on the cathode surface. Red dashed circles show the location of two potholes.

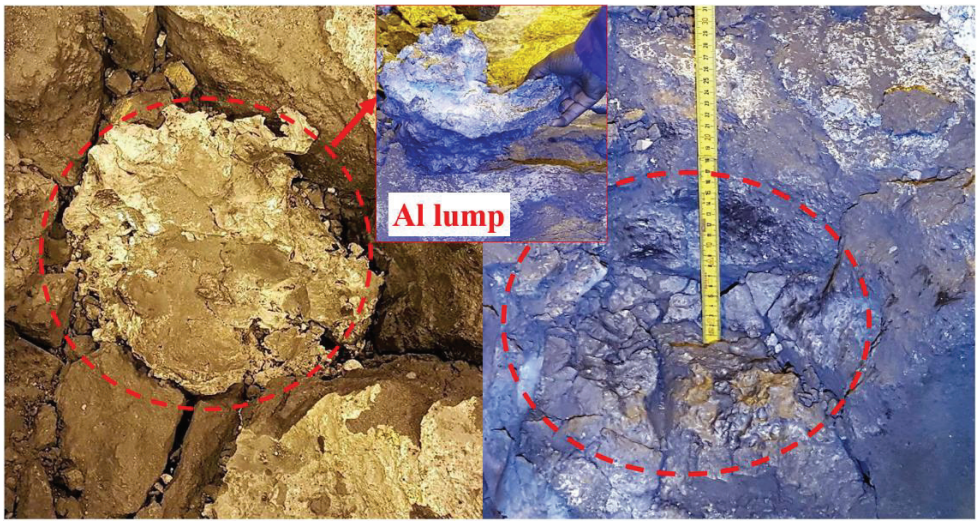

Figure 4.53. A pothole on pot 5 filled with aluminium. Insert is the Al lump removed from the pothole. Pitting can be observed within the pothole.

4.6. Autopsy of Pot 6

4.6.1 Macroscopic observation

Pot 6, a Søderberg technology pot arranged end-to-end, was investigated to study the influence of current distribution on the wear pattern considering the different anode configuration of Søderberg pots. An image of the spent potlining is shown in Figure 4.54. The general wear profile of this pot was relatively uniform as compared to the W and WW wear patterns of the prebaked pots; Figure 4.55 displays the measured wear pattern. Cathode Wear was observed mostly on the cathode surface position under the anode. Cathode surface locations outside the anode position and towards the ends of the cathode blocks displayed the least wear.

The top surface of the spent potlining was covered by a layer of frozen electrolyte, sludge and aluminium carbide. A close look at the top surface of this spent potlining showed the occurrence of pitting all over the surface. This is illustrated in Figure 4.56.

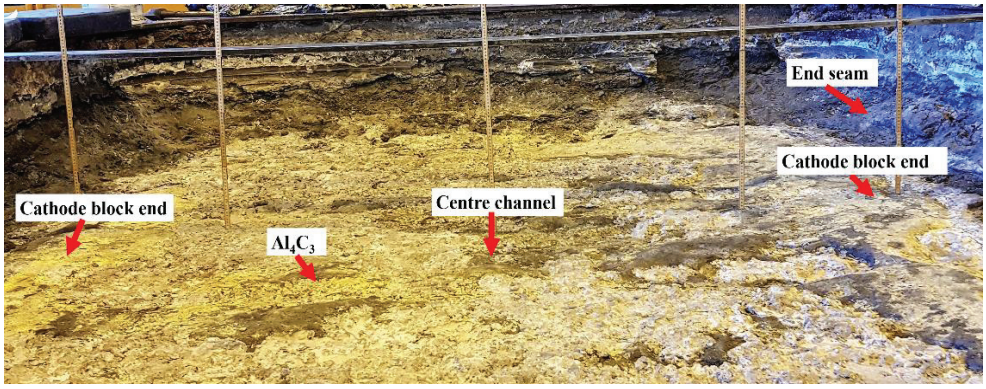

Figure 4.54. Cathode surface of pot 6 showing the least worn out cathode block ends, the centre channel and other features.

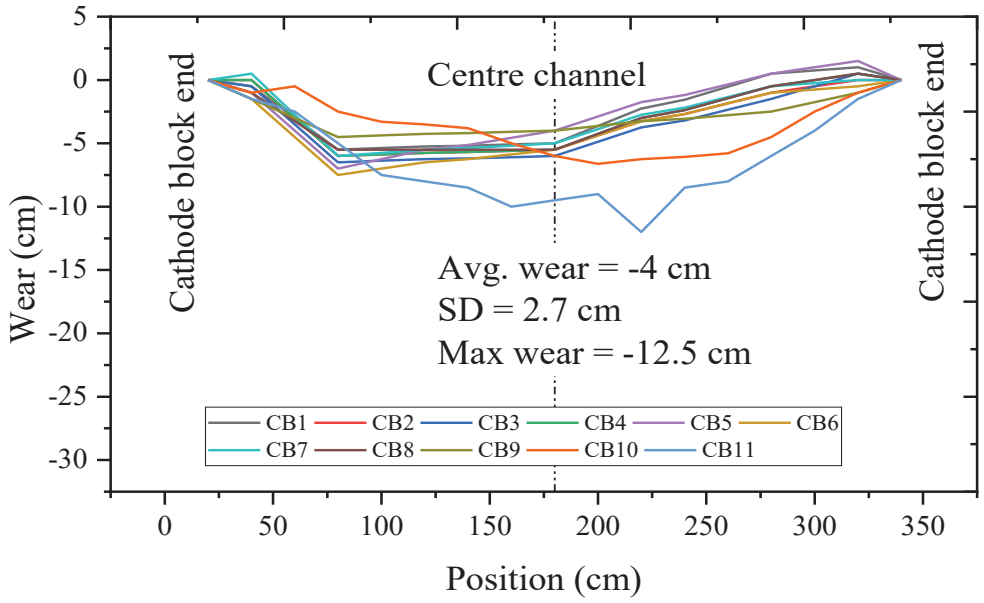

Figure 4.55. Wear pattern measured across pot 6 at different positions, CB1 corresponds to cathode block 1 and CB2 cathode block 2 and so on. Data used for the plots are given in Appendix 10A.

.

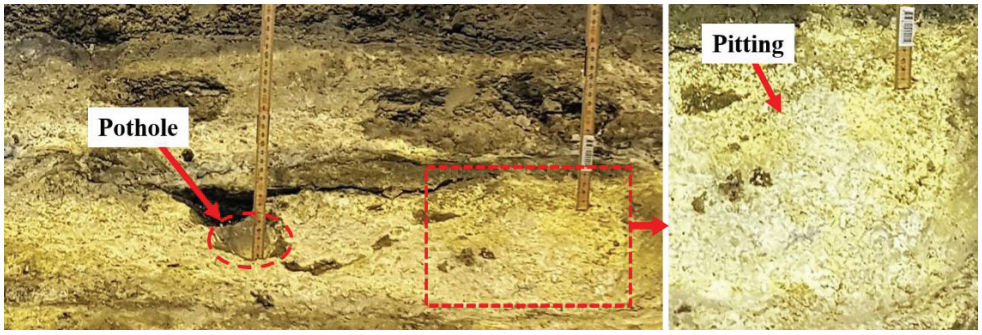

Figure 4.56. Pitting on the cathode surface of pot 6. The pothole and pitting locations are highlighted in the figure.

4.6.2 Microscopic observation

Optical microscopy together with SEM and EDS was used to obtain additional data on the microstructure of the carbon cathode material and phases present at the cathode surface. Optical micrographs showing the microstructure and the wear profiles at the carbon surface are given in Figures 4.57 and 4.58. From the optical images, the wear profile along the aggregate which tends to be relatively uniform and smooth at low magnification appear not to be smooth at high magnifications. Figure 4.58 show a relatively rough interface at the high magnification.

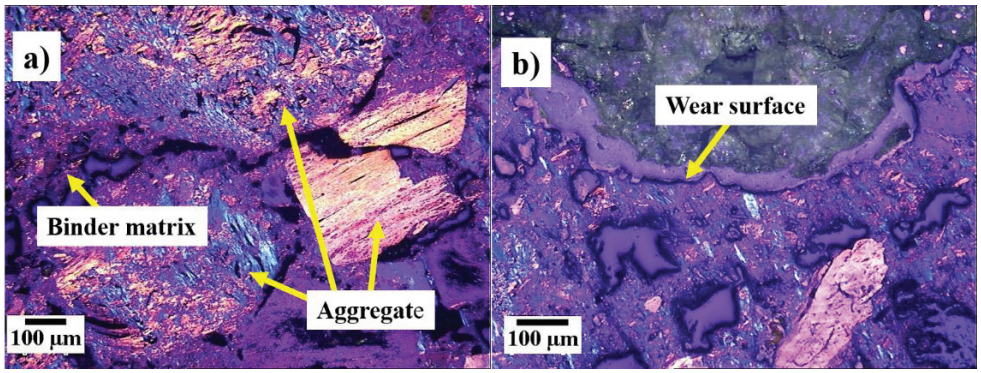

Figure 4.57. a) Microstructure of carbon cathode material of pot 6. b) Wear surface at the carbon-electrolyte interface. Additional information is given in Appendix 10D.

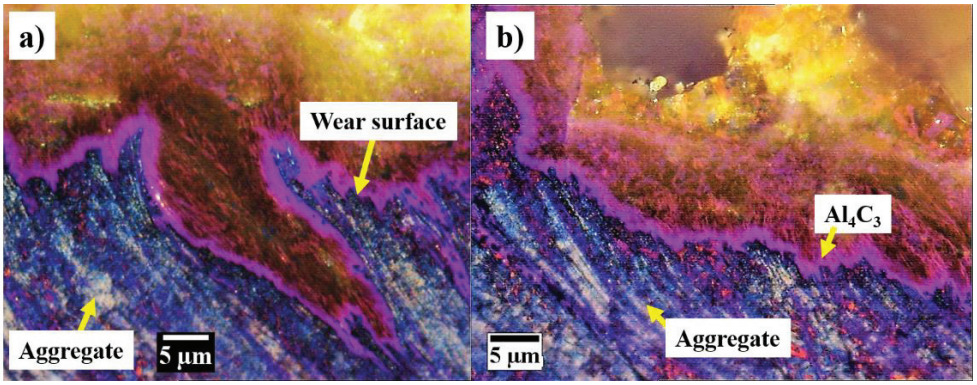

Figure 4.58. Uneven wear surface at carbon-electrolyte interface of pot 6 at high magnification (a and b). Additional information is given in Appendix 10D.

EDS analysis of the interface confirmed the presence of phases such as aluminium carbide, cryolite and alumina. It was also noticed that the aluminium carbide layer was covered by a phase rich in alumina on some parts of the cathode surface. Figure 4.59 displays the phases observed on the cathode surface.

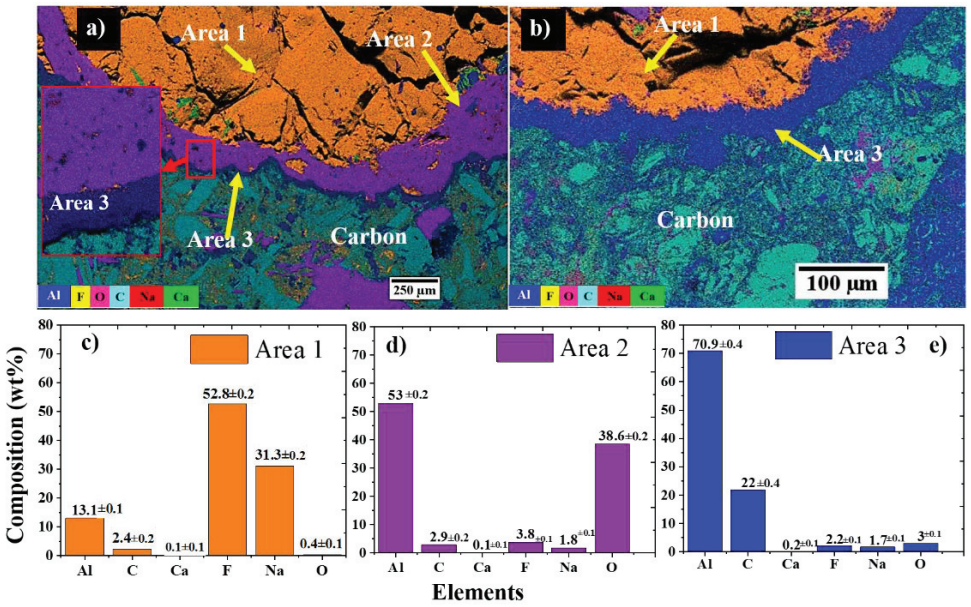

Figure 4.59. Phases at the carbon-electrolyte interface. a) Element map of a cathode surface covered with sludge. b) Element map of cathode surface with no sludge. c) The chemical composition of cryolite at carbon-electrolyte interface. d) The chemical composition of alumina at the carbon-electrolyte interface. e) The chemical composition of aluminium carbide at the carbon-electrolyte interface.

4.7. Summary of Autopsies

Macroscopic observations of pot 1 and 3 revealed the presence of a layer of electrolyte covering the cathode surface with aluminium carbide below the layer of electrolyte and in direct contact with the cathode surface. The non-uniform WW wear pattern was also observed as the overall wear pattern of these pots and the ramming joints were seen to be less worn out than their neighbouring cathode blocks. Potholes of different sizes and shapes were observed at the locations with the highest wear such as the cathode block ends. These highest wear locations were observed to be characterized by pitting. Smaller sized circular erosion patterns were also seen within the pitting location. The ramming joints also had pitting on them. Overlapping pitting at the same location of the cathode surface was also identified. The carbon cathode linings were fully impregnated by bath and the ramming joints contained more bath than their neighbouring cathode blocks. Aluminium carbide was also found within the pores of the carbon cathode lining as well as on the cathode surface. A uniform wear surface along the carbon-electrolyte interface suggesting non-preferential wear of the binder matrix and coke aggregates was identified. No evidence of coke aggregate pull-out could be observed, instead, remains of partly worn-out coke aggregates could be seen within the carbon matrix at the wear surface. Measurement of the average pitting size and the average coke aggregate size yielded no correlation between them. High magnification optical microscopy images of the wear surface at the carbon-electrolyte interface showed signs of a chemically etched surface. Phases indicative of a relatively basic bath was found in the bath on the cathode surface.

The results from pot 2, 4 and 5 also showed a layer of electrolyte and aluminium carbide covering the cathode surface with the carbide layer in direct contact with the carbon cathode. The general wear pattern of these pots was characterized by the non-even W wear pattern. Potholes of different sized and shapes were observed close to the carbon cathode block ends where the wear was highest. Al lump was found in one of the potholes. Pitting was observed all over the cathode surface of these pots, in contrast to pot 1 and 3 where the pitting was mostly visible at the cathode block ends. Pot 5, a relatively young pot of 1028 days also showed pitting on the cathode surface. The pitting at the cathode block ends of pots 2 and 4 appeared larger in size than those observed close to the centre channel. Overlapping pittings were also seen at various locations including locations with potholes. A uniform wear surface indicative of a non-preferential wear pattern at the carbon-electrolyte interface. Additionally, remains of partly worn-out graphite aggregates were observed within the carbon matrix at the carbon-electrolyte interface. Similar to the observations from pots 1 and 3, no indication of coke aggregate pull-out could be seen within the carbon matrix at the wear surface. Phases confirming the basic nature of the bath in contact with the cathode surface were observed in bath and carbon cathode samples from the spent potlinings.

The layer of electrolyte and aluminium carbide was also identified on the cathode surface of the Søderberg pot (pot 6). In addition to the layer of electrolyte and aluminium carbide, deposits of sludge were observed. The wear was generally uniform across the cathode surface with the cathode block ends location showing the least wear and the centre channel showing relatively higher wear. No distinct wear was observed at the cathode block end locations which fell outside the anode shadow. Pitting was also seen all over the cathode surface. A relatively uniform wear indicative of non-preferential wear was also observed for this pot. Finally, a wear surface indicative of chemical etching was observed across the carbon-electrolyte interface.

5

Chapter 5. Results from Wetting Measurements

5.1. Physical Properties of the Materials

Density, air permeability and surface roughness were measured for all the carbon cathode materials employed in the wetting tests. Data on the open porosity of the samples was obtained from the suppliers [108]. Table 5.1 summarizes the physical properties of the materials. The surface topography and roughness of the materials are shown in Figure 5.1 and 5.2. The profiles of the carbon materials in Figure 5.1 and 5.2 give an indication of how deep the pores within the materials are. The surface roughness of the materials can be ranged in the order anthracitic > graphitic > graphitized carbon > graphite (G348). Large pores (~mm) in the anthracitic material are evident, while the size of the pores in the graphitized and graphite materials (EG and G348) are significantly smaller, particularly in the case of the graphite G348 showing a smooth surface profile relative to the other three materials. Graphite (G348) is not used as a traditional cathode material in the aluminium industry, it was, however, used to investigate if all carbon materials behave in the same way or not with respect to wetting.

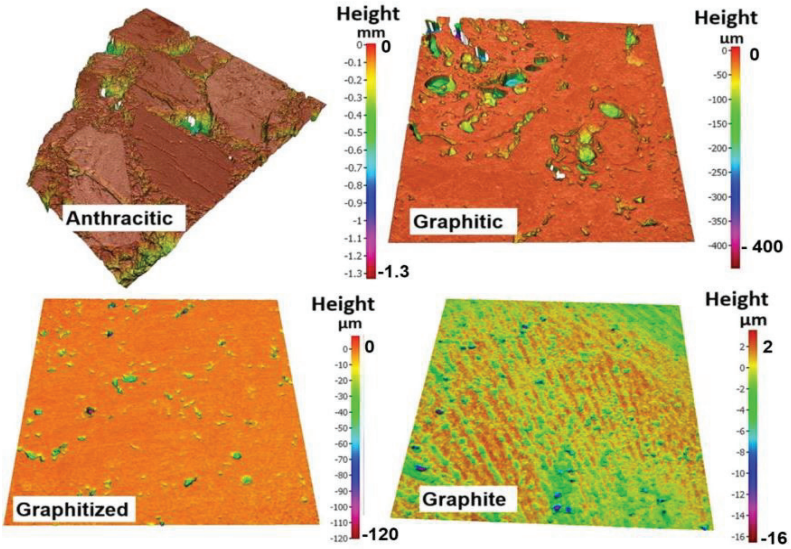

Figure 5.1. The surface topography images of the four carbon materials measured by an optical profilometer. Beside the profile images are the profile height ranges within each material.

5.1. Physical Properties of the Materials

Table 5.1. The physical properties of the four carbon samples used for the wetting tests.

Carbon Type (Trade name)	Density [g/cm^3]	Roughness [µm]	Air Permeability [nPm]	Open Porosity [%]
Anthracitic (G0320)	1.45±0.013	29.6	1.65±0.18	19
Graphitic (PB10)	1.63±0.004	18.2	1.12±0.12	20
Graphitized (EG)	1.74±0.005	8.4	0.49±0.01	13.5
Graphite (G348)	1.92	1.3	NA	8

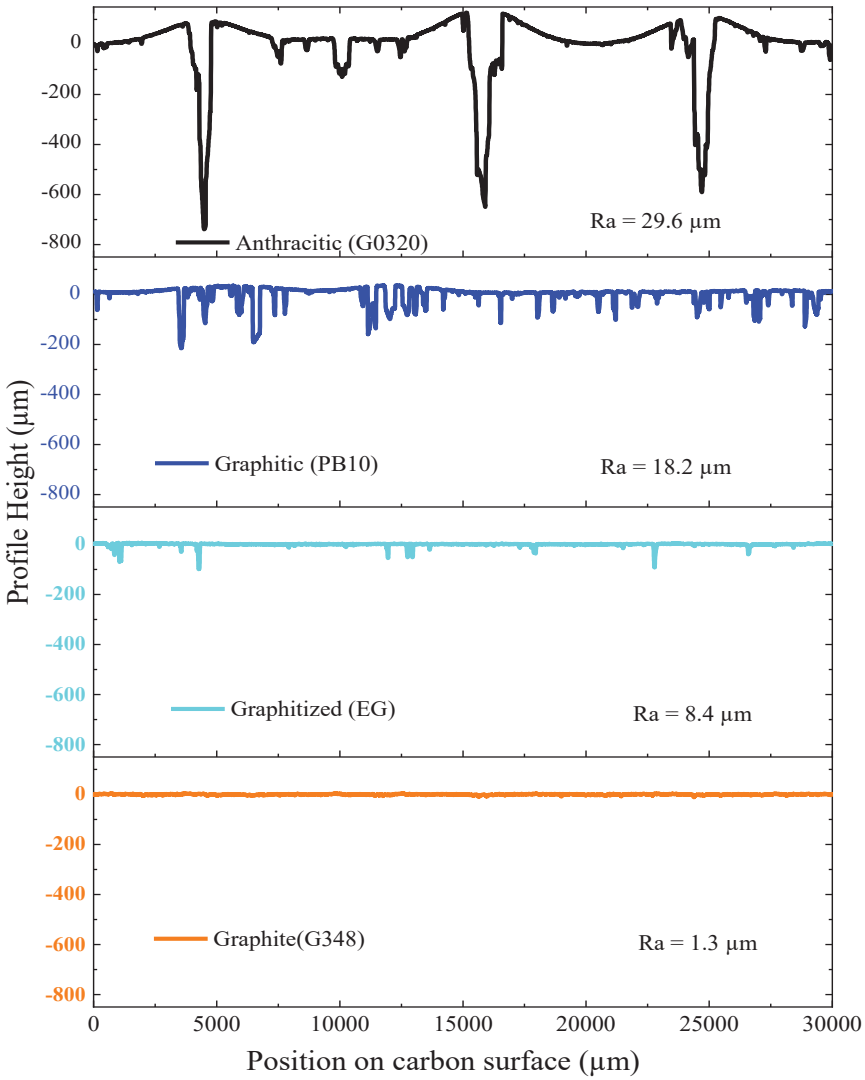

Figure 5.2. The surface profile of the four carbon materials used in the experiments. Ra refers to the surface roughness of the materials.

5.2. Immersion -Emersion Data

A representative change in the weight of a cylindrical carbon sample during an immersion/emersion cycle in the crucible containing molten electrolyte and aluminium is shown in Figure 5.3. The changes in the weight is explained referring to the numbers in the figure. The weight of the sample is constant between positions 1 and 2, where position 2 corresponds to the contact position or the zeroth corrected position (determination of the contact position is given in Appendix 10E). An instant change is observed when the sample gets in touch with the molten electrolyte due to the formation of a meniscus at position 2. For samples wetted by the molten electrolyte, a weight increase is seen at position 2, see green curve in Figure 5.4, while for samples not wetted, a weight decrease is realized at position 2, see red curve in Figure 5.4. Upon further immersion, the weight, in both cases of wetting and non-wetting, decreases continuously as the sample is submerged into the molten electrolyte from position 2 to 3 due to the buoyancy effect. At position 3, the final position for molten electrolyte, the sample encounters molten metal and a change in the slope is recorded due to the formation of a metal meniscus around the sample. The sample penetrates completely into the metal at position 4. The weight gradually decreases upon further immersion to position 5 due to the buoyancy effect. The sample was then kept at this position for 30 or 60 s before the emersion cycle was commenced. The carbon samples were cathodically polarized by a constant current at the final positions, position 3 for the electrolyte and position 5 for the metal, of the immersion cycle.

During the emersion, the weight of the sample followed roughly the same path as the immersion until the sample was about to be lifted out of the liquid electrolyte. It was noticed that the weight of the sample continued to increase beyond the original contact position. This behaviour was, however, different for wetting and non-wetting situations. At position 6 in Figure 5.3, the meniscus is broken, and the recorded weight returns close to the original weight of the sample before immersion. The changes in weight at the contact position depend on the kind of meniscus formed at the liquid surface as illustrated by the insert in Figure 5.4. A liquid that wets a solid sample will form a concave meniscus upon contact during immersion and pull it downwards into the liquid, resulting in a weight increase as illustrated by the green curve in Figure 5.4. A liquid that does not wet a solid sample, on the other hand, will form a convex meniscus and push the sample upwards resulting in a weight decrease as shown by the red curve in Figure 5.4.

The weight of the sample recorded during immersion/emersion were corrected for the buoyancy effect. The weight corrected for buoyancy effect is called the corrected weight, m_σ, and was calculated by the formula given in Equation 5.1

$$m_\sigma = (m_m - m_o) + f_b \times \Delta x \qquad (5.1)$$

where m_m is the measured weight, g, m_o is the weight of the sample in gas, g, f_b is the buoyancy correction factor, g/cm, and Δx is the difference between the actual position and the reference position of the sample, cm. The reference position refers to the position where the sample came in physical contact with the liquid during immersion. The buoyancy correction factor, which represents the change in weight due to buoyancy per unit immersion depth, is given by

$$f_b = \pi r^2 \Delta\rho \tag{5.2}$$

where r (cm) is the radius of the sample and $\Delta\rho$ (g/cm^3) is the density difference between the liquid and gas (or second liquid).

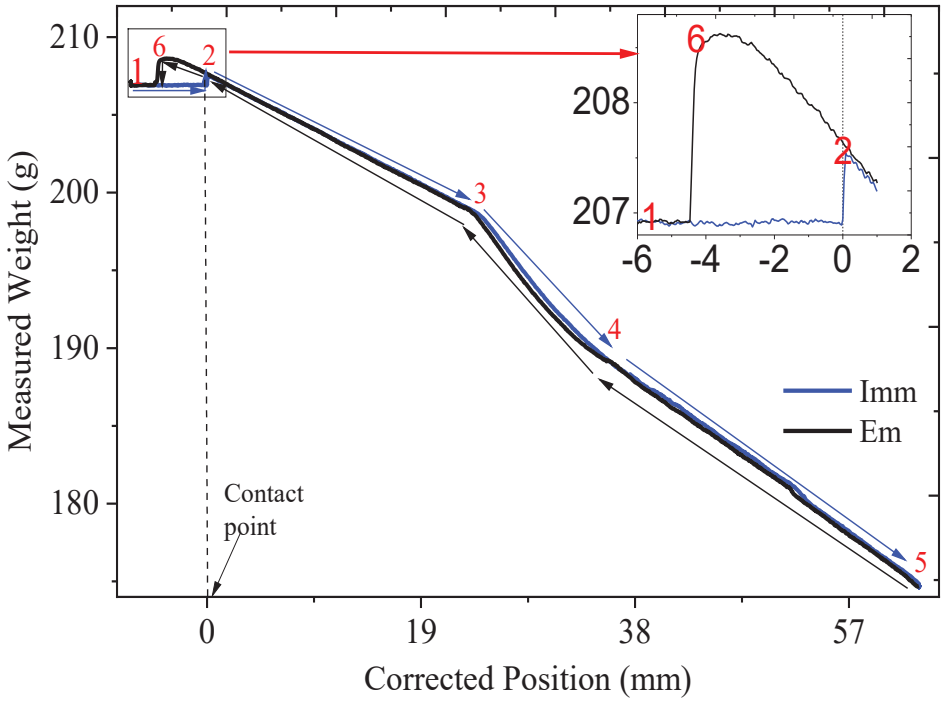

Figure 5.3. The weight of the sample as a function of the position of the sample relative to the position of the electrolyte surface during immersion/emersion cycle. Positions 1-6 are explained in the text. Insert is a magnified area of the initial part of immersion and final part of the emersion cycles. Imm stands for immersion cycle while Em represents the emersion cycle.

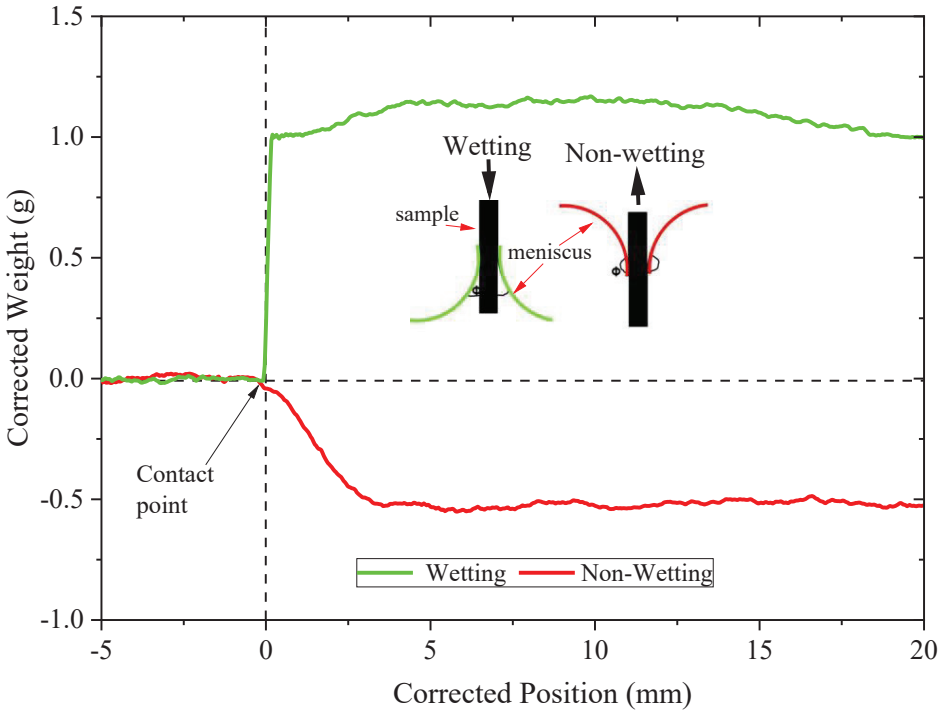

Figure 5.4. The corrected weight close to the region where the sample encounters the electrolyte during immersion illustrating a wetting and non-wetting situation. Insert shows meniscus formed by the liquids (a red non-wetting liquid and a green wetting liquid).

5.2.1 Wetting Tests in Molten Electrolyte

The buoyancy corrected data for wetting experiments in only molten electrolyte is shown in Figure 5.5 for the four carbon materials. In these experiments, none of the carbon materials were polarized prior to emersion. The experiments revealed that the molten electrolyte did not wet the carbon materials during the complete immersion/ emersion cycle. Increasing the holding time at the final position before emersion did not change the wettability of the materials. The corrected weight is negative and relatively constant during the whole cycle, see Figure 5.5. It can also be seen that for this non-wetting situation, the weight of the samples return to the original weight after the cycle was finalized and the sample was lifted out of the liquid. The apparent noise in the weight signal is due to the deviation from the perfect cylindrical symmetry of the carbon samples due to surface roughness and open pores.

5.2. Immersion -Emersion Data

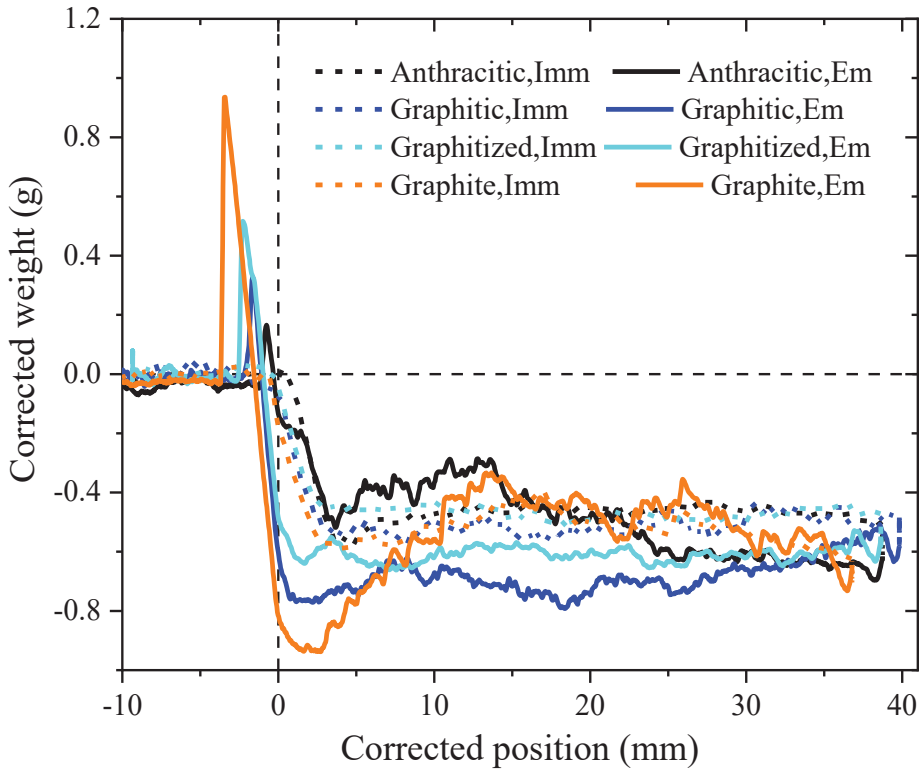

Figure 5.5. The corrected weight of the four carbon materials during an immersion-emersion cycle with only molten electrolyte present and no cathodic polarization of the carbon cathode materials. Additional data is provided in Appendix 10E.

The wetting experiments with the molten electrolyte were repeated with new carbon cathode samples except that cathodic polarization of the carbon samples was applied for 30 s at the final immersion position of the samples. The buoyancy corrected data for these experiments is shown in Figure 5.6. The same non-wetting behaviour as shown in Figure 5.5 was observed during immersion. However, during the period where the sample became polarized at a constant vertical position, the corrected weight changes sign from negative to positive. The time dependence of the weight during the polarization period is shown in the insert in Figure 5.6. The figure clearly demonstrates the rapid weight increase as the voltage is turned on. The transition from a non-wetting to a wetting state is clearly shown by the behaviour during the emersion cycle in Figure 5.6. The final weight of the wetted carbon samples after they were drawn out of the melt was observed to be higher than their initial weight before the start of experiments. This observation is in sharp contrast to the non-wetted carbon samples shown in Figure 5.5, where the weight of the carbon samples before and after the experiments was observed to be the same. The additional weight after the emersion cycle shown in Figure 5.6 is due to molten electrolyte either located at the surface and/or inside the open porosity in the materials.

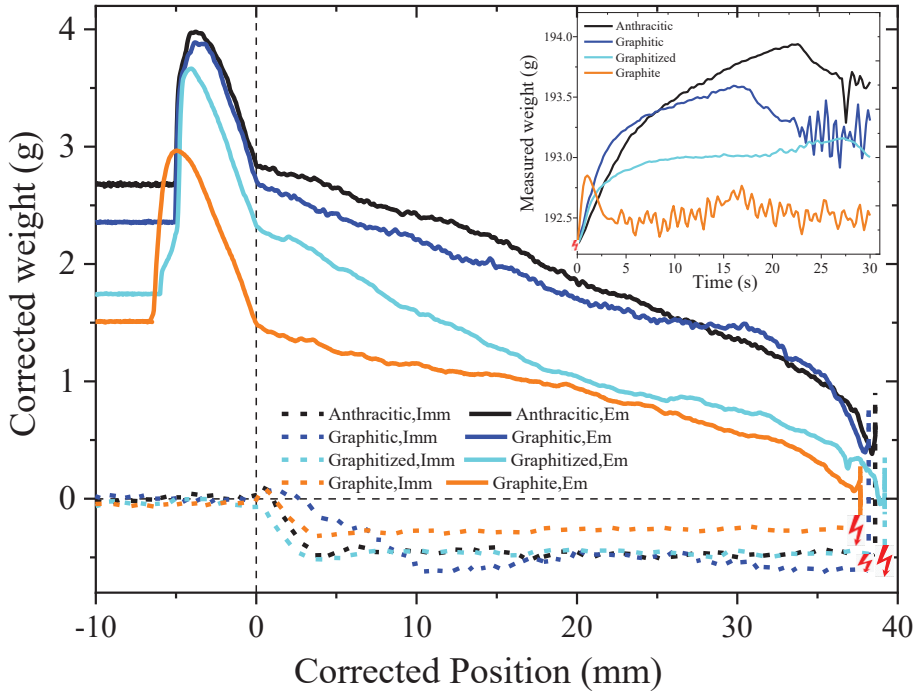

Figure 5.6. The corrected weight of the carbon samples during the immersion-emersion cycle with only molten electrolyte present and the carbon samples are cathodically polarized. Red power symbol indicates the position of the onset of polarization. Insert illustrates the time dependence of the weight during polarization. Additional data is provided in Appendix 10E.

The immersion/emersion cycles were repeated for the samples in Figure 5.5, but this time without polarization. The data for this second immersion/emersion cycle is shown in Figure 5.7a. In this case, the data demonstrates that the molten electrolyte is wetting the carbon materials throughout the whole cycle. This is shown by the characteristic positive weight change at the contact point. Data from successive cycles after the first cycle with polarization demonstrated that the wettability, achieved during the 30 s polarization of the sample, remained for some time. Successive cycles during a period of 24 hours demonstrated that most of the weight gained during the 30 s polarization was gradually lost in the repeating cycles. Data showing this behaviour is shown in Figure 5.7b. The successive immersion-emersion cycles over a period of 24 hours after the polarization for the graphitized cathode sample is displayed in Figure 5.8. The clear decrease in the corrected weight after the cycles can only be explained by a decline in the total amount of electrolyte remaining on the surface and inside the pores. Further evidence for this is given in chapter 5.3.

5.2. Immersion -Emersion Data

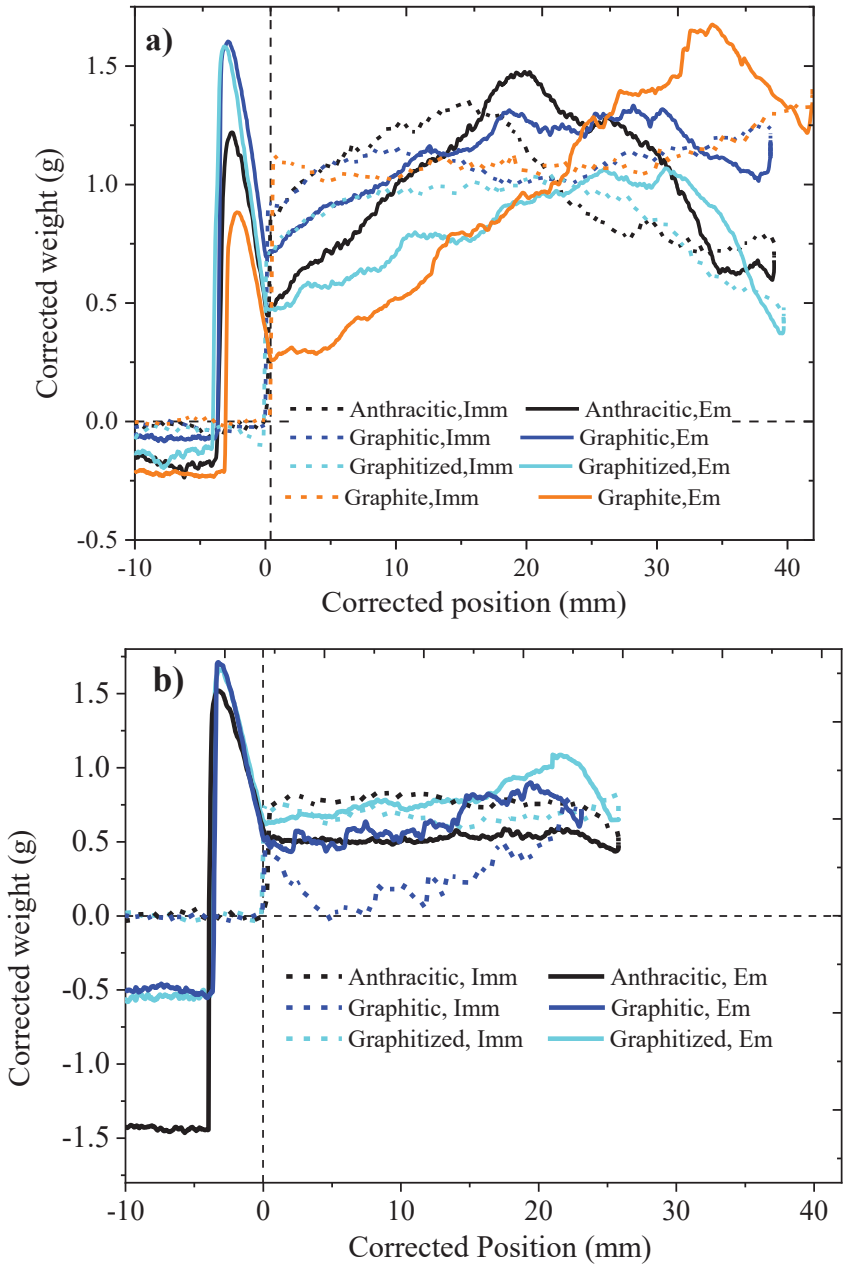

Figure 5.7. The corrected weight of the carbon samples during the immersion-emersion cycle in the molten electrolyte where polarization was applied during the first cycle. a) 30 minutes after the first cycle. b) 24 hours after the first cycle. Only 3 of the materials were tested for a period of 24 hours. Additional data is provided in Appendix 10E.

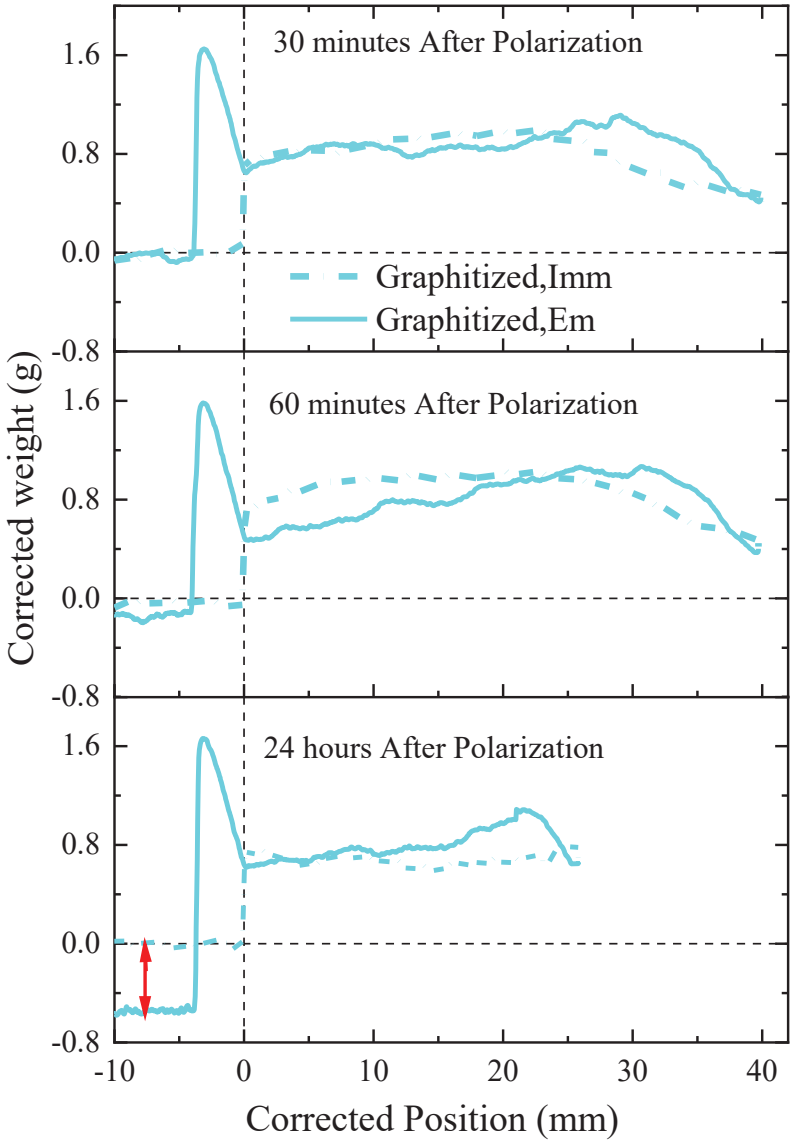

Figure 5.8. The corrected weight of the graphitized sample at different time intervals after the first polarization cycle. Red double arrow line on the last plot illustrates the weight difference between the immersion and emersion cycles. Additional data is given in Appendix 10E.

5.2.2 Wetting Tests in Molten Electrolyte and Aluminium

The wetting behaviour of the carbon materials when the electrolyte was present together with molten aluminium is shown in Figure 5.9. The data demonstrate that all four carbon materials were wetted by the molten electrolyte when Al was present. Wetting of the carbon cathode material was observed to occur upon contact with the

molten electrolyte in equilibrium with Al. A weight increase after emersion indicating electrolyte penetration was also observed. All the data showed wetting prior to polarization, upon polarization for 60 s, the wetting behaviour did not change significantly.

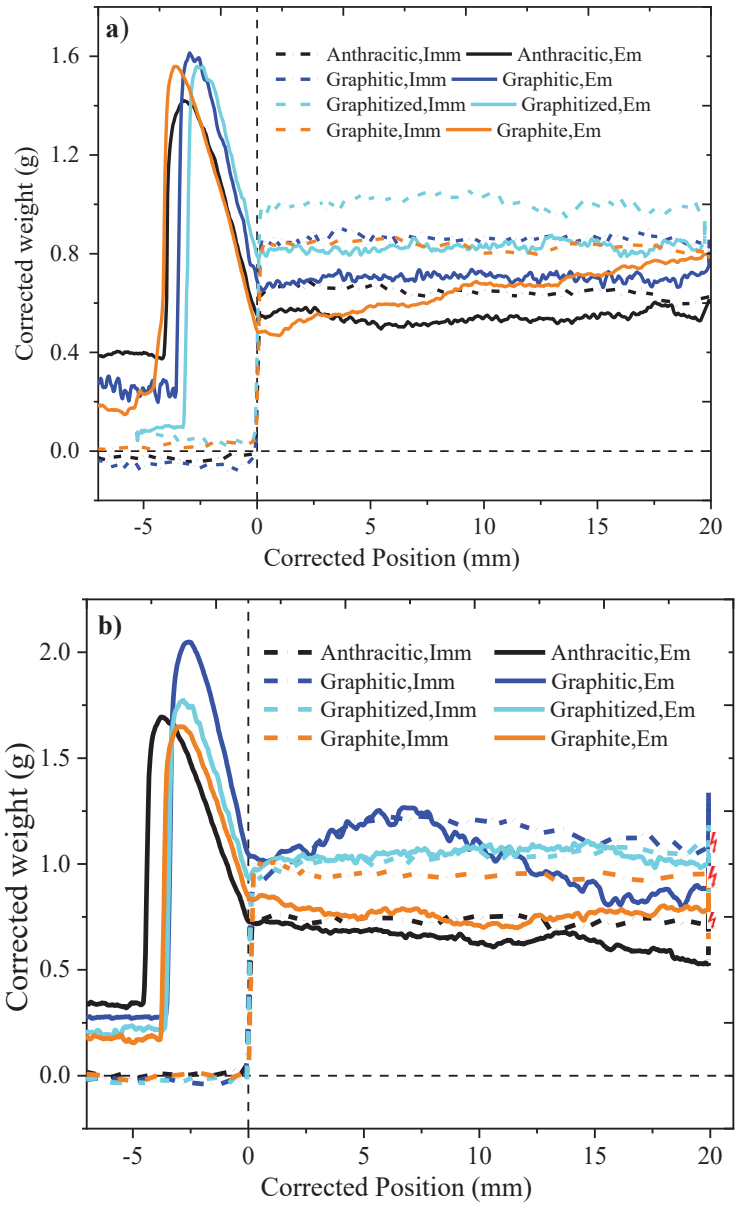

Figure 5.9. The corrected weight of the carbon samples during an immersion-emersion cycle in molten electrolyte and Al. a) All four carbon samples without polarization. b) All four carbon samples with 60 s of cathodic polarization. The red power symbol shows the position of polarization. Additional data is provided in Appendix 10E.

5.2.3 Wetting Tests in Molten Aluminium

The wetting experiments performed in molten Al, with a 10 mm layer of molten electrolyte above Al, is shown in Figure 5.10. Only a negative corrected weight is obtained, and the data demonstrate that molten Al does not wet the carbon materials, with or without polarization.

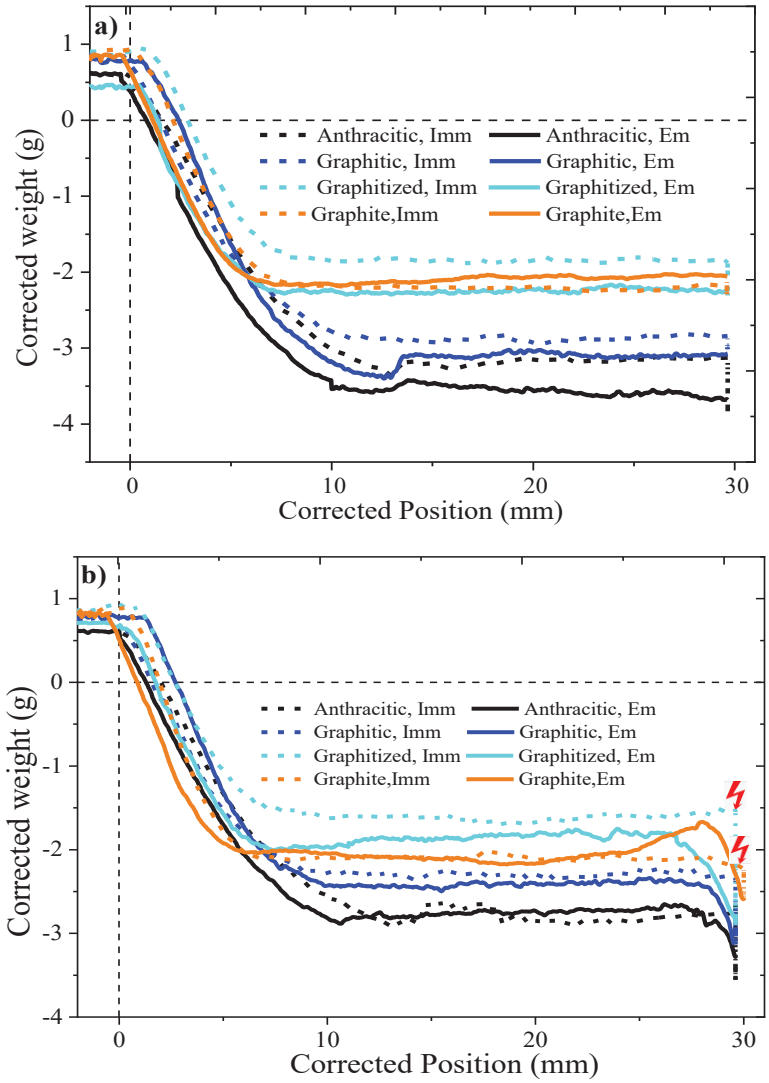

Figure 5.10. The corrected weight of the carbon samples during an immersion-emersion cycle in molten Al. a) All four carbon samples without applying current. b) All four carbon samples with current applied for 60 s. The red power symbol shows where the voltage was switched on. Additional data is provided in Appendix 10E.

5.3. Characterization of Materials after the Wetting Test

Carbon materials that were wetted by the electrolyte, as well as those not wetted, were analysed by electron microscopy after the tests. SEM images of two out of the four carbon cathode samples before and after the tests are shown in Figures 5.11 and 5.12. The images demonstrate that molten electrolyte infiltrates the open porosity of the carbon materials only after wetting has occurred.

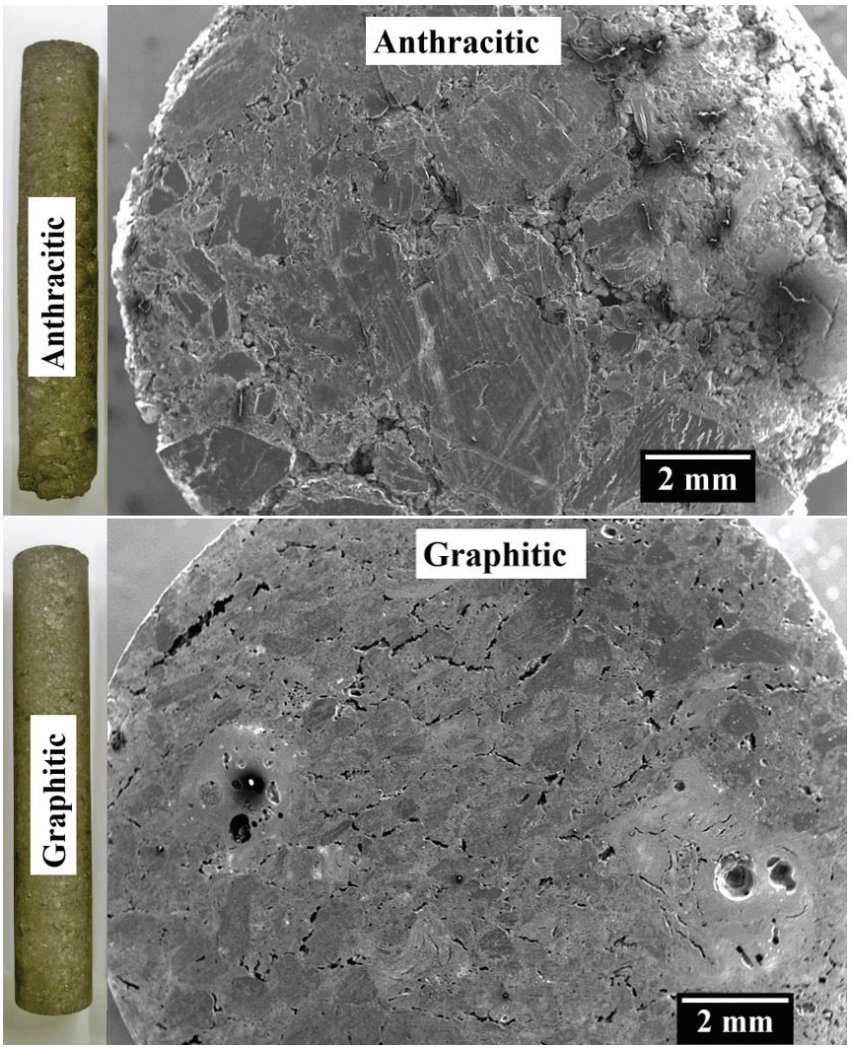

Figure 5.11. Pristine anthracitic and graphitic carbon materials before the wetting tests.

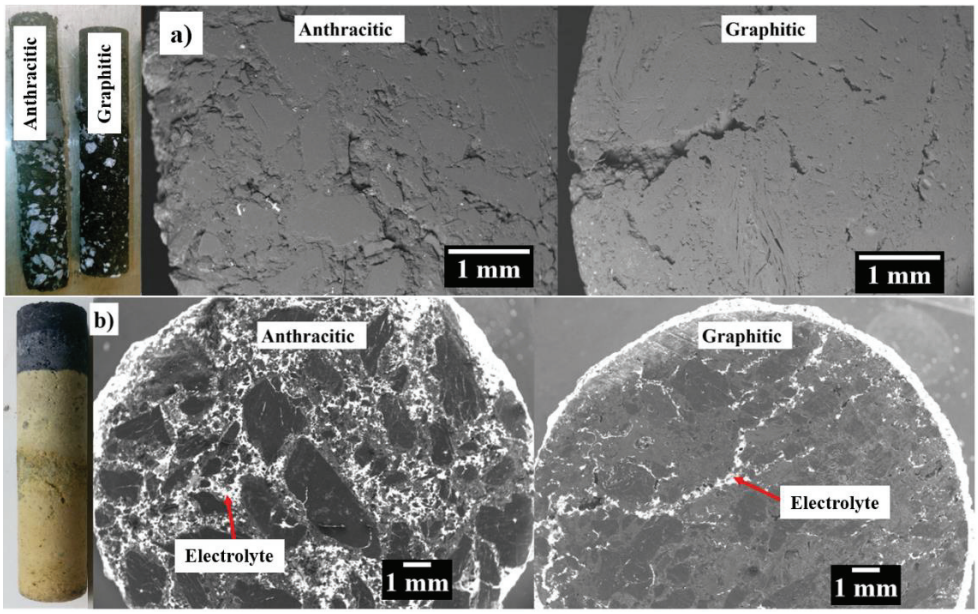

Figure 5.12. Carbon samples after wetting test in molten electrolyte only. a) Anthracitic and graphitic materials where no wetting has occurred. b) Anthracitic and graphitic materials where wetting has occurred. White regions demonstrate solidified electrolyte inside the open pores in the materials.

A quantitative analysis to verify the volume of the carbon cathode material penetrated by the electrolyte is given in table 5.2. The density of the electrolyte at the experimental conditions was taken to be 2.126 g/cm^3 [112]. The volume of electrolyte in the sample was estimated from the electrolyte weight and density, while the volume of the open porosity of the sample was estimated from its geometry. The fraction of the volume of open pores infiltrated by the electrolyte was estimated from these values.

Table 5.2. Quantitative analysis of electrolyte penetration into the carbon cathode samples.

Carbon Cathode Samples	Excess weight due to the electrolyte (g)	The volume of electrolyte (cm^3)	Estimated volume of open porosity (cm^3)	Fraction of open porosity filled with electrolyte (%)
Anthracitic	2.68±0.02	1.26	1.34	93.86
Graphitic	2.36±0.02	1.11	1.41	78.52
Graphitized	1.75±0.03	0.82	0.95	86.26
Graphite	1.51±0.008	0.71	0.57	125

The images in Figure 5.12b show a difference in the amount of electrolyte that penetrates the different carbon materials. The amount of electrolyte within and on the

surface of the four carbon materials according to the calculations shown in Table 5.2 and the SEM images were ranked as anthracitic > graphitic > graphitized > graphite. SEM and EDS analysis were conducted to confirm the presence of electrolyte within the carbon materials of the wetted samples and this is shown in Figure 5.13 below.

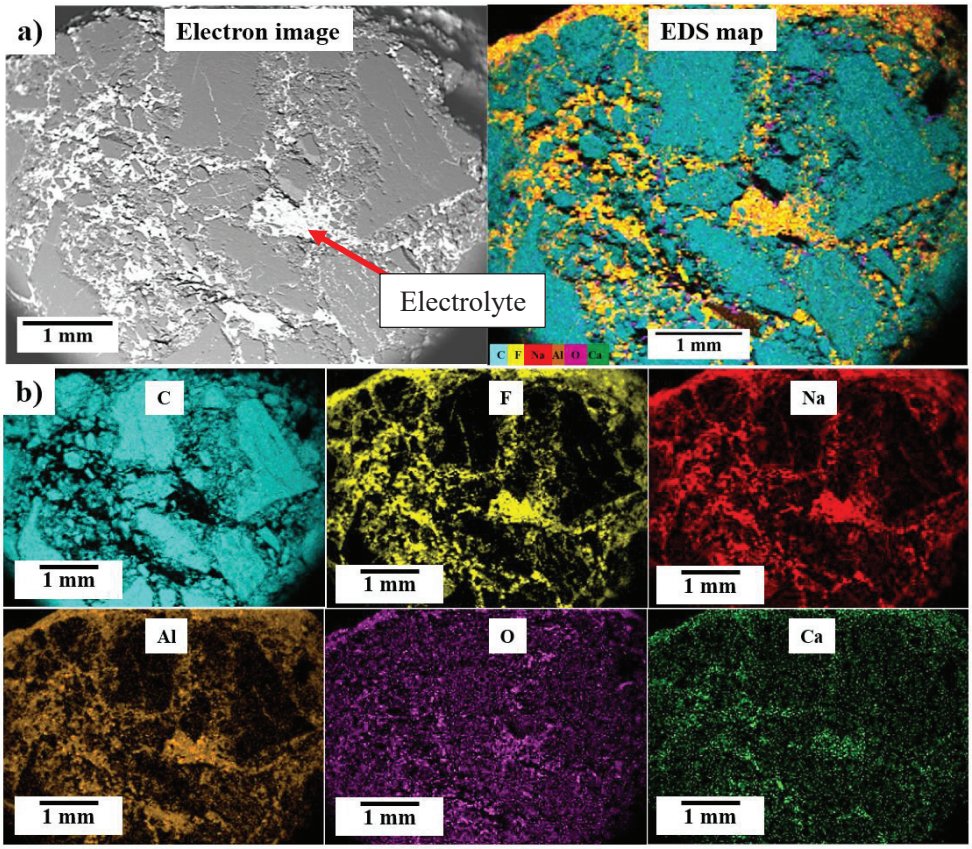

Figure 5.13. Anthracitic cathode sample after wetting test in molten electrolyte. a) SEM image and EDS map of the wetted anthracitic material. b) Elemental maps of the individual elements present.

The high degree of adhesion and physical contact between the carbon materials and the bath at the interface are evident in the images shown in Figure 5.14. The EDS mapping displayed in Figure 5.15 were also used to confirm the presence of solidified electrolyte at the surface of the carbon materials.

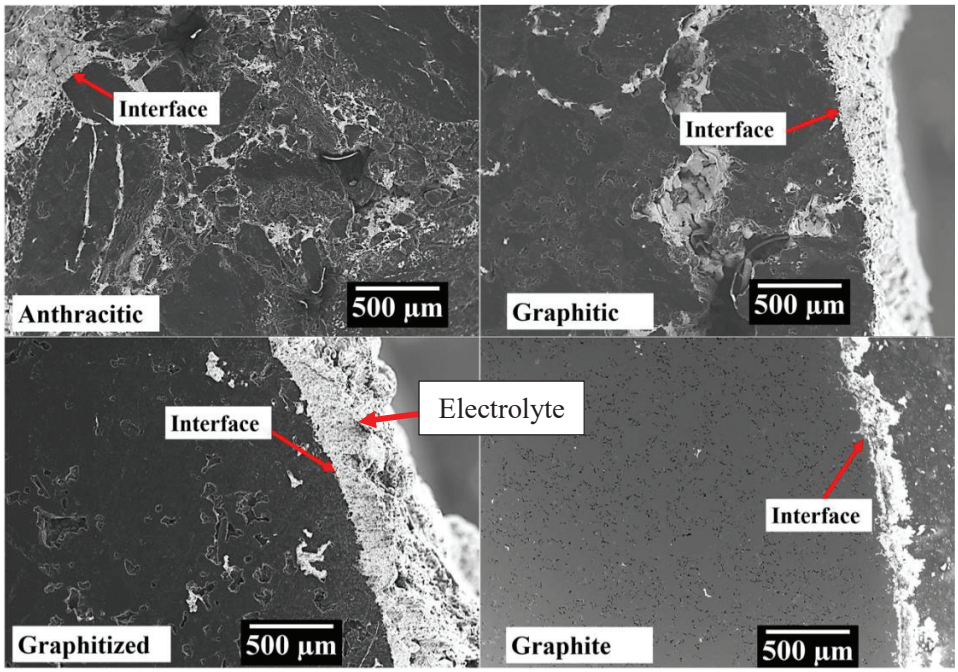

Figure 5.14. Physical bonding between the carbon material and the solidified electrolyte at the interface.

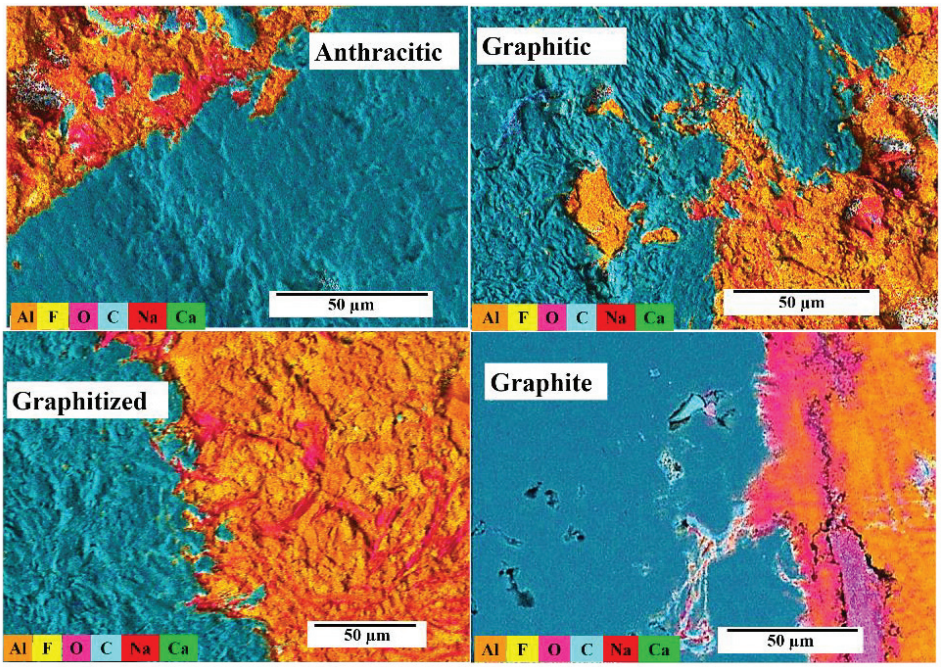

Figure 5.15. EDS mapping of the four carbon materials after the wetting tests in the molten electrolyte with 30 s of polarization.

5.3. Characterization of Materials after the Wetting Test

Carbon samples from wetting tests conducted in molten electrolyte together with molten Al and polarized for a maximum of 300 s were also analysed by electron microscopy. The EDS mapping of the interface for these samples are shown in Figure 5.16. Two distinct layers, one rich in fluorine, sodium, calcium and oxygen and the other rich in aluminium and oxygen were found at the interface between the molten metal and the carbon cathode. The latter is proposed to correspond to a layer of Al_4C_3 that got hydrolysed/oxidised before analysis.

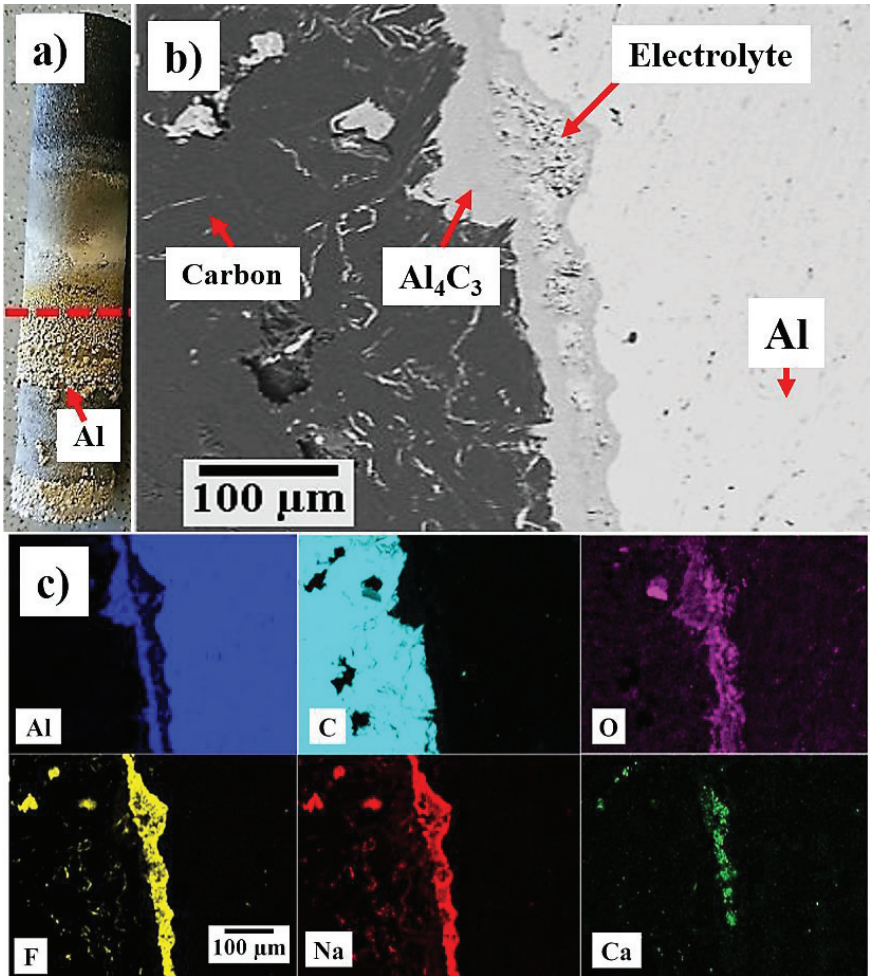

Figure 5.16. Wetting in molten electrolyte and Al where current was applied for 300 s. a) The carbon sample after the wetting test. b) SEM image of the cut cross-section (red dashed lines) showing the carbon-Al interface. c) EDS element mapping of the carbon-Al interface from Figure 5.16b.

Images of the anthracitic and graphitic carbon materials exposed to repeated immersion/emersion cycles are shown in Figure 5.17. The figure shows that the

amount of electrolyte that infiltrates the carbon material after wetting has occurred, as displayed by Figure 5.12b, reduces after some time. This corresponds well with the data presented in Figures 5.7b and 5.8 where the weight of the samples after emersion declined with time. The decline in weight owing to electrolyte loss from the carbon materials might indicate a gradual reduction in wettability.

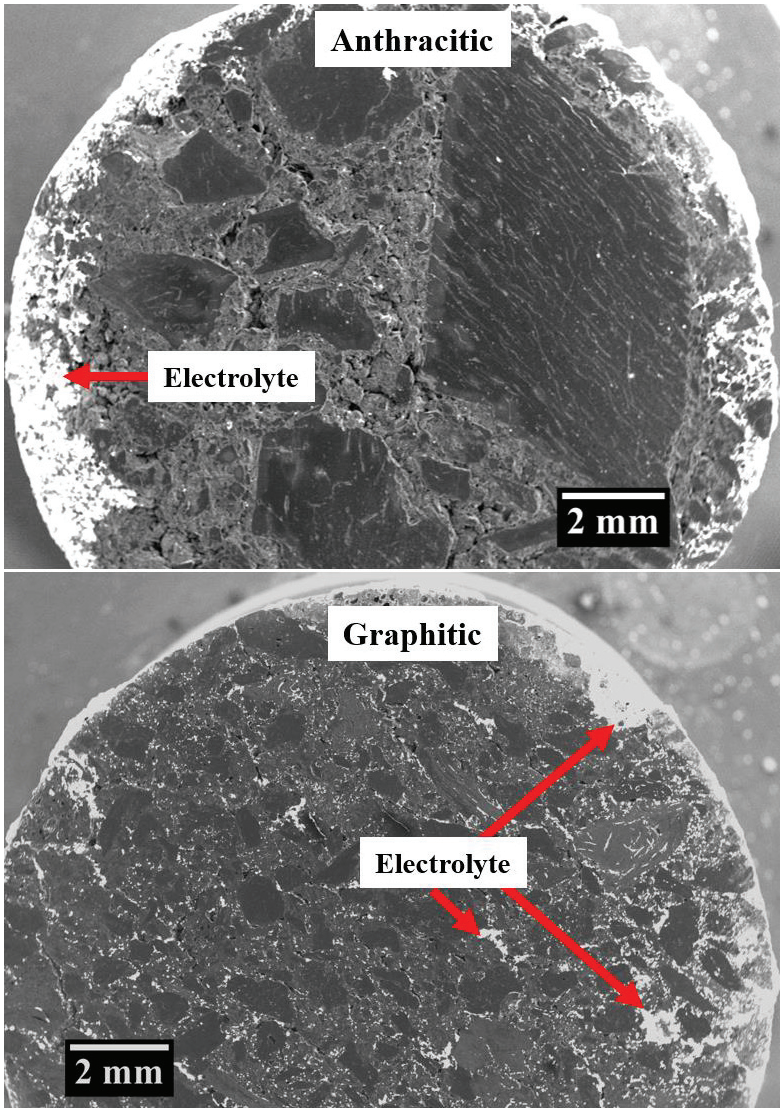

Figure 5.17. SEM images of anthracitic and graphitic carbon samples after 24 hours of wetting tests in the molten electrolyte with 30 s of polarization.

5.4 Summary of Wetting Results

Results from the wetting tests conducted in a melt consisting of only molten electrolyte demonstrated that all the carbon cathode materials are not wetted by the molten electrolyte. It also showed that no penetration of electrolyte into the carbon cathode materials occur without wetting. Cathodic polarization of the carbon samples changed the wettability from a non-wetting condition to a wetting condition and the consequent penetration of electrolyte into the carbon samples. It was also observed that the change in wettability and the resulting electrolyte penetration occurs within seconds of cathodic polarization. More than 50% of the open porosity of all the carbon samples were filled with electrolyte within 30 s of cathodic polarization. The amorphic carbon materials were observed to contain more electrolyte than their less amorphic counterparts. Further measurements after the voltage had been switched off showed that the wetting stays for some time. Tests conducted over a period of 24 hours demonstrated that the wettability achieved during the 30 s cathodic polarization eventually decreases resulting in a decrease in the amount of penetrated electrolyte.

Data from the wetting tests conducted in a melt made up of molten electrolyte and Al showed wetting between all the carbon cathode materials and the molten electrolyte in equilibrium with Al. The carbon materials were also penetrated by the electrolyte, however, the amount of electrolyte that penetrated was observed to be lower than the amount that penetrated during the cathodic polarization of samples in only molten electrolyte. Cathodic polarization of the carbon samples immersed in the melt of molten electrolyte and Al did not seem to change the wetting significantly.

Measurement results from the tests conducted in a melt consisting of molten Al with a 10 mm layer of electrolyte on top showed that the molten metal does not wet any of the carbon cathode materials. Cathodic polarization of the carbon samples did not change the wetting condition. All the carbon cathode samples were found coated with a layer of the electrolyte.

Samples from wetting tests conducted in molten electrolyte and Al where the carbon samples have been polarized for 300 s showed aluminium carbide formation on the surface of the carbon material. SEM/EDS analysis of the interface showed a layer of electrolyte between the aluminium carbide and the metal. Further microscopic analysis of other wetted samples confirmed the presence of electrolyte within the porosity of the carbon materials after wetting has occurred.

6

Chapter 6. Discussions

6.1. Wetting of Carbon Cathodes

The wetting experiment was motivated by the observation of a layer of frozen electrolyte on the surface of the carbon cathode lining as well as to answer the questions of how fast the wettability changes, what causes the change in wettability and what happens when the factors contributing to the change in wettability diminishes. The presence of a film of molten electrolyte between the carbon cathode and the metal pad has been proposed to play an important role for the carbon cathode wear process as it facilitates the formation, dissolution and transport of aluminium carbide [3, 13]. In addition, most of the laboratory experiments conducted to investigate the wettability of the carbon cathode by molten electrolyte and Al [21, 24, 103, 104] has not included factors such as how fast the wettability is changed, the actual factor that changes the wettability and what happens when that factor is removed. The method used in this work enabled to study in situ the wettability of carbon materials and the influence of onset of electrochemical reactions and the infiltration of bath into the carbon materials.

The wetting experiments with only molten electrolyte demonstrate clearly that carbon is not wetted by the molten electrolyte (Figure 5.5). The non-wettability of the carbon cathode by the molten electrolyte agrees with previous observations by Doward [21], Qiu et al. [103] and Kvande et al. [24]. Doward [21] measured a contact angle of 115° for pure cryolite on a graphite substrate. Kvande et al. [24] observed the wetting contact angle to remain constant at 110° to 115° for a cryolitic melt on a carbon cathode. The observed wetting contact angles values mentioned above clearly demonstrate that the bath itself does not wet carbon.

The present data (Figure 5.6) demonstrate that cathodic polarization of the carbon materials improves the wettability of the carbon cathode by the electrolyte in agreement with tests conducted by Qiu et al. [103], Utigard and Toguri [104] and Kvande et al. [24]. The time dependence of weight, see insert Figure 5.6, showed an instant increase when the voltage was switched on. SEM images, like the one shown in Figure 5.12b, support that the increased weight was due to infiltration of the electrolyte into the open pores of the materials resulting from improved wettability. It can also be seen from the insert in Figure 5.6 that the more porous anthracitic material demonstrated the highest increase in weight, while the least porous graphite showed the lowest increase in weight. The SEM image in Figure 5.12b confirms the larger amount of electrolyte within the open porosity of the more porous anthracitic

material relative to the other materials. The instantaneous increase in measured weight upon cathodic polarization suggests an immediate change from a non-wetting to wetting situation introduced by the onset of polarization.

Qiu et al. [103], attributed the change in wettability resulting from cathodic polarization of the carbon electrode in cryolitic-alumina melts to a phenomenon called "Cathodic Attraction". According to Kvande et. al. [24], cathodic polarization induces electro-capillary forces that causes a reduction in the surface tension of the electrolyte at the electrolyte-carbon interface. The reduced surface tension of the electrolyte then results in wetting between the electrolyte and carbon cathode and the resulting electrolyte penetration into the carbon cathode. The author of the present thesis argues that the enhancement in wettability following cathodic polarization of the carbon cathode material is due to the electrochemical reactions initiated by the onset of the polarization. The onset of polarization starts electrochemical reactions that lead to the formation of Na metal on the surface of the carbon cathodes as described by Equations 2.2, 2.3 and 2.4.

Na on the cathode surface is suggested to open the path for bath infiltration [14]. Electrolyte penetration into the carbon would increase the measured weight of the carbon samples immersed in the electrolyte (Figure 5.6). It is proposed that the instant weight increase at the onset of the cathodic polarization is due to the formation of Na on the cathode surface initiated by electrochemical reactions.

A unique observation from the wetting tests conducted in the molten electrolyte is the fast rate at which the weight increases upon cathodic polarization, as shown in the insert in Figure 5.6. The fast increase in weight suggests a surface-related phenomenon as the time necessary for Na diffusion into the bulk of the carbon material is sufficiently longer than the time observed for the wettability to change [46, 113]. Thus, in this work, it is proposed that the presence of Na at the carbon surface is key to the onset of wetting.

Furthermore, it was also demonstrated that the change from non-wettability to wettability achieved during the cathodic polarization remained even after the voltage was switched off, as displayed in Figure 5.7a by positive corrected weights during the immersion and emersion cycles. A possible signature of diminishing wettability, evidenced by the decrease in weight after the emersion cycles, was, however, observed 24 hours after the absence of cathodic polarization as shown in Figures 5.7b and 5.8. A reduction in weight after the emersion cycle demonstrated that the amount of electrolyte that infiltrated into the carbon materials was reduced, this was also confirmed by microscopy (Figures 5.17). It is well documented in the literature that the intercalation of Na into the carbon material is reversed when the factor(s) responsible for the insertion is/are removed [45-49]. This implies that switching off the voltage as was done after the 30 s polarization during the wetting tests reduced the activity and presence of Na within the carbon cathode material. The reduction in

activity and presence of Na will eventually reverse or reduce any induced effect brought by Na, such as wettability in this case. Impaired wettability owing to the absence of Na from the carbon material may allow external factors such as gravitational forces acting on the electrolyte within the carbon material to drain the electrolyte out causing the reduction in the weight recorded. It must, however, be mentioned that apart from the reduction in weight after the emersion cycles, the curves shown in Figures 5.7 and 5.8 showed that all the corrected weights were still positive implying some wetting conditions of the carbon cathode remained. This observation demonstrates that the dewetting process is too slow to have any practical consequence in real operations.

Aluminium carbide can be assumed to be wetted by the molten electrolyte as all the autopsy results showed the electrolyte in direct contact with the carbide on the cathode surface. It can therefore be argued that the presence of Al_4C_3 on the carbon surface may influence the wetting measurements. This is because the measurement will be between the electrolyte and the carbide layer on the carbon surface other than with the carbon material itself. However, for the present wetting tests, no signs of Al_4C_3 could be seen on the surface of the wetted carbon materials after the tests. This could be because the 30 seconds cathodic polarization was too short to allow for any considerable carbide formation. Furthermore, for Al_4C_3 to be formed in the presence of the molten electrolyte and carbon, a contact (wetting) is needed between them as well as Na [3]. Since the electrolyte is known not to wet the carbon, the carbide will form only after contact (wetting) is established and Na is produced. Thus, for the wetting tests in molten electrolyte, it can be argued that Na was solely responsible for the wetting and de-wetting of the carbon by the molten electrolyte.

The carbon materials were shown to be wetted and penetrated by the electrolyte when the electrolyte is in contact with molten Al (Figure 5.9a). This finding is consistent with previous observations by Doward [21], where Al was referred to as a wetting agent for the cryolite melt as a graphite substrate was seen to be completely wetted by a cryolite melt in the presence of metallic Al. It can be argued that the factor inducing the wettability when Al metal is present is in principle the same factor that induced wettability when the carbon cathode sample was cathodically polarized during the test in only molten electrolyte. In this case, the Na activity is inherent to the chemical equilibria between the electrolyte and molten Al represented by Equation 2.3.

Na activity is also initiated during the cathodic polarization represented by Equation 2.2. In both cases, the Na activity results in Na intercalation in the carbon initiated at the surface of the carbon materials. Electrolyte penetration without the application of an electric field was also observed for carbon materials placed in a cryolite melt in equilibrium with molten Al by Tschöpe et al. [14]. Impregnation of electrolyte into the carbon material is a confirmation that the carbon material is wetted by the electrolyte when molten Al is in equilibrium with the electrolyte. This is because

wettability between the carbon cathode and the molten electrolyte is a pre-requisite for the electrolyte penetration into the carbon cathode [24]. Figure 5.9b demonstrates that cathodic polarization of the carbon cathode sample in the presence of molten electrolyte and Al does not change the wettability. It can, therefore, be inferred from these findings that what is needed for improved wettability and the consequent melt penetration is sufficient formation of Na to change the surface properties of the carbon material.

The slight increase in weight of the carbon samples after the emersion cycles where no polarization has occurred as shown in Figure 5.9a is due to the penetration of electrolyte into the carbon cathode material. It is important to notice, however, that the amount of electrolyte that penetrated the carbon material is significantly lower than the amount of electrolyte observed to penetrate the carbon material during the cathodic polarization stage of the test in the molten electrolyte (see Figure 5.6). This significant difference can be explained by the nature of the chemical reaction leading to the formation of Na. During polarization, Na is produced at the electrolyte-carbon interface enhancing the infiltration of the carbon material, while in the case with Al in equilibrium with the electrolyte, Na is produced at the electrolyte-Al interface and Na diffusion is necessary for Na to reach the carbon-electrolyte interface.

The experiments performed with mainly molten Al and a 10 mm layer of electrolyte, to mitigate the effect of the stable oxide layer formed around the metal, demonstrated that the carbon cathode was not wetted by molten Al. The corrected weight of the carbon samples was negative, clearly demonstrating that the molten Al does not wet carbon, see Figure 5.10a. The observation of non-wettability between the carbon cathode and molten Al is consistent with observations by other researchers [21, 104]. The wetting contact angle values measured by these researchers [21, 104] suggested an almost perfect de-wetting scenario between the carbon cathode and molten Al. The wetting test results also showed that the cathodic polarization of the carbon samples did not change the wettability confirming the findings by Utigard and Toguri [104]. Considering the non-wettability of the carbon cathode material by the molten Al as compared to the wettability by the molten electrolyte when Na activity is initiated, the carbon cathode materials would always be preferentially coated by a layer of molten electrolyte when the factors responsible for Na activity are present. It is thus proposed that in the presence of a cryolitic melt, such as the molten electrolyte, no level of direct contact can be established between the carbon cathode material and the molten Al metal. This is consistent with the autopsy observations where virtually no level of direct contact was seen between the carbon cathode and Al metal.

The non-wettability by the liquid Al metal and the perfect wettability by the molten electrolyte during electrolysis conditions, as shown by the present wetting experiments, prove that there will always be a film or layer of molten electrolyte covering the carbon cathode surface. The results also confirm that the formation of Al_4C_3, as shown in Figure 5.16, does not take place by a direct chemical reaction

between carbon and Al. However, the direct contact between the electrolyte and carbon cathode suggest the electrolyte plays an important role in carbide formation. The Al needed for the reaction could be supplied by Al containing entities within the electrolyte. Moreover, Na produced from the equilibrium reaction in Equation 2.3 can react with the Al-containing entities within the electrolyte and carbon to form Al_4C_3 according to the reactions represented by Equations 2.6 and 2.9. The reactions do not require metallic Al to form the carbide.

The observed film of frozen electrolyte between aluminium carbide and Al on the wetted sample, as shown in Figure 5.16, supports the existence of a layer of electrolyte covering the cathode surface during operation.

6.2. Autopsies

6.2.1 Macroscopic Observation

The W wear pattern observed on pots 2, 4 and 5 is a confirmation of previous autopsy findings [3, 9, 10, 39], and it demonstrates high wear at the carbon cathode block ends of the spent potlinings and low wear at the centre channel. The proximity of fresh bath and fast transport rates resulting from high current densities facilitates carbide dissolution and transport into the bulk bath, consequently, resulting in high wear at the cathode block ends. Low current densities, slow transport rates and possible deposition of sludge are among the factors considered to cause the low wear at the centre channels [50].

The WW wear pattern identified for prebaked pots 1 and 3 does also confirm findings from previous autopsies [11, 50]. An inner W wear pattern close to the centre channel was observed in addition to an outer W wear pattern close to the cathode block ends. The outer W wear pattern is explained by the same mechanisms discussed in the previous paragraph. The inner W wear has been proposed to occur due to the periodic removal and renewal of a sludge layer close to the centre channel during the overfeeding-underfeeding cycles of electrolysis cells equipped with alumina point feeders at the centre channel [19].

The cathode block 1 of pots 1 and 3, which was located at the tapping section, displayed the highest wear at the centre channel as compared to the other cathode blocks. This high wear is attributed to the convection patterns generated during metal tapping as it facilitates bath transport from the cathode surface and carbide dissolution. The low wear observed along the surface of cathode block 19, which was located at the off-gas suction point of pots 1 and 3, is attributed to low metal

movement at the off-gas suction section of the pots and, consequently, colder lining (and lower superheat).

The relatively uniform wear, as well as almost no wear difference at the cathode block ends, which fell outside the anode shadows of the Søderberg pot, confirms the importance of current density to the cathode wear. A relatively even current distribution on the cathode due to the lower electrical conductivity of the cathode (less graphitic), will result in less variation in electrochemical wear. Furthermore, this pot was run on a relatively higher Al metal pad and had a relatively large deposit of sludge (see Figure 4.59a). The high metal pad could contribute to a lower metal pad velocity resulting in lower exchange of bath on the carbon cathode surface and consequently low wear due to reduced carbide dissolution and transport. Moreover, the relatively large deposits of sludge could contribute to lower the wear on the cathode surface where it settles. The low wear due to sludge deposit on the carbon cathode surface is proposed to occur by a reduction in access to fresh bath for the dissolution and transport of carbide layer due to the stable sludge layer on top of the aluminium carbide. The low wear at locations with sludge is also explained by the high electrical resistance of sludge [54]. Finally, abrasive wear by sludge on the cathode surface is assumed not to play an important role in cathode wear as it probably doesn't move much [54].

The presence of a layer of electrolyte, covering the cathode surface (see Figures 4.1 and 4.2), and the complete infiltration of the carbon cathode materials by the bath (Figure 4.6) are in line with previous autopsies [3, 9, 11, 38, 114]. The layer of electrolyte was measured to be about 640±300 μm, suggesting variations in the thickness across the cathode surface. The observations are also in line with the wetting experiments presented in Chapter 5. The investigation of wetting demonstrated that the carbon cathode is coated by a layer of electrolyte due to the better wettability of the carbon cathode by the molten electrolyte relative to molten Al. Furthermore, the coating of electrolyte on the carbon cathode will prevent any direct contact between Al metal and carbon cathode. Preferential wetting of the carbon cathode by the molten electrolyte at electrolysis conditions is therefore proposed based on all these observations.

The formation of aluminium carbide directly from Al and C as shown by Equation 2.5 is thermodynamically favourable at all operating conditions. However, the observation of a layer of electrolyte on top of the carbide layer, evidenced by Figure 4.1c, demonstrate that the formation of Al_4C_3 does not occur through a direct contact between carbon and Al. This is also supported by the wetting experiments (Figure 5.16). The absence of wetting between Al and the carbon cathode imply that the carbide formation process would require the transport of either the carbon or Al through the electrolyte layer. The electrolyte already contains Al-containing entities like AlF_3 and transport of Al to the surface is thus favourable compared to transport of C. Thus, Al-containing entities will be transported through the electrolyte to form

aluminium carbide in a reaction with the carbon cathode. Equation 2.6 and 2.9 demonstrate aluminium carbide formation by the electrolyte and the carbon cathode. The equation shows that aluminium carbide formation occurs through a reaction between the Al-containing components such as AlF_3 within the electrolyte and the carbon cathode. Thus, metallic Al is not involved in the reaction which explains the observation of a carbide layer on the cathode surface with an electrolyte layer on top.

The relatively large amount of solidified bath within the porosity of the ramming joints, as compared to the carbon cathode blocks, reflects the higher degree of open porosity in the ramming joints. The wetting experiments presented in Chapter 5 showed that all the different types of carbon cathode materials were penetrated with the electrolyte within seconds of cathodic polarization. These observations confirm wetting as a prerequisite for electrolyte penetration into the carbon material. The carbon materials with large open porosities were observed to be penetrated by higher amounts of electrolyte than those with small open porosities. The high amount of electrolyte due to higher porosity of the ramming joints relative to the denser cathode blocks may account for the lower wear observed at the ramming joints. The electrolyte has a higher electrical resistivity than carbon [2, 3, 110, 111]. Thus, a large amount of electrolyte within the porosity, will add to the already high electrical resistivity of the ramming joint material relative to the carbon cathode block and reduce the electrical current passing through the region with the ramming joints and reduce the current density in this region. It is proposed that the reduced current density would then result in low electrochemical wear.

The observations of potholes on the carbon cathode surface are consistent with other autopsies and studies on potholes formation [3, 115]. Most of the potholes identified from the autopsies were located close to the cathode block ends of the spent potlinings as shown in Figure 4.4c. The cathode block ends of the prebaked pots are known to have higher current densities, thus the presence of potholes at these locations could suggest that current density plays a role in their formation. Potholes are also said to form from clusters of small-sized potholes as shown in Figure 4.4a. A pothole that led to the tapout of pot 3 is displayed in Figure 4.32. Pitting was observed all over the cathode surface where the pothole is located. Furthermore, close observation of the cathode surface at the locations with potholes as shown in Figure 4.5 showed a high degree of pitting. The continuous presence of pitting at locations with very high wear such as pothole locations and the cathode block end, as was observed for all the autopsies conducted, suggest they play an important role in the carbon cathode wear mechanism.

6.2.2 Pitting

Pitting is a term commonly used in the subject of corrosion where it stands for a localized form of corrosion that produces sharply defined cavities or holes within a material [116]. Pitting was identified on all the spent potlinings investigated. It was observed all over the carbon cathode surface of the spent potlinings lined with graphitic cathode blocks and at the cathode block end of those lined with graphitized cathode blocks. The ramming joints between the cathode blocks were also seen to show pitting. Locations with higher wear, such as the cathode block ends, were observed to show larger pittings for the graphitic cathode blocks.

Pitting on the carbon cathode surface has been proposed to occur by a mechanism involving particle detachment as illustrated by Figure 2.10 [16-18]. The hypothesis suggests that the pitting observed on the carbon cathode surface results from voids created by detached aggregates owing to the preferential weakening of the binder matrix as shown in Figure 2.10. If pitting is formed from the voids created by detached aggregates, it should be expected to see a strong correlation between the average aggregate size and the average size of the pitting. Comparison of the average aggregate size and pitting size in this study did, however, not yield any correlation (see Chapter 4). This demonstrates that the pitting examined on the spent potlinings reported in the present thesis did not result from a particle detachment mechanism.

Overlapping and clustered pitting observed at the same location of the cathode surface on the spent potlinings (see Figures 4.19 and 4.34) suggest that new pittings begin to form overlapping with already existing pittings. Thus, the pitting process does not continue indefinitely but stops, allowing new pittings to form close to or overlapping existing locations. This observation, therefore, supports an initiation and a termination mechanism in the wear process.

The differences in the occurrence of pitting on the cathode surface of pots 2, 4 and 5 with graphitic cathode blocks and pots 1 and 3 with graphitized cathode blocks may be explained by the differences in electrical conductivity. Increased current density at the ends of the cathode blocks is directly dependent on the electrical conductivity of the cathode blocks given the same cathode block and collector bar arrangements [12]. The relatively high electrical conducting graphitized cathode blocks would experience an uneven current distribution with the high current densities at the block ends and low current densities at the centre channel area. Contrarily, the relatively lower electrical conductivity of the graphitic cathode blocks would cause a relatively even current density distribution over the cathode surface. The relatively even current density of the graphitic cathode blocks will help even out the pitting occurrence on the cathode surface, while the graphitized cathode blocks due to the peaking of current density at the ends show pitting mostly at their ends.

Moreover, the differences in pitting size between the pitting at the cathode block ends and the centre channel area observed on pots 2 and 4 may also be explained by current densities differences. Despite the relatively even current density distribution over the cathode surface of graphitic cathode blocks relative to the graphitized cathode blocks as mentioned in the previous paragraph, a relatively higher current density can still be expected at the ends of the cathode blocks relative to the centre channels. The high current densities at the cathode block ends will lead to an increase in carbide formation by the electrochemical mechanism. Furthermore, the high current density will induce faster transport rates, leading to faster carbide dissolution and transport away from the cathode surface.

6.2.3 Microscopic Observation

The CT images and the optical micrographs demonstrated clearly the presence of remains of partly eroded carbon aggregates within the carbon matrix at the wear surface at the carbon-electrolyte interface. Remains of partly worn-out carbon aggregates with relatively smooth surfaces within the carbon matrix point to a chemical wear process. Physical or mechanical wear resulting from weaknesses in the carbon material due to the preferential attack of the binder matrix would result in detachment of aggregates from the carbon matrix thereby leaving no remains of the aggregates within the carbon matrix. Moreover, the relatively uniform wear surface suggests there was no preferential wear as such wear would have resulted in an uneven wear surface visible at low magnification. Additionally, the chemical wear process is supported by the wear surface seen at high magnification as shown in Figures 4.12 and 4.58. The wear surface is characteristic of a chemical attack and suggests a gradual chemical etching of the aggregate component within the carbon matrix. These observations suggest that the pitting on the cathode surface does not originate from a physical or mechanical detachment process.

Optical micrographs and element mapping of samples collected from the Søderberg pot, like the one shown in Figure 4.59, displayed a phase rich in alumina on top of the aluminium carbide layer. This alumina rich layer on top of the carbide layer may retard the cathode wear as discussed above

6.3. Initiation and Termination Mechanisms of Cathode Wear

The wetting tests have confirmed the presence of a layer of electrolyte between the metal pad and the carbon cathode surface. The basic nature of the solidified bath in contact with the cathode surface was also confirmed by the phases identified on the cathode surface and within the spent potlining. As shown in Figures 4.15 and 4.26, CaF_2, Na_3AlF_6 and Al_2O_3 were observed for the bath collected from the cathode surface and potholes whereas the acidic compounds $NaCaAlF_6$ and $Na_5Al_3F_{14}$ were observed in addition to Al_2O_3 and Na_3AlF_6 in the bulk bath. The basic nature of the solidified bath in contact with the cathode surface was confirmed by the phases identified within the spent potlining as displayed in Figures 4.27 and 4.49. The Figures reveal a trend of increasing NaF content and a corresponding decrease in Na_3AlF_6 content down the spent potlinings. The increasingly basic nature of the penetrating electrolyte within the spent potlining can be explained by the reactions occurring within the cathode lining.

According to the ternary phase diagram Na_3AlF_6-AlF_3-CaF_2 provided by Craig and Brown [117], shown in Figure 6.1, the phases identified for the bulk bath represent the typical solidified electrolyte used in the industry. The fact that these phases are not observed on the cathode surface supports the hypothesis that the bath on the cathode surface is depleted on AlF_3. As illustrated in the figure, the consumption of AlF_3 shifts the bath composition towards the CaF_2-Na_3AlF_6 binary Alkemade line in the ternary phase diagram. Thus, the presence of these two primary crystallization phases within a bath sample suggests that it is depleted in AlF_3 relative to the bulk electrolyte. The depletion of AlF_3 on the carbon cathode surface is expected based on a predominating reaction between carbon and bath.

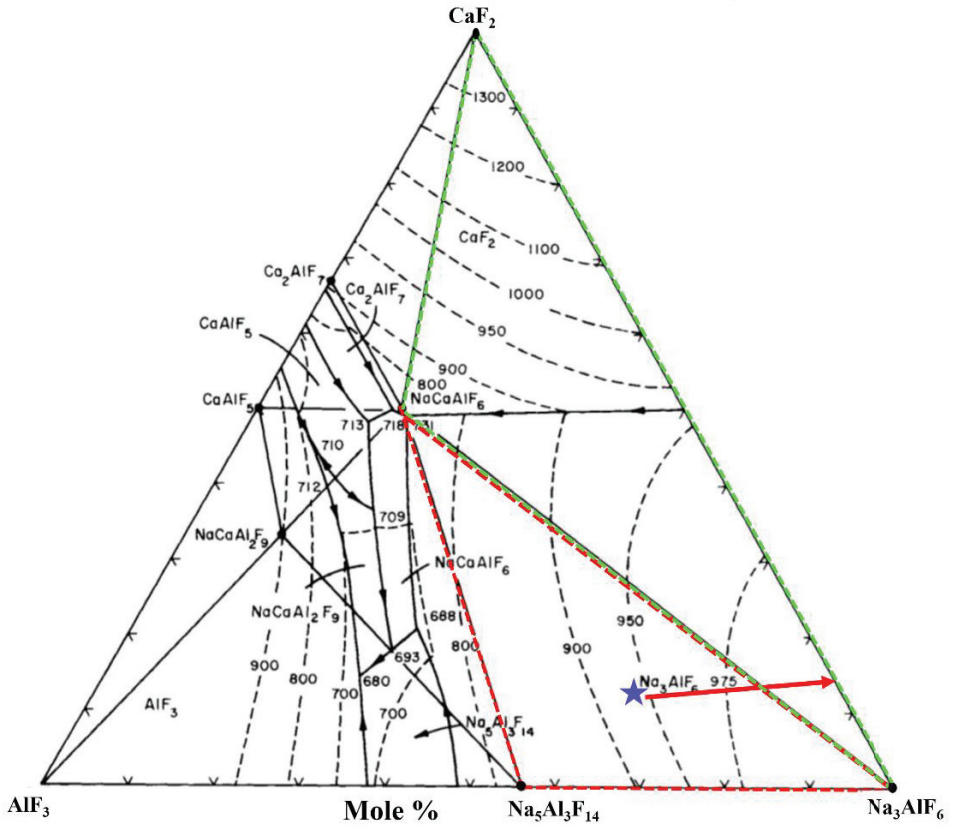

Figure 6.1. Ternary diagram of the Na_3AlF_6-AlF_3-CaF_2 system [117]. Redrawn with permission from Springer Copyright © 1980. Red and green Alkemade triangles show the phases of the bulk and cathode surface baths. Blue star represents the industrial electrolyte composition (Na_3AlF_6-64 mol%, AlF_3-23 mol%, CaF_2- 13 mol%). The red arrow shows the direction of composition change from bulk bath to cathode surface bath.

Variations in the bath chemistry from acidic to relatively basic at the cathode surface indicates the importance of the continuous exchange of bath on the cathode surface for cathode wear. A continuous supply of fresh acidic bath to replace the basic bath on the cathode surface would be required for the wear process to be sustained. The maximum aluminium carbide solubility in the cryolite melt occurs at a cryolite ratio (CR) of 1.8. A continuous supply of fresh acidic bath to the cathode surface would sustain the supply of aluminium ions to the cathode surface for the cathode wear process to continue. Without the perpetual supply of fresh acidic bath and the accompanying aluminium ions, the cathode wear process would be expected to slow down or even stop. AlF_3 is consumed to produce aluminium carbide as shown in Equation 2.6 and 2.9 and to dissolve the carbide layer as shown in Equation 2.7, thus, these reactions will not take place without sufficient concentration of AlF_3 in the bath. Moreover, the ternary phase diagram Na_3AlF_6 - AlF_3 - CaF_2 (Figure 6.1) shows that the liquidus temperature of the bath increases as it becomes depleted in AlF_3. The

composition moves away from the blue star in the direction of the red arrow in the figure. Depletion of AlF_3 will, therefore, result in solidification of the electrolyte at the cathode surface if the bath temperature is not above the liquidus temperature of the composition depleted in AlF_3. Freezing of electrolyte on the cathode surface will slow down or even stop the cathode wear process. The slow down or halting of the cathode wear process due to the electrolyte freezing is proposed due to the low current conductivity of the solid electrolyte as compared to the molten electrolyte. Due to the electrochemical nature of cathode wear, a constant flow of electrical current would be needed for the process to continue. Hence a reduction or termination of the current flow is suggested to slow down or stop the wear process. Dissolution and transport of the carbide, which are important steps in the wear process, will also be strongly affected by solidification of the molten electrolyte.

Based on the present work an initiation and termination process of the cathode wear process is proposed as follows:

1. The formation and dissolution of Al_4C_3 are favoured by available AlF_3 in the molten electrolyte present at the cathode surface.
2. The local consumption of AlF_3 due to the formation of Al_4C_3 results in a more basic bath, which also reduces the dissolution of Al_4C_3 at the surface due to the lower solubility of Al_4C_3 in the basic bath.
3. The reduced content of AlF_3 results in an increased liquidus temperature, which will lead to partial or complete solidification of the molten bath close to the cathode surface.
4. Frozen electrolyte on the carbon cathode surface will terminate or drastically slow the wear process.
5. Supply of fresh molten bath with a higher AlF_3 content will restart the wear process through re-melting of the frozen bath, enhanced carbide formation and dissolution as well as increased electrical conduction. Increased cathode surface temperature and hot running cells can also re-melt the frozen bath and restart the wear process.

Finite element method simulations of the current distribution on a cathode surface covered by a layer of partly solidified electrolyte were performed to give additional support for the hypothesis described above. The model and the distribution of the current densities obtained from the simulation are displayed in Figure 6.2. The results demonstrate that the current density along the cathode block is close to zero at the locations with the frozen bath. The findings suggest that the cathode wear process could be terminated at locations with frozen electrolyte with potentially higher Joule heating around the frozen bath facilitating new wear positions.

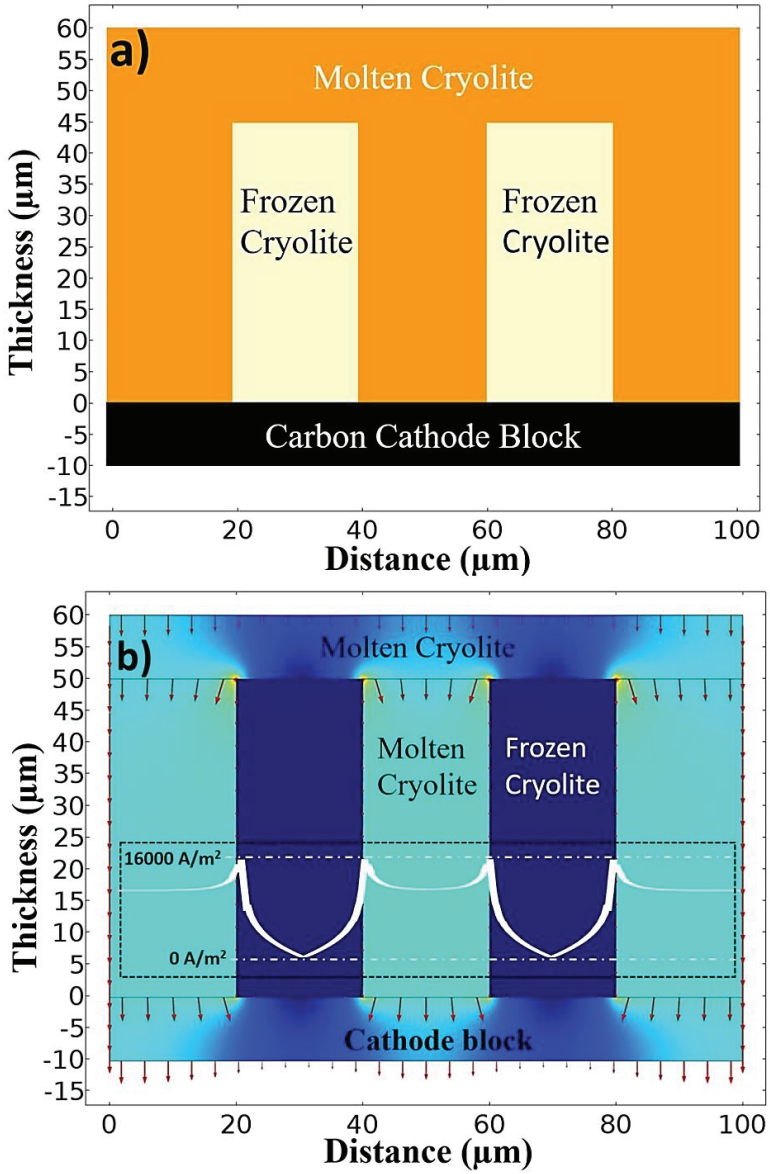

Figure 6.2. Finite element simulation. a) The geometry of the frozen bath used in the simulation. b) Simulation results, red arrows show the current density distribution, colours represent the magnitude of the current density (blue is low, and red is high), insert is the current density distribution along the carbon cathode block.

7

Chapter 7. Conclusions

The cathode wear of the spent carbon cathode bottom lining was investigated by autopsies. Macroscopically, a wear pattern characterized by pitting was observed on all the carbon cathode surfaces of the spent potlinings investigated. The presence of pitting on all types of carbon cathode materials irrespective of the degree of graphitization demonstrate that the formation mechanism(s) of pitting does not depend on the type of carbon material. The appearance of pitting all over the cathode surfaces of graphitic cathode blocks and the higher occurrence at the ends of graphitized cathode blocks, where the wear is highest, point to the importance of cathode current density distribution for pitting formation. The relatively uniform cathode current density distribution on graphitic blocks results in a more even pitting all over the surface. The graphitized blocks had pitting mostly concentrated at their ends due to the peaking of the current densities in this region.

A relatively uniform and smooth surface topography of pitting cavities, observed by X-ray tomography and optical microscopy, suggests that pitting results from a non-preferential chemical/electrochemical corrosion of the aggregate and binder matrix with no evidence of aggregate or particle detachment. Overlapping and clustered pittings observed in the same region of the cathode surface gave support for proposing a hypothesis describing an initiation and termination mechanism of the cathode wear process. Powder X-ray diffraction patterns from solidified bath samples collected from the cathode surface and bulk bath revealed phases distinct to a relatively basic bath on the cathode surface as compared to the bulk bath. Solidification of the basic bath due to its higher liquidus temperature, combined with the low driving force for Al_4C_3 formation and dissolution in the basic bath, provide a physical explanation for the termination of the wear process. A finite element simulation method was performed to support the proposed hypothesis, and the simulations revealed a reduction in current density in regions of the cathode surface covered with frozen bath.

The wettability of the carbon cathode material by the molten electrolyte and aluminium was investigated by the immersion/emersion technique. The study was motivated by the presence of a film of electrolyte between the metal pad and carbon cathode surface observed in the autopsies. The laboratory investigation demonstrated that neither the molten electrolyte nor the liquid aluminium wets the carbon cathode. However, upon cathodic polarization of the carbon cathode material, the molten electrolyte was observed to rapidly wet and penetrate the carbon material. Higher amounts of electrolyte penetrated the more amorphic carbon materials relative to the less amorphic carbon materials. Molten aluminium, on the other hand, was observed

to remain non-wetting to the carbon cathode material even after the cathodic polarization of the carbon material. The molten electrolyte was also noticed to wet and penetrate the carbon materials when it was in equilibrium with molten Al without any form of cathodic polarization of the carbon material. The laboratory tests also confirmed that with the conditions present in an aluminium electrolysis cell, where a liquid Al metal and a cathodically polarized carbon cathode bottom lining are present, a layer or film of the molten electrolyte will always be in direct contact with the carbon cathode due to the enhanced wetting these conditions provide between them.

The present thesis has focused on the local macroscopic and microscopic wear pattern in contrast to previous studies, which has mainly been concentrated on the global macroscopic wear pattern. The findings made from the autopsies and laboratory investigations have shown that pitting on the cathode surface form from chemical/electrochemical corrosion processes involving carbide formation, dissolution and transport and which is likely enhanced by high current densities. Furthermore, it has been shown that an electrolyte film will always be in contact with the carbon cathode in an electrolysis cell due to improved wetting between the electrolyte and carbon cathode provided by the electrolysis conditions.

8

Chapter 8. Outlook

This thesis has shown that carbon cathode wear is characterized by pitting on the carbon cathode surface with locations of high wear showing the most pronounced pitting. The increased presence of pitting at locations of high current densities on the cathode blocks suggests that cathode current density distribution plays a major role in the pitting kinetics on the cathode surface. A more evenly distributed cathode current density is expected to result in a more evenly distributed pitting on the cathode surface as well as reducing the locations with very high wear rates that lead to pothole formation and tapout. Efforts, such as copper inserts in the current collector bars, variable resistivity cathode blocks, etc. can help to even out the cathode current density distribution and, consequently, reduce the most severe wear.

The circular geometry of the pitting observed in this work is not thoroughly explained. Thus, further, work to understand the geometry of pitting cavities on the cathode surface is needed. Systematic studies of pitting on the carbon cathode surface employing techniques such as computer simulations may help to enhance the understanding of the evolution of pitting and the circular geometry of the small cavities.

The need for a high-magnification chemical elemental mapping of the electrolyte coating observed in the pitting is recommended to confirm the gradient in acidity and freezing of bath/electrolyte against the cathode surface. Variations in the chemistry of the electrolyte will affect the proposed cathode wear process since acidic bath leads to more wear while basic bath leads to less wear. The presence of overlapping pitting in the same region on the cathode surface is likely explained by the initiation and termination mechanism brought about by the variations in bath/electrolyte chemistry. Rapid or enhanced exchange of bath at the cathode surface is believed to increase the wear rate. Thus, factors that contribute to reduced metal/bath velocities such as magnetic compensation, may help reduce the exchange rate of the bath at the cathode surface.

It is evident from the tests and autopsies presented in this thesis that a film of electrolyte that enhances cathode wear through aluminium carbide dissolution and transport from the cathode surface exists on the carbon cathode. Consequently, another possible solution that may drastically reduce the wear process is to introduce a cathode material that is better wetted by the molten Al than the electrolyte. Such a cathode material would provide direct contact between the current conductor and the Al cathode, thereby eliminating the film of electrolyte that currently exists between

them. Efforts to avert or reduce cathode wear should, therefore, include the study of cathode materials preferentially wetted by the molten Al.

It is also evident that maintaining good temperature control, both in the cell and at the carbon cathode surface will help reduce cathode wear.

Finally, the present work gives support to the electrochemical nature of carbon cathode wear, nevertheless, the actual electrochemical reactions leading to the formation of aluminium carbide are still not fully understood. Thus, further investigations to fully understand the actual electrochemical reactions taking place are recommended.

Chapter 9. Bibliography

[1] World Aluminium Organization *Primary Aluminium Production* (2018), http://www.world-aluminium.org/statistics/#data.
[2] J. Thonstad, P. Fellner, G.M. Haarberg, J. Hives, H. Kvande, A. Sterten. *Aluminium Electrolysis: Fundamentals of the Hall-Héroult Process*, 3rd ed., Aluminium-Verlag Marketing and Kommunikation GmbH, Düsseldorf, 2001.
[3] M. Sørlie, H.A. Øye. *Cathodes in aluminium electrolysis*, 3rd ed., Aluminium-Verlag, Düsseldorf, 2010.
[4] K. Grjotheim, H. Kvande. *Introduction to Aluminium Electrolysis: Understanding the Hall-Heroult Process*, 2 ed., Aluminium-Verlag, Dusseldorf, 1993.
[5] H. Kvande, P.A. Drabløs. "The Aluminum Smelting Process and Innovative Alternative Technologies," *JOEM 56* (2014), pp. S23-S32.
[6] L. Rivoaland. "Development of a New Type of Cathode for Aluminium Electrolysis," *ICSOBA 41* (2016), pp. 757-765.
[7] O. Martin, B. Allano, E. Barrioz, Y. Caratini, A. Escande, N. Favel. "Low Energy Cell Development on AP Technology (TM)," *Light Metals* (2012), pp. 569-574.
[8] S.Y. Larsen, X.A. Liao, H. Gran, S. Madshus, J.A. Johansen. "Development of High Density Graphitized Cathode Blocks for Aluminium Electrolysis Cells," *Light Metals* (2010), pp. 835-840.
[9] A.T. Tabereaux, J.H. Brown, I.J. Eldridge, T.R. Alcorn. "Erosion of cathode blocks in 180 kA prebake cells," *Light Metals* (1999), pp. 187-192.
[10] P. Reny, S. Wilkening. "Graphite cathode wear study at Alouette," *Light Metals* (2000), pp. 399-404.
[11] E. Skybakmoen, S. Rørvik, A. Solheim, K.R. Holm, P. Tiefenbach, Ø. Østrem. "Measurement of Cathode Surface Wear Profiles by Laser Scanning," *Light Metals* (2011), pp. 1061-1066.
[12] J.M. Dreyfus, L. Joncourt. "Erosion mechanisms in smelters equipped with graphite blocks - A mathematical modeling approach," *Light Metals* (1999), pp. 199-206.
[13] K. Vasshaug. *The influence of the formation and dissolution of aluminium carbide on the cathode wear in aluminium electrolysis cells*, PhD thesis, Norwegian University of Science and Technology, Trondheim, 2008.
[14] K. Tschöpe, A. Støre, A. Solheim, E. Skybakmoen, T. Grande, A.P. Ratvik. "Electrochemical Wear of Carbon Cathodes in Electrowinning of Aluminum," *Jom-Us 65 (11)* (2013), pp. 1403-1410.
[15] M.B. Dell, R.W. Peterson, J.N. Rumble. "Formation of Potholes in Bottom Linings of Hall Cells," *JOM 20 (9)* (1968), pp. 55-58.
[16] E.F. Siew, T. Ireland-Hay, G.T. Stephens, J.J.J. Chen, M.P. Taylor. "A study of the fundamentals of pothole formation," *Light Metals* (2005), pp. 763-769.
[17] P. Rafiei, F. Hiltmann, M. Hyland, B. James, B. Welch. "Electrolytic degradation within cathode materials," *Light Metals* (2001), pp. 747-752.

[18] P. Patel, M. Hyland, F. Hiltmann. "Influence of internal cathode structure on behavior during electrolysis part II: Porosity and wear mechanisms in graphitized cathode material," *Light Metals* (2005), pp. 757-762.
[19] A. Solheim. "Some Hypotheses Concerning Cathode Wear in Aluminium Electrolysis Cells," *MetSoc's Annual Conference of Metallurgists* (2011), pp. 135-142.
[20] M. Sørlie, H.A. Øye. "A Survey on Deterioration of Carbon Linings in Aluminum Reduction Cells," *Metall 36 (6)* (1982), pp. 635-642.
[21] R.C. Doward. "Reaction between aluminium and graphite in the presence of cryolite," *Met Trans B 4 (1)* (1973), pp. 386-388.
[22] R. Ødegard, A. Sterten, J. Thonstad. "On the Solubility of Aluminum in Cryolitic Melts," *Met Trans B 19 (3)* (1988), pp. 449-457.
[23] P. Brilloit, L.P. Lossius, H.A. Oye. "Melt Penetration and Chemical-Reactions in Carbon Cathodes during Aluminum Electrolysis .1. Laboratory Experiments," *Light Metals 1993* (1993), pp. 321-330.
[24] H. Kvande, Z.X. Qiu, K.S. Yao, K. Grjotheim. "Penetration of Bath into the Cathode Lining of Alumina Reduction Cells," *Light Metals* (1989), pp. 161-167.
[25] M. Barber, A. Tabereaux. "The End of an Era for Søderberg Technology in North and South America," *Light Metals* (2014), pp. 809-814.
[26] W. Alsayed, A.M. Al Riyami, M. Al Hammadi, I.O. Al Ali, V.C. Pillai, A.H.A.M. Al Zarouni, S. Akhmetov, M. Reverdy, N. Ahli. "World's Longest Potline Start-up at EMAL," *Light Metals* (2015), pp. 505-510.
[27] M. Fabbri. "Rectifier Operation During Potline Aluminium Electrolysis," *36th International Course on Process Technology of Aluminium* (2018), pp. 311-336.
[28] Norsk Hydro ASA, *Primary Aluminium Production* (2018), https://www.flickr.com/photos/norskhydro/45985341901/.
[29] K.Å. Rye. "Bath Composition " *36th International Course on Process Technology of Aluminium* (2018), pp. 35-49.
[30] H. Kvande. "Bath Compositions for Al Production," *The 17th Course on Fundamentals and their Applications in Aluminium Production* (2013), pp. 41-65.
[31] K.H. Kochling, B. Mcenaney, F. Rozploch, E. Fitzer. "International Committee for Characterization and Terminology of Carbon - 1st Publication of 30 Tentative Definitions," *Carbon 20 (5)* (1982), pp. 445-449.
[32] A. Yurkov. *Refractories for Aluminium: Electrolysis and the Cast House*, Springer International Publishing, Switzerland 2015.
[33] R. Fourcault, B. Samanos. "2nd Australasian Aluminium Smelter Technology Course, Sydney," (1987).
[34] H. Marsh, J. Griffiths. "New Processes and New Applications," *International Symposium on Carbon* (1982), pp. 81.
[35] M. Sørlie, J. Hvistendahl, H.A. Øye. "Early Failure Mechanisms in Aluminum Cell Cathodes," *Light Metals* (1993), pp. 299-308.
[36] M. McClung, R. Zerkle. "Autopsy procedures and results at Century Aluminum of West Vriginia," *Light Metals* (2004), pp. 213-218.
[37] R. Jeltsch. "Use of Cell Autopsy to Diagnose Potlining Problems," *Light Metals* (2009), pp. 1079-1084.

[38] K. Tschöpe, C. Schøning, T. Grande. "Autopsies of Spent Pot Linings - a Revised View," *Light Metals* (2009), pp. 1085-1090.
[39] D. Lombard, T. Beheregaray, B. Feve, J.M. Jolas. "Aluminium Pechiney experience with graphitized cathode blocks," *Light Metals* (1998), pp. 653-658.
[40] C. Krohn, M. Sørlie, H.A. Øye. "Penetration of Sodium and Bath Constituents into Cathode Carbon Materials used in Industrial Cells," *Light Metals* (1982), pp. 953-959.
[41] M.B. Dell. "Reactions between Carbon Linings and Hall Bath. ," *Extractive Metallurgy of Aluminium 2* (1963), pp. 403-416.
[42] E.W. Dewing. "The action of Sodium with Nano-Graphitic Carbon: Reactions Occuring in the Lining of Alumina Reduction Cells," *Transaction of the Metallurgical Society of AIME 227* (1963), pp. 1328-1333.
[43] J. Mittag, E. Bernhauser, H. Friedli. "Sodium, Its Influence on Cathode Life in Theory and Practice," *Light Metals 1992* (1991), pp. 789-793.
[44] K. Tschöpe, C. Schøning, J. Rutlin, T. Grande. "Chemical Degradation of Cathode Linings in Hall-H,roult Cells-An Autopsy Study of Three Spent Pot Linings," *Met Trans B 43 (2)* (2012), pp. 290-301.
[45] J.G. Hop. *Sodium Expansion and Creep of Cathode Carbon*, PhD thesis, Norwegian University of Science and Technology, Trondheim, 2003.
[46] A.P. Ratvik, A. Støre, A. Solheim, T. Foosnaes. "The effect of current density on cathode expansion during start-up," *Light Metals* (2008), pp. 973-978.
[47] Y. Mikhalev, H.A. Øye. "Absorption of metallic sodium in carbon cathode materials," *Carbon 34 (1)* (1996), pp. 37-41.
[48] P. Thomas, D. Billaud. "Electrochemical insertion of sodium into hard carbons," *Electrochim Acta 47 (20)* (2002), pp. 3303-3307.
[49] P. Thomas, D. Billaud. "Sodium electrochemical insertion mechanisms in various carbon fibres," *Electrochim Acta 46 (22)* (2001), pp. 3359-3366.
[50] Ø. Østrem. *Cathode Wear in Hall-Héroult Cells*, PhD thesis, Norwegian University of Science and Technology, Trondheim, 2013.
[51] M.B. Dell. "Potlining Failure Modes," *Light Metals* (1985), pp. 957-966.
[52] M.B. Dell. "Potlining Failures in Aluminum Electrolysis Cells," *JOM 19 (3)* (1967), pp. 14-17.
[53] L.P. Lossius, H.A. Øye. "Melt penetration and chemical reactions in 16 industrial aluminum carbon cathodes," *Met Trans B 31 (6)* (2000), pp. 1213-1224.
[54] P.Y. Geay, B. Welch, P. Homsi. "Sludge in operating aluminium smelting cells," *Light Metals* (2001), pp. 541-548.
[55] J.R. Landry, M.F. Fini, G. Soucy, M. Desilets, P. Pelletier, L. Rivoaland, D. Lombard. "Experimental Investigation of the Impact of Cathode Grade on Sludge Formation at the Cathode Block-Aluminum Interface of Hall-Heroult Cells," *Metall Mater Trans B 50 (1)* (2019), pp. 416-428.
[56] S. Wilkening, P. Reny. "Erosion rate testing of graphite cathode materials," *Light Metals* (2004), pp. 597-602.
[57] X.A. Liao, H.A. Øye. "Carbon cathode corrosion by aluminium carbide formation in cryolitic melts," *Light Metals* (1999), pp. 621-627.
[58] X.A. Liao, H.A. Øye. "Physical and chemical wear of carbon cathode materials," *Light Metals* (1998), pp. 667-674.

[59] S. Toda, T. Wakasa. "Improvement of abrasion resistance of graphitized cathode block for aluminum reduction cells," *Light Metals* (2003), pp. 647-653.
[60] K. Vasshaug, T. Foosnaes, G.M. Haarberg, A.P. Ratvik, E. Skybakmoen. "Formation and Dissolution of Aluminium Carbide in Cathode Blocks," *Light Metals* (2009), pp. 1111-1116.
[61] H. Gudbrandsen, A. Sterten, R. Ødegard. "Cathodic Dissolution of Carbon in Cryolitic Melts," *Light Metals* (1992), pp. 521-528.
[62] P. Patel, M. Hyland, F. Hiltmann. "Influence of internal cathode structure on behavior during electrolysis part III: Wear behavior in graphitic materials," *Light Metals* (2006), pp. 633-638.
[63] F. Hiltmann, P. Patel, M. Hyland. "Influence of internal cathode structure on behavior during electrolysis part I: Properties of graphitic and graphitized material," *Light Metals* (2005), pp. 751-756.
[64] Z. Wang, S. Nobakhtghalati, A. Støre, A. Solheim, K. Tschöpe, A.P. Ratvik, T. Grande. "Cathode Wear in Electrowinning of Aluminum Investigated by a Laboratory Test Cell," *Light Metals* (2016), pp. 897-902.
[65] K. Tschöpe, A. Støre, S. Rørvik, A. Solheim, E. Skybakmoen, T. Grande, A.P. Ratvik. "Investigation of the Cathode Wear Mechanism in a Laboratory Test Cell," *Light Metals* (2012), pp. 1349-1354.
[66] E. Skybakmoen, A.P. Ratvik, A. Solheim, S. Rolseth, H. Gudbrandsen. "Laboratory test methods for determining the cathode wear mechanism in aluminium cells," *Light Metals* (2007), pp. 815-820.
[67] K. Tschöpe, A. Støre, E. Skybakmoen, A. Solheim, T. Grande, A.P. Ratvik. "Critical Reflections on Laboratory Wear Test for Ranking Commercial Cathode Materials in Aluminium Cells," *Light Metals* (2013), pp. 1251-1256.
[68] X. Liao, H.A. Øye. "Method for determination of abrasion resistance of carbon cathode materials at room temperature," *Carbon 34 (5)* (1996), pp. 649-661.
[69] A. Solheim, C. Schøning, E. Skybakmoen. "Reactions in the Bottom Lining of Aluminium Reduction Cells," *Light Metals* (2010), pp. 877-882.
[70] Z.H. Wang, E. Skybakmoen, T. Grande. "Chemical Degradation of Si_3N_4-Bonded SiC Sidelining Materials in Aluminum Electrolysis Cells," *J Am Ceram Soc 92 (6)* (2009), pp. 1296-1302.
[71] Z. Wang, E. Skybakmoen, T. Grande. "Spent Si_3N_4-Bonded SiC Sidelining Materials in Aluminium Electrolysis Cells," *Light Metals* (2009), pp. 353-358.
[72] E. Skybakmoen, J. Kvello, O. Darell, H. Gudbrandsen. "Test and analysis of nitride bonded SiC sidelining materials: Typical properties analysed 1997-2007," *Light Metals* (2008), pp. 943-948.
[73] E. Hagen, M.A. Einarsrud, T. Grande. "Chemical stability of ceramic sidelinings in Hall-Heroult cells," *Light Metals* (2001), pp. 257-263.
[74] O. Paulsen, C. Schøning, O. Darell, A.P. Ratvik. "Aging of Insulating Linings in Aluminium Electrolysis Cells," *Light Metals* (2017), pp. 551-559.
[75] A. Solheim, C. Schøning. "Sodium vapour degradation of refractories used in aluminium cells," *Light Metals* (2008), pp. 967-972.
[76] C. Schøning, T. Grande. "The stability of refractory oxides in sodium-rich environments," *JOM 58 (2)* (2006), pp. 58-61.

[77] O.J. Siljan, C. Schøning, T. Grande. "State-of-the-art alumino-silicate refractories for Al electrolysis cells," *JOM 54 (5)* (2002), pp. 46-55.
[78] C. Schøning, T. Grande, O.J. Siljan. "Cathode refractory materials for aluminium reduction cells," *Light Metals* (1999), pp. 231-238.
[79] O. Siljan. *Sodium Aluminium Fluoride Attack on Alumino-Silicate Refractories*, PhD thesis, Norwegian University of Science and Technology, Trondheim 1990.
[80] Z. Wang. *Aging of Si_3N_4-bonded SiC Sidewall Materials in Hall-Héroult Cells*, PhD thesis, Norwegian University of Science and Technology, Trondheim, 2010.
[81] R. Luneng, S.N. Bertel, J. Mikkelsen, A.P. Ratvik, T. Grande. "Chemical Stability of Thermal Insulating Materials in Sodium Vapour Environment," *Light Metals* (2017), pp. 543-549.
[82] K. Grjotheim, R. Næumann, H.A. Øye. "Formation of Aluminium Carbide in the Presence of Cryolite Melts," *Light Metals* (1977), pp. 233-242.
[83] E.A. Hollingshead, J.A. Brown. "Rate of Solution of Carbon in Molten Aluminium under a Cryolite Melt," *Light Metals* (1982), pp. 625-634.
[84] A.P. Skjølsvik, J. Mittag, H.A. Øye. "Consumption of Cathode Materials due to Al_4C_3 Formation " *Aluminium 67 (67)* (1991), pp. 905-909.
[85] J.L. Xue, H.A. Øye. "Al_4C_3 Formation at the Interface of Al-Graphite and Al-Carbon/Tib_2 Composite," *Light Metals* (1994), pp. 211-217.
[86] B. Novak, K. Tschöpe, A.P. Ratvik, T. Grande. "Fundamentals of Aluminium Carbide Formation," *Light Metals* (2012), pp. 1343-1348.
[87] P. Rafiei, F. Hiltmann, M. Hyland, B. James, B. Welch. "Electrolytic degradation within cathode materials," *Light Metals* (2001), pp. 747-752.
[88] P. Patel, Y. Sato, P. Lavoie. "Determination of the Effect of Pitch-Impregnation on Cathode Erosion Rate," *Light Metals* (2011), pp. 1073-1078.
[89] K. Vasshaug, T. Foosnees, G.M. Haarberg, A.P. Ratvik, E. Skybakmoen. "Wear of carbon cathodes in cryolite-alumina melts," *Light Metals* (2007), pp. 821-826.
[90] Y. Sato, P. Patel, P. Lavoie. "Erosion Measurements of High Density Cathode Block Samples Through Laboratory Electrolysis with Rotation," *Light Metals* (2010), pp. 817-822.
[91] K. Grjotheim, O. Herstad, R. Næumann, H.A. Øye. "Aluminium Carbide and Oxy-Carbide Formation in Alumina Containing Cryolite Melts," *Light Metals* (1978), pp. 107-117.
[92] R. Keller, J.W. Burgman, P.J. Sides. "Electrochemical Reactions in the Hall-Heroult Cathode," *JOM 39 (10)* (1987), pp. A43.
[93] J. Waddington. " Processes Occuring in the Carbon Lining of an Aluminium Reduction Cell," *Extractive Metallurgy of Aluminium Vol 2* (1963), pp. 435-443.
[94] A.M. Martinez, O. Paulsen, A. Solheim, H. Gudbrandsen, I. Eick. "Wetting Between Carbon and Cryolitic Melts. Part I: Theory and Equipment," *Light Metals* (2015), pp. 665-670.
[95] Y. Yuan, T.R. Lee. *Contact Angle and Wetting Properties,* in: G. Bracco, B. Holst (Eds.) Surface Science Techniques, Springer, Berlin Heidelberg, 2013, pp.3-34.
[96] S. Stølen, T. Grande. *Chemical Thermodynamics of Materials*, 1st ed., Wiley, England, 2004.

[97] G. Deyev, D. Deyev. *Surface Phenomena in Fusion Welding Processes*, 1st ed., Taylor & Francis Group, New York, 2006.
[98] B. Schwarz, C. Elsenmenger-Sittner, H. Steiner. "Construction of a high-temperature sessile drop device," *Vacuum 82 (2)* (2007), pp. 186-188.
[99] V.S. Haslund. *Wetting Testing of cathodes for Aluminium Production* MSc thesis, Norwegian University of Science and Technology, 2017.
[100] A. Solheim, H. Gudbrandsen, A.M. Martinez, K.E. Einarsrud, I. Eick. "Wetting Between Carbon and Cryolitic Melts. Part II: Effect of Bath Properties and Polarisation," *Light Metals* (2015), pp. 671-676.
[101] H. Åsheim. *PFC Evolution in the Aluminium Production Process*, PhD thesis, Norwegian University of Science and Technology, Trondheim, 2017.
[102] J.B. Metson, R.G. Haverkamp, M.M. Hyland, J.X. Chen. "The Anode Effect Revisited," *Light Metals* (2002), pp. 239-244.
[103] Z.X. Qiu, Q.B. Wei, K.T. Yuo. "Studies on Wettability of Carbon Electrodes in Aluminium Electrolysis (I)," *Aluminium 59 (9)* (1983), pp. 670-673.
[104] T. Utigard, J.M. Toguri. *Radiographic Observation of the Hall-Heroult Electrolysis in Bench Scale Cells,* 8. Internationale Leichtmetalltagung Leoben-Wien 1987, Aluminium-Verlag, Leoben-Wien 1987, pp.133-137.
[105] C. Sommerseth. *The Effect of Production Parameters on the Performance of Carbon Anodes for Aluminium Production* PhD thesis, Norwegian University of Science and Technology, Trondheim, 2016.
[106] I.A. Eidsvaag. *The Influence of Polarization on the Wetting of Anodes in the Hall-Heroult Process*, MSc thesis, Norwegian University of Science and Technology, Trondheim, 2016.
[107] E. Hagen, *Discipline Manager, Primary Metals Technology at Hydro A.S.*, Personal Communications, e-mail support (2019).
[108] Ukrainsky Grafit Company, *Bottom Blocks,* (2019), http://ukrgrafit.zp.ua/en/masspod.
[109] Carbone Savoie, *Cathodic Products for Aluminium Industry,* (2019), https://www.carbone-savoie.com/cathode-aluminium-products/.
[110] P. Palimaka, S. Pietrzyk. "Research on the Electrical Conductivity of Fluoride Electrolytes NaF-AlF_3-CaF_2 In Liquid And Solid State," *Arch Metall Mater 59 (1)* (2014), pp. 71-75.
[111] J. Hives, J. Thonstad, A. Sterten, P. Fellner. "Electrical-Conductivity of Molten Cryolite-Based Mixtures Obtained with a Tube-Type Cell Made of Pyrolytic Boron-Nitride," *Light Metals 1994* (1994), pp. 187-194.
[112] A. Solheim, *Senior Research Scientist, SINTEF A.S.*, Personal Communications, e-mail support (2017).
[113] Z.H. Wang, A.P. Ratvik, T. Grande, S.M. Selbach. "Diffusion of alkali metals in the first stage graphite intercalation compounds by vdW-DFT calculations," *Rsc Adv 5 (21)* (2015), pp. 15985-15992.
[114] P. Reny, S. Wilkening. "Graphite cathode wear study at Alouette," *Light Metals* (2000), pp. 399-404.
[115] E.F. Siew, T. Ireland-Hay, G.T. Stephens, J.J.J. Chen, M.P. Taylor. "A study of the fundamentals of pothole formation," *Light Metals* (2005), pp. 763-769.

[116] J.R. Davis. *Corrosion: understanding the basics*, ASTM International, Materials Park, Ohio, 2000.
[117] D.F. Craig, J.J. Brown. "Phase Equilibria in the System CaF_2-AlF_3-Na_3AlF_6 and Part of the System CaF_2-AlF_3-Na_3AlF_6-Al_2O_3," *J Am Ceram Soc 63 (5-6)* (1980), pp. 254-261.

10

Chapter 10. Appendices

Appendix A- Cathode Wear Measurements

Wear patterns, potholes and bath film thickness measurement data are given in this section.

Table 10.1A. Wear depth profile measurement data for pot 1. All measurements are in centimetres.

Position	CB1	CB2	CB3	CB4	CB5	CB6	CB7	CB8	CB9	CB10
20	0	0	0	0	0	0	0	0	0	0
40	-16.5	-18	-17	-20	-16.5	-18	-20	-18	-18.5	-19.5
60	-20	-20	-27	-27	-27	-23	-23	-22	-23	-24
80	-19.5	-19	-22.8	-23	-24	-21.5	-21.3	-18.8	-17	-16
100	-16.5	-15.5	-18.5	-19	-21	-20	-18.5	-15.5	-11	-8
120	-18.5	-17.5	-21	-21.1	-22.1	-20.5	-19	-16.2	-11.6	-11.1
140	-18	-17	-20.4	-20.5	-21	-19.3	-17.5	-15.4	-9.8	-9.5
160	-19	-15.8	-19.2	-19.3	-18.5	-16.6	-14.7	-13.7	-6.1	-6.3
180	-19.5	-15	-14.5	-15.5	-15	-15	-12.5	-12	-2.5	-3
200	-20	-16.5	-15.3	-17.8	-16	-16.3	-14.4	-13.5	-4.6	-4.8
220	-19.5	-17.5	-19	-18.8	-19	-17.5	-16.3	-15	-6.8	-6.5
240	-19	-18.5	-20	-19	-21	-18	-18	-16	-10	-8.5
260	-19.5	-20	-21	-20	-22	-19.3	-19	-18	-13	-11.5
280	-20	-20.5	-22	-20.5	-22.5	-19	-20	-17.5	-15.5	-14.8
300	-18	-18.5	-20	-18.5	-21	-18	-19.5	-17	-13.8	-12.8
320	-22	-19.3	-24.5	-24.5	-24.5	-20.3	-22.5	-20.3	-15.8	-15
340	-22.5	-21.5	-28.5	-26	-27	-22.5	-24.5	-23.5	-24.5	-24.5
360	-8.5	-8.5	-19	-19	-19	-11.3	-12.5	-11.8	-8.8	-8.5
380	0	0	0	0	0	0	0	0	0	0
Position	**CB11**	**CB12**	**CB13**	**CB14**	**CB15**	**CB16**	**CB17**	**CB18**	**CB19**	
20	0	0	0	0	0	0	0	0	0	
40	-17	-14.5	-14	-14.5	-14.5	-19	-14	-11.5	-3	
60	-23.5	-19	-19	-20	-22	-27	-20.5	-23	-4.8	
80	-17.8	-16.3	-16.5	-17	-23	-24.3	-16.8	-16.5	-3.8	
100	-13.5	-13.5	-14	-14	-19.5	-21.5	-13	-10	-4.5	
120	-14.5	-15	-15.5	-16	-21	-22.5	-14	-11.3	-5	
140	-10.9	-10.1	-11	-12.5	-18.9	-19.1	-12.4	-9.5	-3.8	
160	-7.4	-7.1	-8.3	-10.3	-15.9	-16.6	-10.2	-6	-2.3	
180	-4	-4	-5.5	-8	-13	-14	-8	-2.5	-2	
200	-7	-6.5	-7.1	-9.8	-14.1	-15.8	-10.5	-5	-2.3	
220	-9.5	-9	-8.8	-11.5	-15.3	-16.5	-12	-7.5	-3.3	
240	-11	-11.5	-10	-13.5	-17.3	-17.3	-14	-9.6	-3.8	
260	-13.5	-14	-12	-15	-18.5	-19	-18	-12.5	-4.5	
280	-15.8	-15	-15.5	-16	-19.5	-22	-22.5	-14.8	-5.3	
300	-14	-11.5	-12	-13.5	-17	-20	-20	-14	-4.5	
320	-18	-14	-14.5	-16	-19	-23.5	-23.5	-19.3	-5.5	
340	-22	-20	-20	-22.5	-22.5	-27	-25	-21.5	-5.5	
360	-11.5	-9.5	-10	-11.3	-15	-13.5	-12.5	-10.8	-3.3	
380	0	0	0	0	0	0	0	0	0	

Table 10.2A. Wear depth profile measurement data for pot 2. All measurements are in centimetres.

Position	CB1	CB2	CB3	CB4	CB5	CB6	CB7	CB8	CB9	CB10	CB11	CB12
20	0	0	0	0	0	0	0	0	0	0	0	0
40	-8.5	-21.8	-16.8	-18.5	-4.7	-3	-17.5	-18.6	-16.2	-2.3	-11.3	-9.6
60	-13.5	-23.9	-22.9	-21.1	-15.7	-11.3	-20	-20.1	-21.5	-10.4	-17.7	-15.6
80	-18.5	-26	-29	-23.6	-26.7	-22.2	-22.5	-21.7	-23.6	-18.6	-24.1	-21.6
100	-17.3	-22.5	-25.2	-20.9	-23.5	-19.1	-19.8	-19.2	-21.2	-16.7	-22.1	-20
120	-16	-19	-21.4	-18.3	-20.3	-15.9	-17.1	-16.6	-18.8	-14.9	-20	-18.4
140	-15.2	-16.6	-18.9	-16.5	-18.1	-13.9	-15.3	-14.9	-17.3	-13.6	-18.6	-17.3
160	-13.6	-12	-13.9	-12.9	-13.8	-9.7	-11.6	-11.6	-14.1	-11.1	-15.9	-15.2
180	-11.9	-7.3	-8.8	-9.4	-9.5	-5.5	-8	-8.2	-10.9	-8.6	-13.2	-13
200	-13.8	-10.1	-11.3	-10.8	-12.8	-8.3	-10.4	-11.6	-13.5	-11.5	-15.1	-12.7
220	-15.6	-12.9	-13.8	-12.3	-16.1	-11.2	-12.8	-15	-16.1	-14.4	-16.9	-12.4
240	-16.9	-14.7	-15.4	-13.3	-18.3	-13.1	-14.4	-17.3	-17.9	-16.4	-18.2	-13.2
260	-19.3	-18.4	-18.8	-15.2	-22.7	-16.9	-17.6	-21.9	-21.4	-20.2	-20.7	-15
280	-21.8	-22.1	-22.1	-17.1	-27.1	-20.7	-20.8	-26.4	-24.9	-24.1	-23.2	-17
300	-11.9	-12	-11	-9.3	-20.4	-16	-15.9	-14.2	-21.5	-20.5	-19	-7.6
320	-2	-1.9	0.1	-1.6	-13.8	-11.5	-10.9	-2	-15	-14	-13	-3.8
340	0	0	0	0	0	0	0	0	0	0	0	0

Table 10.3A. Wear depth profile measurement data for pot 4. All measurements are in centimetres.

Position	CB1	CB2	CB3	CB4	CB5	CB6	CB7	CB8	CB9	CB10	CB11	CB12
20	0	0	0	0	0	0	0	0	0	0	0	0
40	-1	-1	-1	-12	-12	-7	-1	-2	-1	-1	-12	-1
60	-8.5	-9.5	-7.3	-17	-16.3	-11.3	-9.3	-9.8	-8	-7	-16	-3
80	-15	-18	-13.5	-22	-20.5	-15.5	-17.5	-17.5	-15	-14	-20	-5
100	-13.7	-16.4	-11.6	-19.8	-17	-13.2	-14.7	-15	-13.1	-13.2	-18.1	-4.4
120	-12.6	-14.8	-9.8	-17.5	-13.6	-10.8	-11.9	-12.4	-11.3	-11.5	-16.3	-3.9
140	-8.7	-13.8	-8.5	-16	-11.3	-9.3	-10	-10.8	-10	-10.3	-15	-3.5
160	-6.5	-11.6	-6	-13	-6.6	-6.1	-6.3	-7.4	-7.5	-10	-12.5	-2.8
180	-4.7	-9.5	-3.5	-10	-2	-3	-2.5	-4	-5	-6.5	-10	-2
200	-6.7	-11.4	-5.8	-12	-5.4	-5.4	-5.6	-7.3	-9.1	-8.3	-11.9	-3.1
220	-8.6	-13.3	-8.2	-13.9	-8.8	-7.9	-8.7	-10.6	-13.3	-10.5	-13.8	-4.3

Table 10.3A continues on the next page.

Continuation of Table 10.3A.

Position	CB1	CB2	CB3	CB4	CB5	CB6	CB7	CB8	CB9	CB10	CB11	CB12
240	-10.8	-14.5	-9.8	-15.3	-11	-9.5	-10.8	-12.8	-16	-12.3	-15	-5
260	-12.8	-17	-12.9	-17.9	-15.5	-12.8	-14.9	-17.1	-21.5	-16.5	-17.5	-6.5
280	-17.5	-19.5	-16	-20.5	-20	-16	-19	-21.5	-27	-21	-20	-8
300	-8	-9.8	-8	-18.8	-16	-8	-16.5	-16.8	-23	-11	-10.5	-6
320	0	0	0	0	0	0	0	0	0	0	0	0

Table 10.4A. Wear depth profile measurement data for pot 5. All measurements are in centimetres.

Position	CB1	CB2	CB3	CB4	CB5	CB6	CB7	CB8	CB9	CB10	CB11	CB12
40	-17.9	-8.1	-4.5	-2.8	-8.8	-5.7	-6.8	-5.1	-5.1	-5.8	-6.3	-6.4
60	-16.4	-6.3	-1.7	-1.6	-6.3	-2.2	-2	-1.7	-1.8	-2.8	-6.5	-6.6
80	-14.8	-4.5	1.1	-0.3	-3.7	1.4	2.9	1.8	1.5	1	-6.5	-6.6
100	-12.8	-3.3	1.2	0	-2.8	1.4	2.9	2	1.2	0.8	-7.6	-5.8
120	-10.8	-2.1	1.3	0.3	-1.9	1.5	2.8	2.3	0.9	0.5	-5.9	-5
140	-9.5	-1.3	1.4	0.5	-1.3	1.5	2.8	2.4	0.7	0	-4.7	-4.5
160	-6.8	0.3	1.6	1	-0.1	1.6	2.8	2.7	0.3	-0.2	-2.4	-3.5
180	-4.2	1.9	1.7	1.4	1.1	1.6	2.7	3	-0.1	-0.4	0.5	1
200	-3.6	1	0.8	1.3	0.8	1.2	1.3	2.1	-0.1	-0.2	-1.1	-3.5
220	-2.9	0.1	-0.1	1.1	0.6	0.8	-0.2	1.1	-0.1	-0.2	-2.3	-4.5
240	-2.5	-0.5	-0.8	1	0.4	0.5	-1.1	0.5	-0.1	-0.2	-3	-5.2
260	-1.6	-1.7	-2	0.8	0.1	0	-3.1	-0.8	-0.1	-0.4	-4.5	-6.6
280	-0.8	-2.9	-3.2	0.6	-0.3	-0.5	-5	-2	-0.1	-1.3	-6	-8
300	-2	-1.9	0.5	1.3	-0.1	-1.4	-16	-3.9	-2.6	-2.1	-17.5	-7.1
320	-3.3	-0.9	0.5	0.5	0.5	-2.2	-27	-5.8	-5.1	-2.9	-29	-6.2

Table 10.5A. Wear depth profile measurement data for pot 6. All measurements are in centimetres.

Position	CB1	CB2	CB3	CB4	CB5	CB6	CB7	CB8	CB9	CB10	CB11	CB12
40	1	0	0.5	0.5	1.5	-0.5	0	0.5	-1	-4	-4.5	1
60	0.8	-0.5	-0.5	0	1	-0.8	-0.3	0	-1.8	-4.8	-6	0.8
80	0.5	-1	-1.5	-0.5	0.5	-1	-0.5	-0.5	-2.5	-5.5	-7.5	0.5
100	-0.5	-1.8	-2.3	-1.4	-0.3	-1.8	-1.3	-1.4	-2.8	-5.8	-7.6	-0.5
120	-1.6	-2.7	-3.2	-2.4	-1.2	-2.7	-2.2	-2.4	-3.1	-6.1	-7.7	-1.6
140	-2.3	-3.3	-3.8	-3	-1.8	-3.3	-2.8	-3	-3.3	-6.3	-7.8	-2.3
160	-3.6	-4.4	-4.9	-4.3	-2.9	-4.4	-3.9	-4.3	-3.6	-6.6	-7.9	-3.6
180	-5	-5.5	-6	-5.5	-4	-5.5	-5	-5.5	-4	-7	-8	-5
200	-5.1	-5.6	-6.1	-5.6	-4.6	-5.9	-5.2	-5.5	-4.1	-7.3	-8.8	-5.1
220	-5.2	-5.7	-6.2	-5.7	-5.1	-6.3	-5.4	-5.5	-4.2	-7.6	-9.7	-5.2
240	-5.3	-5.8	-6.3	-5.8	-5.5	-6.5	-5.5	-5.5	-4.3	-7.8	-10.3	-5.3
260	-5.4	-5.9	-6.4	-5.9	-6.3	-7	-5.8	-5.5	-4.4	-8.1	-11.4	-5.4
280	-5.5	-6	-6.5	-6	-7	-7.5	-6	-5.5	-4.5	-8.5	-12.5	-5.5
300	-3	-3	-3.5	-3	-4	-4.5	-2.8	-3.3	-3	-5.5	-7.5	-3
320	-0.5	0	-0.5	0	-1	-1.5	0.5	-1	-1.5	-2.5	-2.5	-0.5

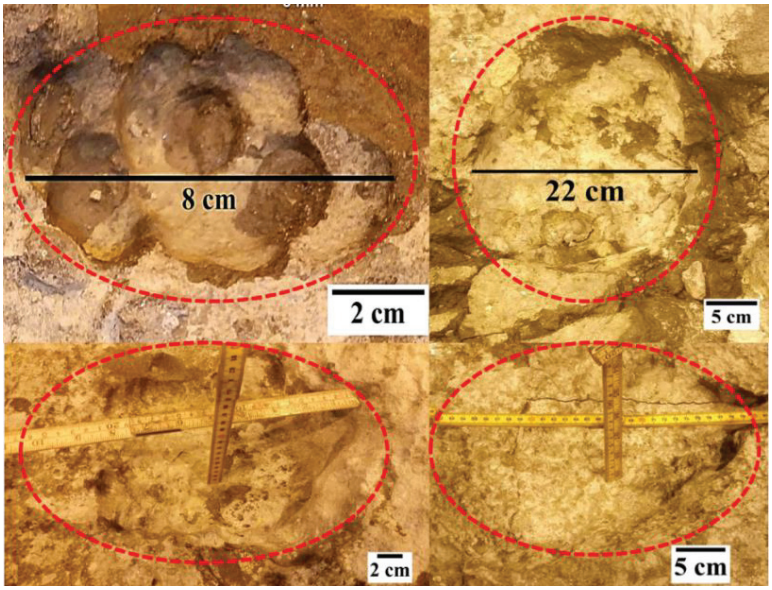

Figure 10.1A. Additional optical photographs of potholes.

Table 10.6A. Pothole measurement data for pot 1. All measurements are in centimetres.

Position on CB	CB1	CB1	CB2	CB2	CB3	CB3	CB4	CB4
	Diameter (cm)	Depth (cm)	Diameter (cm)	Depth (cm)	Diameter (cm)	Depth (cm)	Diameter (cm)	Depth (cm)
20								
40								
60			50.2	9.5	48.0	9.0		
80								
100								
120								
140								
160								
180								
200								
220								
240								
260								
280								
300					3.5	1.5	4.2	2.1
320					9.6	4.5		
340			50.0	10.0	44.6	7.8		
360								
380								

Table 10.6A continues on the next page.

Continuation of Table 10.6A

Position on CB	CB5	CB5	CB6	CB6	CB7	CB7	CB8	CB8
	Diameter (cm)	Depth (cm)	Diameter (cm)	Depth (cm)	Diameter (cm)	Depth (cm)	Diameter (cm)	Depth (cm)
20								
40								
60			50.0	9.0			52.0	9.5
80								
100								
120								
140								
160								
180								
200								
220								
240								
260								
280								
300			4.0	1.8				
320			10.5	5.2				
340			51.0	9.8			52.8	10.5
360								
380								

Position on CB	CB9 Diameter (cm)	CB9 Depth (cm)	CB10 Diameter (cm)	CB10 Depth (cm)	CB11 Diameter (cm)	CB11 Depth (cm)	CB12 Diameter (cm)	CB12 Depth (cm)
20								
40								
60			40.2	7.0	38.2	6.1	39.5	6.8
80								
100								
120								
140								
160								
180								
200					8.0	3.5		
220					3.5	1.5		
240					4.5	1.5		
260					4.6	1.5		
280					4.2	2.1		
300			3.9	1.5	4.3	1.5		
320					2.4	1.0	4.2	1.5
340			40.8	7.8	42.2	8.1	40.8	7.4
360								
380								

Table 10.6 A continues on the next page.

Continuation of Table 10.6A.

Position on CB	CB13	CB13	CB14	CB14	CB15	CB15	CB16	CB16
	Diameter (cm)	Depth (cm)	Diameter (cm)	Depth (cm)	Diameter (cm)	Depth (cm)	Diameter (cm)	Depth (cm)
20								
40								
60	38.1	6.2	38.0	6.2	48.2	8.2	49.0	8.6
80								
100								
120								
140								
160								
180								
200								
220								
240								
260								
280								
300								
320							4.6	1.5
340	42.0	8.0	38.8	7.1	50.8	8.7	52.3	11.2
360								
380								

Position on CB	CB17	CB17	CB18	CB18	CB19	CB19		
	Diameter (cm)	Depth (cm)	Diameter (cm)	Depth (cm)	Diameter (cm)	Depth (cm)		
20								
40								
60	48.5	8.4	52.3	13.0				
80								
100								
120								
140								
160								
180								
200								
220								
240								
260								
280								
300								
320	4.1	1.5	4.3	1.5				
340	52.0	11.3	53.0	13.0				
360								
380								

Appendix A- Cathode Wear Measurements

Table 10.7A. Pothole measurement data for pot 2. All measurements are in centimetres.

Position on CB	CB1	CB1	CB2	CB2	CB3	CB3	CB4	CB4
	Diameter (cm)	Depth (cm)	Diameter (cm)	Depth (cm)	Diameter (cm)	Depth (cm)	Diameter (cm)	Depth (cm)
20								
40								
60			4.5	1.5	5.5	1.5		
80								
100								
120								
140								
160								
180								
200								
220								
240								
260					3.0	1.0		
280	2.5	0.9	14.0	4.0	10	4		
300			42	18.5				
320								
340								

Position on CB	CB5	CB5	CB6	CB6	CB7	CB7	CB8	CB8
	Diameter (cm)	Depth (cm)	Diameter (cm)	Depth (cm)	Diameter (cm)	Depth (cm)	Diameter (cm)	Depth (cm)
20								
40								
60	21	12			6	2	6.5	2
80	2.5	1	3.5	1	4	1.5	2	0.5
100								
120								
140								
160								
180								
200								
220								
240	3	1.5	3	1.5	3.5	1.5	6	3.5
260	11	4.5					14	11
280			55	19.3				
300								
320								
340								

Table 10.7A continues on the next page.

Continuation of Table 10.7A.

Position on CB	CB9	CB9	CB10	CB10	CB11	CB11	CB12	CB12
	Diameter (cm)	Depth (cm)	Diameter (cm)	Depth (cm)	Diameter (cm)	Depth (cm)	Diameter (cm)	Depth (cm)
20								
40								
60								
80	3.5	2.0						
100								
120								
140								
160								
180								
200								
220								
240	5.0	3.0						
260								
280	48.0	16.5			22	11.0	32.0	12.0
300								
320								
340								

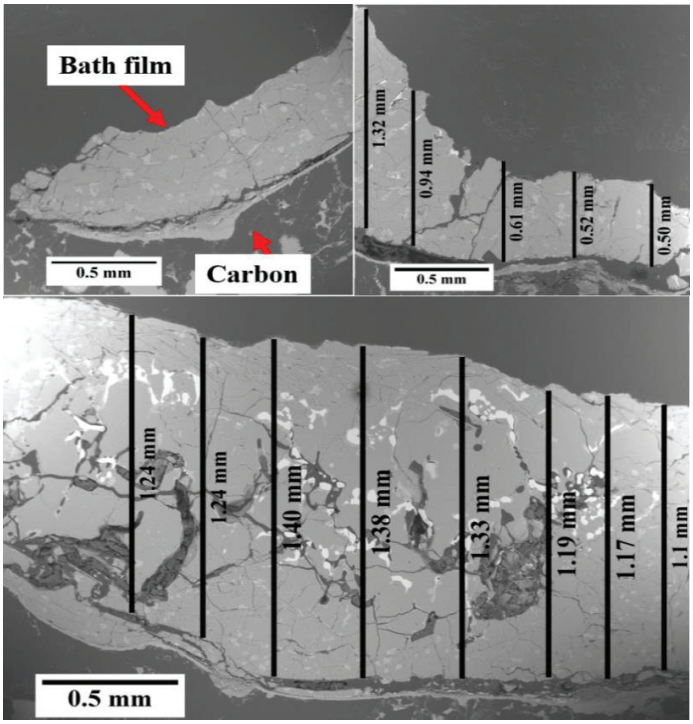

Figure 10.2A. Typical bath film thickness on the cathode surface of pot 1.

Table 10.8A Data from bath film thickness measurements. All measurements are in micrometres.

Measurement	Bath film (µm)	Measurement	Bath film (µm)	Measurement	Bath film (µm)	Measurement	Bath film (µm)
1	850	13	465	25	649	37	471
2	750	14	420	26	1399	38	416
3	850	15	398	27	1375	39	536
4	450	16	459	28	1334	40	354
5	470	17	437	29	1188	41	936
6	450	18	390	30	1173	42	610
7	351	19	453	31	1105	43	543
8	549	20	490	32	1245	44	461
9	519	21	489	33	1236	45	529
10	408	22	508	34	491	46	528
11	432	23	476	35	511	47	456
12	533	24	561	36	454	48	435

Appendix B. Measurement of Pitting size on cathode surfaces.

This section provides additional data on the pitting size measurement.

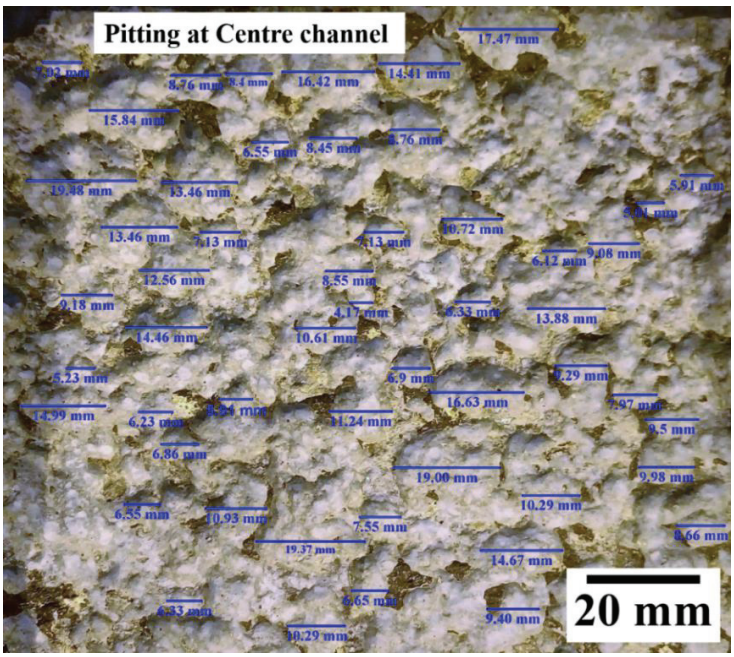

Figure 10.1B. Pitting size measurements at the centre channel area of pot 2.

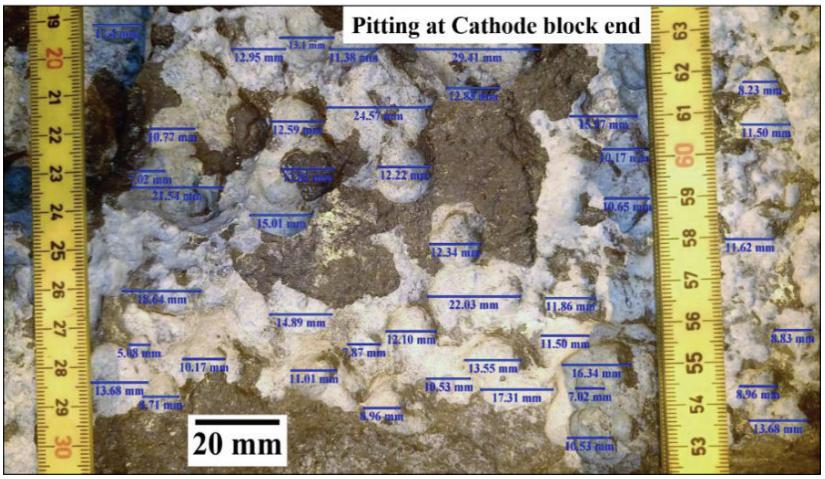

Figure 10.2B. Pitting size measurement at the cathode block end of pot 2.

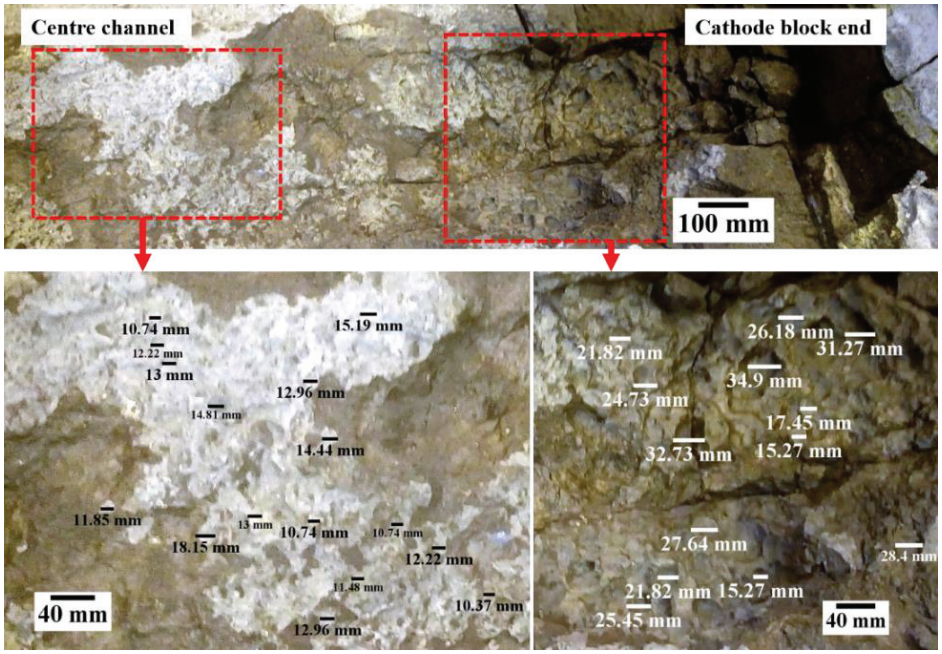

Figure 10.3B. Pitting size measurement on cathode block 2 of pot 4.

Pitting sizes were measured all over the cathode surface of pot 2 and 4 as they displayed visible pitting all over the cathode surface. The measurement of pitting sizes on pot 3 was concentrated at the cathode block ends as no visible pitting could be observed at the centre channel areas. Figure 10.4B shows the distinct pitting at the cathode block ends of pot 3.

Appendix B. Measurement of Pitting size on cathode surfaces.

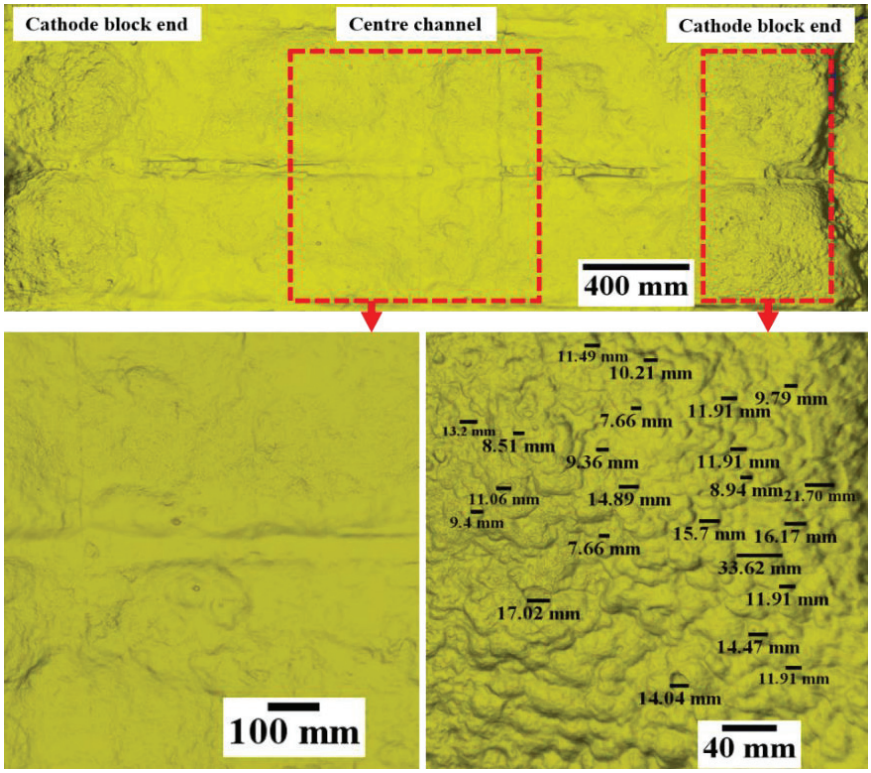

Figure 10.4B. Pitting at the cathode block ends of pot 3.

Table 10.1B. Measurement data for pitting on pot 2.

Pitting number	Centre channel pitting size(mm)	CB End pitting size(mm)	Pitting Number	Centre channel pitting size(mm)	CB End pitting size(mm)	Pitting number	Centre channel pitting size(mm)	CB End pitting size(mm)
1	4.2	8.8	51	19.5	7	101	6	18.8
2	5	11.8	52	10.7	10.5	102	14.8	10.2
3	5.2	6	53	6.5	29.4	103	8.8	20
4	5.9	10.9	54	4.7	12.8	104	6.5	14.2
5	5.9	8.4	55	7.1	12.3	105	5.4	14.8
6	6.1	10.9	56	4.5	22	106	6.2	21.4
7	6.2	14	57	7.1	13.6	107	4.1	11.7
8	6.3	16.3	58	5.5	17.3	108	7.9	19.6
9	6.3	12	59	4.3	10.5	109	10.5	15.4
10	6.5	11.6	60	7.8	12.1	110	17.8	22.9
11	6.5	19.4	61	5.7	12.2	111	5.8	18.5
12	6.7	23.4	62	8.6	24.6	112	8.7	10.4
13	6.9	29.9	63	5.2	11.4	113	20.6	18.6
14	6.9	12.3	64	4.7	7.9	114	10.1	13.5
15	7	22.2	65	7.6	9	115	10.9	13.5
16	7.1	16.7	66	5.2	11	116	10.6	25.4

Table 10.1B continues on the next page.

Continuation of Table 10.1B

Pitting number	Centre channel pitting size(mm)	CB End pitting size(mm)	Pitting Number	Centre channel pitting size(mm)	CB End pitting size(mm)	Pitting number	Centre channel pitting size(mm)	CB End pitting size(mm)
17	7.1	18.1	67	10.5	14.9	117	8.2	20.6
18	7.5	36	68	4.7	15	118	10.6	21
19	8	25	69	7.9	12.8	119	15.1	16.2
20	8.4	13.5	70	6.5	12.6	120	6.5	22.1
21	8.6	12.3	71	5.7	12.6	121	7	29.6
22	8.7	12.1	72	12.9	13.1	122	6.4	21.7
23	8.8	10	73	6.4	11.4	123	16	18.1
24	8.8	16.3	74	6.5	10.8	124	9.5	20
25	9.1	17.5	75	7.6	7	125	5.7	12.7
26	9.2	15.1	76	7.8	21.5	126	7.2	23.5
27	9.3	18.1	77	5.7	18.6	127	6.2	22.9
28	9.4	12.6	78	6.4	5.1	128	7.1	24.1
29	9.5	13.3	79	8.8	10.2	129	6	20.9
30	10	14.9	80	18.6	13.7	130	6.9	18.7
31	10.3	10.9	81	7.8	8.7	131	5.5	36.2
32	10.3	28.5	82	8.9	9.4	132	7.6	29.8
33	10.6	4.4	83	16.9	18.1	133	7.6	21.9
34	10.7	7.1	84	17.2	28.9	134	7.4	11.1
35	10.9	8.5	85	9.7	16.1	135	11.7	17.4
36	11.2	5.2	86	7.9	13.9	136	9.3	11.4
37	12.6	5	87	9.2	15.9	137	15.2	8.9
38	13.5	14.1	88	9.9	15	138	9	15.6
39	13.5	8.3	89	5.9	23.8	139	8.3	28.9
40	13.9	8.2	90	10.2	28.3	140	8.4	16.5
41	14.4	11.5	91	14.5	24.8	141	8.1	34.9
42	14.5	11.6	92	16.8	15	142	9.1	15.2
43	14.7	8.8	93	7.9	14.4	143	10.3	18.1
44	15	9	94	14	15	144	6.4	17.8
45	15.8	16	95	10.2	13.9	145	12.4	20.9
46	16.4	10.2	96	6.8	13.6	146	12.1	18.1
47	16.6	10.7	97	7.2	17.6	147	12.2	19.1
48	17.5	11.9	98	9.1	7.2	148	9.1	23.5
49	19	11.5	99	8.7	12	149	8.8	24.1
50	19.4	16.3	100	5.6	14.1	150	21.9	14.9

Table 10.2B. Pitting measurement data for pot 3. All measurements are in millimetres (mm).

Pitting number	Pitting size (mm)- CB13	Pitting size (mm)- CB14	Pitting size (mm)-CB15	Pitting size (mm)-CB16
1	11	7	16	9
2	15	11	20	8
3	5	15	10	7
4	4	5	6	14
5	6	4	5	4
6	6	6	5	7
7	8	6	5	6
8	5	8	6	6
9	7	5	6	11
10	6	6	8	10
11	19	7	4	7
12	5	6	6	5
13	5	6	4	6
14	7	19	4	4

Table 10.2B continues on the next page

Appendix B. Measurement of Pitting size on cathode surfaces.

Continuation of Table 10.2B

Pitting number	Pitting size (mm)- CB13	Pitting size (mm)- CB14	Pitting size (mm)-CB15	Pitting size (mm)-CB16
15	7	5	13	7
16	4	5	32	11
17	6	7	8	11
18	9	7	6	10
19	7	4	6	6
20	6	5	10	3
21	8	6	7	14
22	6	9	5	6
23	6	7	6	10
24	6	6	17	16
25	13	8	10	6
26	6	8	6	7
27	7	7	6	6
28	7	5	10	12
29	7	6	5	25
30	8	8	4	10
31	8	11	5	10
32	7	14	5	4
33	7	11	10	8
34	5	5	8	7
35	17	10	6	4
36	7	9	9	5
37	11	8	4	5
38	15	11	5	7
39	5	7	4	5
40	4	8	7	9
41	6	11	4	5
42	6	6	2	8
43	8	6	4	5
44	5	12	8	7
45	6	10	7	6
46	7	5	7	7
47	6	6	11	8
48	6	11	7	4
49	19	8	10	7
50	5	14	18	6
51	5	5	8	7
52	7	8	4	5
53	7	8	8	7
54	4	8	8	5
55	5	19	5	7
56	6	14	5	6
57	9	11	11	5
58	7	7	7	6
59	6	10	5	5
60	8	10	4	6
61	8	6	4	8
62	7	10	5	4
63	5	10	5	6
64	6	8	14	6
65	8	6	7	4
66	7	6	7	5

Table 10.2B continues on the next page

Continuation of Table 10.2B

Pitting number	Pitting size (mm)- CB13	Pitting size (mm)- CB14	Pitting size (mm)-CB15	Pitting size (mm)-CB16
67	33	4	10	5
68	8	4	9	5
69	4	10	11	5
70	10	9	7	5
71	6	8	5	6
72	9	8	5	8
73	4	9	17	7
74	2	29	5	6
75	3	6	11	4
76	9	9	11	5
77	4	7	13	7
78	11	6	7	8
79	9	5	5	8
80	5	5	4	6
81	5	4	6	6
82	6	10	16	6
83	5	5	9	11
84	4	4	6	11
85	5	5	7	5
86	6	7	7	8
87	7	4	7	7
88	10	7	6	8
89	5	9	4	6
90	6	14	5	6
91	7	22	15	10
92	7	8	7	4
93	7	4	13	11
94	6	5	14	7
95	8	6	3	5
96	4	6	7	10
97	6	5	6	9
98	5	8	8	7
99	6	12	13	5
100	9	7	10	8
101	9	7	6	7
102	15	6	5	8
103	8	7	7	6
104	15	6	8	4
105	13	8	9	10
106	10	7	8	5
107	7	6	7	6
108	8	6	14	5
109	8	8	4	4
110	11	5	7	3
111	12	6	6	5
112	13	5	6	3
113	11	6	11	4
114	12	11	10	6
115	10	8	7	6
116	4	7	5	5
117	11.5	4	6	6
118	9.3	5	4	5
119	8.7	3	7	7
120	9.2	12	11	7

Table 10.2B continues on the next page

Continuation of Table 10.2B

Pitting number	Pitting size (mm)- CB13	Pitting size (mm)- CB14	Pitting size (mm)-CB15	Pitting size (mm)-CB16
121	5.9	8	11	13
122	6.6	7	10	9
123	9.4	11	6	6
124	8.2	9	3	10
125	14.3	5	14	7
126	8.2	2	6	27
127	7.9	4	10	14
128	9.4	4	16	5
129	15.6	5	6	6
130	4.7	7	7	5
131	8.5	4	6	6
132	7.5	24	12	5
133	7.5	27	25	5
134	10.1	6	10	8
135	13.5	5	10	8
136	16.5	4	4	6
137	10.2	4	8	8
138	6.1	6	7	7
139	7.3	5	4	2
140	8.5	9	5	26
141	10.6	6	5	9
142	9.1	5	7	3
143	8.2	4	5	30
144	8.3	5	9	6
145	10.4	7	5	6
146	10.1	5	8	6
147	10	7	5	7
148	11	5	7	7
149	8.1	3	6	9
150	10.8	4	7	5
151	10.3	6	8	4
152	11.4	6	4	4
153	7.4	5	7	5
154	11.2	8	6	5
155	9.7	36	7	7
156	11.9	6	5	28
157	11.6	8	7	6
158	10.8	6	5	5
159	7.6	6	7	6
160	8.8	6	6	5
161	13	13	5	7
162	13.3	6	6	8
163	12.4	7	5	5
164	10.8	7	6	6
165	6.4	7	8	5
166	16	8	4	28
167	8.3	8	6	6
168	12.5	7	6	5
169	12.4	7	4	4
170	12.9	5	5	5
171	7.8	17	5	5
172	10.5	7	5	4

Table 10.2Bcontinues on the next page

Continuation of Table 10.2B

Pitting number	Pitting size (mm)- CB13	Pitting size (mm)- CB14	Pitting size (mm)-CB15	Pitting size (mm)-CB16
173	5.6	11	5	7
174	11.9	15	5	5
175	7.8	5	6	4
176	11.6	4	8	7
177	12.5	6	7	5
178	8.2	6	6	9
179	7.9	8	4	5
180	14.7	5	5	5
181	8.5	6	7	6
182	9.4	7	8	7
183	8.4	6	8	10
184	10.1	6	6	4
185	7.9	19	6	5
186	14.3	5	6	4
187	10.3	5	11	7
188	8.6	7	11	8
189	9.1	7	5	6
190	8.4	4	8	4
191	9	5	7	6
192	9.3	6	8	33
193	9.2	9	6	8
194	9	7	6	6
195	8	6	10	6
196	7.5	8	4	5
197	5.9	8	11	7
198	5.6	7	7	7
199	8.4	5	5	11
200	7.9	6	10	8
201	10.4	8	9	4
202	10.3	7	7	4
203	8.7	33	5	7
204	9.2	8	8	7
205	5.9	4	7	8
206	6.6	10	8	7
207	9	6	6	6
208	7.1	9	4	10
209	11.5	7	10	6
210	10	4	5	8
211		2	6	6
212		3	5	8
213		9	4	7
214		4	3	5
215		11	5	6
216		9	3	6
217		5	4	5
218		5	6	9
219		6	6	6
220		5	5	16
221		4	6	5
222		5	5	6
223		6	7	5
224		7	7	9
225		10	13	7
226		5	9	7

Table 10.2B continues on the next page

Continuation of Table 10.2B

Pitting number	Pitting size (mm)- CB13	Pitting size (mm)- CB14	Pitting size (mm)-CB15	Pitting size (mm)-CB16
227		6	6	7
228		7	10	7
229		7	7	7
230		7	27	6
231		7	14	4
232		5	5	10
233		6	6	7
234		8	5	5
235		7	6	3
236		4	5	7
237		6	5	4
238		5	8	5
239		6	8	9
240		9	6	5
241		9	8	10
242		6	4	8
243		15	2	12
244		8	4	6
245		15	8	7
246		13	7	6
247		10	7	8
248		7	11	10
249		8	7	3
250		8	10	4
251		11	18	4
252		12	8	4
253		13	4	2
254		11	8	3
255		12	8	4
256		10	5	5
257		10	5	4
258		4	11	5
259		4	7	6
260		6	5	6
261		7	4	8
262		6	4	9
263		6	5	5
264		7	5	6
265		5	14	7
266		5	7	5
267		5	7	6
268		6	10	7
269		5	9	5
270		10	11	6
271		8	7	5
272		8	5	6
273		34	5	4
274		6	17	4
275		5	5	4
276		31	11	4
277		6	11	5
278		6	13	5

Table 10.2B continues on the next page

Continuation of Table 10.2B

279		6	7	5
280		7	5	5
281		7	4	5
282		7	6	5
283		13	16	5
284		9	9	5
285		25	6	16
286		21	7	30
287		3	7	9
288		8	7	6
289		7	6	6
290		5	4	28
291		7	5	4
292		6	15	6
293		9	7	5
294		20	13	4
295		8	14	5
296		6	3	5
297		7	7	17
298		5	6	5
299		4	8	4
300		7	13	10
301		7	10	7
302		4	6	7
303		4	5	6
304		7	7	6

Table 10.3B. Pitting measurement data for pot 4. Centre channel area (Centre pitting) and cathode block ends (End pitting). All measurements are in millimetres (mm).

Pitting number	**Centre pitting size (mm)**	**End pitting size (mm)**	**Pitting number (mm)**	**Centre pitting size (mm)**	**End pitting size (mm)**
1	12	14.2	51	11.4	17.5
2	9.7	14.8	52	13.8	21.3
3	9.9	21.4	53	20.2	19.1
4	4.6	11.7	54	12.8	27.3
5	6.3	19.6	55	13.8	15.9
6	17.7	15.4	56	7.4	27.9
7	9.3	22.9	57	6.7	21.9
8	17.2	18.5	58	9.3	15.9
9	17.9	10.4	59	14.1	25.7
10	9.3	18.6	60	7.4	14
11	8.4	13.5	61	15.7	15.5
12	7.6	13.5	62	14.4	15.5
13	9.3	25.4	63	11.5	13.1
14	6.8	20.6	64	7.4	17.9
15	9.9	21	65	7.7	22.4
16	7.4	16.2	66	9.9	16.6
17	10.3	22.1	67	13.8	27.8
18	9.3	29.6	68	9	14.8
19	9.9	21.7	69	9.9	36.7
20	5.1	18.1	70	9	18.6
21	7.6	20	71	8.7	20.2
22	6.1	12.7	72	9.9	12.9

Table 10.3B continues on the next page

Continuation of Table 10.3B

Pitting number	Centre pitting size (mm)	End pitting size (mm)	Pitting number (mm)	Centre pitting size (mm)	End pitting size (mm)
23	8.9	23.5	73	13	11
24	20.5	22.9	74	8	9.3
25	11	24.1	75	8	17.9
26	6.8	20.9	76	8	20
27	6.8	18.7	77	10.6	20
28	5.1	36.2	78	8.7	10.5
29	8.7	29.8	79	8.7	10.5
30	6.8	21.9	80	11.5	17.9
31	9.5	11.1	81	11.5	14.3
32	13.7	17.4	82	7.7	16.4
33	10.3	11.4	83	14.4	13.4
34	12.9	8.9	84	8	15.2
35	8.4	15.6	85	9	15
36	13.7	28.9	86	9	19.8
37	6.1	16.5	87	10.3	7.6
38	11.4	34.9	88	25	26.2
39	6.8	4.4	89	17.9	11.6
40	14.3	5	90	14.7	11.2
41	10.6	5.1			
42	13.9	5.2			
43	8.4	6			
44	6.3	19.1			
45	5.3	23.5			
46	10.1	24.1			
47	10.1	14.9			
48	14.4	33.6			
49	5.5	31.4			
50	8.9	18.1			

Appendix C. Measurement of Aggregate size by Linear Intercept method.

Aggregates size measurement data using the linear intercept method are given in Tables 9.1C. All measurements are in millimetres (mm). The results obtained from cathode block 15 is summarized in Figure 10.1C.

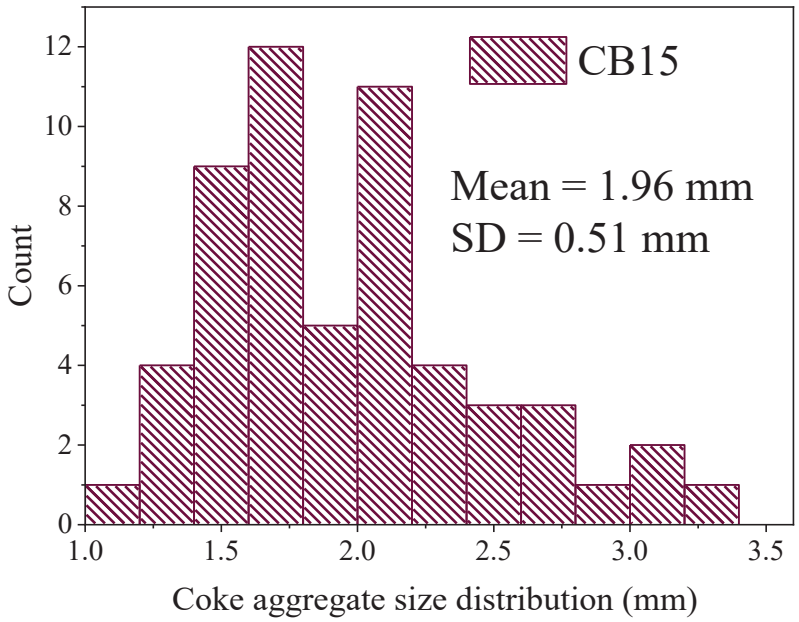

Figure 10.1C. Coke aggregate size distribution using linear intercept method.

Table 10.1C. Measurement data from linear intercept method for pot 3. All measurements are in millimetres.

Line number	Aggregate size(mm)-CB13	Aggregate size(mm)-CB14	Aggregate size(mm)-CB15	Line number	Aggregate size(mm)-CB13	Aggregate size(mm)-CB14	Aggregate size(mm)-CB15
1	2.1	2.4	2.6	51	1.3	2.1	2.9
2	1.5	2.4	2.1	52	2.4	2.8	2.2
3	2.4	2.1	2.5	53	2.6	1.6	3.2
4	1.6	1.8	1.6	54	3.1	2.5	3.1
5	1.8	2	1.9	55	2.6	2.3	1.8
6	1.7	2.4	1.6	56	1.9	1.5	1.8
7	2	3.2	1.7	57	1.7	2	
8	2.5	1.8	1.4	58	1.1	2.6	
9	2.1	1.8	1.6	59	1.6	2.7	
10	1.9	2.5	1.5	60	2.4	1.8	
11	2	1.8	1.2	61	2.6	2.2	
12	1.8	1.7	1.6	62	1.8	2.3	
13	1.8	1.7	2	63	1.6	2.5	
14	1.6	1.5	2.2	64	1.1	2	
15	2.2	2.6	1.4	65	1.4	1.7	
16	2.3	1.9	1.6	66	1.6	2.6	
18	2.2	1.8	2.2	68	1.4	1.8	
19	3.2	2.7	2.2	69	1.5	2.8	
20	2.9	1.8	1.2	70	1.5	2.3	
21	2.4	2.2	1.4	71	1.6	1.9	
22	2.2	1.6	1.4	72	2.5	1.3	
23	2.4	2	1.7	73	1.7	1.9	
24	1.9	1.7	1.3	74	2.1	1.7	
25	2.3	2	1.3	75	2.3	2.7	

Table 10.1C continues on the next page

Continuation of Table 10.1C

Line number	Aggregate size(mm)-CB13	Aggregate size(mm)-CB14	Aggregate size(mm)-CB15	Line number	Aggregate size(mm)-CB13	Aggregate size(mm)-CB14	Aggregate size(mm)-CB15
26	2.1	1.8	1.7	76	1.6	2.8	
27	3.1	1.8	2.2	77	1.6	2.5	
28	2.9	2.8	1.6	78	1.9	2	
29	2.3	1.8	1.7	79	1.7	2.4	
30	2.1	2.3	3.4	80	1.2	1.6	
31	1.3	1.6	2.2	81	1.6	2.3	
32	2.2	1.9	2	82	2.1	1.7	
33	3	1.7	1.7	83	1.8	1.8	
34	2	2.5	1.7	84	1.6	1.9	
35	3	1.5	2.1	85	2.5	1.8	
36	2.1	2	2.2	86	1.8	1.5	
37	2.9	2.3	2.2	87	1.7	1.7	
38	2	1.9	1.5	88	2.1	1.5	
39	1.6	1.6	2.6	89	1.8	1.5	
40	2.3	1.6	2.2	90	2.6	2.1	
41	1.7	2.8	1.5	91	1.7	1.6	
42	2.1	1.7	1.5	92	2		
43	2.3	2.2	2	93	2.2		
44	1.7	1.6	2	94	2		
45	2.8	2.5	1.7	95	2.1		
46	1.7	2	2.1				
47	1.9	2.3	2.4				
48	2.2	2.4	2.8				
49	1.2	2.5	2.4				
50	1.8	2.5	2.5				

Appendix D. CT scanning, Optical, SEM and EDS Data

This section provides additional data from the CT scanning, optical microscopy, SEM and EDS analysis.

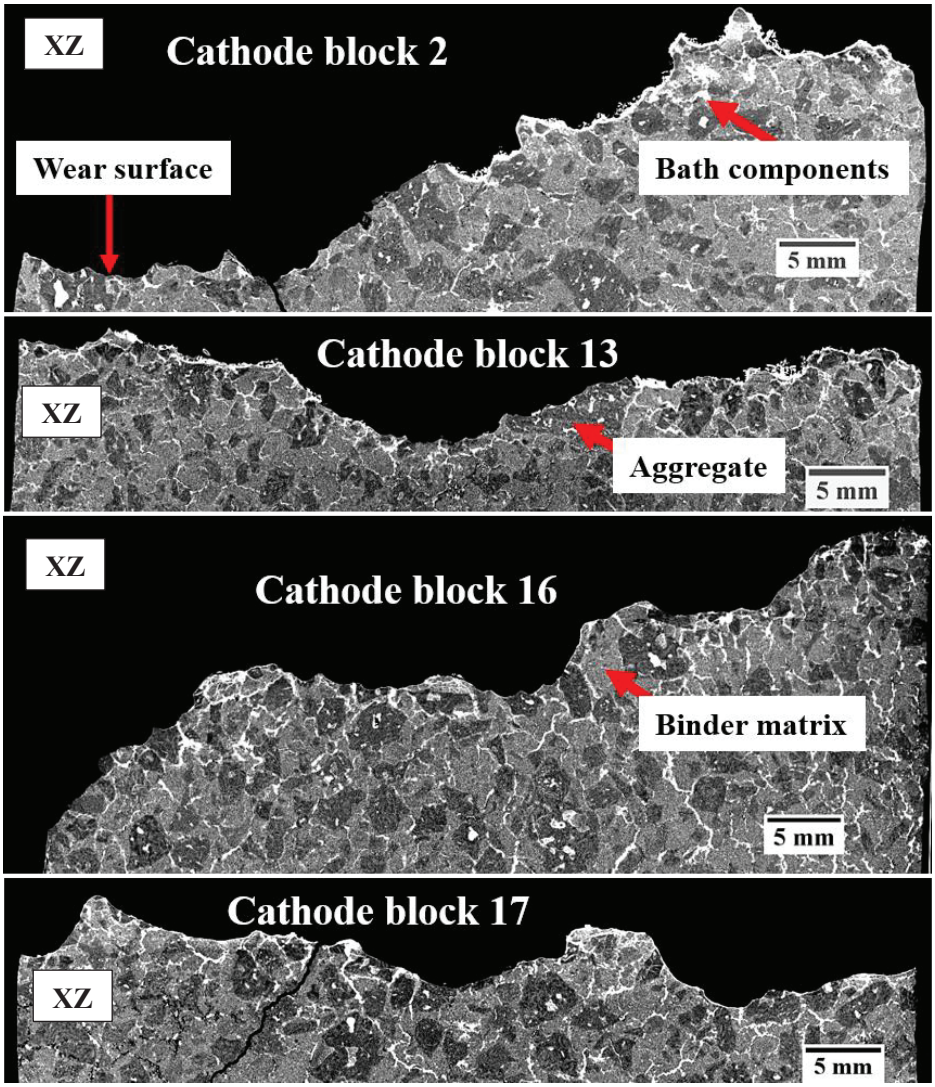

Figure 10.1D. Wear surface along the carbon-electrolyte interface of pot 3 in the XZ orientation. Four carbon samples collected from four cathode blocks.

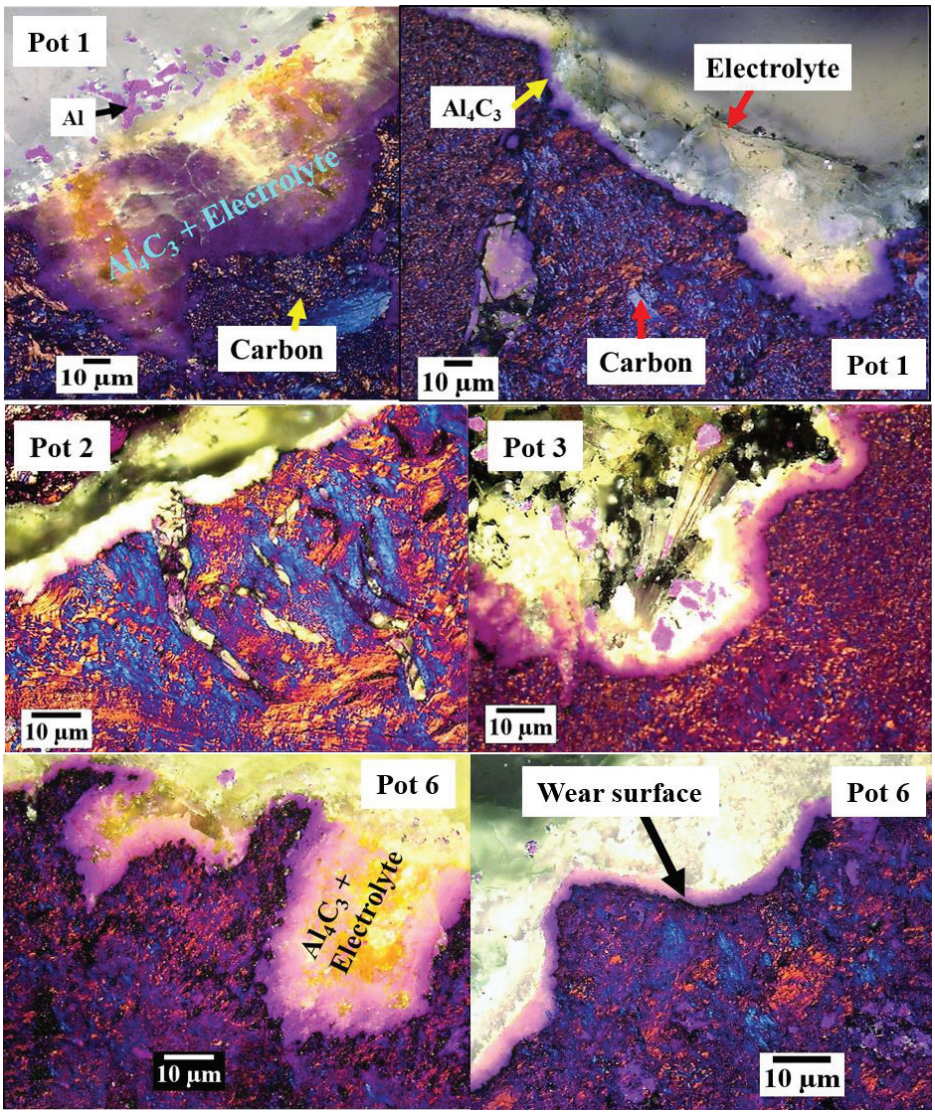

Figure 10.2D. Wear surface at the carbon-electrolyte interface at high magnification.

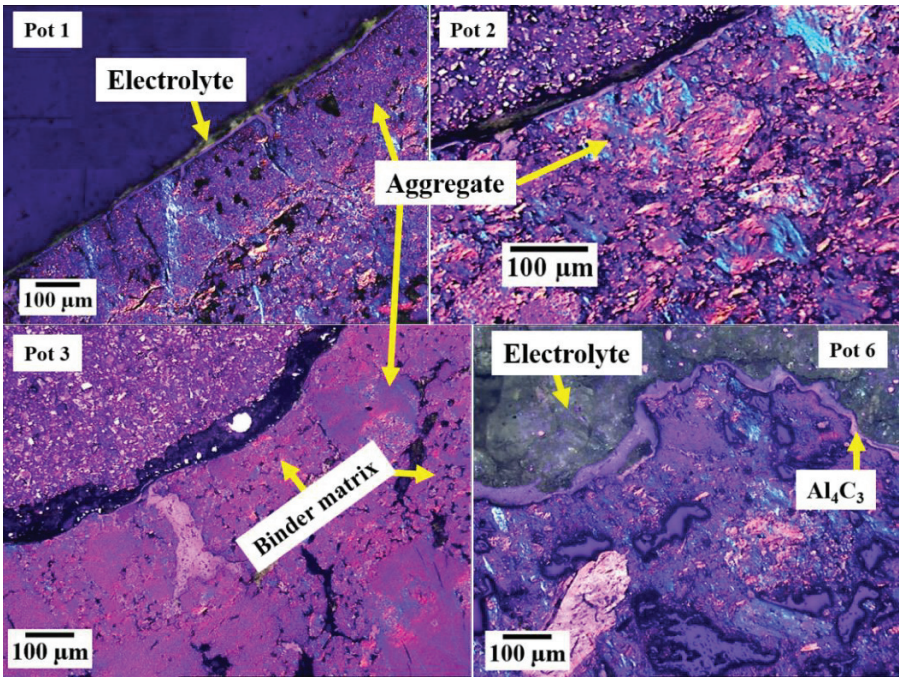

Figure 10.3D. Wear surface at the carbon-electrolyte interface.

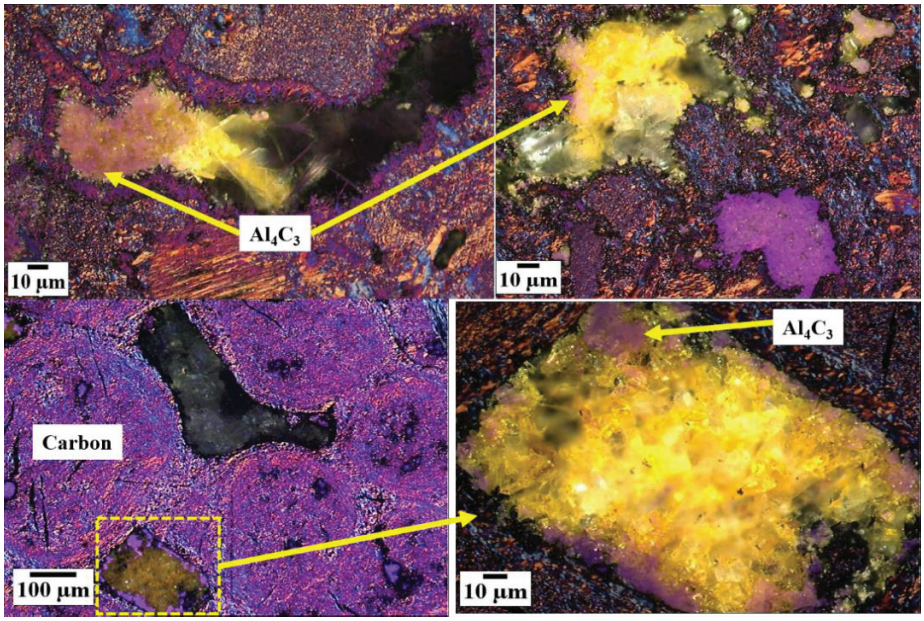

Figure 10.4D. Presence of aluminium carbide within the pores of the carbon material.

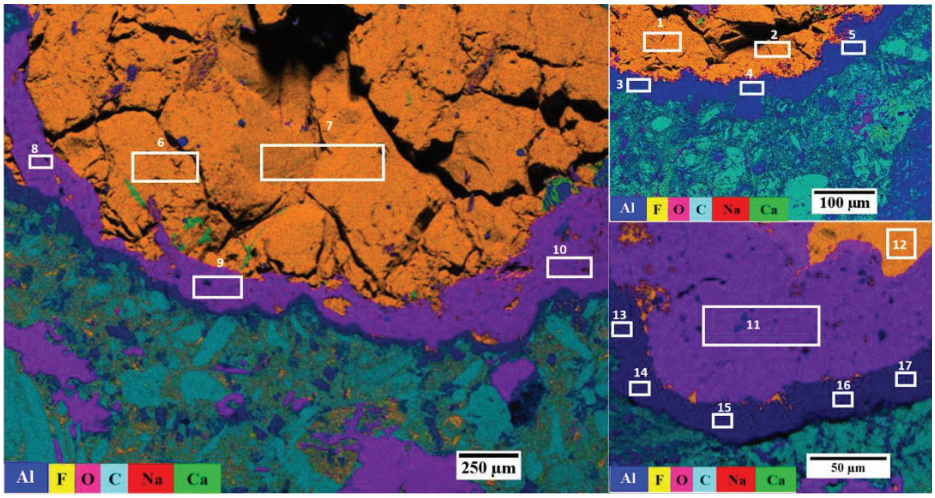

Figure 10.5D. Phases at the carbon-electrolyte interface of pot 6. White rectangles indicate locations of data acquisition.

Table 10.1 D. EDS elemental mapping data acquired from Figure 4.1D. All measurements are in wt%.

Area		Al	C	O	F	Na	Ca
1	**Mean**	14	2.2	0.4	52.4	30.8	0.1
1	**SD**	0.1	0.2	0.1	0.2	0.2	0.1
2	**Mean**	12.5	1.9	0.2	53.4	32	0
2	**SD**	0.1	0.2	0.1	0.2	0.2	0.1
3	**Mean**	69.7	19.1	4.6	3.9	2.5	0
3	**SD**	0.4	0.4	0.1	0.1	0.1	0.1
4	**Mean**	73	22.3	2	1.5	1.1	0.2
4	**SD**	0.4	0.4	0.1	0.1	0.1	0.1
5	**Mean**	73.2	22.6	1.8	1.1	1	0.3
5	**SD**	0.4	0.4	0.1	0.1	0	0.1
6	**Mean**	12.3	3.2	0.5	52.6	31.2	0.2
6	**SD**	0.1	0.2	0.1	0.2	0.2	0.1
7	**Mean**	13.5	0	0.6	53.7	31.5	0.7
7	**SD**	0.1	0	0.1	0.2	0.2	0.1
8	**Mean**	51.8	2.6	36.7	6.2	2.6	0.1
8	**SD**	0.2	0.2	0.2	0.1	0.1	0.1
9	**Mean**	53.9	3.1	40	1.9	1.1	0.1
9	**SD**	0.2	0.2	0.2	0.1	0.1	0.1
10	**Mean**	54.9	1.4	41.6	1.3	0.8	0
10	**SD**	0.2	0.2	0.2	0.1	0.1	0
11	**Mean**	55.6	1.4	42	0.5	0.5	0
11	**SD**	0.2	0.2	0.2	0.1	0.1	0
12	**Mean**	12.9	2.5	0.3	51.7	32.5	0
12	**SD**	0.1	0.2	0.1	0.2	0.2	0.1

Table 10.1D continues on the next page

Continuation of Table 10.1D

Area		Al	C	O	F	Na	Ca
13	**Mean**	71.8	22.3	2.6	1.8	1.3	0.2
13	**SD**	0.4	0.4	0.1	0.1	0.1	0.1
14	**Mean**	72.5	24.8	1.5	0.5	0.6	0.1
14	**SD**	0.4	0.4	0.1	0.1	0	0.1
15	**Mean**	71.3	22.2	3.5	1.3	1.4	0.3
15	**SD**	0.4	0.4	0.1	0.1	0.1	0.1
16	**Mean**	68.8	22.3	2.4	3.6	2.3	0.5
16	**SD**	0.3	0.4	0.1	0.1	0.1	0.1
17	**Mean**	69.6	22.3	4	2	2.1	0.1
17	**SD**	0.4	0.4	0.1	0.1	0.1	0.1

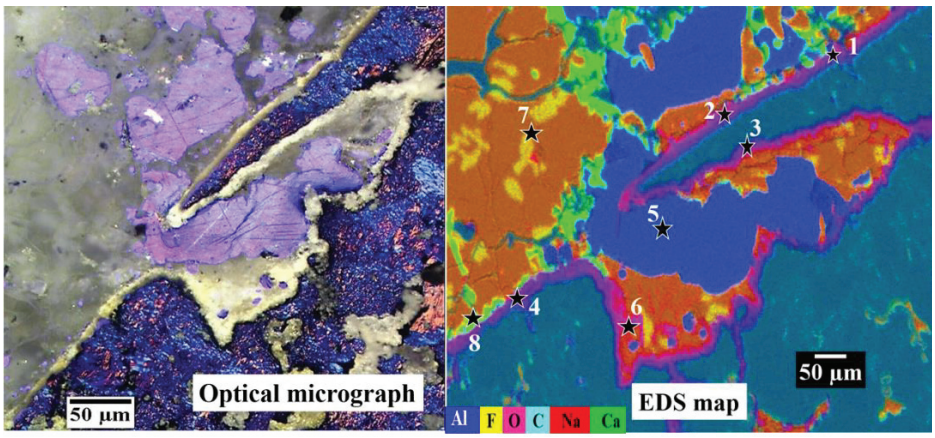

Figure 10.6D. Phases at the carbon-electrolyte interface of pot 1. Black stars indicate the locations for data acquisitions. Table 10.2 summarizes the data acquired.

Table 10.2D. EDS elemental mapping data acquired from Figure 10.6D. All measurements are in wt%

Area		Al	C	O	F	Na	Ca
1	**Mean**	43.6	28.6	16.8	6.7	3.9	0.3
1	**SD**	0.2	0.3	0.2	0.1	0.1	0.1
2	**Mean**	40.8	25.9	25.7	4.3	3	0.3
2	**SD**	0.2	0.3	0.2	0.1	0.1	0.1
3	**Mean**	43.5	30.2	20.8	3	2.2	0.4
3	**SD**	0.2	0.3	0.2	0.1	0.1	0.1
4	**Mean**	36.1	19.8	30.2	6.1	1.3	6.4
4	**SD**	0.2	0.2	0.2	0.1	0.1	0.1
5	**Mean**	89	10	1	0	0	0
5	**SD**	0.1	0.2	0.1	0	0	0
6	**Mean**	18.1	12.9	11.5	38.3	14.7	4.6
6	**SD**	0.1	0.2	0.1	0.2	0.1	0.1
7	**Mean**	12.3	5.3	0.4	52	29.8	0.3
7	**SD**	0.1	0.2	0.1	0.2	0.2	0.1
8	**Mean**	4	6.5	5.4	41.3	0.8	42
8	**SD**	0.1	0.1	0.1	0.2	0.1	0.2

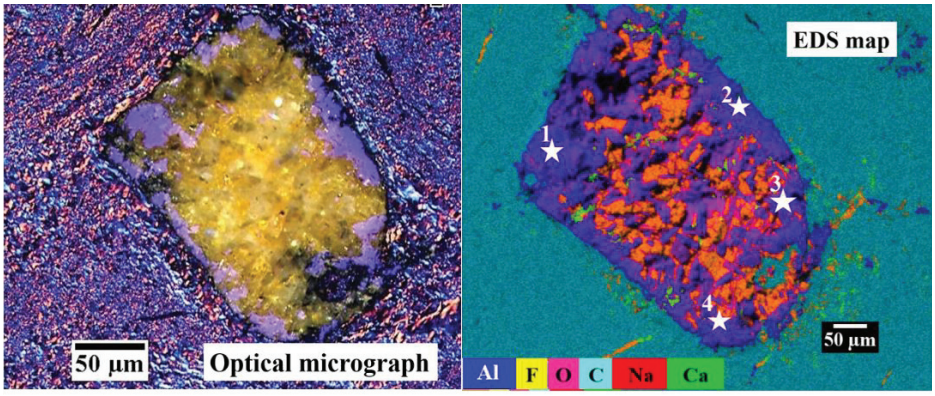

Figure 10.7D. Al_4C_3 within the porosity of the carbon cathode material. White stars indicate location for data acquisition.

Table 10.3D. EDS elemental mapping data acquired from Figure 10.7D. All measurements are in wt%

Area		Al	C	O	F	Na	Ca
1	**Mean**	51.7	12.7	34.6	0.8	0.2	0.1
1	**SD**	0.2	0.3	0.2	0.2	0	0.1
2	**Mean**	59.2	13.8	26.8	0.1	0.2	0
2	**SD**	0.3	0.3	0.2	0	0	0
3	**Mean**	39.8	14.6	37.9	4.8	2.5	0.4
3	**SD**	0.2	0.3	0.2	0.1	0.1	0.1
4	**Mean**	38.9	26	25.1	6.2	3	0.8
4	**SD**	0.4	0.5	0.3	0.2	0.1	0.2

Appendix E. Additional Data from Wetting Measurements

This section contains wetting measurement data. The data include immersion-emersion cycles data, optical micrographs. SEM images. EDS maps as well as wt% of the individual elements found in the phases detected. Considering the large data gathered from the wetting measurements, only parts of the raw data from the anthracite cathode sample test in molten electrolyte is presented here. The table for the measurement data displays the time for the test, duration of the tests, weight of the cathode sample, position of the sample with respect to the melt, the cell voltage and the current.

Table 10.1E. Data from air permeability measurement. Perm stands for the air permeability.

Material	Length (mm)	Perm (nPm)	Material	Length (mm)	Perm (nPm)	Material	Length (mm)	Perm (nPm)
Anthracite	55.3	1.61	Graphitic	51	1.21	Graphitized	47.1	0.48
Anthracite	55.3	1.51	Graphitic	49.7	0.94	Graphitized	49.3	0.49
Anthracite	56	1.85	Graphitic	52	1.18	Graphitized	48.2	0.49
Anthracite	54	1.46	Graphitic	53.5	1.29	Graphitized	47.5	0.50
Anthracite	54.2	1.69	Graphitic	50	1.03			
Anthracite	56	1.99	Graphitic	51	1.07			
Anthracite	55	1.49						

Table 10.2E. Geometric density measurement data.

Carbon Material	Height (cm)	Diameter (cm)	Weight (g)	Volume ($cm^{3)}$	Density (g/cm^3)
Anthracite	5.5	5.0	158.6	108.6	1.46
Anthracite	5.5	5.0	159.2	108.6	1.47
Anthracite	5.6	5.0	158.3	110.0	1.44
Anthracite	7.8	5.0	221.8	153.2	1.45
Anthracite	2.1	5.0	58.8	40.4	1.45
Anthracite	2.1	5.0	59.8	41.0	1.46
Anthracite	2.1	5.0	58.9	40.8	1.44
Anthracite	2.1	5.0	58.7	40.4	1.45
Anthracite	2.1	5.0	59.4	41.8	1.42
Anthracite	2.1	5.0	59.1	41.2	1.44
Graphitic	5.1	5.03	164.543	101.3	1.62
Graphitic	4.97	5.02	160.612	98.4	1.63
Graphitic	3.2	4.98	101.851	62.3	1.63
Graphitic	6.16	5	197.515	121.0	1.63
Graphitic	2.12	5.03	68.52	42.1	1.63
Graphitic	2.12	5.035	68.72	42.2	1.63
Graphitic	2.05	5.035	66.42	40.8	1.63
Graphitic	2.08	5.03	67.22	41.3	1.63
Graphitic	2.05	5.03	66.32	40.7	1.63
Graphitic	2.08	5.03	67.75	41.3	1.64
Graphitized	4.71	5.04	162.402	94.0	1.73
Graphitized	2.1	5.03	72.52	41.7	1.74
Graphitized	2.1	5.03	72.62	41.7	1.74

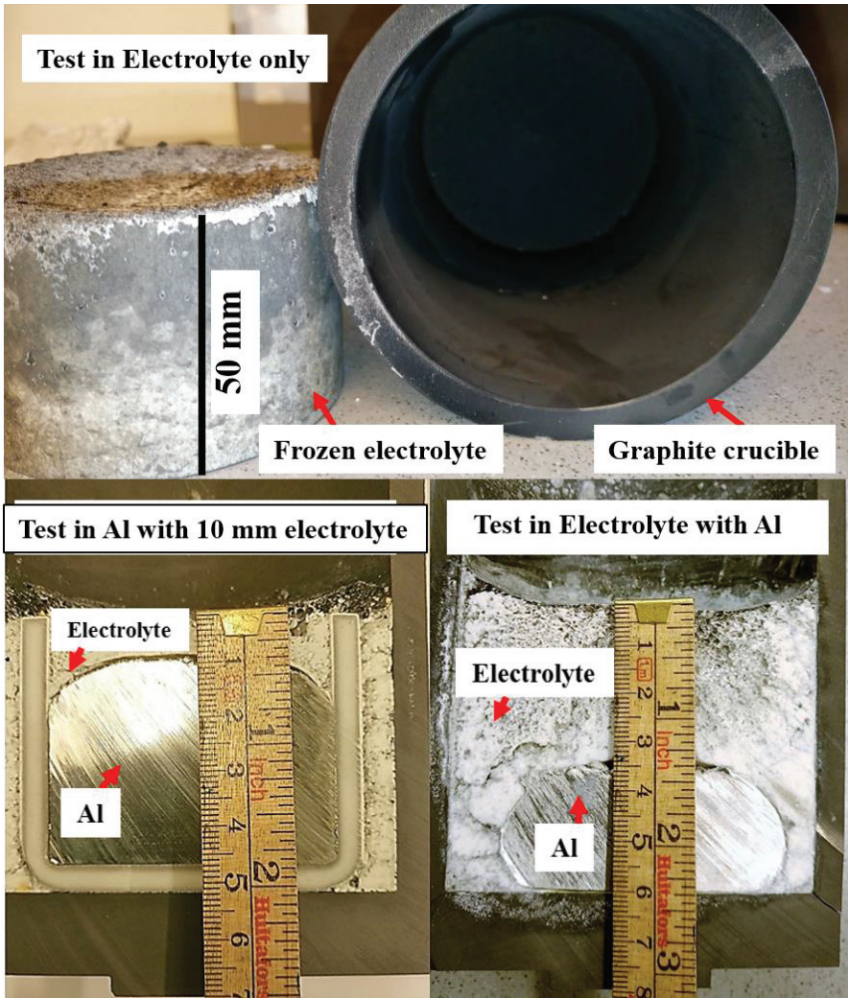

Figure 10.1E. Crucible and frozen electrolyte and Al after wetting tests.

The raw data obtained from the wetting experiments consisted of a Notepad file containing data regarding time and duration, position, weight, temperature above the melt, graphite support temperature, cell voltage and current. The contact point for all the tests was determined from a plot of the raw data obtained during the immersion cycle such as shown in Figure 10.2E.

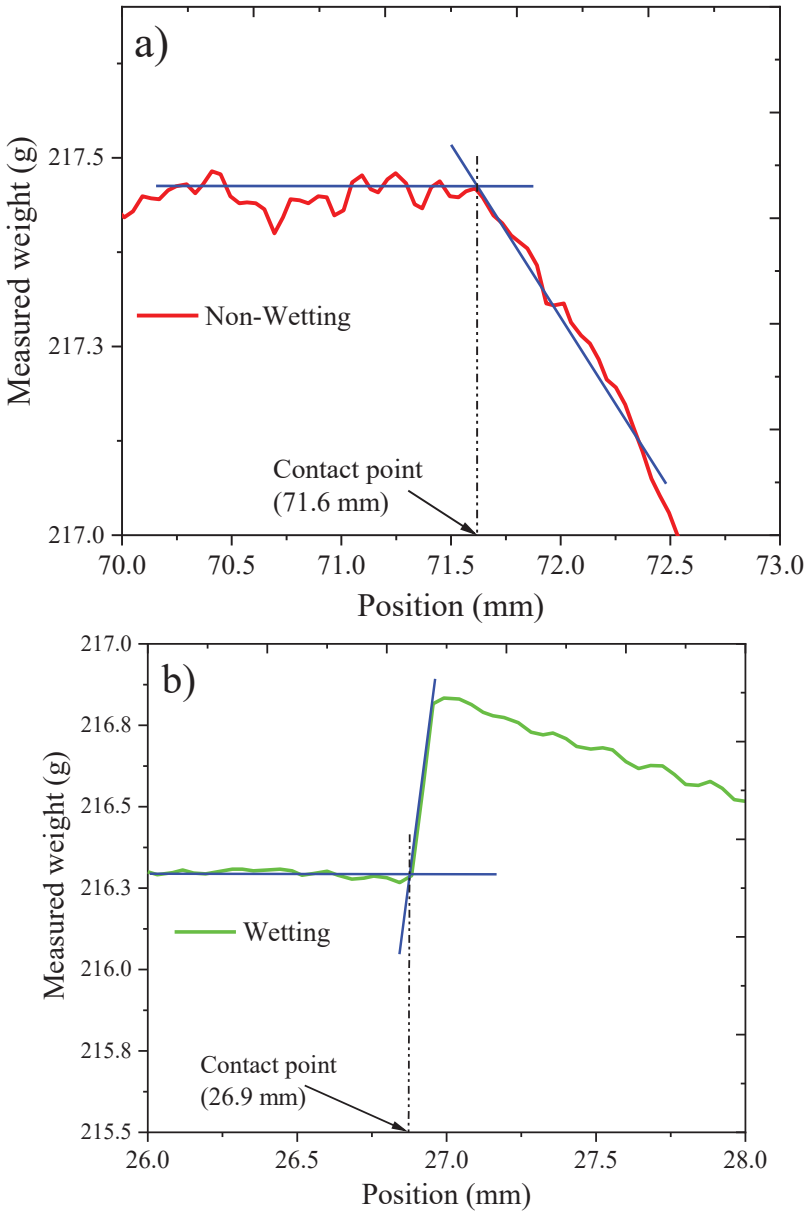

Figure 10.2E. Raw data plots for finding contact point. a) Non-wetting situation. b) Wetting situation.

Appendix E. Additional Data from Wetting Measurements

Table 10.3E. Summary of Results for Wetting Tests in Molten Electrolyte

		No Polarization			Prior to Polarization	30s Polarization		After Polarization		24 hours After Polarization
Test	Samples	Avg. corr. Weight. Immersion (g)	Avg. corr. Weight. Emersion (g)	Avg. Weight gained (g)	Avg. corr. Weight. Immersion (g)	Avg. corr. Weight. Emersion (g)	Avg. Weight gained (g)	Avg. corr. Weight. Immersion (g)	Avg. corr. Weight. Emersion (g)	Avg. weight. Loss (g)
1	Anthracitic	-0.62±0.03	-0.4±0.07	0	-0.86±0.04	1.06±0.28	1.63±0.02	0.8±0.06	1.84±0.24	
2	Anthracitic	-0.65±0.03	-0.63±0.08	0	-0.46±0.02	1.84±0.39	2.28±0.03	1.06±0.21	1.16±0.17	1.44±0.03
3	Anthracitic	-0.53±0.07	-0.74±0.05	0	-0.87±0.07	2.51±0.52	4.67±0.03	1.58±0.09	1.35±0.09	
4	Anthracitic	-0.49±0.02	-0.57±0.10	0	-0.53±0.02	1.79±0.27	2.13±0.01	1.85±0.11	2.22±0.13	
5	Graphitic	-0.58±0.03	-0.81±0.03	0	-0.45±0.03	1.94±0.21	1.93±0.02	0.62±0.03	1.33±0.09	
6	Graphitic	-0.51±0.04	-0.12±0.11	0	-0.53±0.05	1.64±0.21	2.04±0.01	0.83±0.03	1.18±0.23	0.57±0.03
7	Graphitic	-0.36±0.14	-0.48±0.11	0	-0.48±0.05	2.66±0.45	3.94±0.04	1.55±0.07	1.27±0.16	
8	Graphitic	-0.50±0.02	-0.70±0.04	0	-0.48±0.11	1.45±0.31	1.52±0.02	1.10±0.05	1.26±0.14	

Table 10.3E. Summary of Results for Wetting Test in Molten Electrolyte

		No Polarization			Prior to Polarization	30s Polarization		After Polarization		24 hours After Polarization
Test	Samples	Avg. corr. Weight. Immersion (g)	Avg. corr. Weight. Emersion (g)	Avg. Weight gained (g)	Avg. corr. Weight. Immersion (g)	Avg. corr. Weight. Emersion (g)	Avg. Weight gained (g)	Avg. corr. Weight. Immersion (g)	Avg. corr. Weight. Emersion (g)	Avg. weight Loss (g)
9	Graphitized	-0.6±0.02	-0.81±0.1	0	-0.6±0.02	1.28±0.26	1.39±0.03	0.80±0.02	0.74±0.06	
10	Graphitized	-0.44±0.03	-0.48±0.15	0	-0.48±0.03	1.39±0.21	1.25±0.03	0.55±0.05	0.89±0.06	0.54±0.03
11	Graphitized	-0.43±0.02	-0.63±0.03	0	-0.5±0.02	1.56±0.74	2.78±0.02	1.31±0.25	1.14±0.05	
12	Graphitized	-0.49±0.03	-0.69±0.08	0	-0.53±0.02	1.22±0.35	1.56±0.01	0.85±0.05	0.89±0.20	
13	Graphite	-0.42±0.05	-0.40±0.07	0	-0.64±0.01	0.61±0.07	1.51±0.03	0.80±0.04	1.03±0.18	

Appendix E. Additional Data from Wetting Measurements

Table 10.4E. Summary of Results for Wetting in Electrolyte with Al

		No Polarization			Prior to Polarization	30s Polarization	
Test	Samples	Avg. corr. Weight. Immersion (g)	Avg. corr. Weight. Emersion (g)	Avg. Weight gained (g)	Avg. corr. Weight. Immersion (g)	Avg. corr. Weight. Emersion (g)	Avg. Weight gained (g)
1	Anthracitic	0.75±0.02	0.57±0.08	0.10±0.02	0.73±0.02	0.56±0.08	0.35±0.02
2	Anthracitic	0.11±0.03	1.59±0.09	1.45±0.01	0.68±0.01	0.48±0.08	0.20±0.01
3	Anthracitic	0.72±0.04	1.58±0.28	0.37±0.01	1.49±0.2	0.94±0.01	0.2±0.01
4	Graphitic	0.57±0.06	0.52±0.06	0.27±0.08	0.83±0.05	0.54±0.05	0.17±0.02
5	Graphitic	-0.11±0.10	0.89±0.13	0.8±0.03	1.51±0.05	1.48±0.06	0.29±0.04
6	Graphitized	0.98±0.02	0.76±0.02	0.47±0.02	1.04±0.08	1.06±0.06	0.22±0.02
7	Graphitized	0.27±0.08	0.89±0.01	0.53±0.01	0.58±0.07	0.76±0.05	0.57±0.02
8	Graphitized	-0.1±0.05	1.1±0.14	0.48±0.06	1.09±0.09	1.14±0.07	0.32±0.02
9	Graphite	0.66±0.04	0.44±0.05	0.11±0.02	0.94±0.02	0.74±0.02	0.35±0.02
10	Graphite	-0.35±0.07	0.69±0.01	0.54±0.03	0.76±0.02	0.75±0.02	0.12±0.02

Table 10.5E. Summary of Results for Wetting in molten Al

		No Polarization			Prior to Polarization	30s Polarization	
Test	Samples	Avg. corr. Weight. Immersion (g)	Avg. corr. Weight. Emersion (g)	Avg. Weight gained (g)	Avg. corr. Weight. Immersion (g)	Avg. corr. Weight. Emersion (g)	Avg. Weight gained (g)
1	Anthracitic	-2.95±0.02	-3.12±0.07	0	-2.48±0.03	-2.91±0.05	0
2	Anthracitic	-2.65±0.1	-2.82±0.07	0	-2.79±0.07	-2.77±0.04	0
3	Anthracitic	-2.87±0.03	-2.45±0.09	0	-2.53±0.17	-2.92±0.4	0
4	Graphitic	-2.88±0.04	-3.06±0.03	0	-2.88±0.08	-2.99±0.05	0
5	Graphitic	-2.21±0.07	-2.61±0.08	0	-1.95±0.03	-2.11±0.02	0
6	Graphitic	-3.76±0.07	-3.62±0.12	0	-3.17±0.06	-3.47±0.06	0
7	Graphitized	-1.46±0.2	-1.15±0.08	0	-1.63±0.02	-2.12±0.06	0
8	Graphitized	-1.93±0.03	-1.15±0.1	0	-2.6±0.03	-2.71±0.03	0
9	Graphite	-2.21±0.03	-2.07±0.03	0	-2.21±0.02	-2.09±0.03	0

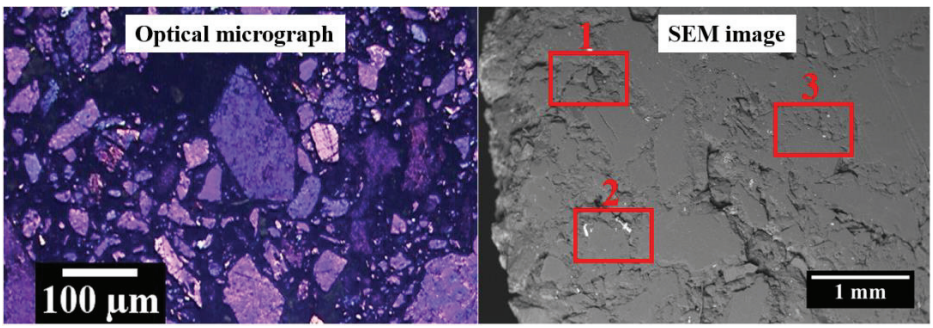

Figure 10.3E. Non-wetted anthracitic cathode sample after wetting test. Red rectangles indicate the data collections areas.

Table 10.6E. EDS elemental mapping data for the individual elements from Figure 10.1E. All measurements are in wt%

Area		Al	C	O	F	Na	Ca
1	**Mean**	0	93.6	5.1	0	0	0
1	**SD**	0.2	0.4	0.2	0	0	0.1
2	**Mean**	0.4	90.5	8.3	0	0	0
2	**SD**	0	0.2	0.1	0.1	0	0
3	**Mean**	0.3	89.2	9.7	0	0	0.1
3	**SD**	0	0.1	0.1	0	0	0

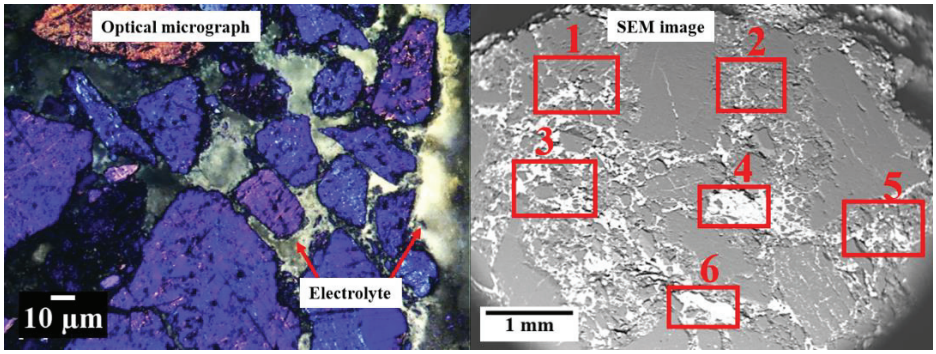

Figure 10.4E. Wetted anthracitic cathode sample after wetting test. Red numbered rectangles indicate location of data acquisitions.

Table 10.7E. EDS elemental mapping data from Figure 10.2E. All measurements are in wt%

Area		Al	C	O	F	Na	Ca
1	**Mean**	3.6	74.1	7.3	9.2	4.5	1.3
1	**SD**	0.1	0.2	0.1	0.1	0.1	0.1
2	**Mean**	3	74.9	4.1	12.4	4.6	1
2	**SD**	0.1	0.2	0.1	0.1	0.1	0.1
3	**Mean**	5.1	68.2	5.2	14.2	5.8	1.5
3	**SD**	0.1	0.2	0.1	0.2	0.1	0.1
4	**Mean**	7	58.4	8.8	17.1	7.5	1.2
4	**SD**	0.1	0.3	0.2	0.2	0.1	0.1
5	**Mean**	4.4	70.5	5.4	12.8	5.1	1.7
5	**SD**	0.1	0.2	0.1	0.1	0.1	0.1
6	**Mean**	5.1	62.8	7.1	16.4	7.2	1.4
6	SD	0.1	0.3	0.1	0.2	0.1	0.1

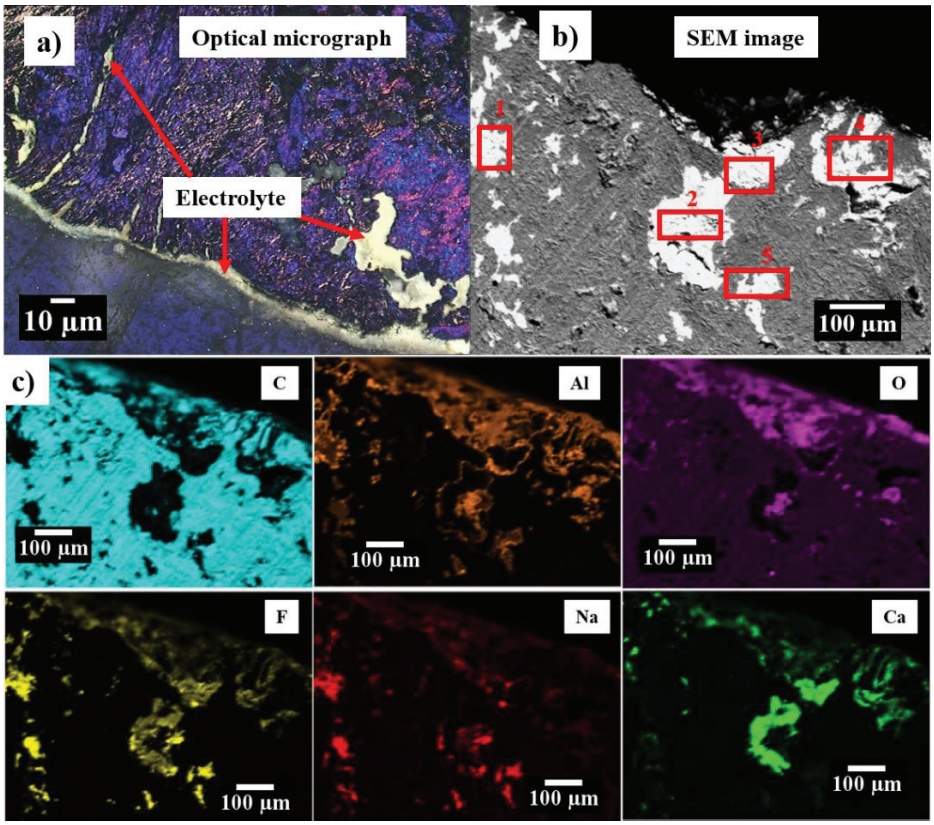

Figure 10.5E. Wetted graphitic cathode sample after wetting test. a) Optical micrograph with red arrows showing the locations of the electrolytes. b) SEM image, red numbered rectangles show locations for EDS data acquisition. c) EDS elemental maps acquired from the SEM image in Figure 4.3Eb.

Table 10.8E. EDS elemental mapping data for the individual elements from Figure 10.3E. All measurements are in wt%

Area		Al	C	O	F	Na	Ca
1	**Mean**	10.2	12.2	2.2	50	22	3.4
1	**SD**	0.1	0.2	0.1	0.2	0.1	0.1
2	**Mean**	13.6	5.1	0.5	53.8	21.6	5.4
2	**SD**	0.1	0.2	0.1	0.2	0.1	0.1
3	**Mean**	3.6	10	7.2	39.2	1.4	38.6
3	**SD**	0.2	0.1	0.2	0.2	0.1	0.1
4	**Mean**	12.1	18.3	4.1	43.1	18.2	4.2
4	**SD**	0.2	0.1	0.1	0.2	0.1	0.1
5	**Mean**	13.2	12.2	0.6	51.2	21.6	1.2
5	**SD**	0.2	0.2	0.1	0.2	0.1	0.1